

Decentralized control of sound radiation from periodically stiffened panels

Noah H. Schiller

Dissertation submitted to the Faculty of the
Virginia Polytechnic Institute and State University
in partial fulfillment of the requirements for the degree of

Doctor of Philosophy
in
Mechanical Engineering

Chris R. Fuller, Chair
William T. Baumann
Randolph H. Cabell
Martin E. Johnson
William R. Saunders

December 13, 2007
Blacksburg, Virginia

Copyright 2007, Noah H. Schiller

Decentralized control of sound radiation from periodically stiffened panels

Noah H. Schiller

(ABSTRACT)

Active structural acoustic control has previously been used to reduce low-frequency sound radiation from relatively simple laboratory structures. However, significant implementation issues have to be addressed before active control can be used on large, complex structures such as an aircraft fuselage. The purpose of this project is to extend decentralized structural control systems from individual bays to more realistic airframe structures. In addition, to make this investigation more applicable to industry, potential control strategies are evaluated using a realistic aft-cabin disturbance identified from flight test data.

This work focuses on decentralized control, which implies that each control unit is designed and implemented independently. While decentralized control systems are relatively scalable, performance can be limited due to the destabilizing interaction between neighboring controllers. An in-depth study of this problem demonstrates that the modeling error introduced by neighboring controllers can be expressed as the product of the complementary sensitivity function of the neighboring control unit multiplied by a term that quantifies the diagonal dominance of the plant. This understanding can be used to improve existing control strategies. For instance, decentralized performance can often be improved by penalizing control effort at the zeros of the local control model. This stabilizes each control unit and reduces the modeling error induced on neighboring controllers. Additional analyses show that the performance of decentralized model-based control systems can be improved by augmenting the structural damping using robust, low-authority control strategies such as direct velocity feedback and positive position feedback. Increasing the structural damping can supplement the performance of the model-based control strategy and reduce the destabilizing interaction between neighboring control units. Instead of using low-authority controllers to stabilize the decentralized control system, another option is to modify the model-based design. Specifically, an iterative approach is developed and validated using real-time control experiments performed on a structural-acoustic system with poles close to the stability boundary, non-minimum phase zeros, and unmodeled dynamics. Experiments demonstrate that the iterative control strategy, which combines frequency-shaped linear quadratic Gaussian (LQG) control with loop transfer recovery (LTR), is capable of achieving 12 dB peak reductions and a 3.6 dB integrated reduction in radiated sound power from a rib-stiffened aluminum panel.

This work was supported by the Structural Acoustics Branch at NASA Langley Research Center under contract number NCC-1-02043.

Acknowledgements

First, I would like to thank the National Institute of Aerospace (NIA) for offering a unique and rewarding graduate education program. Specifically, I'd like to thank Rita, Steve, Lisa, and Dr. Grossman, for making sure the classes ran smoothly despite being hundreds of miles away from many of the main campuses.

Next, I need to thank everyone in the Structural Acoustics Branch at NASA Langley Research Center for their help with various aspects of this project. In particular, I'd like to thank Dan, Doug, Gary, John, Joe, Tony, and Johnny, for entertaining lunch conversations through the years that provided a welcome break from my research. I am grateful for the assistance provided by Carlton, Clyde, and Jay during the experimental portion of this work. I certainly appreciate the support of Rich and Kevin, who ensured that the project was funded, and provided guidance and technical insight upon request. I also need to thank my office mates for their friendship, advice, and for much needed distractions. This includes: Joe, John, Adam, Mike, and Aaron (honorary office mate).

My mentor, Dr. Ran Cabell, was instrumental in this project. He oversaw the development and direction of this thesis and provided assistance and guidance at every step. His contribution is sincerely appreciated. I need to thank the rest of my committee members as well: Dr. Will Saunders for inspiring and encouraging me to pursue a Ph.D. in the first place; Dr. Martin Johnson and Dr. William Baumann for reviewing my dissertation and for providing helpful suggestions during the preliminary and final exams. Finally, I want to thank my advisor, Dr. Chris Fuller. I am grateful for the freedom he gave me to explore various ideas that were not always successful. His advice and guidance are very much appreciated. Ultimately, this work would not have been possible without his support, which I am extremely grateful for.

I also need to thank my family, who has provided support and encouragement throughout my life.

Finally, I want to thank my wonderful wife Bethany for being there for me during graduate school. Her unwavering love, patience, companionship, and countless home-cooked meals are all sincerely appreciated. I am immensely grateful to have her in my life.

Contents

1	Introduction	1
1.1	Background	1
1.1.1	Structural control	3
1.1.2	Control strategies	3
1.1.3	Decentralized control	6
1.2	Scope and objectives	7
1.3	Organization	8
2	Stiffened panel	10
2.1	Numerical model	11
2.1.1	Structural model	11
2.1.2	Piezostructure	13
2.1.3	Structural-acoustic coupling	15
2.1.4	Simulated disturbance	17
2.2	Experimental setup	26
2.2.1	Test article	26
2.2.2	Structural Acoustic Loads and Transmission facility	28
2.2.3	Acoustic excitation	31
2.2.4	Experimental procedure	34
3	Linear quadratic control	36
3.1	Full-state feedback	36
3.1.1	Continuous-time stability margins	38
3.1.2	Discrete-time stability margins	39
3.2	State estimation	39
3.3	Linear quadratic Gaussian (LQG) control	41
3.4	Frequency shaping	43
3.5	Loop recovery	45

3.6	Simple example	46
3.7	Summary	50
4	Decentralized control of interacting subsystems	51
4.1	Background	52
4.1.1	Numerical simulation	53
4.1.2	Experimental example	55
4.2	Frequency-shaped LQG	57
4.3	Frequency-shaped loop recovery	60
5	Low-authority control	63
5.1	Triangularly shaped strain actuators	65
5.1.1	HAC/LAC	68
5.1.2	Macro-Fiber Composite (MFC) actuator	71
5.1.3	Flexible boundary	72
5.2	Large rectangular actuator	74
5.3	Experimental results	80
5.4	Summary	82
6	Indirect adaptive control	84
6.1	Controller initialization	86
6.2	Update procedure	87
6.2.1	Disturbance model	87
6.2.2	Effort weighting term	89
6.2.3	Design evaluation	89
6.3	Validation	91
6.3.1	Case 1: Structural excitation	91
6.3.2	Case 2: Acoustic disturbance	92
6.3.3	Case 3: Radiation mode estimates	95
6.4	Scalability	96
7	Summary and conclusions	99
A	Piezoelectric coupling	105
B	Disturbance rejection	111
B.1	Stability	112

B.2	Unstructured uncertainty	112
C	Disturbance model	115
C.1	Flight idle: Turbulent boundary layer noise	115
C.2	Maximum climb: Shock-cell and TBL noise	117
D	Feedforward control	121
D.1	Background	121
D.2	Numerical simulations	126
D.3	Experimental results	131
E	Simulink diagrams	135

List of Figures

1.1	A sketch of the sidewall of an aircraft.	2
1.2	Block diagrams of: (a) a centralized control system; and (b) a two-channel decentralized control system.	5
2.1	Diagram of the clamped, stiffened panel.	11
2.2	Mode shapes for the first eighteen structural modes of the clamped two-bay structure.	12
2.3	The diagrams show: (a) a conventional piezoceramic wafer; and (b) an interdigitated electrode pattern.	14
2.4	Radiation efficiencies of the first sixteen radiation modes for the structure.	17
2.5	Point forces are used to simulate the response of a randomly excited panel.	19
2.6	The figure shows the spatial coherence for a: (a) TBL excitation; and (b) shock-cell noise.	20
2.7	Power spectral density of boundary-layer noise (dash-dotted blue line), the combined excitation (solid black line), and shock-cell noise (dashed red line).	20
2.8	Radiated sound power with tension (thick black line) and without tension (thin red line).	21
2.9	The figure shows the relationship between the resonance frequencies on the tensioned and un-tensioned structures.	22
2.10	The power spectral densities of the original disturbance (solid black line) and frequency shifted disturbance (dashed red line).	22
2.11	The desired disturbance is generated by passing white noise inputs through a filter matrix.	23
2.12	The figure shows the normalized sound power integrated from 50 to 800 Hz for each of the first eight radiation modes.	25
2.13	The figure shows the radiated sound power calculated using: a 5×6 grid of measurement points (dotted red line); a 7×8 grid of measurement points (dotted blue line); and a 12×12 grid of measurement points (solid black line).	25
2.14	The figures show: (a) a photograph of the stiffened aluminum test panel as seen from the reverberation chamber; and (b) a diagram of the other side of the panel showing the lead vinyl sheet and transducers.	27
2.15	The pictures show the test panel, as seen from the anechoic chamber.	28
2.16	The diagrams show: (a) the transducers used for high-authority control; and (b) the transducers used for low-authority control.	28

2.17	Diagram of the Structural Acoustic Loads and Transmission (SALT) facility at NASA Langley Research Center.	29
2.18	The block diagram shows the high-authority and low-authority control systems.	30
2.19	The disturbance is generated using a loudspeaker in the anechoic chamber.	31
2.20	Power spectral density of the frequency shifted excitation (solid black line), the desired excitation (dash-dotted blue line), and the measured excitation (thin red line).	32
2.21	The figure shows the magnitude of the frequency response function and coherence between the drive signal and the microphone.	33
2.22	The power spectral density of the drive signal required to achieve the desired spectral shape in front of the panel.	33
2.23	Estimate of the acoustic power radiated from the two bays due to the acoustic excitation.	33
2.24	Operating deflection shapes due to the acoustic excitation.	34
2.25	The figure shows the experimental frequency response function between the PZT actuator and the summed accelerometers on the lower bay.	35
2.26	The figure shows the experimental frequency response function between the PZT actuator and the summed accelerometers on the upper bay.	35
3.1	The figure shows an LQR block diagram with unity feedback.	38
3.2	Estimator block diagram.	40
3.3	LQG diagram	42
3.4	Augmented plant model used to shape the control effort.	44
3.5	Diagram of an augmented plant model used to shape the disturbance path. The figures show: (a) a general block diagram; and (b) a diagram expressed in terms of the disturbance model and control path.	44
3.6	Simple 3-DOF spring-mass-damper model.	47
3.7	Nyquist plot of the open-loop frequency response with an LQR controller (solid blue lines), and an LQG controller. The LQG controller is designed with (a) $Q_n = 10^3$ (dashed green line); and (b) $Q_n = 10^9$ (dash-dotted red line).	48
3.8	Magnitude of the open-loop FRF (solid black line), closed-loop FRF with an LQR controller (solid blue line), closed-loop FRF with the standard LQG controller (dashed green line), and closed-loop FRF with an LQG/LTR design (dash-dotted red line).	48
3.9	Magnitude of the original disturbance model (dashed green line), and the frequency-shaped disturbance model (dash-dotted red line).	49
3.10	Nyquist plot of the discrete system with an LQR controller (solid blue line), LQG controller (dashed green line), and frequency-shaped LQG/LTR design (dash-dotted red line). For clarity, the response is only shown from 0.68 – 2.5 Hz. The figure on the right shows an expanded view of the response on the left.	49
3.11	Magnitude of the open-loop FRF (solid black line), closed-loop FRF with an LQR controller (solid blue line), closed-loop FRF with an LQG controller (dashed green line), and closed-loop FRF with a frequency-shaped LQG/LTR design (dash-dotted red line).	50
4.1	Block diagram of a decentralized control system [adapted from Cabell et al. (2003)].	51

4.2	Two-channel decentralized control system. The figures show: (a) the standard block diagram; and (b) a rearranged diagram highlighting the additive error introduced by neighboring controllers.	52
4.3	Block diagrams demonstrating that neighboring control loops affect both the plant dynamics and the disturbance.	53
4.4	The figure shows the Bode diagram of the open-loop response from u_2 to y_2 (solid blue line), along with the new response generated by including the neighboring control loop (dashed red line).	54
4.5	The power spectra of the open-loop response (solid black line), nominal closed-loop response (solid blue line), and combined closed-loop response (dashed red line).	55
4.6	Magnitude of the open-loop frequency response for (a) G_{11} (solid black line) and G_{12} (dashed red line); (b) G_{22} (solid black line) and G_{21} (dashed red line).	56
4.7	Interaction metric for the two-bay laboratory system.	56
4.8	The figure shows the measured power spectra of the open-loop response on the upper bay (solid black line), the nominal closed-loop response (solid blue line), and the actual closed-loop response (dashed red line).	57
4.9	The figure shows the amplitude of the nominal plant model on the upper bay (solid black line), the standard frequency independent effort-weighting term (dashed red line), and the shaped effort-weighting term (solid green line).	58
4.10	The open-loop response (solid black lines), standard LQG response (dashed red lines), and frequency-shaped LQG response (solid green lines). The figures show: (a) the simulated power spectra; and (b) the measured power spectra.	58
4.11	The figure shows the measured power spectra of the open-loop response (solid black line), the closed-loop response with the standard LQG controller on the lower bay (dashed red line), and the closed-loop response with the frequency-shaped LQG controller on the lower bay (solid green line).	59
4.12	The figure shows the simulated power spectra of the open-loop response on the lower bay (solid black line), the nominal closed-loop response simulated using only the controller on the lower bay (solid blue line), and the actual closed-loop response simulated with both controllers (dashed red line).	60
4.13	The figure shows the magnitude of the nominal disturbance model (dashed red line) and the modified disturbance model used to exploit loop recovery (solid green line).	61
4.14	The figure shows the simulated power spectra of the open-loop response on the lower bay (solid black line), the closed-loop LQG response using the nominal disturbance model (dashed red line), and the closed-loop LQG response exploiting loop recovery (solid green line).	61
5.1	The figure shows closely located point velocity sensors positioned at the tip of triangular piezoelectric patch actuators.	66
5.2	Triangular strain actuators represented in terms of point forces and line moments [adapted from Gardonio and Elliott (2005)].	67
5.3	The frequency response function for the circled transducer pair shown in Figure 5.1 (solid black line), and the frequency response function using a 50% smaller actuator (dashed red line).	68

5.4	The figures show the Nyquist plots of the open-loop frequency response functions for the sensor-controller-actuator transfer functions from 0-5 kHz. A feedback controller with a gain of 1.1 is used in the figure on the left, while a first-order low-pass filter with a corner frequency at 2000 Hz and a gain of 2.4 is used in the figure on the right.	69
5.5	Radiated sound power from the structure with no control (solid black line), using DVF with a gain of 1.1 (solid red line), and using a first-order low-pass filter with a corner frequency at 2000 Hz and a gain of 2.4 (dashed blue line).	69
5.6	The diagram shows a combined HAC/LAC configuration using the triangular actuators along the boundaries.	70
5.7	The radiated sound power from the structure before control (solid black line), using standard LQG controllers (dashed red line), and using both LQG and DVF (dash-dotted blue line).	70
5.8	Nyquist plot of the sensor-controller-actuator transfer function using LQG control (solid red line), and using DVF and LQG control (dash-dotted blue line).	71
5.9	Frequency response functions for a modified MFC actuator and point sensor (solid black line), and an ideal point force actuator and velocity sensor located at the vertex of the triangular actuator (dashed red line).	72
5.10	The diagram shows closely located point sensors and triangular actuators positioned on either side of the stiffener.	73
5.11	The frequency response functions for a standard triangularly shaped piezoelectric actuator and point sensor pair located along the flexible boundary (solid black line), and for the modified MFC actuator and point sensor pair (dashed red line).	73
5.12	The diagram shows a large piezoelectric patch actuator with five point velocity sensors.	74
5.13	The frequency response function between the piezoelectric actuator and the sum of the point sensors shown in Figure 5.12.	74
5.14	The diagrams show: (a) the 200 Hz mode shape and the transducer placement; and (b) the normalized transverse displacement of the stiffener in the top figure, and the normalized transverse displacement along a vertical line, centered on the plate, in the bottom figure.	75
5.15	The frequency response functions using an ideal 1-D actuator and the sum of: five point sensors (solid black line); and twenty point sensors (dashed red line).	76
5.16	The diagram shows a large MFC actuator positioned along the stiffener along with five point velocity sensors.	76
5.17	The frequency response function between the MFC actuator and the sum of the point sensors shown in Figure 5.16.	76
5.18	The diagram shows a large MFC actuator positioned along the stiffener along with five point sensors distributed over both bays.	77
5.19	The frequency response function for the actuator-sensor pair shown in Figure 5.18.	77
5.20	Radiated sound power with no control (solid black line) and using DVF (solid red line) with the transducer configuration shown in Figure 5.18.	78
5.21	The diagrams show: (a) a combined HAC/LAC configuration with an MFC actuator along the stiffener; and (b) the Nyquist plot of the sensor-controller-actuator transfer function using LQG control (solid red line), and using DVF and LQG control (dash-dotted blue line).	79
5.22	The radiated sound power from the structure before control (solid black line), using only DVF (solid green line), using LQG controllers (dashed red line), and using both LQG and DVF (dash-dotted blue line).	79

5.23	Radiated sound power before control (solid black line), and using PPF (solid red line). . . .	80
5.24	Nyquist plot of the sensor-controller-actuator transfer function shown in Figure 5.18. Positive position feedback is used for control.	80
5.25	The experimental frequency response function estimated from the MFC drive signal to the summed and integrated accelerometers.	81
5.26	The Nyquist plot of the measured sensor-actuator frequency response function with a feedback gain of 0.7.	82
5.27	Radiated sound power without control (solid black line), using DVF (solid red line), and using PPF control (dashed blue line).	82
6.1	The indirect adaptive control strategy is divided into two separate processes: a real-time process occurring at every sample (solid lines), and a slower process that updates the controller infrequently (dashed lines).	85
6.2	The amplitude of the old disturbance model (solid black line), the magnitude of the Fourier transform of the current disturbance estimate (solid blue line), and the amplitude of the new disturbance model (dashed red line).	89
6.3	Flow chart of the evaluation process.	90
6.4	The amplitude of the initial LQG design (solid blue lines), and the amplitude of the final design (dashed red lines). The graphs show: (a) the amplitude of the disturbance model; and (b) the amplitude of the frequency-shaped effort weighting term.	92
6.5	The power spectra of the sensor response on the upper bay, before control (solid black line), with the initial LQG controller (solid blue line), and with the final design (dashed red line).	93
6.6	The power spectra of the sensor response on the upper bay, before control (solid black line), with a standard decentralized LQG design (solid green line), and with the adaptive control strategy (dashed red line).	93
6.7	The amplitude of the initial disturbance model (solid blue line), the amplitude of the final disturbance model (dashed red line), and the amplitude of the measurement noise model (dash-dotted green line).	94
6.8	The power spectra of the measured response on the upper bay driven by an acoustic disturbance, before control (solid black line), using the initial controller (solid blue line), and using the final design (dashed red line).	95
6.9	The total radiated sound power from the two-bay structure before control (solid black line), and using the final controller (dashed red line).	95
6.10	The total radiated sound power from the two-bay structure before control (solid black line), using a single radiation mode estimate (solid blue line), and using six radiation mode estimates (dashed red line).	96
6.11	The figures show: (a) a sketch of the decentralized control problem; and (b) a block diagram of the system reduced to a simple model with an additive uncertainty term.	97
A.1	The diagrams show: (a) a conventional piezoceramic wafer; and (b) an interdigitated electrode pattern.	105
A.2	The diagrams show: (a) the direction convention; and (b) the material and global coordinate systems.	107

A.3	The figures show the electric fields in: (a) a conventional piezoceramic wafer; (b) an MFC actuator [adapted from Bevan (2000)].	109
A.4	Equivalent MFC configuration.	110
B.1	Disturbance rejection.	111
B.2	The figures show: (a) a simple Nyquist diagram illustrating the concepts of gain and phase margins; and (b) an example demonstrating the relationship between multiplicative uncertainty and the required stability margins.	112
B.3	The figure shows: a) the actual plant; b) the plant model with additive uncertainty; and c) the plant model with multiplicative uncertainty [adapted from Bitmead et al. (1990)].	114
C.1	Shock-cell noise is generated when shocks in the exhaust plume interact with turbulence structures in the mixing layer.	116
C.2	Boeing QTD1 flight test.	116
C.3	Streamwise variation of the power spectral density during maximum climb.	118
C.4	Estimate of the power spectrum for shock-cell noise (at transducer 53).	118
C.5	Magnitude squared coherence between pressure transducers 49 and 53 during maximum climb.	118
C.6	Spatial correlation during maximum climb.	119
C.7	Measured and fit spatial coherence at 609 Hz during maximum climb (relative to transducer 49).	120
D.1	General FIR filtering problem.	122
D.2	The figures show: (a) a simple feedforward control system; and (b) a rearranged diagram valid for linear time-invariant systems.	124
D.3	Block diagram of the filtered reference LMS algorithm.	125
D.4	Feedforward diagram showing the location of the transducers used for control.	126
D.5	Block diagram of the single-reference, two-channel decentralized feedforward control system.	127
D.6	Simulated power spectra of the open-loop responses (solid black lines) are compared with the closed-loop responses (dashed red lines). The simulation is performed using: (a) a spatially correlated disturbance representative of shock-cell noise; and (b) an uncorrelated disturbance similar to TBL noise.	128
D.7	The figure shows the frequency shifted spectra for TBL noise (dash-dotted blue line), shock-cell noise (dashed red line), and the combined excitation (solid black line).	128
D.8	The power spectra of the open-loop response (solid black line) and closed-loop response (dashed red line) simulated using the combined excitation.	129
D.9	Coherence between the reference signal and the error signal on the upper bay. The simulations are performed using a reference signal centered above the panel (dashed blue line), using a time-advanced reference signal 0.476 m upstream of the panel (solid red line), and using a time-advanced reference signal 1.43 m upstream of the panel (dash-dotted green line).	129

D.10	Simulated power spectra of the open-loop response (solid black lines) is compared with the closed-loop response simulated using a delayed reference signal centered above the panel (dashed blue line) and using a time-advanced reference signal 0.476 m upstream of the panel (solid red line).	130
D.11	Radiated sound power without control (solid black line), and using the delayed reference sensor directly above the panel (dashed red line).	130
D.12	Coherence between the reference signal and the error signal from the lower bay (solid black line), and the coherence between the reference signal and the error signal from the upper bay (dash-dotted blue line).	131
D.13	The figure shows the time record for a subset of filter coefficients.	132
D.14	The power spectra of the measured responses before control (solid black lines) and using the converged feedforward controller (dashed red lines). The figures show: (a) the measured response on the lower bay; and (b) the measured response on the upper bay.	132
D.15	A general block diagram for a feedforward control system.	133
D.16	The magnitude of the feedback path from the piezoelectric actuator on the lower bay to the microphone.	133
D.17	The radiated sound power from the structure before control (solid black line) and using the converged feedforward control system (dashed red line).	134
E.1	Diagram of the high-authority feedback control system.	135
E.2	Diagram of the LQG subsystem.	136
E.3	Diagram of the low-authority feedback control system.	136
E.4	Diagram of the feedforward control system.	137
E.5	Diagram of the FXLMS subsystem.	138

List of Tables

2.1	Dimensions and physical properties of the two-bay model	12
2.2	Material properties for two types of piezoceramic actuators.	14
3.1	Summary of the standard optimal regulation and estimation problems.	42
C.1	Time delay relative to pressure transducer 41	119

Nomenclature

a	acceleration, height
b	length
c	speed of sound, damping
c^E	short circuit stiffness matrix
d	disturbance signal, strain constant
e	error signal, piezoelectric material constant
f	frequency, force
f_s	sample rate
g	subsystem
h	thickness
i	index
j	$\sqrt{-1}$, index
k	wavenumber, discrete frequency variable, stiffness, gain
l	length
m	number of inputs, mass, moment, slope
n	discrete time variable, state noise
p	pressure, cross correlation vector
r	separation distance, filtered reference signal
s	Laplace transform variable
t	time
u	control signal
v	velocity, voltage, measurement noise
w	disturbance, FIR filter coefficients
x	coordinate, state, reference signal
y	coordinate, output signal

z	coordinate, z-transform variable
A	state matrix
B	input matrix
C	output matrix, controller, damping matrix
D	direct transmission matrix
DM	disturbance model
E	noise input matrix
F	controller
G	plant, shear modulus
GM	gain margin
I	identity matrix
J	cost function
K	stiffness matrix, gain matrix
L	correlation lengths, observer gain matrix
L_u	elastic differential operator
L_ϕ	electrical differential operator
M	mass matrix
N	number of filter coefficients, number of interdigitated electrodes
P	power, filter matrix, spectral factor
PM	phase margin
Q	state weighting matrix, eigenvector
\tilde{Q}	output weighting matrix
Q_n	disturbance covariance
R	radiation resistance matrix, autocorrelation matrix
\tilde{R}	effort weighting matrix
R_n	measurement noise covariance
S	area, spectral density, solution of the Riccati equation, sensitivity function
S_p	spatial aperture
T	complementary sensitivity function, stress transformation matrix
U	velocity
Y	Young's modulus
Z	acoustic impedance

α	empirical constant, leakage parameter
β	empirical constant, leakage parameter
χ	spatial domain
Δ	uncertainty
ϵ	strain
η	generalized displacement
γ	coherence, strain
λ	eigenvalue, effort weighting model
Λ	eigenvalue
μ	convergence coefficient
ν	Poisson's ratio
Φ	eigenfunction
Φ_v	assumed potential distribution
ρ	density
σ	radiation efficiency, normal stress
Θ	electromechanical coupling matrix
τ	update parameter, shear stress
ω	angular frequency
ξ	modal damping ratio

Chapter 1

Introduction

Aft-cabin noise in commercial jets is an occupational hazard for flight crew and an inconvenience for passengers. Problems associated with prolonged exposure to high noise levels include hearing loss and increased stress levels, which in turn can increase the risk of other serious health problems such as a stroke or heart attack (Boden-Albala and Sacco 2000; Willich et al. 2006). To address these risks, increasingly stringent occupational noise regulations have been proposed by the European Union (European Union 2003). In addition to added pressure by regulatory agencies, passengers and airlines are also demanding a quieter cabin environment. With a projected 2.8 trillion dollar market for new commercial aircraft in the next 20 years (Boeing 2007), there is a large financial incentive to address this problem.

While traditional passive treatments, such as poro-elastic foam, are effective at high frequencies, they are usually inadequate at frequencies below 500 Hz due to size and weight constraints. Therefore, researchers have investigated active techniques designed to reduce interior noise for well over two decades (Nelson and Elliott 1992; Fuller et al. 1996). Although there are many ways to approach the cabin noise problem, this investigation is restricted to primary structural control. This strategy uses structural control inputs on the fuselage to reduce the sound transmitted through the structure. In general, the aircraft fuselage consists of orthogonal supports covered by a thin aluminum skin, as shown in Figure 1.1. The supports, called ring frames and stringers, segment the fuselage into a collection of rectangular bays. While active control results have been promising on individual bays, significant implementation issues must be addressed before active control systems are implemented on an aircraft fuselage containing hundreds of bays (Cabell et al. 2003). In particular, while centralized strategies have been used to simultaneously reduce the sound radiation from multiple bays, they require a high level of connectivity, are computationally intensive, and can be sensitive to transducer failures. On the other hand, decentralized strategies, which control each bay independently using only local information, are simple, computationally intensive, and scalable. Unfortunately the performance of decentralized strategies is often limited due to the unmodeled interaction between neighboring controllers (Gibbs and Cabell 2002). Therefore, the goal of this project is to develop a more effective decentralized structural control strategy designed to reduce sound radiation from multiple aircraft-style bays.

1.1 Background

Initial active noise control (ANC) systems were designed to cancel the offending sound field using acoustic control sources. For instance, in 1936 Lueg received a patent for a technique to control sound waves in a duct using a loudspeaker driven by an upstream microphone, which provided time-advanced information about the disturbance. One of the first ANC systems for interior cabin noise was proposed in 1953 by Olson and May. They proposed using a microphone and loudspeaker placed in the back of a seat to create a local

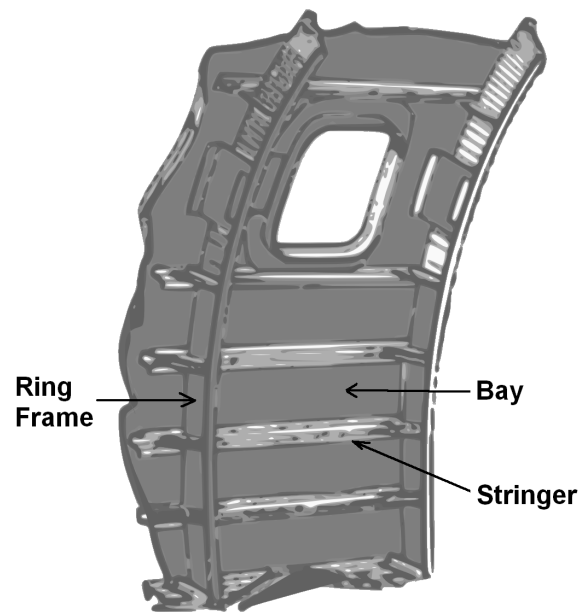


Figure 1.1: A sketch of the sidewall of an aircraft.

zone of quiet around the head of a passenger. More recent research by Rafaely et al. (1999), has shown that a practical implementation of this strategy can be effective for broadband noise up to several hundred hertz. Since the objective of these control systems is to reduce the sound pressure level in the vicinity of error microphones, they are called local control approaches. In contrast, global control approaches using acoustic sources have primarily been restricted to tonal disturbances, such as propeller-induced cabin noise. In 1990, Elliott et al. presented results from active control experiments performed on a British Aerospace 748 twin turboprop aircraft. The active control system consisted of 16 loudspeakers and 32 microphones distributed throughout the cabin. Using this system, Elliott et al. (1990) achieved a 13 dB global reduction in the fundamental harmonic, and reduced the second and third harmonics by up to 12 dB. Similar ANC systems are now commercially available for some turboprop aircraft (Emborg et al. 1998). While ANC using acoustic control sources can be effective for tonal disturbances, this strategy is not practical for global attenuation of broadband noise (Clark and Gibbs 1999).

A less invasive alternative to scattering acoustic sources throughout the cabin is to position the actuators on or near the walls of the fuselage in an effort to reduce the sound transmitted into the aircraft. In 1988, Deffayet and Nelson performed a theoretical study investigating active control of sound radiation from a simply-supported panel using acoustic monopoles. Their results predicted that the number of monopoles required to produce substantial reductions in the radiated power depends on the panel mode. This indicates that many acoustic control sources may be required to provide global control if the sound source is complex. As a result, researchers have investigated other ways to reduce the sound radiated from the sidewall of an aircraft.

1.1.1 Structural control

Many promising and novel strategies have been proposed in the past two decades to reduce the sound transmitted through the fuselage, including active foam (Guigou and Fuller 1999; Fuller et al. 2000; D'Angelo 2004), double panel designs (Gardonio and Elliott 1999; Carneal and Fuller 2004), and fluidic wallpaper (Czech and Anderson 2003). However, one of the most promising approaches appears to be active structural acoustic control (ASAC). This technique uses structural control inputs to modify the velocity distribution of the fuselage such that the overall sound power radiated from the sidewall of the aircraft is reduced (Fuller 1987; Fuller and Jones 1987). While active vibration control (AVC) can also be used to reduce the sound power radiated from a structure, ASAC minimizes sound radiation by modifying the structural response instead of eliminating it. Thus, ASAC can require fewer control channels and less control power (Fuller et al. 1996). Fuller et al. (1991) showed that ASAC reduces the radiated sound power by both suppressing and restructuring the modal response of the structure. For a panel excited at resonance, ASAC tends to suppress the structural modes that radiate most efficiently. In contrast, when the panel is excited off resonance, modal restructuring tends to be the dominant control mechanism. Modal restructuring changes the relative phase of the structural modes, resulting in a more complex vibration pattern that does not radiate as efficiently. Therefore, the vibration levels can actually increase while the overall radiated sound power from the structure decreases. A detailed description of ASAC is provided by Fuller et al. (1996).

Early ASAC research focused on designing structural actuators and used microphones scattered throughout the far field to provide an estimate of radiated sound power. To develop more practical systems, researchers began to replace error microphones in the far field with sensors integrated with the structure. Much of the work on structural error sensors was inspired by the concept of independently radiating surface velocity distributions, called radiation modes. Elliott and Johnson (1993) described the concept of radiation modes using existing formulations expressed either in terms of the amplitude of structural modes (Cunefare 1991; Baumann et al. 1991) or in terms of the velocity of elemental radiators (Nelson et al. 1987). While the sound radiation due to one structural mode or elemental radiator is dependent on other modes or radiators, radiation modes are independent of one another. Using this concept, researchers developed distributed strain sensors (Clark and Fuller 1992; Collins et al. 1994; Johnson and Elliott 1995; Charette et al. 1998) and accelerometer arrays (Maillard and Fuller 1998; Gibbs et al. 2000; Lee et al. 2002), which measure the velocity distributions that radiate most efficiently. Note that for sufficiently low excitation frequencies, such that the panel dimensions are small relative to the acoustic wavelength, the first radiation mode closely corresponds to the volume velocity of the structure. Since active control is most effective at low frequencies where the first radiation mode dominates, the output of a single volume velocity sensor is often sufficient for ASAC (Johnson and Elliott 1995).

1.1.2 Control strategies

Control algorithms for interior noise control applications are typically selected based on whether or not a reference signal is available. In general, feedforward control is used if a reference is available, while feedback is used if no reference signal is available. Adaptive feedforward controllers, such as the filtered-x LMS (FXLMS) algorithm, are often used for propeller aircraft since a reference signal unaffected by the control inputs can be obtained from an engine tachometer. In the case of propeller noise, the disturbance is tonal, which makes control relatively easy. For example, the adaptive filter only requires two parameters to

control a single tone (Elliott 2001). In contrast, feedforward control of stochastic disturbances is much more difficult. In order to control random disturbances, the reference must be time-advanced, since future values of the disturbance are not predictable. Therefore, feedforward control systems for broadband disturbances are much less common in the noise control literature.

In contrast, feedback control algorithms do not require a reference signal and are therefore better suited for broadband disturbances such as TBL noise. A common approach for broadband disturbance rejection is to feed back signals from accelerometers or piezoelectric transducers to piezoceramic actuators bonded to the structure (Clark et al. 1998). One particularly simple and robust control strategy uses a distributed array of actuator/sensor pairs with local feedback loops, as described by Elliott et al. (2002). If the transducer pairs are collocated and dual, then any passive (energy dissipative) control law, such as negative rate feedback, will guarantee unconditional stability of the closed-loop system (Balas 1979). Unfortunately, real transducer pairs are never perfectly matched, which eliminates the passive property of the system at high frequencies. Despite this limitation, researchers have shown promising results using real transducer pairs (Petitjean and Legrain 1996; Petitjean et al. 2002; Bianchi et al. 2004). For instance, Bianchi et al. (2004) showed that sixteen independent control units, each consisting of a single accelerometer and a small rectangular piezoceramic patch, could be used to reduce the amplitude of the first five resonances of a panel by 12-18 dB. Recently, Gardonio and Elliott (2005) extended this work to show that the performance of the control system could be improved using triangular actuators distributed around the perimeter of a simply supported panel. The triangular shape improves the stability bounds of the system, allowing higher feedback gains and therefore better performance. In general, rate feedback using collocated transducer pairs augments the inherent damping in the structure, and is therefore well suited for lightly damped metallic structures such as the aluminum sidewall of an aircraft. However, the conservative nature of this approach provides stability guarantees at the expense of performance. Therefore, this strategy is often referred to as low-authority control (LAC) (Aubrun 1980). Another disadvantage of this approach is the need for a large number of independent actuator/sensor pairs. While the actuators and sensors are typically light and compact, the control electronics are not. Since a power amplifier is required for each independent actuator, the weight of the entire control system could make the approach impractical.

Modern feedback control systems, on the other hand, are typically implemented with a relatively simple array of sensors and actuators (Clark and Cox 1999; Viperman and Clark 1999; Gibbs et al. 2004). Often the transducers are not collocated or dual, and a frequency weighted cost function, typically based on radiation filters, is used to focus control energy on the velocity distributions that radiate most efficiently. Therefore, modern feedback control is referred to as a high-authority control (HAC) approach (Aubrun and Ratner 1984).

One of the first papers discussing the use of modern feedback techniques for active structural acoustic control was written by Baumann et al. (1991). They proposed that the structural acoustic control problem could be solved using linear quadratic Gaussian (LQG) theory. Their formulation involved the derivation of a radiation filter, which provided a measure of the radiated sound power based on modal velocity inputs. An optimal feedback controller was then designed by incorporating a state-space realization of the radiation filter with the structural model. The resulting controller minimized a cost function expressed in terms of the total radiated sound power from the structure.

Since HAC strategies, such as LQG control, are model based, the performance of the controller depends on

the fidelity of the control model (Doyle 1978). Poorly modeled dynamics can cause spillover and destabilize the closed-loop system. Note that in the context of this work, spillover is the undesired amplification of the response with respect to the open-loop system. Despite this limitation, researchers have experimentally shown that HAC approaches can be used effectively to reduce the radiated sound power from simple structures (Vipperman and Clark 1999; Gibbs et al. 2004).

While HAC has been used successfully on simple structures, significant implementation issues must be addressed before active control can be implemented on an aircraft fuselage consisting of several hundred bays (Cabell et al. 2003). For example, consider the general feedback control system shown in Figure 1.2 (a). In this figure, the control inputs are denoted u and the measured outputs are denoted y . The plant G can be defined as

$$G = \begin{bmatrix} g_{11} & g_{12} & \cdots & g_{1m} \\ g_{21} & g_{22} & \cdots & g_{2m} \\ \vdots & \vdots & \ddots & \vdots \\ g_{m1} & \cdots & & g_{mm} \end{bmatrix} \quad (1.1.1)$$

where g_{ij} is the transfer function from the i^{th} actuator to the j^{th} sensor. In this example, the plant is assumed to be square with m inputs and outputs. Therefore, the optimal multichannel controller C can be expressed as an $m \times m$ array of transfer functions. The objective of the control problem is to design the fully-coupled controller to minimize a given cost function. While the resulting controller is optimal, centralized control may not be practical on systems with a large number of inputs and outputs since it requires a high level of connectivity, which can result in excessive wiring and weight. In addition, centralized control is computationally intensive, and can be sensitive to transducer failures.

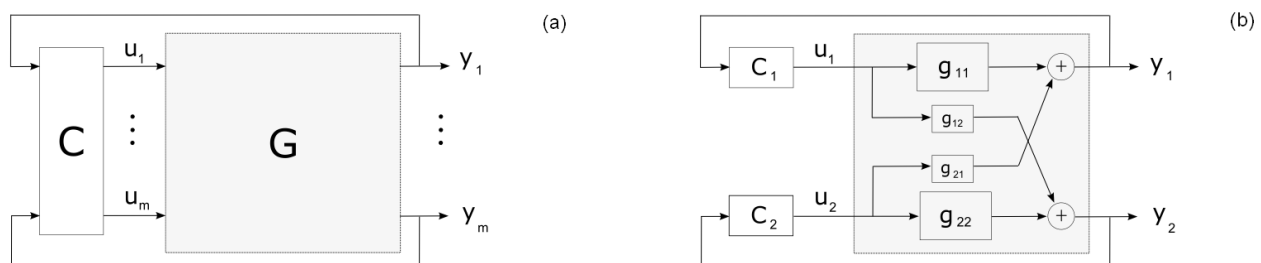


Figure 1.2: Block diagrams of: (a) a centralized control system; and (b) a two-channel decentralized control system.

One way to reduce the computational complexity of the control system is to use a simplified hierarchical control strategy. For instance, Fuller and Carneal (1993) proposed using a reduced-order central processor to control an array of actuators. In their work, an optimal drive signal for a single "master" actuator was calculated to minimize a global performance metric. Drive signals for each additional actuator were then determined sequentially by varying the phase of the "master" drive signal. Specifically, the drive signal was scaled by $+1$, -1 , and 0 while recording the global cost function. The condition that achieved the best result was kept, and then the drive signal for the next "slave" actuator was determined. This approach was later validated experimentally by Carneal and Fuller (1995). Another relatively simple control strategy, proposed

by Kidner and Fuller (2000), uses a central digital controller to tune the gains of local analog feedback loops. While the local loops are simple and robust, the central controller improves overall performance by tuning the gain of each loop to minimize a global cost function. Although these types of control approaches are relatively simple and computationally efficient, a high level of connectivity is required to acquire global performance measurements and to communicate between the central processor and each local control unit. Unfortunately, this can limit the scalability of the system.

1.1.3 Decentralized control

Decentralized control has received a lot of attention in response to the scalability problems associated with centralized control strategies. Decentralized control implies that groups of inputs and outputs can be paired together such that the plant G can be divided into multiple subsystems that can be controlled independently, as shown in Figure 1.2 (b). Since each subsystem is controlled using only local information, the resulting controller is simple, computationally efficient, and scalable. However, since the cross terms g_{ij} are neglected during the design, the control system is no longer optimal. In fact, Gibbs and Cabell (2002) showed that the unmodeled interaction between neighboring control units can even destabilize the decentralized control system.

Recent active structural control research has attempted to avoid potential stability problems by using matched actuator/sensor pairs with an energy dissipative control law (Petitjean and Legrain 1996; Elliott et al. 2002; Gardonio and Elliott 2004). As we discussed earlier, if the transducer pairs are truly collocated and dual, then any passive control law guarantees the unconditional stability of the closed-loop system (Balas 1979). Therefore, a decentralized system would be stable regardless of the interaction between subsystems. While simple and robust, this strategy does have limitations. For example, recall that real transducer pairs are never perfectly collocated and dual, which eliminates the passive properties of the system at high frequencies. In addition, the approach provides stability guarantees at the expense of performance and is therefore referred to as a low-authority control (LAC) strategy (Aubrun 1980).

Instead of using conservative controllers, another option commonly used in both process and flight control is to design and implement optimal controllers sequentially (Skogestad and Postelthwaite 1996; Morari and Zafiriou 1998). Unfortunately, since each loop is designed and closed successively, subsequent control loops can degrade the performance of previously defined controllers. Therefore iteration is often necessary as demonstrated by Gibbs and Cabell (2002). In their work, an iterative sequential loop closure strategy was used to simultaneously reduce the sound radiation from six aircraft-style bays. Unfortunately, this approach requires global coordination during the design process. In addition, since the design is performed sequentially, the amount of time required to design the entire control system will depend on the total number of control units in the system.

Various hierarchical control architectures have also been proposed to address problems associated with decentralized control (Frampton 2001; Scholte and D'Andrea 2003; D'Andrea and Dullerud 2003). However, unlike decentralized approaches, these strategies require communication between subsystems. For instance, Frampton (2004) considered a distributed control strategy, which uses information from groups of sensors to calculate optimal drive signals. Since information is only shared among a limited subset of control units, the complexity of each control law is not expected to change as the overall size of the system increases. There-

fore, while the strategy is scalable, it requires continuous communication between neighboring subsystems, and is therefore more complicated than standard decentralized strategies.

Another alternative is to use interaction metrics to help design the decentralized control system. This approach was originally developed for the process control industry (Morari and Zafiriou 1998), and has recently been applied to the structural control problem by Cabell et al. (2003). Although there are many different types of interaction metrics, the simplest one provides a quantitative measure of the diagonal dominance of the plant at each frequency. Since the interaction between subsystems is due to the off-diagonal terms in the plant model, this metric highlights frequencies where neighboring controllers are likely to interact. This information can then be used to design local controllers, which are robust in the necessary frequency bands. Alternatively, more complicated metrics can be used to identify magnitude bounds for each controller, which will guarantee the closed-loop stability of the coupled system. However, since interaction metrics are based only on a frequency-response description of the plant and do not take into account the dynamics of each controller, the magnitude bounds can be conservative. Another disadvantage of interaction metrics is that they require a frequency-response description of the entire coupled plant, which may be difficult to obtain in practice.

Another option is to use independent time-varying controllers on each subsystem. Time-varying strategies allow each controller to compensate for unexpected performance variations caused by interacting subsystems. An obvious disadvantage of this approach is the increased computational complexity associated with time-varying designs. In general, time-varying strategies can be divided into two categories, direct and indirect adaptive approaches. Direct adaptive strategies typically utilize simple filter structures and update the controller coefficients at every sample to minimize a given cost function. On the other hand, indirect strategies design the controller 'off-line' and update the control coefficients much less frequently (Elliott 2001). A brief review of both types of time-varying strategies is included in Chapter 6.

While researchers have proposed many ways to address the limitations associated with decentralized control, further work is necessary to develop a simple and effective strategy to reduce sound transmission through large periodically stiffened structures, such as the aircraft fuselage. The next section discusses the scope of this project and presents our approach to this problem.

1.2 Scope and objectives

Recall that the overall goal of this project is to develop a simple, effective, and scalable control strategy designed to reduce sound radiation into the aft-cabin. However, to limit the scope of this work, only primary structural control is considered. Also note that while a brief feasibility study of feedforward control for aft-cabin noise is included in Appendix D, the lack of an acceptable reference signal makes the approach unpractical. Therefore, the work presented in the body of this paper focuses exclusively on feedback control. In particular, only decentralized feedback control strategies are considered due to the connectivity, computational load, and fault tolerance issues associated with centralized strategies. In addition, while an aircraft fuselage may contain several hundred bays, the investigation is limited to a flat panel segmented into two bays by a flexible stiffener. Therefore, the objective of this work is to investigate decentralized control of sound radiation from a stiffened panel.

The project begins with the development of a numerical model capable of studying this problem. In par-

ticular, a finite element model of a stiffened panel is used to generate a state-space model of the structure. The dynamics of surface mounted piezoelectric actuators as well as the acoustic response of the structure are then modeled. Finally, the disturbance is simulated to match aft-cabin noise. The next step is to study the interaction between decentralized LQG controllers. Low-authority strategies are then considered in an effort to avoid the destabilizing interaction between neighboring controllers. The advantages of a combined high-authority/low-authority control (HAC/LAC) strategy are also discussed. While the numerical results are promising, real-world limitations severely limit achievable performance. Therefore an indirect adaptive linear quadratic Gaussian / loop transfer recovery (LQG/LTR) approach is proposed. This approach updates each controller independently in response to changes in the measured response. Finally, the strategy is validated experimentally on a built-up aluminum structure representative of the sidewall of an aircraft.

The significant contributions of this effort include:

- the development of a numerical model that describes the structural-acoustic response of a stiffened panel excited by spatially correlated random pressure fields
- a study of the limitations of traditional decentralized control strategies designed to reduce sound radiation from periodically stiffened structures
- a detailed investigation of low-authority control strategies using strain based actuators and point sensors
- the development of a simple, scalable, and effective linear quadratic Gaussian / loop transfer recovery (LQG/LTR) strategy for coupled subsystems
- experimental validation of the LQG/LTR strategy on a built-up aluminum test structure

1.3 Organization

This project begins with the development of a powerful and flexible numerical model capable of evaluating decentralized control strategies on coupled subsystems excited by correlated random loads. Decentralized LQG control is then studied followed by low-authority and combined HAC/LAC strategies. Finally, an indirect adaptive approach based on robust control theory is proposed and evaluated. All of the control strategies are evaluated both numerically and experimentally on structural-acoustic systems with poles close to the stability boundary, non-minimum phase zeros, and unmodeled dynamics. A more detailed description of the contents of each chapter is included below.

Chapter 2 describes the numerical model and test structure, which are both used to evaluate potential decentralized control strategies. The description of the numerical model is divided into four parts, beginning with the structural dynamics of the stiffened panel. Next, piezoelectric patches are coupled to the structural model and the elemental radiator formulation is used to estimate the acoustic radiation from the panel. The structural-acoustic response due to a simulated aft-cabin excitation is then presented. The next section includes descriptions of the stiffened aluminum test article and test facility. Finally, the acoustic excitation is described, and the experimental procedure is outlined.

Chapter 3 presents background information on linear quadratic control. This chapter begins with a review of the optimal state regulation problem, which includes discussions on the robust stability of both continuous and discrete-time designs. Next, the optimal stochastic estimator is described, and then LQG control is discussed. Since state estimates are used instead of the actual system states, the LQG design can have arbitrarily poor stability margins (Doyle 1978). Therefore, the next two sections discuss frequency shaping and loop transfer recovery, which can both be used to improve the robustness of the LQG design. The chapter concludes with a simple numerical example, which applies the concepts discussed in the chapter.

Chapter 4 discusses the limitations of standard, model-based decentralized control strategies. The first portion of the chapter introduces the decentralized control problem and demonstrates why the cross coupling between subsystems limits achievable performance. The second portion of this chapter demonstrates that frequency-shaped linear quadratic control approaches can be used to improve standard decentralized designs. While these approaches are shown to be effective, they require *a priori* knowledge of the frequency bands where spillover is likely to occur. Since this information may not be available in practice, alternative control approaches are investigated in subsequent chapters.

Low-authority control strategies are investigated in Chapter 5, beginning with a background section, which reviews some common low-authority structural control strategies, such as direct velocity feedback (DVF) and positive position feedback (PPF). Numerical simulations are then used to study the limitations of existing LAC strategies and evaluate alternate approaches. Based on the numerical work, a single transducer configuration is selected and evaluated experimentally on the stiffened aluminum test structure. Despite the attractive numerical performance, the experimental results show that real-world limitations can severely degrade achievable performance.

Chapter 6 focuses on a time-varying control strategy designed to compensate for poor uncertainty models. The first section includes a brief discussion on frequency-shaped LQR control and disturbance estimation. The next section describes the update procedure, which is used to account for unmodeled dynamics introduced by neighboring control loops. After describing the control strategy, experimental results are used to validate the approach. A discussion pertaining to system scalability is then included.

A summary is included in Chapter 7 along with major conclusions and suggestions for future work. The appendices contain the equations of motion for a piezostucture, followed by background information on disturbance rejection. Next, the aft-cabin disturbance is described, and the feasibility of using feedforward control to suppress broadband aft-cabin noise is discussed. The final appendix contains the Simulink diagrams used in this project.

Chapter 2

Stiffened panel

This chapter describes the numerical model and test article, which are both used to evaluate potential decentralized control strategies. Since it is not practical to evaluate control strategies on the entire pressurized cylindrical fuselage, researchers typically simplify the problem by considering a single bay bounded by ring frames in the circumferential direction and stringers in the longitudinal direction, as shown in Figure 1.1. In addition, the curvature of the fuselage is also usually neglected without a significant loss of accuracy (Graham 1996). However, pressurization, which is modeled by applying in-plane tension to the structure, is an important characteristic since it can reorder the modes and raise the fundamental resonance frequency by a factor of 4 to 10 (Henry and Clark 1999; Gibbs et al. 1999; Maury et al. 2001). Although a tensioned test structure is relatively easy to model numerically, it can be difficult to build in the laboratory. Consequently, many experimental investigations are still performed on un-tensioned structures. Therefore a typical analytical study might consider a clamped flat tensioned panel, while experimental investigations often neglect in-plane loading for simplicity.

While including only a single bay in the control model is convenient for academic studies, it is not representative of the aircraft sidewall at low frequencies where the structural wavelengths are long and the motion of both the panel and stiffeners is important (Mixson and Wilby 1991). In addition, a single bay model neglects the structural coupling between bays, which tends to destabilize decentralized control systems (Gibbs and Cabell 2002). Therefore, more realistic structural models are required in order to effectively transition active control strategies from single-bay laboratory structures to more realistic multiple-bay systems. Since the purpose of this work is to develop a practical control strategy for the aft cabin, the model and test structure must take into account the motion of the stiffeners and the resulting structural coupling between bays. Therefore, the numerical model consists of a clamped panel partitioned into two bays by a flexible stiffener. Similarly, the test article is a rib-stiffened aluminum structure representative of the sidewall of an aircraft. Since in-plane tension can not be incorporated experimentally, it is also neglected in the numerical model. Note that the lack of in-plane loading necessarily shifts the resonance frequencies of the structure, which is addressed by shifting the spectrum of the excitation, as we describe later in this chapter.

The following section includes a detailed description of the numerical model, beginning with the structural dynamics of the stiffened panel. Next, piezoelectric patches are coupled to the structural model and the elemental radiator formulation is used to estimate the acoustic radiation from the panel. The structural-acoustic response due to a simulated aft-cabin excitation is then presented. The experimental setup is presented following the numerical model. This section begins with descriptions of the stiffened aluminum test article and test facility. Next the acoustic excitation is described, and finally the experimental procedure is outlined.

2.1 Numerical model

The purpose of the numerical model is to enable a thorough investigation of the problem by providing a convenient mechanism to evaluate potential transducer configurations and control laws without the time and expense associated with experimental work. In addition, the numerical simulations also provide the ability to simulate a diverse class of excitations, which may be difficult to reproduce in the laboratory. The description of the model is divided into four parts, beginning with the equations of motion describing the structural response of a stiffened panel.

2.1.1 Structural model

On a typical aircraft, the stringers span a larger distance between supports and are also more flexible than the ring frames. Therefore it is common to consider multiple bays set between rigid ring frames and stiffened by flexible stringers (Gardonio and Elliott 1999; Vaicaitis et al. 1985, 1980). As a result, the numerical model used in this work consists of a flat clamped panel partitioned into two bays by a flexible stringer, as shown in Figure 2.1. The dimensions and material properties of the two-bay structure, included in Table 2.1, are representative of the sidewall of a commercial aircraft. To account for manufacturing variability, the stiffener is offset from the middle of the panel by 8 mm. This makes the two bays slightly different sizes so that the modes on both bays do not coincide. In addition, all edges of the stiffened panel are assumed to be clamped.

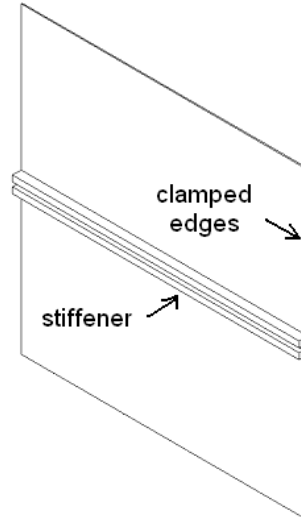


Figure 2.1: Diagram of the clamped, stiffened panel.

Analytical models of relatively simple stiffened panels have been created using transfer matrix and finite element-strip methods (Lin 1969; Chang and Vaicaitis 1982). These techniques can be used to analyze two-dimensional structures when the eigenfunctions in one direction are already known. However, a more general approach is to perform a normal modes analysis of the structure using numerical finite element methods. For this work, a finite element model of the stiffened panel was created using MSC.NASTRAN. A normal modes analysis was then used to generate the generalized mass and stiffness matrices, and to

Table 2.1: Dimensions and physical properties of the two-bay model

Material	6061-T6 Aluminum
Dimensions (l_x, l_y, h)	(0.476, 0.380, 0.0013) m
Stiffener offset	0.008 m
Density (ρ)	2680 kg/m ³
Young's modulus (Y)	6.93×10^{10} Pa
Poisson's ratio (ν)	0.33
Modal damping ratio (ξ)	0.01

determine the eigenproperties of the 60 lowest frequency transverse modes. The first eighteen modes of the two-bay panel are shown in Figure 2.2.

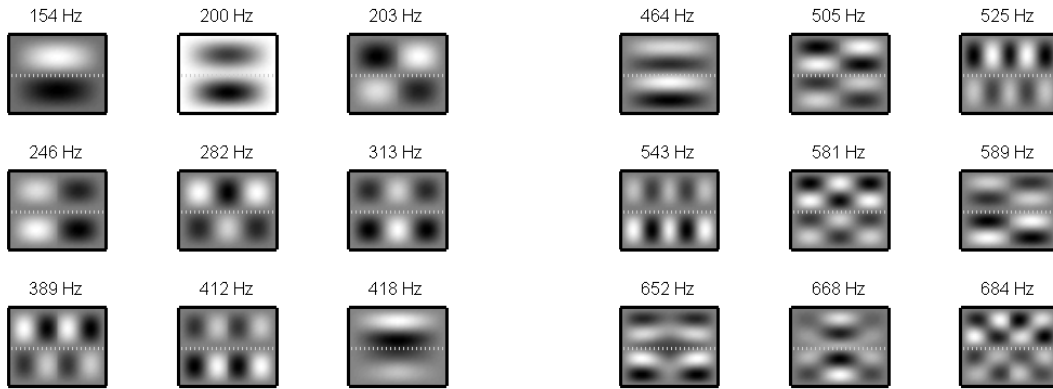


Figure 2.2: Mode shapes for the first eighteen structural modes of the clamped two-bay structure.

The generalized equations of motion for the flexible structure can be expressed as

$$M_s \ddot{\eta} + C_s \dot{\eta} + K_s \eta = B_f f \tag{2.1.1}$$

where η is a vector of generalized displacements, M_s is the generalized mass matrix, C_s is the damping matrix, K_s is the stiffness matrix, B_f is the forcing matrix, and f is a vector of structural forces.

Recall that since the structure is modeled using the FE method, the generalized mass and stiffness matrices are determined directly from the FE model. However, the structural damping matrix is defined explicitly such that the modal damping ratio for each mode is 0.01. In this case, the forcing matrix is defined as

$$B_f = [\Phi_r^T(\mathbf{x}_{f_1}) \quad \dots \quad \Phi_r^T(\mathbf{x}_{f_n})] \tag{2.1.2}$$

where \mathbf{x}_f are the coordinates of each point force input and Φ_r are the eigenfunctions obtained from the normal modes analysis.

The system can also be rewritten in state-variable form as,

$$\begin{aligned}\dot{x}(t) &= Ax(t) + Bu(t) \\ y(t) &= Cx(t) + Df(t)\end{aligned}\tag{2.1.3}$$

where

$$x(t) = \begin{bmatrix} \eta(t) \\ \dot{\eta}(t) \end{bmatrix},\tag{2.1.4}$$

$$A = \begin{bmatrix} 0 & I \\ -M_s^{-1}K_s & -M_s^{-1}C_s \end{bmatrix}, \quad B = \begin{bmatrix} 0 \\ M_s^{-1}B_f \end{bmatrix},\tag{2.1.5}$$

$$C = [0 \quad \Phi_r], \quad D = [0].\tag{2.1.6}$$

Note that the C matrix is defined such that the output of the system is velocity.

2.1.2 Piezostructure

This section presents the equations of motion for a piezostructure, which is defined as a mechanical structure with embedded piezoelectric transducers (Clark et al. 1998). Two of the most common types of piezoelectric materials used in vibration control are a ceramic composed of lead zirconium titanate (PZT), and a polymer made of polyvinylidene fluoride (PVDF). While piezoceramic materials have a high elastic modulus and strain constant, polymer films are relatively lightweight and flexible. Therefore, piezoceramic transducers are typically used as actuators, while polymer films are used as sensors.

Traditional piezoceramic wafers are often used as strain actuators in vibration control applications due to their compact size and high-bandwidth capabilities. A diagram of a traditional PZT wafer is shown in Figure 2.3 (a). Notice that while the uniform electrode on the surface of the wafer applies an electric field through the thickness of the piezoceramic material, the in-plane strain is what actually couples to the structure.

The electromechanical efficiency of a piezoelectric actuator is indicated by strain constants, d_{ij} , which relate the applied electric field in the i^{th} direction to the free strain in the j^{th} direction. For instance, traditional monolithic wafers take advantage of the d_{31} effect, which means that an applied electric field in the 3-direction induces strain in the 1-direction.

An alternative interdigitated electrode (IDE) configuration, shown in Figure 2.3 (b), improves performance by applying the electric field in the plane of the actuator (d_{11}). For typical piezoceramics, the induced strain in the poling direction is approximately three times the strain off-axis. Therefore, d_{11} actuators can be used more efficiently than d_{31} actuators.

Additional improvements are achieved by embedding piezoceramic fibers in an epoxy substrate. This makes the actuator more flexible and durable than traditional monolithic wafers. An example of this type of actuator

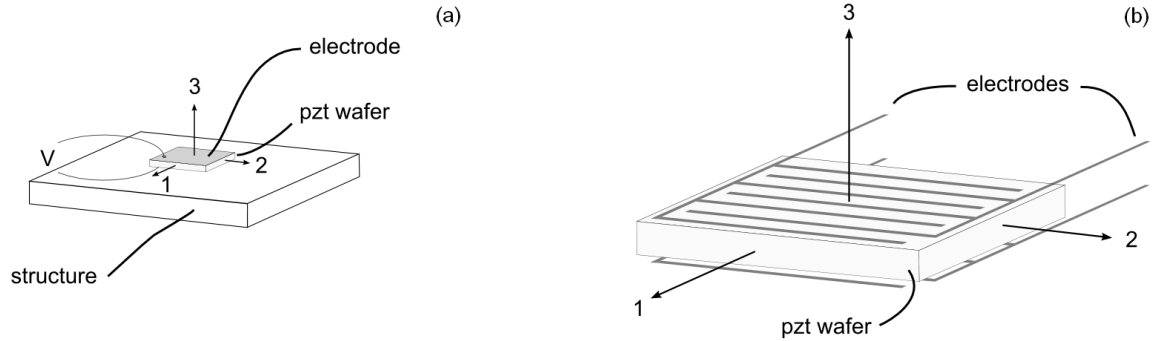


Figure 2.3: The diagrams show: (a) a conventional piezoceramic wafer; and (b) an interdigitated electrode pattern.

is the Macro-Fiber Composite (MFC) actuator developed at NASA Langley Research Center (Wilkie et al. 2000) and distributed by *Smart Material Corp.* For comparison, Table 2.2 lists the material properties for a traditional PZT actuator manufactured by *Piezo Systems, Inc.* and an MFC actuator manufactured by *Smart Material Corp.*

Table 2.2: Material properties for two types of piezoceramic actuators.

	Traditional PZT	MFC
Density, ρ_p (kg/m ³)	7800	4750
Elastic modulus, Y_1 (Pa)	6.6×10^{10}	3.034×10^{10}
Elastic modulus, Y_2 (Pa)	6.6×10^{10}	1.586×10^{10}
Poisson's ratio, ν_{12}	0.3	0.31
Poisson's ratio, ν_{21}	0.3	0.16
Shear modulus, G_{12} (Pa)	2.5×10^{10}	5.52×10^9
Strain constant, d_{11} (m/V)	0	400×10^{-12}
Strain constant, d_{12} (m/V)	0	-170×10^{-12}
Strain constant, d_{31} (m/V)	-190×10^{-12}	0
Strain constant, d_{32} (m/V)	-190×10^{-12}	0

Aside from the efficiency and durability advantages of anisotropic actuators, such as the MFC, another advantage that will be discussed in more detail in Chapter 5 is the ability to provide directional actuation. Unlike a traditional monolithic actuator in which the electric field couples to both in-plane directions equally ($d_{31} = d_{32}$), the interdigitated electrode pattern enables the application of the electric field in a particular in-plane direction ($d_{11} \neq d_{12}$).

The coupled electromechanical equations of motion for a piezostucture are considered next. Note that since this formulation is available in numerous texts, including Hagood et al. (1990) and Clark et al. (1998), only a brief overview is included here while additional details are included in Appendix A. As presented in Hagood et al. (1990), a generalized form of Hamilton's principle can be used to derive the coupled electromechanical equations of motion:

$$[M_s + M_p] \ddot{\eta} + C_s \dot{\eta} + [K_s + K_p] \eta = B_f f + \Theta v \quad (2.1.7)$$

where η is a vector of generalized displacements, M_s is the structural mass matrix, M_p is the piezoceramic mass matrix, C_s is the structural damping matrix, K_s is the structural stiffness matrix, K_p is the piezoceramic stiffness matrix, B_f is the forcing matrix, Θ is the electromechanical coupling matrix, f is a vector of structural forces, and v is a vector of applied voltages (Clark et al. 1998; Viperman and Clark 1999). Note that definitions of each of these terms are included in Appendix A for standard piezoceramic actuators as well as anisotropic actuators such as the MFC.

To make the model more amenable to control design, the system is commonly rewritten in state-variable form as,

$$\begin{aligned} \dot{x}(t) &= Ax(t) + Bu(t) \\ y(t) &= Cx(t) + Du(t) \end{aligned} \quad (2.1.8)$$

where

$$x(t) = \begin{bmatrix} \eta(t) \\ \dot{\eta}(t) \end{bmatrix}, \quad u(t) = \begin{bmatrix} f \\ v \end{bmatrix}, \quad (2.1.9)$$

$$A = \begin{bmatrix} 0 & I \\ -M^{-1}K & -M^{-1}C_s \end{bmatrix}, \quad B = \begin{bmatrix} 0 & 0 \\ M^{-1}B_f & M^{-1}\Theta \end{bmatrix}, \quad (2.1.10)$$

$$C = [0 \quad \Phi_r], \quad D = [0 \quad 0], \quad (2.1.11)$$

and

$$M = M_s + M_p, \quad K = K_s + K_p. \quad (2.1.12)$$

Once again, the C matrix is defined such that the output of this system is velocity.

2.1.3 Structural-acoustic coupling

Since the goal of this project is to reduce the radiated sound power from the structure, the numerical model has to include an estimate of acoustic radiation. One way to approximate radiated sound power is to pass a vector of modal velocity amplitudes through a radiation filter, which can be defined as the stable minimum-phase spectral factor of the radiation resistance matrix (Baumann et al. 1991). In this context, the diagonal terms of the radiation resistance matrix are the self-radiation resistances and the off-diagonal terms are the mutual-radiation resistances (Baumann et al. 1991; Cunefare 1991). Another way to estimate acoustic radiation is to filter an array of discrete velocity measurements as discussed by Elliott and Johnson (1993). Using this technique, the acoustic power estimate is completely independent of the system model. Therefore, the approach is well suited for experimental work since the formulation is expressed in terms of discrete velocity measurements instead of in terms of the amplitudes of structural modes. As a result, the numerical model and experimental work discussed in this paper use the elemental radiator formulation.

Following the formulation in Elliott and Johnson (1993), an array of point-velocity measurements is used to

estimate acoustic radiation. In particular, the power radiated by an array of elemental sources is calculated as

$$\bar{P}(\omega) = \frac{S}{2} \text{Re}[\mathbf{v}^H(\omega) \mathbf{p}(\omega)] \quad (2.1.13)$$

where S is the area of each elemental radiator, ω is the angular frequency, $\mathbf{v}(\omega)$ is a vector of the complex normal velocities of each elemental source, and $\mathbf{p}(\omega)$ is a vector of complex acoustic pressures directly in front of each radiator. Note that the acoustic pressure can be expressed in terms of the matrix of specific acoustic impedances $\mathbf{Z}(\omega)$ as

$$\mathbf{p}(\omega) = \mathbf{Z}(\omega) \mathbf{v}(\omega). \quad (2.1.14)$$

Using this relationship, Equation 2.1.13 can be rewritten as

$$\bar{P} = \frac{S}{2} \text{Re}[\mathbf{v}^H(\omega) \mathbf{Z}(\omega) \mathbf{v}(\omega)] = \mathbf{v}^H(\omega) \mathbf{R}(\omega) \mathbf{v}(\omega) \quad (2.1.15)$$

where the radiation resistance matrix, $\mathbf{R}(\omega)$, is defined as

$$\mathbf{R}(\omega) = \frac{S}{2} \text{Re}[\mathbf{Z}(\omega)] = \frac{\omega^2 \rho S^2}{4\pi c} \left(\frac{\sin k\mathbf{r}}{k\mathbf{r}} \right) \quad (2.1.16)$$

where ρ is the density of air, c is the speed of sound in air, $k = \omega/c$, and \mathbf{r} is a symmetric matrix that defines the distance between each elemental radiator. Note that this formulation assumes the panel is set in an infinite rigid baffle and radiates into free space. In addition, it is assumed that each elemental radiator is vibrating entirely in phase, and is small compared with the acoustic wavelength (Elliott and Johnson 1993).

One way to calculate the total radiated sound power from the structure is to post process the point velocity measurements using the radiation resistance matrix. Another alternative is to decompose \mathbf{R} into its spectral factors and then fit the magnitude response to obtain a radiation model. The second approach is often preferred since it enables the use of modern controllers designed to minimize cost functions based on radiated sound power (Baumann et al. 1991). However, this approach requires a state-space representation of the frequency-dependent \mathbf{R} matrix, which can be excessively large. For instance, if 50 velocity measurements are acquired, then 2500 transfer functions must be modeled. Since the dynamic compensator is typically on the same order as the augmented plant, this is not a practical solution. Therefore, a curve fitting technique called radiation modal expansion (RME) is often used to reduce the order of the radiation model, as described by Gibbs et al. (2000). Essentially, the dominant radiation modes are identified by performing a singular value decomposition of the radiation matrix at one particular frequency. Since the radiating mode shapes are similar at each frequency, the mode shapes corresponding to one frequency can be used to calculate RME coefficients for every other frequency in the bandwidth. A model of the RME system is then created by curve fitting the dynamics associated with the dominant RME coefficients.

Next, it is important to consider how many radiation modes are needed to generate an accurate model. If we assume that all radiation modes are excited to an equal amplitude, then the radiation efficiency plot shown in Figure 2.4 can be used to determine the number of modes required to achieve a given accuracy (Elliott

and Johnson 1993). Note that the radiation efficiency $\sigma(\omega)$ is defined as

$$\sigma(\omega) = \frac{2}{\rho c S_T} \lambda(\omega) \quad (2.1.17)$$

where S_T is the total area of the radiator and $\lambda(\omega)$ are the eigenvalues of $R(\omega)$. By comparing the relative contribution of each mode at 800 Hz, we find that 8 modes account for 90 % of the radiated power, while 12 modes are required to account for 99 % of the power. However, it is important to note that this is a conservative estimate since it assumes each radiation mode is excited equally. Ultimately, the modal contribution will be determined by the characteristics of the structure and disturbance. Therefore this topic is revisited after the disturbance is defined.

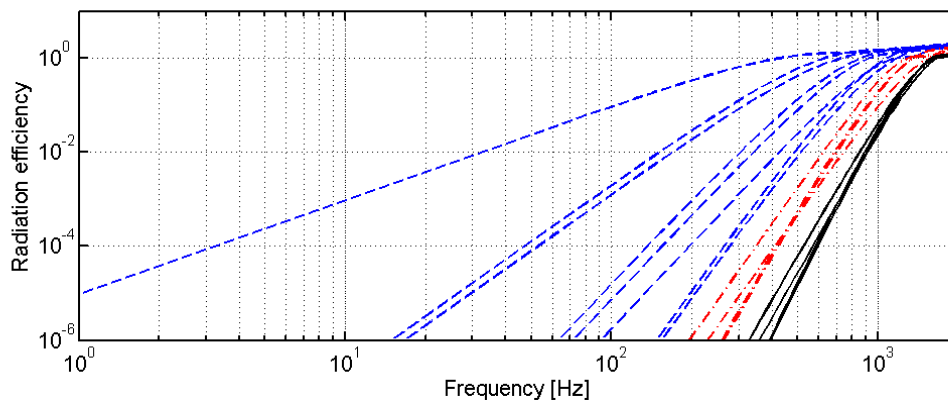


Figure 2.4: Radiation efficiencies of the first sixteen radiation modes for the structure.

2.1.4 Simulated disturbance

The spatial and spectral characteristics of the excitation necessarily affect the structural-acoustic response of the structure. For instance, Maury et al. (2002) showed that diffuse excitations couple to a structure differently than TBL noise. As a result, noise control techniques that work effectively in a diffuse field, may not provide the same level of attenuation in more realistic noise environments. Therefore, it is important to evaluate control strategies using appropriate disturbance models. Since the control strategies investigated in this project are designed for the aft-cabin, this section describes an approach used to simulate the structural-acoustic response due to aft-cabin noise. Note that for this project, aft-cabin noise is assumed to be dominated by shock-cell and TBL noise (Mixson and Wilby 1991). While TBL noise is caused by the random pressure fluctuations in the turbulent boundary layer, shock-cell noise can be approximated by a collection of phased monopoles located in the engine exhaust plume (Harper-Bourne and Fisher 1974).

Typically, researchers calculate the response of randomly excited elastic panels using space-frequency (Thomas and Nelson 1995; Tang et al. 1996; Heatwole et al. 1997) or wavenumber-frequency formulations (Strawderman 1990; Graham 1997; Maury et al. 2002). For instance, Maury et al. (2002) described a wavenumber-frequency formulation, which can be used to model the structural-acoustic response of a simply-supported panel excited by a large class of random disturbances. In particular, expressions for the

acoustic radiation and kinetic energy of the panel were compared using a diffuse field, fully-developed TBL excitation, and a mutually-uncorrelated pressure field. Although this formulation is computationally efficient, the technique is not easily incorporated into control studies.

Another option is to calculate the response using a space-frequency description of the disturbance. For instance, Thomas and Nelson (1995) used a space-frequency formulation to define excitation filters for a simply-supported plate excited by a turbulent boundary layer. The excitation filters generate the appropriate modal forces given uncorrelated white noise inputs. By combining a state-space realization of these filters with a structural-acoustic model, Thomas and Nelson were able to use optimal control theory to solve the structural-acoustic control problem. While this approach is convenient for control studies, it is not easy to develop excitation filters for more complicated structures. In addition, including a state-space representation of the disturbance necessarily increases the size of the control model. For instance, Heatwole et al. (1997) found that 296 states were required to model 50 excitation filters (one for each structural mode). Since the compensator is typically on the same order as the plant, this approach is not always practical.

Instead of fitting the disturbance with a state-space model, another alternative is to simulate the response directly using a discrete array of point sources that match the spatial and spectral characteristics of the disturbance. For instance, Montgomery (2004) simulated the structural-acoustic response of a finite element model of the aircraft fuselage using point forces that matched a statistical description of the random pressure field. Another investigation, performed by Maury et al. (2004) and Elliott et al. (2005), studied the feasibility of simulating random pressure fields in the laboratory using a dense array of acoustic sources.

The approach used in this project is similar to Montgomery (2004), since the structural-acoustic model is excited using a discrete array of point forces, as depicted in Figure 2.5. One of the advantages of this approach is that it is easy to incorporate with control studies. However, the technique can be computationally intensive since a discrete time-domain realization of the disturbance must be generated before the structural response can be simulated. Specifically, this is accomplished by sampling the continuous disturbance at the location of each source. The resulting discrete model, often in the form of a spectral density matrix, defines the statistics of the pressure field at each source location. Once the statistical model is known, time-domain drive signals can be generated without knowledge of the dynamics of the structure. Note that this assumes negligible fluid loading since the structural response is assumed to have no effect on the disturbance. The response of the randomly excited system can then be simulated using the time-domain drive signals. Each of these steps is described in more detail below.

Spectral density matrix

Recall that the goal of this project is to reduce aft-cabin noise. Therefore, we need a discrete representation of this particular type of disturbance. While the characteristics of the disturbance are discussed in more detail in Appendix C, a brief summary is also included here. Note that since the engine exhaust is supersonic at cruise, both shock-cell and TBL noise contribute to the exterior forcing field (Mixson and Wilby 1991). Therefore, both types of excitations are considered here, beginning with boundary layer noise.

One of the most popular boundary layer noise models was proposed by Corcos (1963). The Corcos model is a statistical representation based on experiments and is often used due to its simplicity. The Corcos model

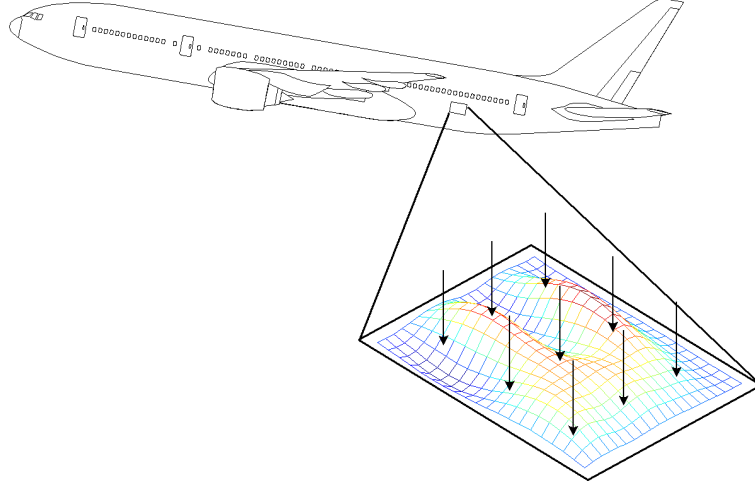


Figure 2.5: Point forces are used to simulate the response of a randomly excited panel.

describes the cross-spectral density of a TBL excitation as

$$S_{AB}(r_x, r_y, \omega) = S_{pp}(\omega) e^{-\frac{|r_x|}{L_x}} e^{-\frac{|r_y|}{L_y}} e^{-\frac{j\omega r_x}{U_c}} \quad (2.1.18)$$

where $S_{pp}(\omega)$ is the point power spectral density, r_x and r_y are the separation distances in the streamwise and spanwise directions respectively, ω is the angular frequency, and U_c is the convection velocity. The correlation lengths are defined as

$$L_x = \frac{\alpha_x U_c}{\omega} \quad \text{and} \quad L_y = \frac{\alpha_y U_c}{\omega} \quad (2.1.19)$$

where α_x and α_y are empirical constants. In this investigation, $\alpha_x = 8$ and $\alpha_y = 1.2$, which is consistent with Elliott et al. (2005). The convection velocity is taken as $U_c = 198$ to match the flight test data used in Appendix C. Notice that the cross-spectral density of the pressure field is described in terms of the power-spectral density, the spatial coherence in the x and y directions, and an $e^{-\frac{j\omega r_x}{U_c}}$ term that accounts for the time lag between points in the streamwise direction.

The characteristics of shock-cell noise are considered next. Specifically, the cross-spectral density is assumed to be of the form (Montgomery 2004)

$$S_{AB}(r_x, r_y, \omega) = S_{pp}(\omega) e^{-\sqrt{\left(\frac{|r_x|}{L_x}\right)^2 + \left(\frac{|r_y|}{L_y}\right)^2}} e^{-j\omega \sqrt{\left(\frac{r_x}{U_x}\right)^2 + \left(\frac{r_y}{U_y}\right)^2}} \quad (2.1.20)$$

where $L_x = \beta_x/\omega$, $L_y = \beta_y/\omega$, U_x is the phase velocity in the streamwise direction, U_y is the phase velocity in the spanwise direction, and β_x and β_y are empirical constants. While this formulation is similar to the traditional Corcos model, the more general non-separable form for the spatial coherence term is used and the phase relationship has been modified to incorporate time delay in both the spanwise and streamwise directions. For this work, both empirical constants as well as the phase velocities are fit to data acquired from exterior pressure measurements made on the aft fuselage, as discussed in Appendix C.

To highlight the differences in the spatial characteristics between boundary layer and shock-cell noise, consider Figure 2.6, which shows the spatial coherence for each excitation at 700 Hz. The spatial coherence is shown as a function of separation distance in the spanwise and streamwise directions. In the middle of each figure, the spatial separation is zero, and therefore the coherence equals one. In general, the coherence decreases as the separation distance increases. Notice that the TBL excitation has more correlation in the flow direction than in the spanwise direction and is much less correlated than shock-cell noise.

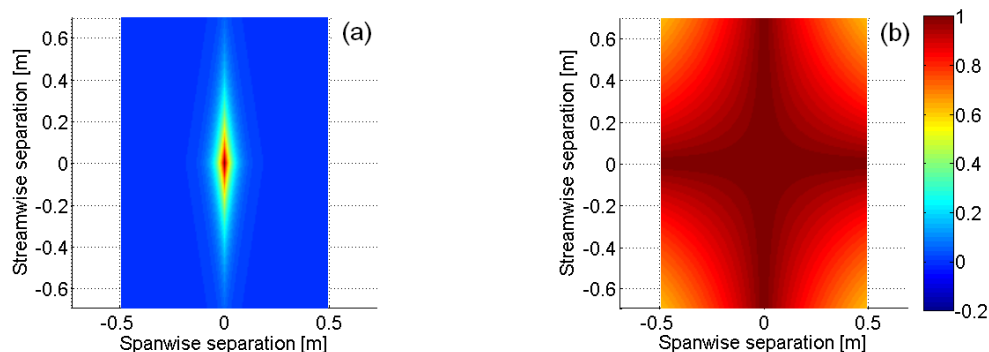


Figure 2.6: The figure shows the spatial coherence for a: (a) TBL excitation; and (b) shock-cell noise.

To this point, we have not discussed the spectral characteristics of either type of disturbance. Notice that the power spectral density term, $S_{pp}(w)$, used in both disturbance models is independent of position. This implies that the disturbance is homogeneous. Note that although this is not accurate over the entire fuselage, the approximation is adequate over the span of a few bays on the aft cabin. The spectral density estimates for both types of disturbances are based on flight test data, as described in Appendix C. Specifically, the spectral density for TBL noise is estimated from data obtained with engines at flight idle, while the power spectral density for shock-cell noise is estimated by subtracting the TBL spectrum from the combined excitation measured at maximum climb conditions. The three spectra are compared in Figure 2.7.

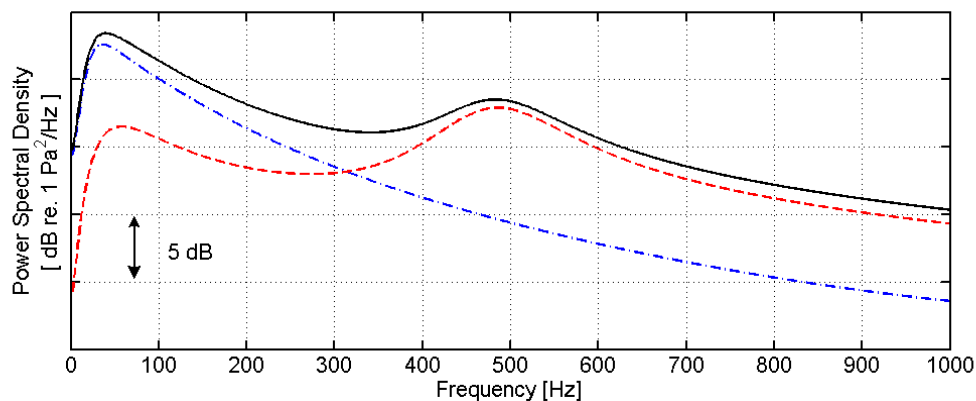


Figure 2.7: Power spectral density of boundary-layer noise (dash-dotted blue line), the combined excitation (solid black line), and shock-cell noise (dashed red line).

Recall that since the test article is not tensioned, in-plane loading was also neglected in the numerical

model. Unfortunately, neglecting tension shifts the resonance frequencies of the structure to lower frequencies. While this might not be important if the disturbance was broadband, aft-cabin noise has a spectral peak between 400 and 600 Hz, as shown in Figure 2.7. Since the structural resonance frequencies are shifted due to the lack of tension, the disturbance will not couple to the correct structural modes. Therefore, the excitation is also shifted to lower frequencies to compensate for the lack of in-plane loading. This is accomplished by temporarily generating a second structural model, which does include tension. Specifically, tension is included to simulate cabin pressurization as estimated by Henry and Clark (1999). Tensile loads of 51.0×10^3 N/m in the x-direction and 102×10^3 N/m in the y-direction are used to approximate the stresses generated on a 2 m radius cylinder at an altitude of 40,000 ft, which is internally pressurized to atmospheric pressure at 10,000 ft. To demonstrate the affect of in-plane loading on the structural-acoustic response, consider Figure 2.8, which shows the radiated sound power from both the tensioned and un-tensioned models. Notice that including tension shifts the first resonance of the structure from 154 Hz to 509 Hz, while the second resonance at 199 Hz is shifted to 387 Hz. Therefore, tension not only raises the resonance frequencies but also reorders the modes.

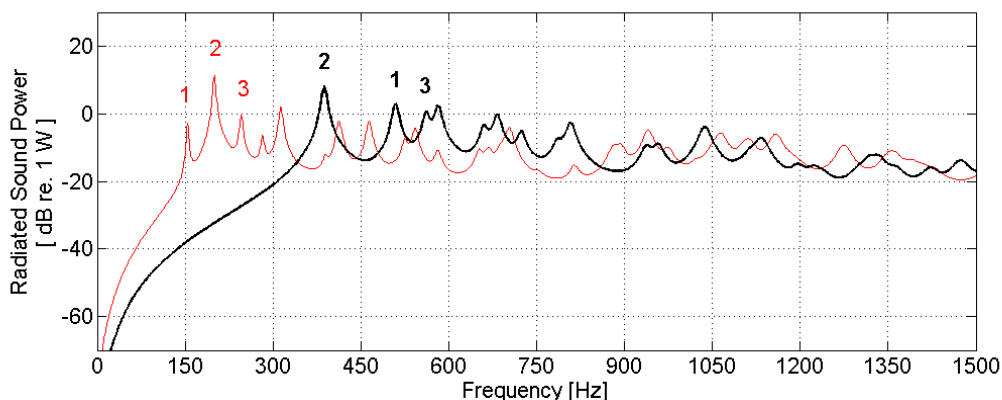


Figure 2.8: Radiated sound power with tension (thick black line) and without tension (thin red line).

A normal modes analysis is then used to compare the mode shapes of the tensioned and un-tensioned models. The resonance frequencies of the un-tensioned structure f_o are plotted versus the resonance frequencies of the same modes on the tensioned structure f_t , as shown in Figure 2.9. A straight line fit of the data yields the simple relationship $f_o = 0.7f_t - 150$, which provides a first-order approximation of the impact tension has on the resonance frequencies of this structure. This relationship is then used to shift the power spectral density of the excitation, as shown in Figure 2.10. Although only the combined spectrum is shown in the figure for clarity, the spectra for both the TBL and shock-cell excitations are also shifted. Once again, the reason for shifting the disturbance is to align the spectral content of the excitation with the appropriate structural resonances.

At this point, the spectral density matrices for both TBL and shock-cell noise have been fully defined. Therefore, the next section describes how to generate time-domain realizations of the disturbance using these spectral density matrices.

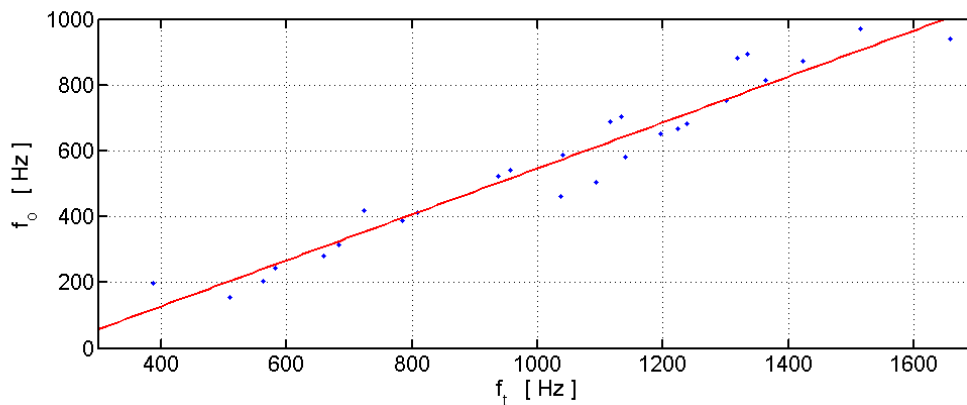


Figure 2.9: The figure shows the relationship between the resonance frequencies on the tensioned and un-tensioned structures.

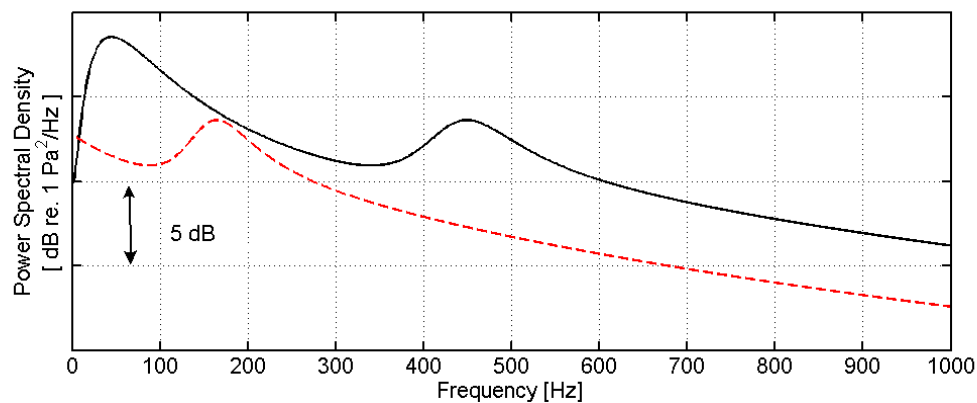


Figure 2.10: The power spectral densities of the original disturbance (solid black line) and frequency shifted disturbance (dashed red line).

Discrete array of point loads

While there are numerous techniques available to generate time histories once the spectral density matrix is defined, the spectral representation method is a particularly popular technique (Shinozuka and Jan 1972; Shinozuka and Deodatis 1991; Deodatis 1996). Essentially, correlated time-domain drive signals are generated for each source by combining cosine terms with weighted amplitudes and random phase angles. The amplitude of each cosine term is based on the Cholesky decomposition of the discrete spectral density matrix. The spectral representation method is commonly used to analyze nonlinear structures excited by random loads such as earthquakes or ocean waves. It is also used to model wind loading on buildings and vehicle response to random surface roughness.

However, the approach used for this work is similar to Elliott et al. (2005), and is depicted in Figure 2.11. Essentially, a set of signals d are generated by filtering an equal number of uncorrelated white reference

signals x through the filter matrix P . This can be expressed as

$$d(k) = P(k)x(k) \quad (2.1.21)$$

or

$$S_{dd}(k) = S_{pp}(k)S_{xx}(k) \quad (2.1.22)$$

where $S_{pp}(k) = P(k)P^H(k)$ and $S_{xx}(k) = E[x(k)x^H(k)] = I$. Therefore

$$S_{dd}(k) = P(k)P^H(k). \quad (2.1.23)$$

Recall that the discrete spectral density matrix S_{dd} defines the spatial and spectral characteristics of the pressure field at the location of each source. In particular, the diagonal elements of S_{dd} correspond to the power spectral densities and the off-diagonal elements are the cross-spectral densities. Note that this matrix is Hermitian ($S_{dd} = S_{dd}^H$) and positive definite (all of its eigenvalues are positive) (Elliott et al. 2002).

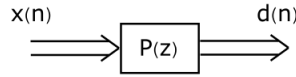


Figure 2.11: The desired disturbance is generated by passing white noise inputs through a filter matrix.

One way to factor S_{dd} is to perform an eigenvalue/eigenvector decomposition at each discrete frequency k such that

$$S_{dd}(k)Q(k) = Q(k)\Lambda(k) \quad (2.1.24)$$

where $Q(k)$ is a matrix of eigenvectors and $\Lambda(k)$ is a diagonal matrix of real positive eigenvalues. Since S_{dd} is Hermitian, the matrix is also normal ($S_{dd}^H S_{dd} = S_{dd} S_{dd}^H$), which implies that $Q(k)$ is a unitary matrix ($Q^{-1} = Q^H$) (Elliott 2001). Therefore

$$S_{dd}(k) = Q(k)\Lambda(k)Q^{-1}(k) = Q(k)\Lambda(k)Q^H(k) \quad (2.1.25)$$

and since $\Lambda^{1/2} = (\Lambda^{1/2})^H$,

$$S_{dd}(k) = (Q\Lambda^{1/2})(Q\Lambda^{1/2})^H. \quad (2.1.26)$$

Therefore, $P(k)$ can be defined as

$$P(k) = Q\Lambda^{1/2}. \quad (2.1.27)$$

Unfortunately, fitting $P(k)$ with a state-space model can generate a prohibitively large model. Therefore, independent realizations of the random reference, x , are instead processed by the filter matrix to generate

time-domain drive signals for each source. In particular, the aft-cabin disturbance is generated by adding together time-domain drive signals for boundary layer noise with signals generated for shock-cell noise. Note that the spectrum of the combined excitation matches the dashed red line shown in Figure 2.10.

Next, consider the source density required to accurately model the excitation. Elliott et al. (2005) investigated this problem by performing a proper orthogonal decomposition of the target spectral density matrix. This was used to determine the minimum number of uncorrelated components required to model the target pressure field. A one-dimensional analysis indicated that one uncorrelated component per correlation length is required to model a TBL pressure field in the spanwise direction, while two components are required per correlation length in the streamwise direction (Elliott et al. 2005). Note that the additional component in the streamwise direction is necessary to model the convective nature of the disturbance. Although the disturbance considered here is a combination of TBL and shock-cell noise, boundary layer noise is much less correlated than shock-cell noise. Therefore, the characteristics of the TBL excitation determine the minimum number of sources required to accurately reproduce the excitation. Since the correlation lengths, as shown in Equation 2.1.19, are inversely proportional to frequency, the number of sources required to approximate the disturbance is determined by the upper bound on the frequency range of interest. For example, at 800 Hz Equation 2.1.19 can be used to calculate the correlation lengths for boundary layer noise as $L_x = 0.32$ m and $L_y = 0.046$ m. Since the panel is 0.476 m by 0.38 m, this analysis suggests that at least 3 sources are required in the x-direction and 8 sources are necessary in the y-direction to model the excitation through 800 Hz. In this project, the disturbance is simulated using 5 sources in the x-direction and 10 sources in the y-direction.

After defining the disturbance, it is beneficial to reconsider the structural-acoustic model. In particular, recall that our preliminary analysis suggested that 12 radiation modes were required to capture 99 % of the sound power radiated from the structure (assuming each radiation mode was excited equally). However, using the actual excitation it is possible to more accurately predict how many radiation modes should be included in the model. In particular, Figure 2.12 shows the radiated sound power contributed by each radiation mode, normalized by the total radiated sound power from the structure driven by the simulated excitation. For this project, two modes are sufficient to capture 99 % of the radiated sound power, while the first 6 modes contribute more than 99.9 % of the integrated power from 50 to 800 Hz. It is clear from this example that each radiation mode is not excited equally. Therefore, only the first 6 radiation modes are included in the structural-acoustic model.

Next, briefly consider the density of the measurement grid. Recall that the elemental radiator formulation assumes that each element is small compared to the acoustic wavelength. At 800 Hz, the acoustic wavelength in air is 0.425 m. Since the structure is 0.476 m by 0.38 m, this requirement can be met using a relatively coarse grid. However, the formulation also assumes that each radiator is vibrating entirely in phase. A quick glance at the first eighteen mode shapes of the structure, shown in Figure 2.2, suggests that this assumption is more restrictive. Therefore, a convergence study is used to investigate the impact of measurement density on the radiated sound power estimate, as shown in Figure 2.13. The figure shows that a 5×6 grid of points achieves a nice compromise between measurement density and accuracy through 800 Hz. In particular, a model with this measurement density captures more than 90 % of the energy radiated from the structure in the 50 to 800 Hz bandwidth. Therefore, a 5×6 grid of measurement points is used for both the numerical model, and also the experimental investigation discussed in the next section.

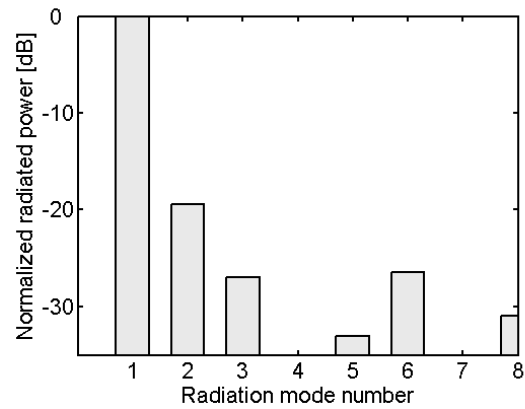


Figure 2.12: The figure shows the normalized sound power integrated from 50 to 800 Hz for each of the first eight radiation modes.

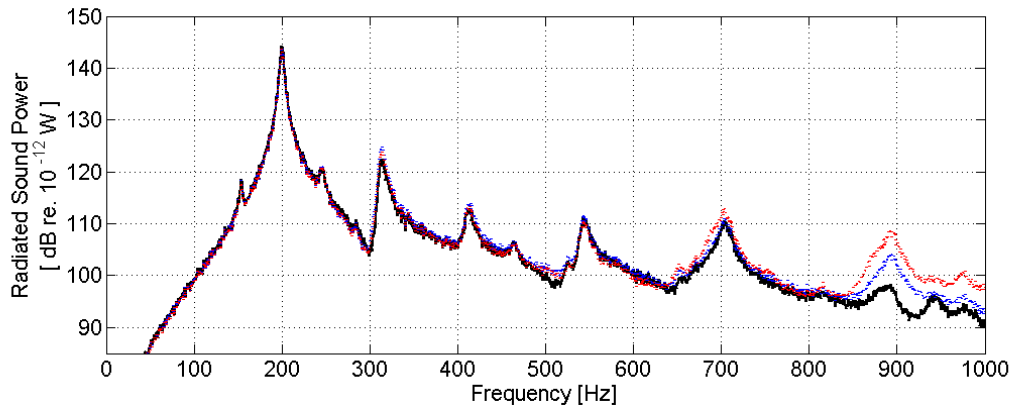


Figure 2.13: The figure shows the radiated sound power calculated using: a 5×6 grid of measurement points (dotted red line); a 7×8 grid of measurement points (dotted blue line); and a 12×12 grid of measurement points (solid black line).

In summary, the sound power radiated by the structure is estimated using a reduced order radiation model, as described by Gibbs et al. (2000). The radiation model contains 6 radiation modes, which account for more than 99.9 % of the radiated power from the structure up to 800 Hz (this assumes that the characteristics of the disturbance match aft-cabin noise). The final structural-acoustic model contains 138 states, which includes 60 structural modes and 6 radiation modes. While an excitation filter describing the exterior pressure field is not included with the model, a diverse class of disturbances can be easily simulated using an array of point loads. Therefore, the numerical model presented here provides a powerful and flexible tool, which enables detailed studies of the interaction between control units under realistic loading conditions. The next section describes the experimental setup, which is used to evaluate the control strategies in the laboratory.

2.2 Experimental setup

Laboratory experiments introduce additional complexity, which is often lacking in the numerical models. Therefore, in addition to investigating each control system numerically, many are also evaluated experimentally in the Structural Acoustic Loads and Transmission (SALT) facility at NASA Langley Research Center. The purpose of this section is to describe the experimental setup, which includes the test article, facility, acoustic excitation, and the experimental procedure. This section begins with a description of the test article, which consists of piezoelectric actuators and accelerometers mounted on a stiffened aluminum panel.

2.2.1 Test article

The test article consists of a flat aluminum skin-stringer panel, representative of the fuselage of an aircraft below the window line. The 1.17 m by 1.17 m panel, shown in Figure 2.14, is segmented into 10 approximately equal size bays by horizontal stringers and vertical frames. The nominal dimensions of each bay are 0.48 m \times 0.19 m, and the skin is 0.0127 m thick. This built-up aluminum structure is used to introduce some of the complexity of the real fuselage without including curvature or in-plane tension. For logistical reasons, only two bays are controlled simultaneously. Therefore, a lead-vinyl sheet with a surface density of 5 kg/m² is attached to the remaining bays. The lead-vinyl mass loads the structure and reduces the natural frequency of the low-order global mode, which can not be controlled effectively using small strain-based actuators mounted on only two bays. A preliminary normal modes analysis of the panel shows that including the lead-vinyl sheet shifts the resonance frequency of the global mode from 75 Hz to 23 Hz without significantly affecting the resonance frequencies of the local modes. Note that adequate frequency separation between the local and global modes is necessary to accurately evaluate the performance of the two-bay control system.

Radiated sound power is estimated experimentally in the same way it was calculated numerically. In particular, the RME technique is used to generate a reduced order radiation model, which in turn is used to estimate radiated sound power from a grid of structural measurements (Gibbs et al. 2000). However, instead of using point velocity sensors, miniature accelerometers (Endevco 2250A-10) are used to measure the structural response. Specifically, a 5 \times 6 array of accelerometers is used to estimate the radiated sound power from the two bays of interest. Each accelerometer is located at the center of equally sized sections of the panel considered as elemental radiators. The locations of the 30 accelerometers are shown in Figure 2.14 (b). Notice

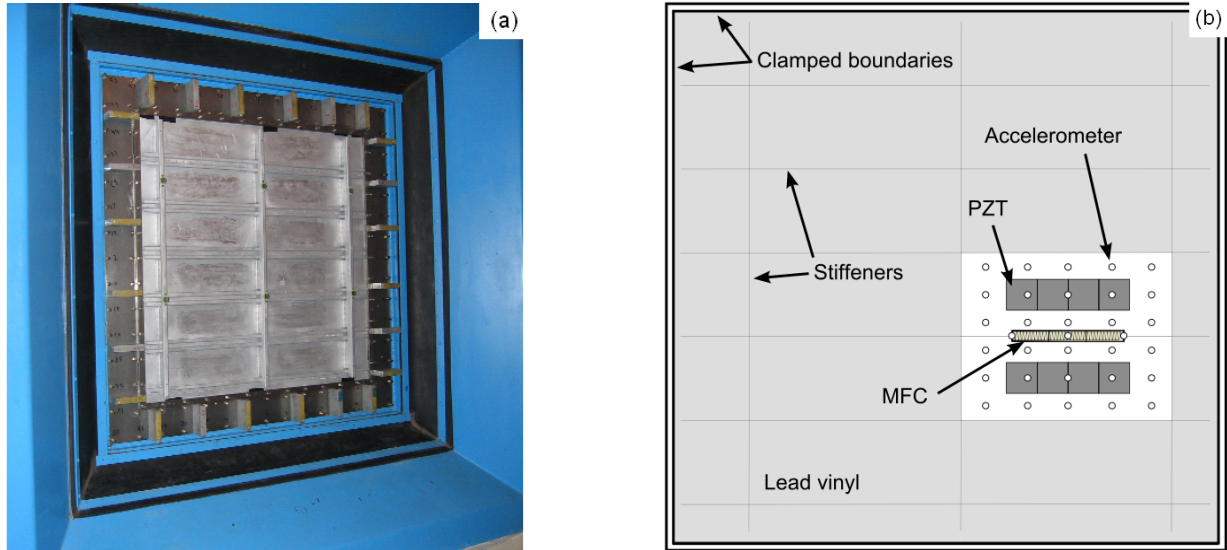


Figure 2.14: The figures show: (a) a photograph of the stiffened aluminum test panel as seen from the reverberation chamber; and (b) a diagram of the other side of the panel showing the lead vinyl sheet and transducers.

that since acceleration is measured, a modified form of the radiation resistance matrix is used. Specifically,

$$\bar{P} = \mathbf{a}^H(\omega) \tilde{\mathbf{R}}(\omega) \mathbf{a}(\omega) \quad (2.2.1)$$

where

$$\tilde{\mathbf{R}}(\omega) = \frac{S}{2} \text{Re}[\mathbf{Z}(\omega)] = \frac{\rho S^2}{4\pi c} \left(\frac{\sin kr}{kr} \right). \quad (2.2.2)$$

In addition to accelerometers, PSI-5A4E piezoceramic patch actuators from *Piezo Systems, Inc.* are also mounted on the structure as shown in Figure 2.14 (b). Each 0.0724 m square piezoceramic actuator is first encapsulated in a thin insulating film before being bonded to the aluminum panel using M-Bond AE-10 strain gage adhesive. Four actuators are mounted and wired together to approximate one larger center mounted actuator on each bay, as shown in Figure 2.15. These actuators cover 20 % of the surface area and add approximately 10 % to the mass of each bay. The selection of a single center mounted piezoelectric patch per bay is based on the controller complexity study performed by Gibbs et al. (2004). Their work showed that a single piezoelectric patch along with the summed response from a set of accelerometers placed in a diamond pattern around each actuator achieved a good compromise between controller complexity and performance. Therefore, a similar transducer configuration is also used for the HAC systems investigated in this project. In particular, Figure 2.16 (a) shows how the transducers used for the HAC systems are wired together.

In addition to the PZT actuators, three M-8528-P1 actuators from *Smart Material Corporation* are also bonded to the structure as shown in Figure 2.14 (b). The dimensions of each actuator are 0.086 m by 0.028 m. Once again, the actuators are mounted side by side and wired together to approximate a single

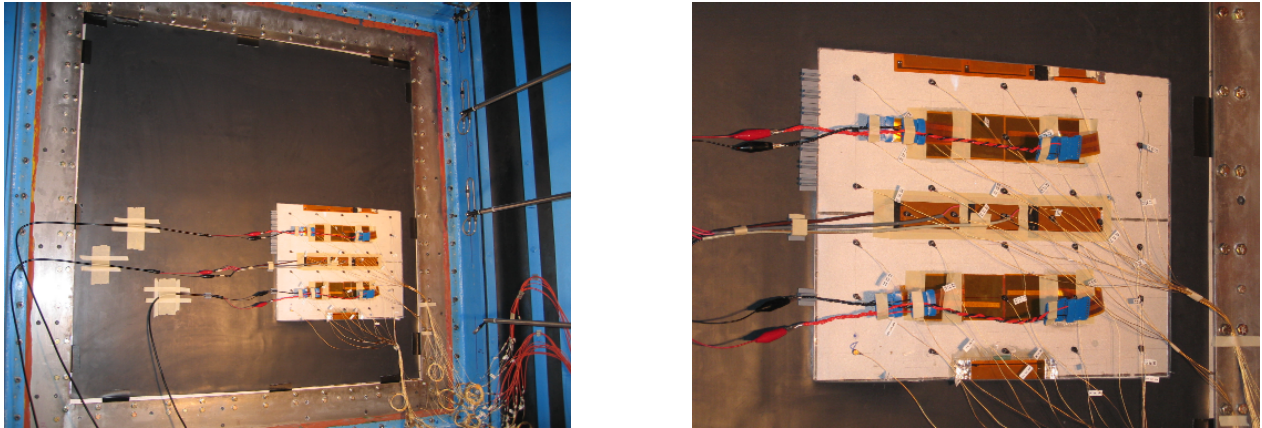


Figure 2.15: The pictures show the test panel, as seen from the anechoic chamber.

larger actuator. Note that this actuator only covers 4% of the surface area and adds just 2% to the mass of each bay. The selection and placement of the actuator is discussed in detail in Chapter 5. Five accelerometers are used in combination with this actuator to evaluate low-authority control strategies, as depicted in Figure 2.16 (b).

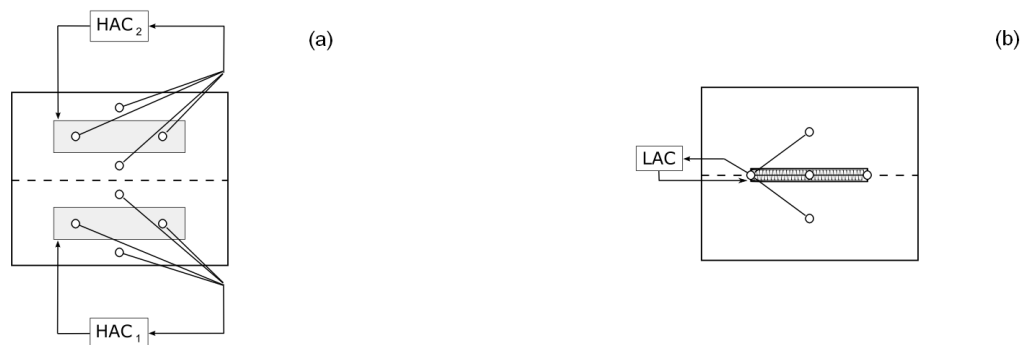


Figure 2.16: The diagrams show: (a) the transducers used for high-authority control; and (b) the transducers used for low-authority control.

2.2.2 Structural Acoustic Loads and Transmission facility

The stiffened aluminum panel is mounted in the transmission loss window in the Structural Acoustic Loads and Transmission (SALT) facility at NASA Langley Research Center. A diagram of this facility is shown in Figure 2.17. Note that to approximate free field conditions, the walls of the anechoic chamber are covered with more than 4800 polyurethane acoustic wedges, and the dimensions of the chamber, from wedge tip to wedge tip, are 4.57 m high, by 7.65 m wide, by 9.63 m long (Grosveld 1999). Although the test article is mounted between the reverberant and anechoic rooms, the test procedure is quite different than an ordinary transmission loss test. In particular, the source is located in the anechoic chamber, and performance is evaluated using structural sensors instead of microphones or intensity probes. As explained in the following

section, a loudspeaker placed in the anechoic chamber is used to represent the exterior aft-cabin noise source. Therefore, the panel models the fuselage of the aircraft, while the reverberation chamber acts as a very rough approximation of the interior cabin. Specifically, the reverberation chamber has a total internal volume of 278 m^3 with splayed walls to promote a diffuse environment. The sound field in the chamber is diffuse down to approximately 80 Hz (Grosveld 1999). Therefore, individual room resonances should not dominate the panel response in the bandwidth of interest.

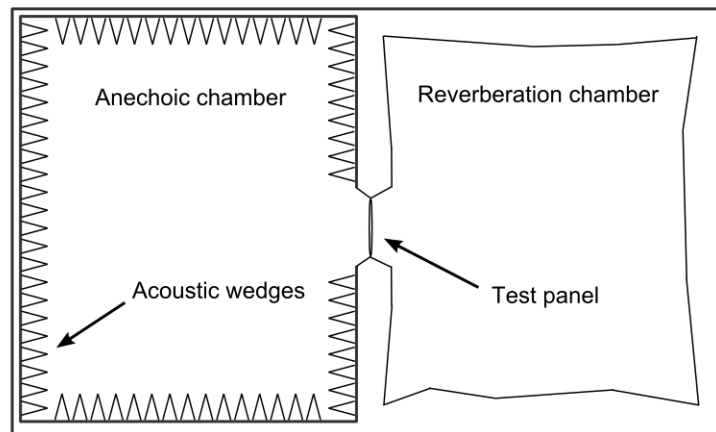


Figure 2.17: Diagram of the Structural Acoustic Loads and Transmission (SALT) facility at NASA Langley Research Center.

Next, consider Figure 2.18, which shows a diagram of the data acquisition and control systems. Notice that two separate systems are used, one enclosed by the dashed blue rectangle shown in the top of the diagram, and the second enclosed in the dashed red rectangle shown in the bottom of the diagram. Both systems are implemented using xPC Target, which is a powerful tool used for real-time control and data acquisition. In this case, xPC Target is implemented using three desktop computers connected by a local ethernet network. One computer is configured as the host, while two additional computers, called targets, are used to implement the high-authority and low-authority control systems and acquire data. Each control system is initially designed on the host PC using MATLAB Simulink before being compiled and downloaded to the appropriate target computer.

The first data acquisition and control system, contained within the dashed blue rectangle shown in the top of the diagram, acquires data from the 30 accelerometers evenly distributed over the structure. However, before each signal is acquired, it is first amplified and filtered using PCB Piezotronics signal conditioning units (Model 481 A). These units have built-in 8th order low-pass filters, which are used to roll off the input signals above 1 kHz. Each signal is then sampled at 3 kHz using data acquisition cards from UEI ($2 \times$ PD2-MFS-8-300/16 and $1 \times$ PD2-MF-16-2M/14H). In addition to providing a performance estimate, a subset of the 30 acceleration measurements is also used for control. Specifically, the summed responses from 4 accelerometers is passed to each digital controller. The outputs from the controllers, labeled as HAC_1 and HAC_2 , are converted to analog signals before passing through 1 kHz reconstruction filters implemented using 4th order Ithaco 4113 filters. The output signals are then amplified using custom piezoelectric amplifiers labeled as amp_2 and amp_3 . The output of each amplifier drives one of the PZT actuators. Note that

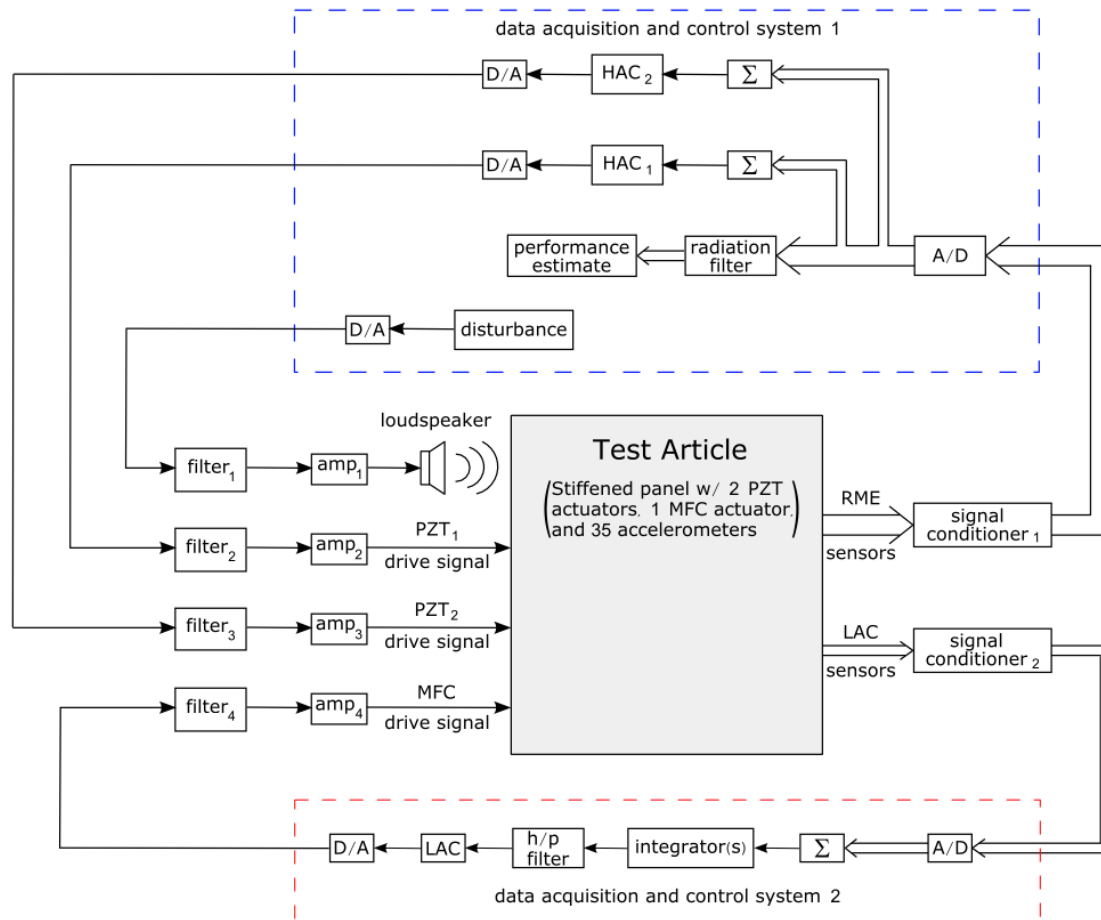


Figure 2.18: The block diagram shows the high-authority and low-authority control systems.

since the PZT amplifiers are connected to $\pm 25\text{V}$ power supplies (not shown in the diagram), a 1 V input signal produces a 25 V output signal. In addition to driving the PZT actuators, this system also supplies the disturbance signal, which is filtered by an Ithaco 4113 filter and amplified using a Carver Magnetic Field Power Amplifier (Model TFM-42). The physical disturbance is then generated using two Altec 515C 15" loudspeakers mounted in an Altec 817A vented bass horn cabinet.

Meanwhile, the second data acquisition system, contained within the dashed red rectangle in the bottom of Figure 2.18, implements the low-authority control system. Specifically, signals from the 5 accelerometers, shown in Figure 2.16 (b), are fed through a PCB signal conditioning unit. Since this system operates at 10 kHz, the corner frequency for the anti-aliasing filters is set at 5 kHz. The signals are then sampled using a PD2-MFS-8-300/16DG data acquisition card from *UEI*. The sampled data is summed and integrated either once to yield velocity or twice for position. Integration is approximated by filtering acceleration using the low-pass filter, $0.01/(z - 0.99)$. However, since this filter does not approximate an integrator at low frequencies, DC phase can destabilize the control system. Therefore a high-pass filter, $0.9922(z - 1)/(z - 0.9844)$, is also included to roll-off low-frequency gain. After integrating and filter-

ing the summed response, the low-authority control law is implemented. The output of this system is then passed through a reconstruction filter with a corner frequency of 5 kHz. This signal drives a Trek PZD 2000 High Voltage Amplifier, which in turn powers the MFC actuator.

2.2.3 Acoustic excitation

As we have previously discussed, the response of the structure is dependent on both the spectral and spatial characteristics of the disturbance. While shock-cell noise can be roughly approximated by a single point source (Montgomery 2004), boundary layer noise is more difficult to reproduce in the laboratory (Elliott et al. 2005). However, at maximum climb conditions, shock-cell noise dominates the response over much of the bandwidth of interest, as shown in Figure 2.7. Therefore, the experimental investigation neglects boundary-layer noise and approximates shock-cell noise with a loudspeaker. Note that to approximate a source in the free field, the loudspeaker is positioned in the anechoic chamber instead of the reverberation chamber. For this project, two Altec 515C 15" loudspeakers mounted in an Altec 817A vented bass horn cabinet are used to generate the acoustic excitation. The location of the cabinet is selected such that the phase velocity of the disturbance roughly matches the phase velocity calculated from the flight test data. In particular, to approximate a phase velocity of 1000 m/s the loudspeaker is positioned such that the angle of incidence of the acoustic excitation is 20° . Therefore, the loudspeaker is positioned 6.1 m away from the front wall, and 2.2 m to the side of the test section, as shown in Figure 2.19. The height of the speaker is aligned with the height of the test section.

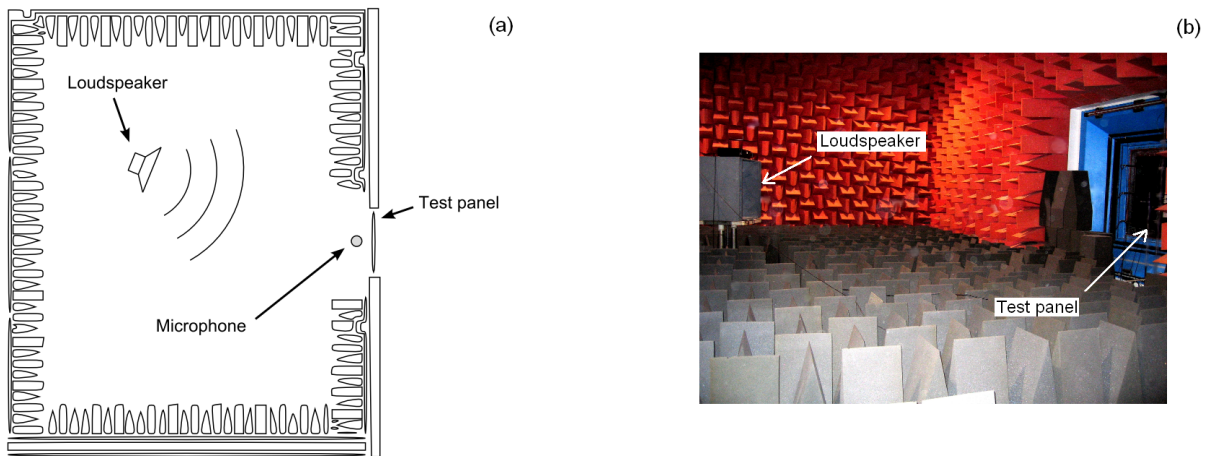


Figure 2.19: The disturbance is generated using a loudspeaker in the anechoic chamber.

In addition to approximating the phase velocity and spatial characteristics, the excitation is also required to match the frequency shifted spectral shape shown by the dashed red line in Figure 2.10. However, due to limitations associated with the acoustic driver, the high and low-frequency components of the excitation are rolled off, as shown by the dash-dotted blue line in Figure 2.20. In particular, the response of the loudspeaker is limited to the 80 -1000 Hz bandwidth. Although the loudspeaker is capable of operating down to 60 Hz, the low frequency response of the panel is dominated by global modes, which are not easily suppressed by local controllers mounted on only two bays. In addition, recall that the reverberation chamber is only diffuse

down to 80 Hz. Therefore rolling off the excitation below 80 Hz reduces the amplitude of low-frequency global modes as well as resonances due to low-frequency room modes.

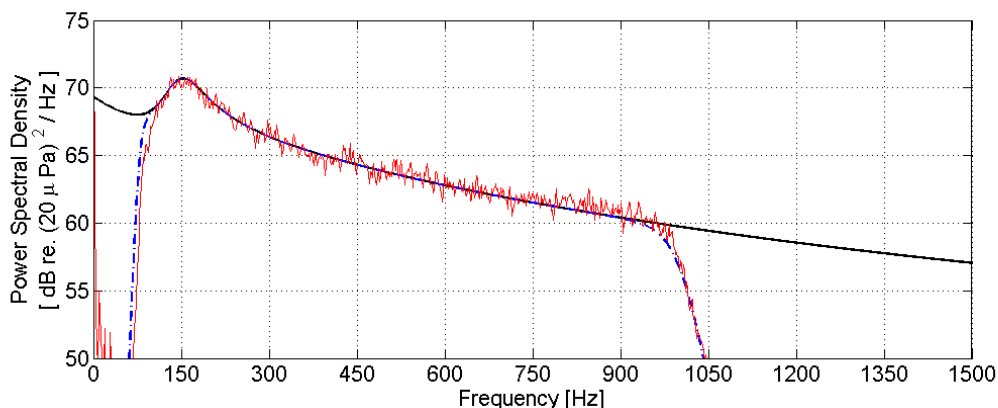


Figure 2.20: Power spectral density of the frequency shifted excitation (solid black line), the desired excitation (dash-dotted blue line), and the measured excitation (thin red line).

To generate a pressure field with the correct spectral characteristics, it is necessary to account for the dynamics of the disturbance path. Therefore a 1/4 in diameter PCB 130B10 condenser microphone positioned directly in front of the panel is used to measure the pressure field in response to a bandlimited white noise input into the loudspeaker. The input/output data is then used to estimate a model of the system. The magnitude of the frequency response function is shown in Figure 2.21. The shape of the output signal is then calculated based on the desired spectral shape, shown in Figure 2.20, and the magnitude response, shown in Figure 2.21. In particular, the power spectral density of the output signal required to generate the desired acoustic response directly in front of the panel is shown in Figure 2.22. A time-domain drive signal is then generated by filtering a white reference signal through an excitation filter, as described in Section 2.1.4. Figure 2.20 compares the desired response (dash-dotted blue line) with the measured response (thin red line). For reference, note that the OLSPL measured directly in front of the panel is approximately 95 dB in these experiments.

Next, consider the open-loop response due to the frequency-shaped acoustic disturbance. In particular, the radiated sound power from the structure is shown in Figure 2.23. Notice that the overall radiated sound power is dominated by the low frequency peaks at 118 Hz, 134 Hz, and 150 Hz. In addition, the response rolls off sharply above 1000 Hz, and below 80 Hz due to the shaped excitation. For reference purposes, the operating deflection shapes of the test section are shown in Figure 2.24. Notice that at 118 Hz the lower bay vibrates in its (1,1) bay mode while the deflection of the upper bay is relatively small. In comparison, at 134 Hz there is considerable coupling between both bays. Specifically, both bays vibrate in their (1,1) bay modes in-phase with one another. Note that the stiffener also deflects at this frequency. At higher frequencies, such as at 305 Hz, the deflection of the stiffener is not significant. At this frequency, the upper bay vibrates in its (3,1) bay mode in combination with a smaller in-phase response on the lower bay.

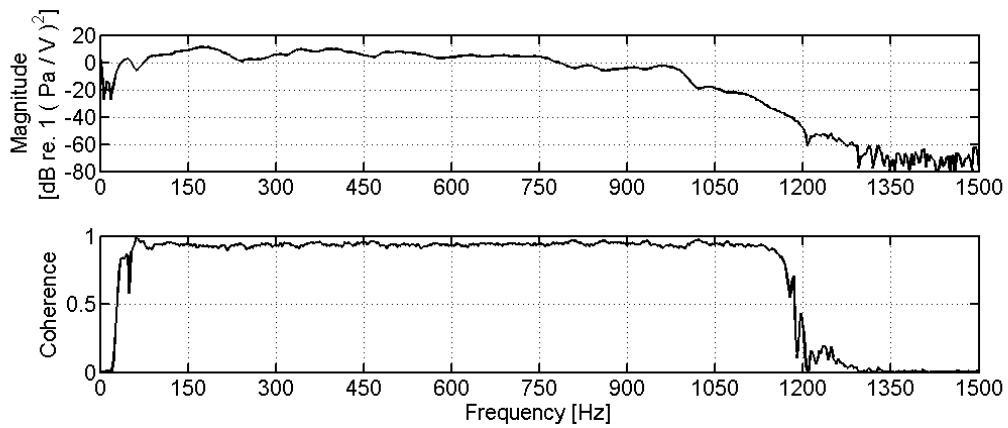


Figure 2.21: The figure shows the magnitude of the frequency response function and coherence between the drive signal and the microphone.

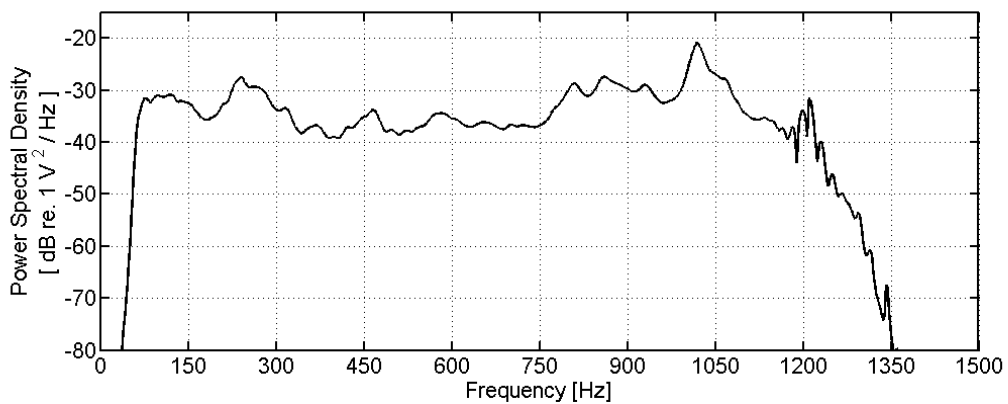


Figure 2.22: The power spectral density of the drive signal required to achieve the desired spectral shape in front of the panel.

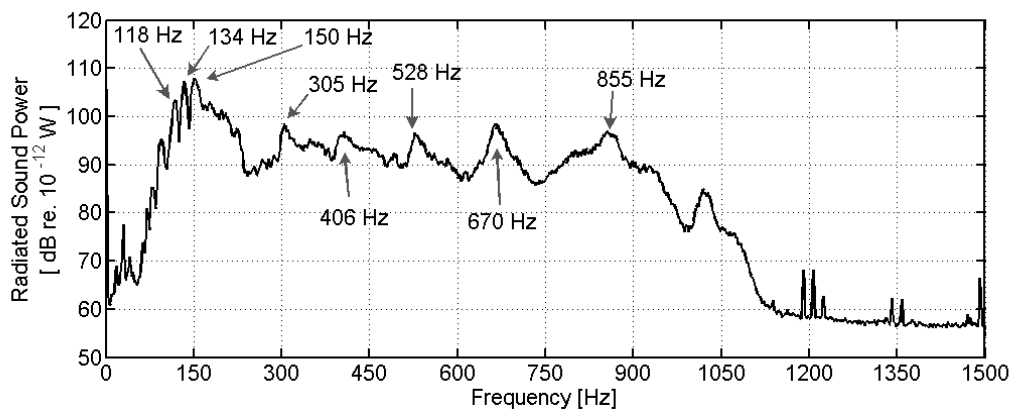


Figure 2.23: Estimate of the acoustic power radiated from the two bays due to the acoustic excitation.

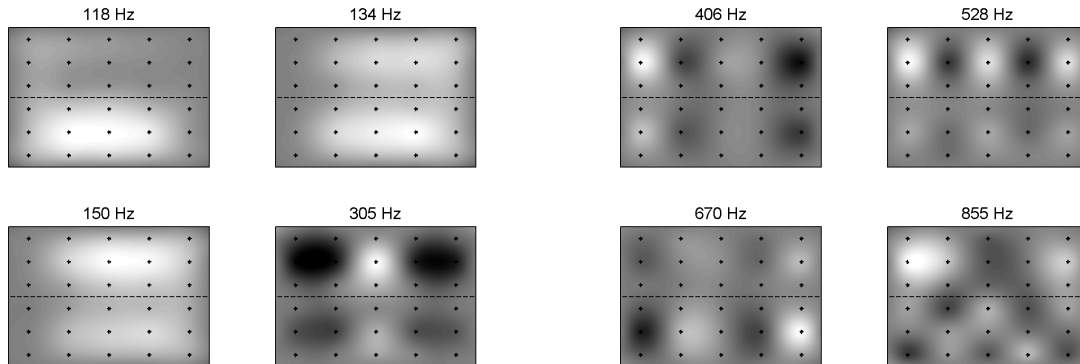


Figure 2.24: Operating deflection shapes due to the acoustic excitation.

2.2.4 Experimental procedure

At this point, it is beneficial to briefly discuss some of the steps involved in a typical control experiment. The first step is to drive each actuator with an independent broadband random excitation while logging the response from each set of sensors. Frequency response function estimates are then generated from the input-output data as shown in Figure 2.25 and Figure 2.26. These figures show the response from each of the PZT actuators to their corresponding sensor (consisting of the summed response from 4 accelerometers). Notice that since the transducers are not collocated, the phase is not bounded between $\pm 90^\circ$. Therefore, this transducer configuration would not be appropriate for direct velocity feedback. However, high-authority control strategies, such as LQG control, do not require collocated transducers. Instead, a state-space model of the system is used to design these controllers. For this work, the state-space models are generated using the observer/Kalman filter identification (OKID) algorithm described by Juang (1994). The OKID algorithm uses experimental time-domain input/output data to compute observer Markov parameters, which are then used to estimate the pulse-response sequence for the system. The eigensystem realization algorithm (ERA) is then used to extract a state-space model from the pulse-response sequence. The OKID algorithm is implemented using the `okid.m` function in the SOCIT toolbox for MATLAB.

For this project, 75th order models are sufficient to accurately model each single-input single-output system in the bandwidth of interest. Once the control models are identified, the local controllers are designed. Since the design process is the focus of subsequent chapters, it is not discussed here. Instead, it is sufficient to point out that after each controller is designed, they are implemented using xPC Target. Note that the Simulink diagrams used to implement the control systems are included in Appendix E. Once the controllers are turned on, closed-loop data is acquired and the performance of the control system is evaluated by comparing open and closed-loop measurements.

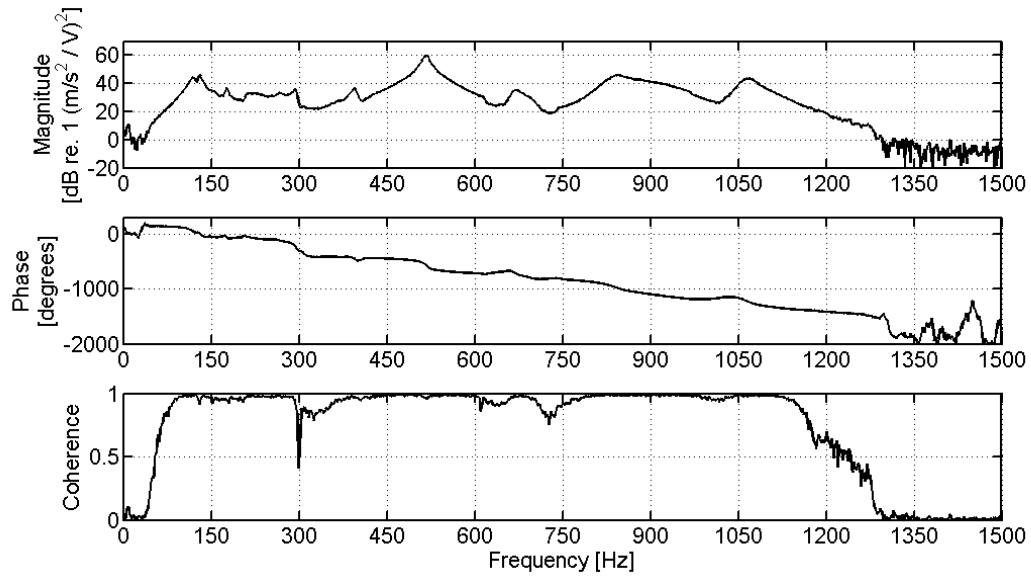


Figure 2.25: The figure shows the experimental frequency response function between the PZT actuator and the summed accelerometers on the lower bay.

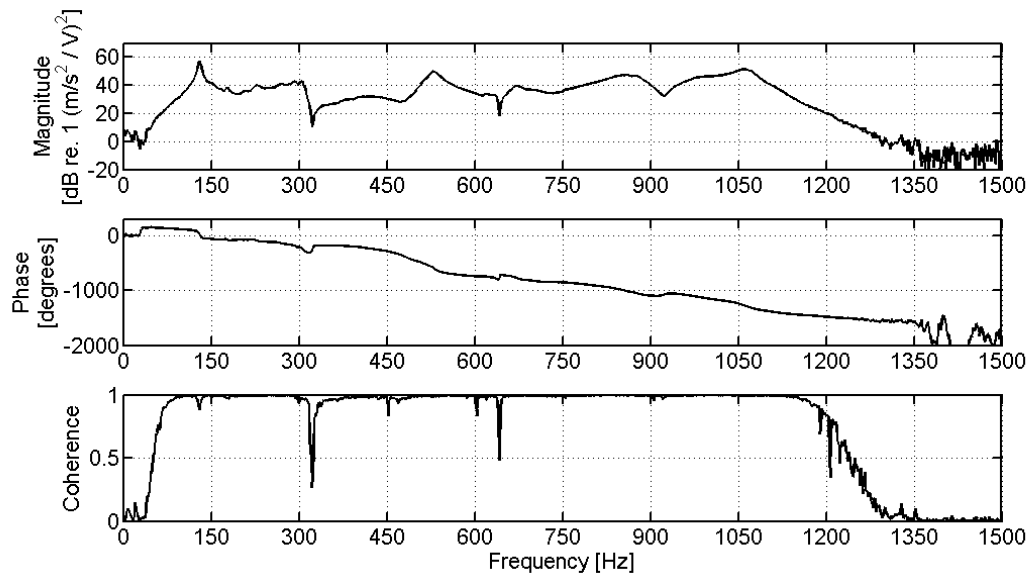


Figure 2.26: The figure shows the experimental frequency response function between the PZT actuator and the summed accelerometers on the upper bay.

Chapter 3

Linear quadratic control

This chapter presents background information on linear quadratic (LQ) control. Although all of the concepts reviewed here are presented in other texts including an excellent reference by Anderson and Moore (1990), the material discussed in this chapter summarizes particular aspects relevant to this project. One of the primary advantages of LQ control is that it provides analytical design procedures that can be used to calculate optimal linear control laws. In particular, the control laws are designed to minimize quadratic cost functions, which can explicitly account for conflicting design parameters. Another advantage of LQ control is that it typically outperforms classical control strategies. Therefore it is often referred to as high-authority control (HAC) (Aubrun and Ratner 1984).

A practical LQ strategy called linear quadratic Gaussian (LQG) control has been used successfully in many active structural control applications (Petitjean and Legrain 1996; Clark et al. 1998; Gibbs et al. 2000). Since LQG control is also relatively simple and well understood, it is the only high-authority strategy considered in this work. Essentially, the LQG controller is designed by independently solving optimal state regulation and state estimation problems. The state regulation problem assumes that all of the system states are measurable and is solved by calculating the optimal feedback gain matrix, which minimizes a quadratic function containing performance and control effort terms. However, since full-state measurements are rarely available in practice, state estimates are typically fed back in place of the actual system states. The state estimates are calculated using a Kalman observer, which generates optimal estimates for a particular noise environment. Like other high-authority control strategies, LQG control is model based. Therefore performance ultimately depends on the fidelity of the control model. In order to improve performance and stability in the presence of modeling error, LQG designs are often either frequency-shaped or modified using loop transfer recovery techniques (Anderson and Moore 1990).

This chapter begins with a review of the optimal state regulation problem, which includes discussions on the robust stability of both continuous and discrete-time designs. Next, the optimal stochastic estimator is described, and then LQG control is discussed. Since state estimates are used instead of the actual system states, the LQG design can have arbitrarily poor stability margins (Doyle 1978). Therefore, the next two sections discuss frequency shaping and loop transfer recovery, which can both be used to improve the robustness of the LQG design. The chapter concludes with a simple numerical example, which applies the concepts discussed in this chapter.

3.1 Full-state feedback

The purpose of this section is to briefly review the solution to the full-state feedback problem and highlight the stability guarantees associated with the linear quadratic regulator (LQR). For this discussion, we assume

the system is time-invariant and the weighting matrices are constant. Although these assumptions are not necessary in order to solve the general state regulation problem, this is the simplest and most commonly used formulation (Preumont 2002). Consider the linear system

$$\dot{x}(t) = Ax(t) + Bu(t) \quad (3.1.1)$$

where $x(t)$ is the state vector, $u(t)$ is the input, A is the state matrix, and B is the input matrix. Additionally, assume the system is stabilizable, which means that all of the uncontrollable modes are asymptotically stable (Anderson and Moore 1990). If the controller is designed to minimize the infinite-time quadratic cost function

$$J = \int_0^{\infty} (x(t)^T Q x(t) + u(t)^T R u(t)) dt \quad (3.1.2)$$

with the symmetric nonnegative definite state weighting matrix Q and the symmetric positive definite matrix R , then the optimal control law can be expressed in the simple form

$$u(t) = -Kx(t) \quad (3.1.3)$$

where $K = R^{-1}B^T S$, and S satisfies the continuous-time algebraic Riccati equation

$$SA + A^T S - SBR^{-1}B^T S + Q = 0 \quad (3.1.4)$$

Note that this equation is solved in various software packages including MATLAB.

Next, assume the cost function is expressed in terms of the plant outputs $y(t)$ instead of the system states, such that

$$J = \int_0^{\infty} (y(t)^T \tilde{Q} y(t) + u(t)^T \tilde{R} u(t)) dt \quad (3.1.5)$$

where \tilde{Q} is the output weighting matrix, \tilde{R} is the new effort weighting matrix, and $y(t)$ is defined as

$$y(t) = Cx(t) + Du(t) \quad (3.1.6)$$

with the output matrix C and the direct transmission matrix D . Note that for the remainder of this chapter, the explicit dependence on t will be dropped for notational convenience. Therefore, Equation 3.1.6 will simply be written as $y = Cx + Du$.

At this point, notice that if Equation 3.1.6 is plugged into Equation 3.1.5, then the cost function can be rewritten as

$$J = \int_0^{\infty} (x^T Q x + u^T R u + 2x^T N u) dt \quad (3.1.7)$$

where $Q = C^T \tilde{Q} C$, $R = D^T \tilde{Q} D + \tilde{R}$, and $N = C^T \tilde{Q} D$. Now complete the square

$$x^T Q x + u^T R u + 2x^T N u = x^T (Q - N R^{-1} N^T) x + (u + R^{-1} N^T x)^T R (u + R^{-1} N^T x)$$

and notice that the cost function can be written in the familiar form

$$J = \int_0^\infty (x^T Q_o x + u_o^T R u_o) dt \quad (3.1.8)$$

where $Q_o = Q - N R^{-1} N^T$ and $u_o = u + R^{-1} N^T x$. Next, rewrite Equation 3.1.1 in terms of u_o

$$\dot{x} = A_o x + B u_o \quad (3.1.9)$$

where $A_o = A - B R^{-1} N^T$. If we again assume that the system is stabilizable, R is positive definite, and now Q_o is nonnegative definite, then the optimal feedback gain matrix $K = R^{-1} B^T S$ can be found by solving the standard algebraic Riccati equation using the new system matrix A_o along with the new state weighting matrix Q_o .

3.1.1 Continuous-time stability margins

An attractive feature of state feedback is that robustness is guaranteed. For example, if the system is represented using unity feedback, as shown in Figure 3.1, then the return difference equality can be used to show that

$$|1 + K(j\omega I - A)^{-1} B| \geq 1 \quad \text{for all } \omega, \quad (3.1.10)$$

in the scalar case (Anderson and Moore 1990, pg. 105). Notice that Equation 3.1.10 imposes geometric constraints on the Nyquist plot of the open-loop transfer function. Specifically, the Nyquist plot can not pass within a circle of radius one centered at $(-1, 0)$. Therefore, the continuous-time full-state feedback system has an infinite upside gain margin, a downside margin of $1/2$, and a phase margin of at least 60° .

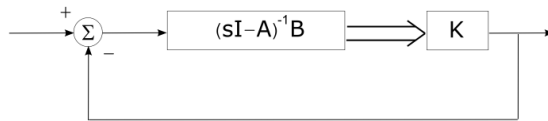


Figure 3.1: The figure shows an LQR block diagram with unity feedback.

Similar guarantees exist for multiple inputs, however in this case the singular values of the return difference, $I + K(j\omega I - A)^{-1} B$, are lower bounded by one (Anderson and Moore 1990). Since the closed-loop system is stable as long as the multiplicative uncertainty is less than the smallest singular value of the return difference (Bitmead et al. 1990), then the continuous-time LQR design is guaranteed to be stable provided the multiplicative uncertainty is less than one at every frequency.

3.1.2 Discrete-time stability margins

Since higher-order controllers are often implemented digitally, it is helpful to extend the stability results to the discrete-time system. Therefore, consider the discrete-time model

$$\begin{aligned} x_{k+1} &= Ax_k + Bu_k \\ y_k &= Cx_k + Du_k \end{aligned} \quad (3.1.11)$$

Again, we are interested in the infinite horizon optimal control problem with the familiar cost function

$$\begin{aligned} J &= \sum_{k=1}^{\infty} y_k^T \tilde{Q} y_k + u_k^T \tilde{R} u_k \\ &= \sum_{k=1}^{\infty} x_k^T Q x_k + u_k^T R u_k + 2x_k^T N u_k \end{aligned} \quad (3.1.12)$$

where $Q = C^T \tilde{Q} C$, $R = D^T \tilde{Q} D + \tilde{R}$, and $N = C^T \tilde{Q} D$. Once again, the cost function can be rewritten as

$$J = \int_0^{\infty} (x^T Q_o x + u_o^T R u_o) dt \quad (3.1.13)$$

where $Q_o = Q - NR^{-1}N^T$ and $u_o = u + R^{-1}N^T x$. The optimal control law is expressed as

$$u_k = -Kx_k \quad (3.1.14)$$

where $K = (B^T S B + R)^{-1} B^T S A_o$, and S now satisfies the discrete-time algebraic Riccati equation

$$A_o^T S A_o - S - A_o^T S B (B^T S B + R)^{-1} B^T S A_o + Q_o = 0 \quad (3.1.15)$$

with $A_o = A - BR^{-1}N^T$.

Once again, the return difference equality can be used to show that for the scalar system

$$|1 + K(e^{j\omega T} I - A)^{-1} B| \geq \gamma \quad \text{for all } \omega, \quad (3.1.16)$$

where $0 < \gamma \leq 1$ (Anderson and Moore 1990, pg. 136). Therefore, the Nyquist plot is restricted from entering a circle centered at $-1 + 0j$ with a radius of γ . Since $0 < \gamma \leq 1$ the discrete-time case still has guaranteed stability margins, although they are necessarily less attractive than the continuous-time margins.

3.2 State estimation

While state feedback requires that all states are measurable, this is rarely possible in practice. Therefore it is often necessary to reconstruct the state vector x using a stochastic estimator, as shown in Figure 3.2. Notice that the estimator consists of a model of the plant with an additional feedback loop used to ensure \hat{x} converges to x sufficiently quickly. The feedback signal is generated by multiplying the measurement error $y_v - \hat{y}$ by the observer gain matrix L . However, since the feedback signal is generated using the noisy output measurement y_v , increasing the magnitude of L improves convergence speed while amplifying the

measurement noise. Therefore, the optimal choice of L involves a tradeoff between measurement noise sensitivity and convergence speed. As we will show, the optimal solution to the state estimation problem is based on the relative amplitude of the state and measurement noise, shown in Figure 3.2 as n and v respectively.

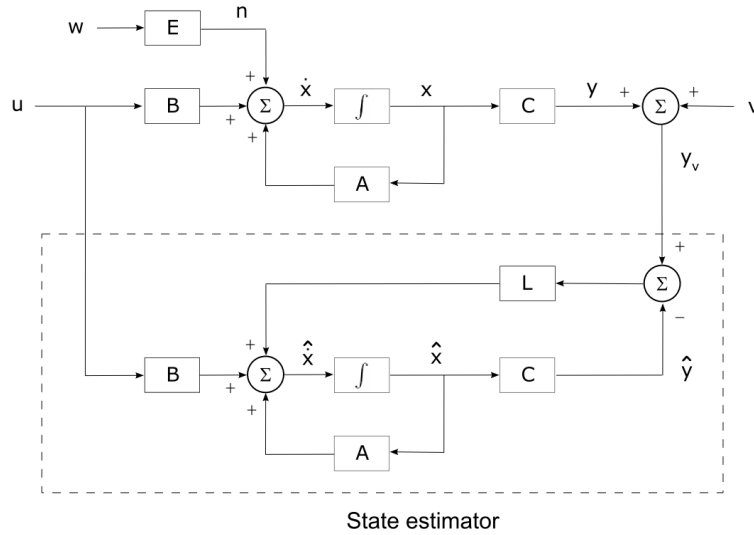


Figure 3.2: Estimator block diagram.

Before discussing the full stochastic design, it is beneficial to first consider the deterministic system (ie $w = v = 0$),

$$\begin{aligned} \dot{x} &= Ax + Bu \\ y &= Cx \end{aligned} \tag{3.2.1}$$

with the full-state observer (also called the Luenberger observer),

$$\dot{\hat{x}} = A\hat{x} + Bu + L(y - C\hat{x}). \tag{3.2.2}$$

Notice that the observer equation is based on both the system model $A\hat{x} + Bu$, and the output error $y - C\hat{x}$ multiplied by the observer gain L . Since the goal of the estimator is to reconstruct the system states, it is convenient to rewrite Equation 3.2.2 as

$$\dot{e} = (A - LC)e \tag{3.2.3}$$

where the estimation error e is defined as $e = x - \hat{x}$. Notice that if the eigenvalues of $A - LC$ have negative real parts, then e will approach zero at an exponential rate. Therefore the choice of L affects the rate at which \hat{x} approaches x . Based on the deterministic design, it might be tempting to choose L such that the error decays as rapidly as possible. However, as we will show next, measurement noise sets a practical limit on convergence speed.

At this point, consider the stochastic system

$$\begin{aligned}\dot{x} &= Ax + Bu + Ew \\ y_v &= Cx + v\end{aligned}\tag{3.2.4}$$

where the disturbance w and measurement noise v are assumed to be white, gaussian, and of zero mean. Additionally, the noise processes are assumed to be independent with known covariances of $Q_n = E[ww^T]$ and $R_n = E[vv^T]$ (where $E[\]$ denotes the expectation operator). The stochastic observer, which is also referred to as the Kalman-Bucy filter, can be written as

$$\begin{aligned}\dot{\hat{x}} &= A\hat{x} + Bu + L(y_v - C\hat{x}) + Ew \\ &= (A - LC)\hat{x} + Bu + Ly_v + Ew\end{aligned}\tag{3.2.5}$$

where E is the noise input matrix. Again, the observer can be expressed in terms of the estimation error,

$$\dot{e} = (A - LC)e + Ew - Lv.\tag{3.2.6}$$

Notice that increasing L shifts the eigenvalues of $(A - LC)$ farther into the left-half s-plane, which makes e decay more rapidly. Although this makes the estimate less sensitive to the disturbance w , it increases the estimate's sensitivity to high-frequency measurement noise v . Therefore, the optimal stochastic estimator is designed to tradeoff speed of convergence with measurement noise sensitivity.

Although the physical similarities between the problems of state regulation and estimation are not obvious, the solutions are very similar. For instance, if we make standard assumptions that the system and weighting terms are time-invariant, R_n is positive definite, EQ_nE^T is nonnegative definite, and the pair (A, C) is detectable (all unobservable states are asymptotically stable), then the optimal observer gain matrix can be calculated as

$$L = SC^T R_n^{-1}\tag{3.2.7}$$

where S is the solution to the algebraic Riccati equation

$$SA^T + AS - SC^T R_n^{-1} CS + EQ_n E^T = 0\tag{3.2.8}$$

Additionally, if the pair (A, H) is stabilizable (where $H^T H = EQ_n E^T$), then the estimator is asymptotically stable (Anderson and Moore 1990). Notice the similarities between the optimal estimation and regulation problems, as shown in Table 3.1 (Preumont 2002). Due to these similarities, the two problems are referred to as duals of one another.

3.3 Linear quadratic Gaussian (LQG) control

The linear quadratic Gaussian (LQG) controller uses state estimates *in lieu* of state measurements in a full-state feedback design. Fortunately, due to the separation principle, the calculation of the state estimates and the full-state gain matrix are separate problems. Therefore, the LQG controller is designed by independently solving for the optimal state regulator and Kalman estimator. The controller is then implemented by

Table 3.1: Summary of the standard optimal regulation and estimation problems.

Linear quadratic regulator	
Gain:	$K = R^{-1}B^T S$
Riccati equation:	$SA + A^T S - SBR^{-1}B^T S + Q = 0$
Closed-loop system:	$\dot{x} = (A - BR^{-1}B^T S) x$
Kalman-Bucy filter	
Gain:	$L = SC^T R_n^{-1}$
Riccati equation:	$SA^T + AS - SC^T R_n^{-1}CS + EQ_n E^T = 0$
Closed-loop system:	$\dot{e} = (A - SC^T R_n^{-1}C) e$

combining the two designs as shown in Figure 3.3.

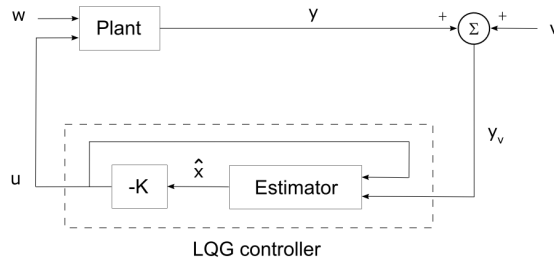


Figure 3.3: LQG diagram

To formulate the LQG problem, consider the time-invariant plant

$$\begin{aligned} \dot{x} &= Ax + Bu + Ew \\ y_v &= Cx + v \end{aligned} \tag{3.3.1}$$

and the Kalman-Bucy observer

$$\dot{\hat{x}} = A\hat{x} + Bu + L(y_v - C\hat{x}) + Ew \tag{3.3.2}$$

where L is the optimal observer gain matrix. The LQG control law is

$$u = -K\hat{x} \tag{3.3.3}$$

where K is the solution of the LQR problem. Combining Equations 3.3.1-3.3.3 gives the closed-loop system equations

$$\begin{bmatrix} \dot{x} \\ \dot{e} \end{bmatrix} = \begin{bmatrix} A - BK & BK \\ 0 & A - LC \end{bmatrix} \begin{bmatrix} x \\ e \end{bmatrix} + \begin{bmatrix} E & 0 \\ E & -L \end{bmatrix} \begin{bmatrix} w \\ v \end{bmatrix} \tag{3.3.4}$$

$$y = \begin{bmatrix} C & 0 \end{bmatrix} \begin{bmatrix} x \\ e \end{bmatrix} \quad (3.3.5)$$

where $e = x - \hat{x}$ is the estimation error.

Although the linear quadratic regulator has guaranteed stability margins, similar guarantees are not available for the LQG design due to the introduction of the observer (Doyle 1978). However, this is not to say that the stability margins are necessarily poor, only that there are no guarantees. Therefore the robustness of each LQG design must be evaluated on a case by case basis. If the margins are found to be unacceptable, then frequency shaping or loop recovery may be used to improve the design, as discussed in the following sections.

3.4 Frequency shaping

A weakness of the standard LQG formulation is that the design parameters are frequency independent. Frequency shaping offers additional design flexibility, which can be used to improve overall performance. Frequency-shaped LQG designs are generated by shaping the state regulator, the Kalman estimator, or both. The first part of this section explains how frequency shaping is applied to the regulator design.

To shape the state regulator, the plant model is augmented with filter dynamics to produce additional frequency-weighted outputs. The frequency-shaped outputs are then included in the cost function and the optimal feedback gain matrix is calculated to minimize this function. For example, shaping is often used to roll-off high-frequency effort since plant models tend to be less accurate at high frequencies (Anderson and Mingori 1985; Elliott and Sutton 1996). This is accomplished by augmenting the plant with high-pass filters to produce additional outputs u_f , as shown in Figure 3.4. Note that since the filter equation is solved in the computer, the states x_f are known and therefore only the states of the structure have to be measured (or estimated) (Cabell et al. 2006). For the moment, assume that the original plant is a single-input single-output (SISO) system. If the filter transfer function is assumed to be $C_f^T (sI - A_f)^{-1} B_f$ and the plant is expressed as $C^T (sI - A)^{-1} B$, then the augmented plant model is

$$\begin{aligned} \dot{x}_a &= A_a x_a + B_a u \\ y_a &= C_a x_a \end{aligned} \quad (3.4.1)$$

where

$$x_a = \begin{bmatrix} x \\ x_f \end{bmatrix}, \quad y_a = \begin{bmatrix} y \\ u_f \end{bmatrix}, \quad A_a = \begin{bmatrix} A & 0 \\ 0 & A_f \end{bmatrix}, \quad B_a = \begin{bmatrix} B \\ B_f \end{bmatrix}, \quad \text{and} \quad C_a = \begin{bmatrix} C & 0 \\ 0 & C_f \end{bmatrix}.$$

The cost function can then be expressed as

$$\begin{aligned} J &= \int_0^\infty (y_a^T Q y_a + r u^2) dt \\ &= \int_0^\infty (q_1 y^2 + q_2 u_f^2 + r u^2) dt \end{aligned} \quad (3.4.2)$$

where the non-negative definite matrix Q is defined as $Q = \begin{bmatrix} q_1 & 0 \\ 0 & q_2 \end{bmatrix}$, and r is a positive scalar. As

shown in Equation 3.4.2, the effort penalty at each frequency is the sum of the frequency dependent and independent terms. Finally, the optimal control law can be calculated as

$$u = -K_a x_a \tag{3.4.3}$$

where the feedback gain matrix $K_a = r^{-1} B_a^T S$ and S satisfies the algebraic Riccati equation

$$S A_a + A_a^T S - S B_a r^{-1} B_a^T S + Q = 0 \tag{3.4.4}$$

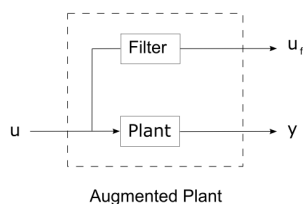


Figure 3.4: Augmented plant model used to shape the control effort.

In addition to shaping the effort weighting term, frequency shaping can also be used to shape the performance variable. For example, in active structural acoustic control (ASAC) applications, the system model is augmented with radiation filters (Fuller et al. 1996; Clark et al. 1998). Researchers have shown that minimizing a cost function expressed in terms of radiated sound power requires fewer control channels and less control power to achieve levels of performance comparable to conventional structural control systems. This is due to the fact that ASAC suppresses or restructures the structural modes that radiate most efficiently without expending energy on inefficient radiators (Fuller et al. 1996).

Next, consider frequency-shaped state estimation. Although the conventional Kalman estimator is designed assuming white process and measurement noise, this is often unrealistic. Therefore, the standard Kalman design is often frequency shaped to account for colored-noise processes. The frequency-shaped Kalman filter is generated by first augmenting the plant with shaping filters, as shown in Figure 3.5 (a), and then designing the estimator for the augmented system.



Figure 3.5: Diagram of an augmented plant model used to shape the disturbance path. The figures show: (a) a general block diagram; and (b) a diagram expressed in terms of the disturbance model and control path.

A more convenient representation for our purposes is to combine the disturbance path and filter dynamics into a single disturbance model $P(s)$, as shown in Figure 3.5 (b). The control path is now represented as $G(s)$. Notice that the output disturbance d can be generated by passing white noise w through the shaping filter $P(s)$. If the outputs are measurable, then $P(s)$ can be estimated by fitting the spectrum of the measured output with a stable state-space model. In general, the disturbance model can be estimated from either open- or closed-loop data if both u and $G(s)$ are known. Note that in order to estimate the disturbance from output measurements, we must assume that d is much larger than the measurement noise.

We conclude this section with a few observations. First, notice that frequency shaped designs can be expressed as standard LQ designs using augmented system models (Anderson and Moore 1990). While shaping the controller can provide additional flexibility and improved performance, the design is necessarily more complicated. Instead of simply selecting weighting terms, the designer must also select appropriate shaping filters. In addition, since the system model is augmented with filter dynamics, the order of the controller is increased. Although controller reduction techniques are available as discussed by Anderson and Moore (1990, chap. 10), minimizing the order of the controller is beyond the scope of the present project. The next section presents loop transfer recovery, which can also be used to improve the robustness of LQG designs.

3.5 Loop recovery

As presented earlier, the guaranteed stability margins associated with full-state feedback are lost when the estimator is introduced. In response to this problem, the loop transfer recovery (LTR) procedure was developed by Doyle and Stein (1979) to asymptotically "recover" the properties of the full-state feedback design. Essentially, LTR modifies the estimator such that the LQG system inherits the robustness of the state regulator. As the name implies, the robustness of the regulator is "recovered" by making the LQG loop transfer function approach that of the state regulator (Bitmead et al. 1990). Notice from Figure 3.1 that the LQR loop transfer function is

$$L_{LQR} = -K (sI - A)^{-1} B \quad (3.5.1)$$

Similarly, the LQG loop transfer function is

$$L_{LQG} = G(s)F(s) \quad (3.5.2)$$

where the plant transfer function is defined as $G(s) = C (sI - A)^{-1} B$, and the LQG controller is $F(s) = -K (sI - A + BK + LC)^{-1} L$.

As described by Anderson and Moore (1990), if the plant is stabilizable, completely observable, time-invariant and also minimum phase, then in the limit as the amplitude of the disturbance model approaches infinity, the open-loop LQG transfer matrix L_{LQG} equals that of the state regulator L_{LQR} . Therefore, if the plant is minimum phase, then the guaranteed robustness properties of the state regulator can be recovered by increasing the amplitude of the disturbance model.

There are a number of obvious practical limitations associated with loop transfer recovery. First, since the LQG design is optimal with respect to the nominal stochastic model, artificially changing the distur-

bance model will necessarily result in a suboptimal solution for the nominal noise environment. Therefore, improved robustness is achieved at the expense of nominal system performance. However, since the characteristics of the noise environment are rarely known *a priori*, noise covariance values are often used simply as design parameters. Therefore it is often beneficial to sacrifice some level of nominal performance in exchange for improved robustness.

Another problem associated with loop recovery is the need for high loop gain. This can make the control system overly sensitive to unmodeled dynamics and certain types of plant variations. To avoid these problems, the disturbance model is usually increased incrementally until adequate loop recovery is achieved. The goal is not necessarily to achieve full recovery, but only to generate an acceptable design.

The minimum phase requirement is another serious limitation associated with the LTR strategy. This requirement is necessary since full recovery relies on pole-zeros cancelations. Since unstable pole-zero cancelations are not acceptable, full recovery can only be achieved if the system is minimum phase (Anderson and Moore 1990). However, there are still a number of practical ways to exploit loop recovery when the system is not minimum phase. For example, one of the simplest approaches is to proceed tentatively as if the system were minimum phase, and increase the amplitude of the disturbance model until the maximum robustness is achieved (Anderson and Moore 1990).

Moore and Xia (1987) suggest another alternative using a minimum-phase, all-pass factorization of the plant model. In this case, loop recovery can be used to recover the performance of certain partial state feedback designs. Specifically, designs that only feedback the states of the minimum-phase factor can be recovered. Therefore, if acceptable performance and robustness can be achieved using partial state feedback, then loop recovery can be used to recover those characteristics. Unfortunately, it is not always possible to achieve a robust design using only partial state feedback.

Another option is to use frequency-shaped designs to achieve partial loop recovery in particular frequency bands (Moore et al. 1981). In this case, loop-recovery can still be particularly effective when the non-minimum phase zeros are outside the bandwidth of interest. An additional advantage of frequency-shaped designs is the ability to achieve different performance/robustness trade-offs in different frequency bands (Stein and Athans 1987).

At this point, it is beneficial to make a few observations concerning loop transfer recovery. First, while loop recovery is only guaranteed for minimum phase systems, partial recovery is often possible for nonminimum phase systems (Maciejowski 1985; Bitmead et al. 1990). Next, notice that loop recovery only recovers LQR performance. Therefore if the original LQG controller is more robust than the state regulator, then exploiting loop recovery will make the system less robust, as demonstrated by Bitmead et al. (1990). Finally, note that if the system is not minimum phase, then the characteristics of the regulator will affect the amount of loop recovery we can achieve (Zhang and Freudenberg 1990).

3.6 Simple example

Before concluding this chapter, it is helpful to present a simple example, which reviews the concepts of frequency shaping and loop recovery. Consider the 3 degree-of-freedom spring-mass-damper system shown in Figure 3.6. In this example, the masses are $m_1 = 1$ kg, $m_2 = 2$ kg, and $m_3 = 0.5$ kg, the dampers, c_1 , c_2 ,

and c_3 , all equal 1 kg/s, and the springs are $k_1 = 100$ N/m, $k_2 = 140$ N/m, and $k_3 = 250$ N/m. As shown in Figure 3.6, the force input u is applied to m_1 and the output y measures the acceleration of m_3 . Note that since the sensor and actuator are separated, the frequency response from u to y is not minimum phase.

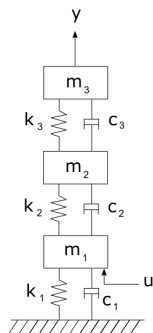


Figure 3.6: Simple 3-DOF spring-mass-damper model.

Initially the plant is assumed to be continuous, and the optimal feedback gain matrix is calculated to minimize the cost function

$$J = \int_0^{\infty} (y^T \tilde{Q} y + u^T \tilde{R} u) dt \quad (3.6.1)$$

with the output weighting $\tilde{Q} = 1$, and the effort weighting $\tilde{R} = 0.1$. In this example, a random Gaussian disturbance is assumed to enter the system through the control path. Therefore, the optimal observer gain matrix is calculated without an explicit disturbance model. In other words, there is no need to augment the system model with an explicit disturbance model since the noise input matrix equals the control input matrix. The nominal estimator is designed using the disturbance covariance $Q_n = 10^3$, and the measurement noise covariance $R_n = 1$. In addition to the nominal estimator, a 2nd design is also calculated using a larger disturbance covariance of $Q_n = 10^9$ to exploit broadband loop recovery.

Figure 3.7 compares the Nyquist diagrams for the state feedback design, the standard LQG design with $Q_n = 10^3$, and the LQG/LTR design using $Q_n = 10^9$. Since the plant is continuous with no direct feedthrough term, the LQR system has an infinite gain margin and a phase margin of 64° . In comparison, the nominal LQG design has a gain margin of 5.8 dB with a phase margin of 47° . Notice that even though the plant is not minimum phase, partial loop recovery is still achieved by increasing Q_n . In particular, the LQG/LTR design has a gain margin of 19 dB with a phase margin of 57° . As the LQG loop transfer function approaches the LQR design, closed-loop performance also converges, as shown in Figure 3.8. However, since the system is not minimum phase, complete recovery of the LQR design should not be expected as the disturbance covariance is increased further.

Next we investigate frequency-shaped LTR using a discrete version of the system model sampled at 20 Hz. Notice that since the disturbance enters through the control input, the nominal disturbance model is identical to the plant model. Frequency-shaped loop recovery is exploited in this example by increasing the magnitude of the disturbance model by 6 dB at 1.3 Hz. This is accomplished by shaping the magnitude of the nominal disturbance model by hand, and then fitting the response with a stable state-space system. The plant is then

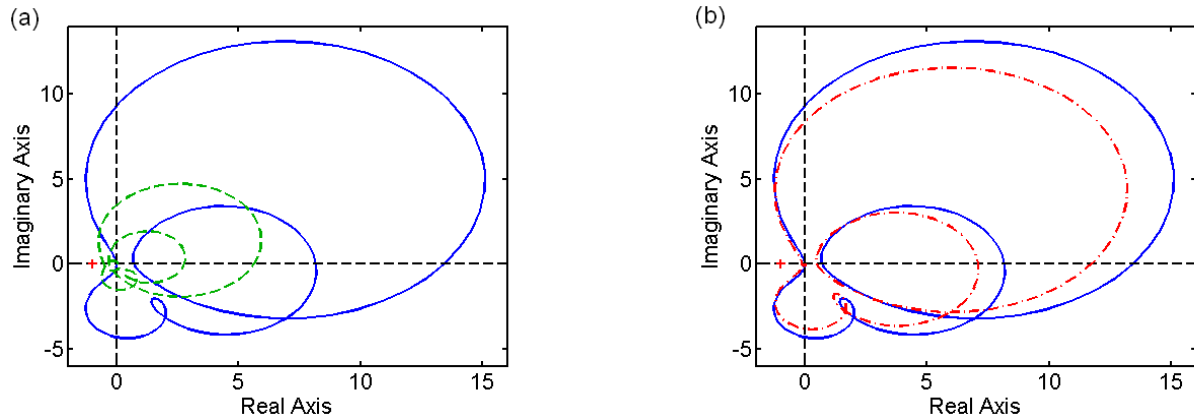


Figure 3.7: Nyquist plot of the open-loop frequency response with an LQR controller (solid blue lines), and an LQG controller. The LQG controller is designed with (a) $Q_n = 10^3$ (dashed green line); and (b) $Q_n = 10^9$ (dash-dotted red line).

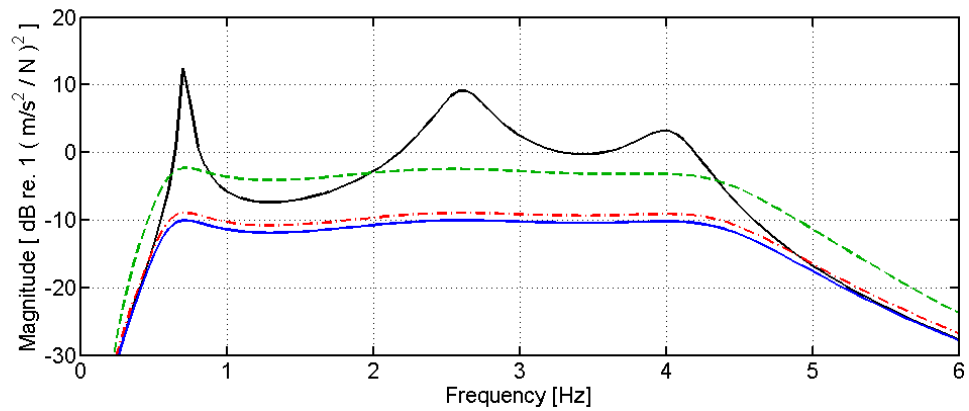


Figure 3.8: Magnitude of the open-loop FRF (solid black line), closed-loop FRF with an LQR controller (solid blue line), closed-loop FRF with the standard LQG controller (dashed green line), and closed-loop FRF with an LQG/LTR design (dash-dotted red line).

augmented with the shaped disturbance model, and the estimator is redesigned. Figure 3.9 compares the magnitude of the original disturbance model with the frequency-shaped model.

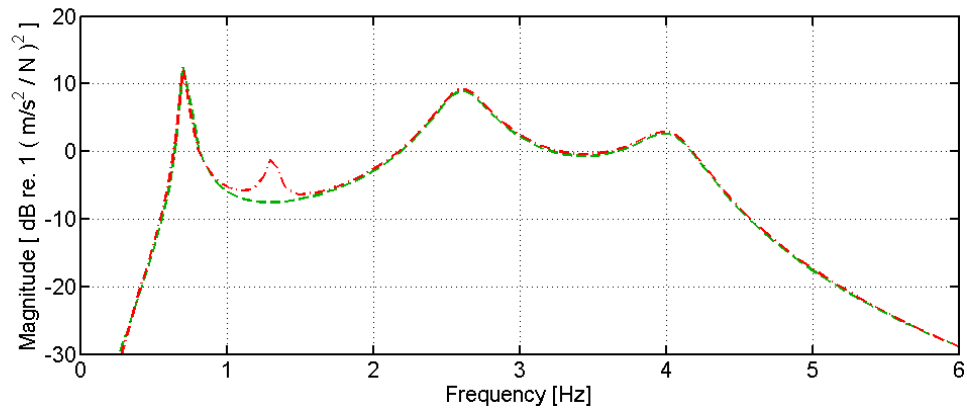


Figure 3.9: Magnitude of the original disturbance model (dashed green line), and the frequency-shaped disturbance model (dash-dotted red line).

Figure 3.10 compares the Nyquist plots of the LQR design, the standard LQG design, and the frequency-shaped LQG/LTR design. For clarity, the response is only shown from 0.68 to 2.5 Hz. Notice that increasing the disturbance model produces an extra loop in the Nyquist plot, allowing the LQG/LTR design to recover LQR performance locally. As a result, frequency-shaped loop recovery improves performance at 1.3 Hz, as shown in Figure 3.11.

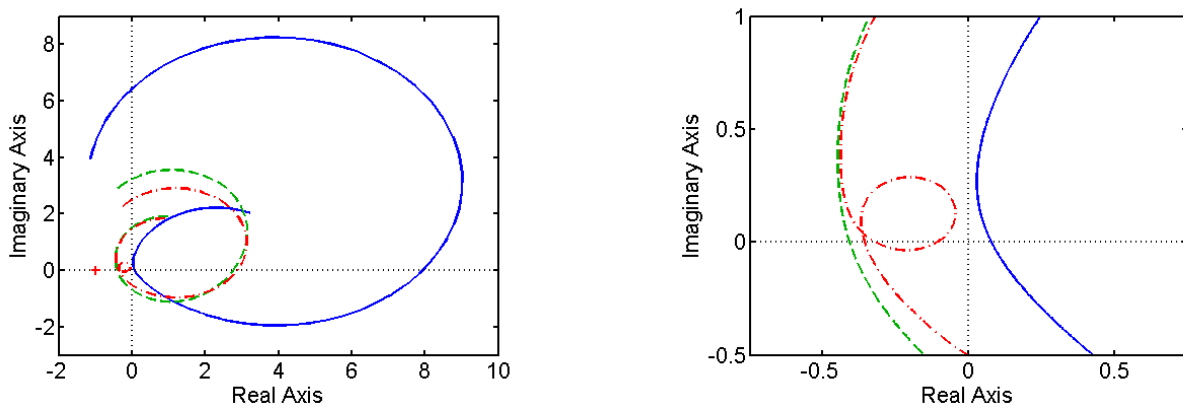


Figure 3.10: Nyquist plot of the discrete system with an LQR controller (solid blue line), LQG controller (dashed green line), and frequency-shaped LQG/LTR design (dash-dotted red line). For clarity, the response is only shown from 0.68 – 2.5 Hz. The figure on the right shows an expanded view of the response on the left.

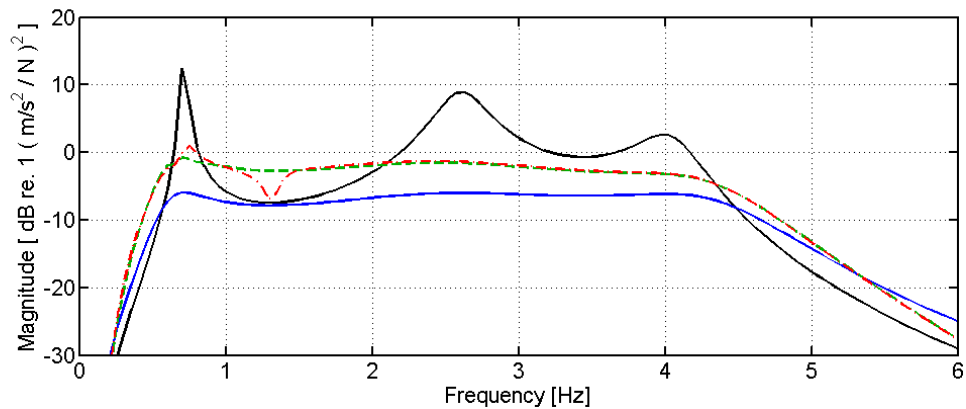


Figure 3.11: Magnitude of the open-loop FRF (solid black line), closed-loop FRF with an LQR controller (solid blue line), closed-loop FRF with an LQG controller (dashed green line), and closed-loop FRF with a frequency-shaped LQG/LTR design (dash-dotted red line).

3.7 Summary

This chapter shows that while continuous-time LQR designs have attractive stability margins (ie $\pm 60^\circ$ phase margins and gain margins of $+\infty$ and -6 dB), the same margins are not guaranteed in the discrete-time case. Despite the fact that there are no guarantees, acceptable robustness is often still available in practice (Maciejowski 1985). Unfortunately, full-state information is rarely available, and therefore state estimates must be used *in lieu* of the actual state measurements. Since the state estimates may be inaccurate, the LQG design can have arbitrarily poor stability margins despite the attractive characteristics of the LQR design (Doyle 1978). If acceptable robustness is not achieved with the nominal LQG design, frequency shaping can often be used to improve robustness. Another option is to modify the estimator in order to achieve partial loop recovery of the state-feedback design. However, this is achieved at the expense of measurement noise immunity, and therefore frequency shaped loop recovery is often preferable since it allows different tradeoffs in different frequency bands (Stein and Athans 1987).

Chapter 4

Decentralized control of interacting subsystems

The purpose of this chapter is to discuss the limitations of standard, model-based decentralized control strategies. Decentralized control implies that each controller is designed and implemented independently using only local information. Therefore, the approach is scalable and also tends to be less sensitive to transducer failures than fully-coupled MIMO designs. Scalability is extremely important for this application since the aircraft fuselage may contain several hundred bays. An example of a generic decentralized control strategy is shown in Figure 4.1. Notice that the i^{th} controller C_i generates a control signal u_i based only on information from the output y_i . This approach is particularly effective if the plant G is diagonally dominant since the cross-coupling between the i^{th} input and the j^{th} output is neglected during the design process. In the context of this work, the diagonal terms of G model the response between actuator/sensor pairs on the same bay, while the off-diagonal terms capture the coupling between sensors on one bay and actuators on another bay. As we will explain later in this chapter, the coupling between transducers on neighboring bays can destabilize decentralized controllers.

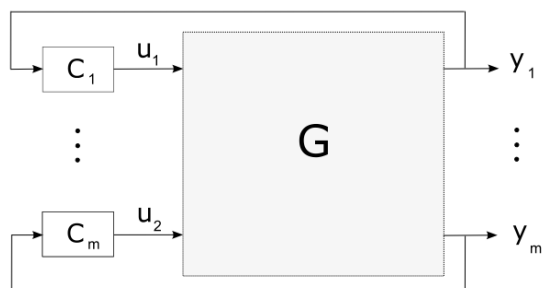


Figure 4.1: Block diagram of a decentralized control system [adapted from Cabell et al. (2003)].

This chapter begins by introducing the decentralized control problem and demonstrating why the cross coupling between subsystems limits achievable performance. In particular, decentralized control of coupled systems is shown to introduce additive error in both the control and disturbance models. Frequency-shaped linear quadratic control approaches are then discussed and are shown to improve standard decentralized designs. While these approaches can be effective, they require *a priori* knowledge of the frequency bands where spillover is likely to occur. Since this information may not be available in practice, alternative control approaches are investigated in subsequent chapters.

4.1 Background

The purpose of this section is to provide background information on decentralized control. For clarity, consider the relatively simple two-input two-output system shown in Figure 4.2 (a). In this example, the plant is defined by

$$G = \begin{bmatrix} G_{11} & G_{12} \\ G_{21} & G_{22} \end{bmatrix} \quad (4.1.1)$$

where G_{ij} denotes the transfer function from the i^{th} actuator to the j^{th} sensor. The block diagram can also be rearranged as shown in Figure 4.2 (b). Although the feedback controller C_2 is designed for the nominal subsystem model G_{22} , notice that the cross-coupling terms (G_{12} and G_{21}) and the controller C_1 introduce an additional path from u_2 to y_2 . Therefore, the combined model from u_2 to y_2 is

$$G_2 = G_{22} + \Delta_{A1} \quad (4.1.2)$$

where $\Delta_{A1} = G_{21}C_1G_{12}/(1 - C_1G_{11})$ is the additive error introduced by C_1 . Note that if the local control system designed for G_{22} is not robust to the modeling error introduced by C_1 , then the coupled system will be unstable. This demonstrates the need for robust local controllers. However, recall that LQG systems can have arbitrarily poor stability margins. Therefore, it is easy to envision a scenario where local LQG controllers could destabilize the coupled system.

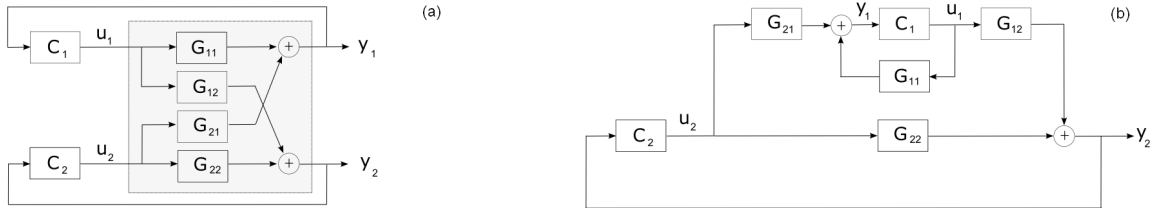


Figure 4.2: Two-channel decentralized control system. The figures show: (a) the standard block diagram; and (b) a rearranged diagram highlighting the additive error introduced by neighboring controllers.

To avoid potential stability problems, the robustness of each design should be checked on a case by case basis. Recall that robust stability is typically expressed in terms of the gain margin, which is a measure of the system's tolerance to multiplicative error. Therefore, it is beneficial to rewrite Equation 4.1.2 as

$$G_2 = G_{22} (1 + \Delta_{M1}) \quad (4.1.3)$$

where $(1 + \Delta_{M1})$ is the multiplicative error, and the multiplicative uncertainty Δ_{M1} is defined as $\Delta_{M1} = \Delta_{A1}/G_{22}$. In this example,

$$\Delta_{M1} = \left(\frac{G_{21}G_{12}}{G_{11}G_{22}} \right) \left(\frac{C_1G_{11}}{1 - C_1G_{11}} \right). \quad (4.1.4)$$

Notice that the first term in parenthesis is a measure of the diagonal dominance of the plant. In particular,

this term will be large if the plant is not diagonally dominant (ie the product of the cross-coupling terms is large with respect to the product of the diagonal terms). On the other hand, the term will be small if the plant is diagonally dominant (ie $G_{11}G_{22} \gg G_{12}G_{21}$). The second term in Equation 4.1.4 is the complementary sensitivity function T_1 , as described in Appendix B. To maintain robust stability, the control system designed for subsystem 2 must be robust in the frequency bands where the plant is not diagonally dominant and at frequencies where T_1 is large.

In addition to introducing unmodeled dynamics, neighboring control loops also change the characteristics of the disturbance. For instance, consider Figure 4.3 (a), which shows the output disturbances d_1 and d_2 . Notice that including C_1 introduces a path from d_1 to y_2 . As a result, the disturbance at y_2 becomes $d_2 + d_1C_1G_{12}/(1 - C_1G_{11})$. This demonstrates that neighboring control loops introduce both modeling error and disturbance variations, as shown in Figure 4.3 (b). Disturbance variations are undesirable since the dynamics of the noise processes are used to design the optimal controller. Since the disturbance model is typically identified from open-loop measurements, the closed-loop system will not necessarily be optimal with respect to the actual disturbance. This can significantly degrade closed-loop performance.

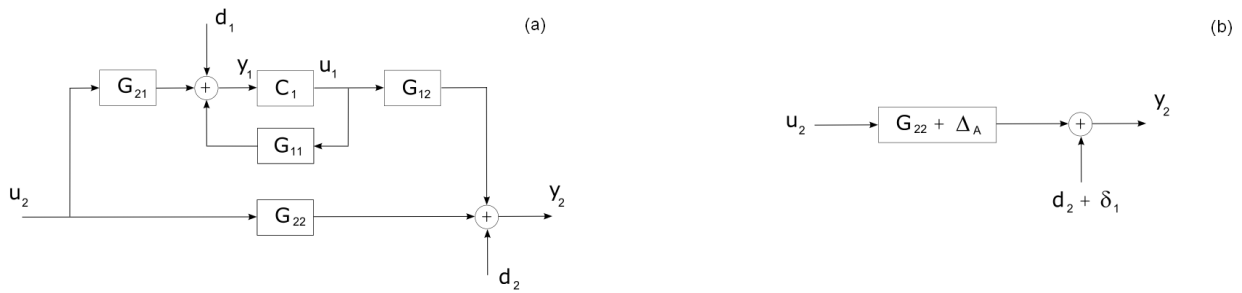


Figure 4.3: Block diagrams demonstrating that neighboring control loops affect both the plant dynamics and the disturbance.

4.1.1 Numerical simulation

To help demonstrate these concepts, consider a simple numerical example using the two-bay model described in Chapter 2. Recall that this model represents a flat panel partitioned into two bays by a stiffener. Since each bay has a single actuator/sensor pair, the plant only contains two inputs and outputs, as shown in Figure 4.2. In this example, independent LQG controllers denoted as C_1 and C_2 are designed for each bay. In addition, the disturbance is assumed to enter through each control path, and therefore both controllers are designed without explicit disturbance models. The controllers are designed with output weighting $\tilde{Q} = 1$, effort weighting $\tilde{R} = 10^{-7}$, disturbance covariance $Q_n = 1$, and measurement noise covariance $R_n = 10^{-4.1}$.

Initially, assume $C_2 = 0$ and consider Figure 4.4, which shows the frequency response from u_2 to y_2 with and without the controller C_1 . Notice that including C_1 changes the dynamics of the system primarily in the 150 – 250 Hz frequency range. To understand why, recall that the multiplicative uncertainty is proportional to the complementary sensitivity function T_1 . The complementary sensitivity function is in turn related to

the sensitivity function S_1 by

$$S_1 + T_1 = 1. \quad (4.1.5)$$

Therefore, $|T_1| \approx 1$ in frequency bands where $|S_1| \ll 1$, and $|T_1| \ll 1$ in frequency bands where $|S_1| \approx 1$. Typically, the feedback controller C_1 is designed such that $|S_1| \ll 1$ over a small bandwidth where the disturbance has significant energy, in exchange for small enhancements ($|S_1| > 1$) over a large range of frequencies where the disturbance has little energy (Elliott 2001). In this particular example, C_1 is designed for an output disturbance with significant energy in the frequency range from 150–250 Hz (ie around the dominant peaks of G_{11}). Therefore, T_1 and thus Δ_{M1} are both relatively large in the 150–250 Hz bandwidth.

Another factor that contributes to the modeling error in this frequency range is the magnitude of the diagonal terms of the plant model. Since multiplicative uncertainty is inversely proportional to the product of the diagonal terms, uncertainty tends to be large at the zeros of G_{11} and G_{22} . In this example, G_{11} and G_{22} have zeros at 180 and 190 Hz respectively.

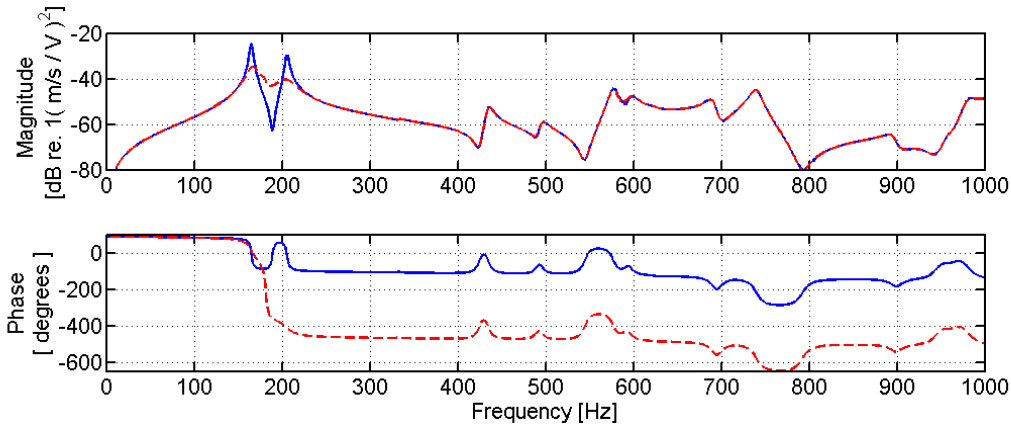


Figure 4.4: The figure shows the Bode diagram of the open-loop response from u_2 to y_2 (solid blue line), along with the new response generated by including the neighboring control loop (dashed red line).

Now consider Figure 4.5, which shows the power spectra of y_2 simulated with and without the controllers C_1 and C_2 . The nominal closed-loop response simulated using only C_2 is shown to effectively suppress the dominant low-frequency peaks with little spillover. However, when C_1 is included, the closed-loop system generates excessive spillover at 180 and 190 Hz. Excessive spillover indicates that the coupled system is not robust to the large multiplicative uncertainty associated with the zeros of G_{11} and G_{22} .

This example demonstrates that decentralized structural controllers can be susceptible to spillover. In particular, the induced modeling error is the product of the complementary sensitivity function and a second term, which quantifies the diagonal dominance of the plant. To ensure the coupled system is stable, the local controllers must be robust in the frequency bands where the modeling error is large. However, since robustness is typically achieved at the expense of performance, the coupling between bays can limit achievable performance.

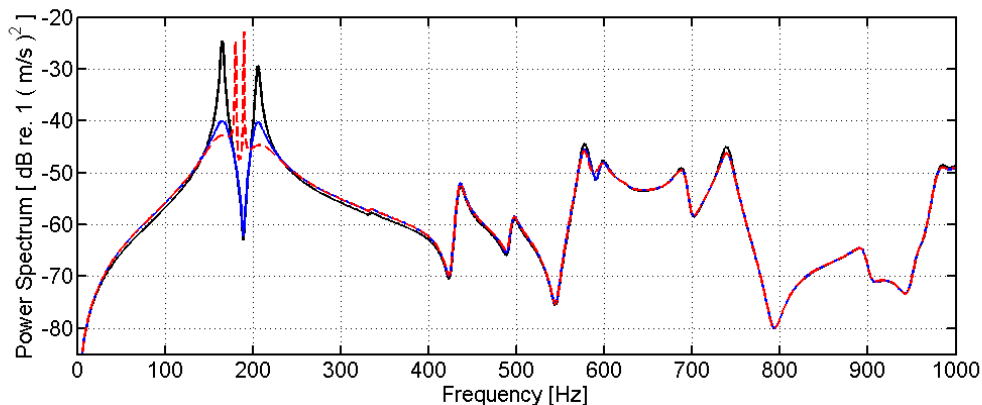


Figure 4.5: The power spectra of the open-loop response (solid black line), nominal closed-loop response (solid blue line), and combined closed-loop response (dashed red line).

4.1.2 Experimental example

Next consider experimental results, which validate these conclusions. Note that all of the experimental data discussed in this paper is acquired on the stiffened aluminum test structure described in Chapter 2. Unlike the numerical model, the test structure includes additional complexities associated with a built-up aluminum structure. For the experiments presented in this chapter, the baseline transducer layout is used, which consists of center mounted piezoelectric actuators along with "sensors" that measure the summed response from accelerometers positioned in a diamond pattern around each actuator. All of the data is collected at 3 kHz using 8th order anti-aliasing filters and 4th order reconstruction filters. All filters have a corner frequency of 1 kHz.

The magnitudes of the open-loop frequency response functions from each input to output are shown in Figure 4.6. The solid lines indicate that the response is acquired using transducers on the same bay, while the dashed lines indicate that the actuator is on one bay while the sensor is on the other bay. Notice that a rough estimate of the diagonal dominance of the plant can be obtained by simply comparing the magnitude of the curves shown in Figure 4.6. For instance, notice that the plant is diagonally dominant at 800 Hz, since the magnitude of the diagonal terms is much larger than the magnitude of the cross terms. On the other hand, the plant is not diagonally dominant around 640 Hz.

Another way to estimate the diagonal dominance is to use an interaction metric, which provides a quantitative measure of the coupling between subsystems. For this discussion, the interaction metric is $|G_{12}G_{21}/G_{11}G_{22}|$, which is simply the ratio of the magnitude of the cross terms over the diagonal terms. Notice that this metric is also the first term in parenthesis in Equation 4.1.4. Therefore the metric is proportional to the multiplicative modeling error generated by neighboring control loops. Figure 4.7 shows that the interaction metric for this system is relatively small at all frequencies other than 300 and 640 Hz. These frequencies correspond to the zeros of the diagonal terms (ie zeros of either G_{11} or G_{22}). Since the multiplicative uncertainty is proportional to the interaction metric, the local controllers should be designed such that each control system is robust at these frequencies.

To evaluate closed-loop performance, independent LQG controllers are designed and implemented on each

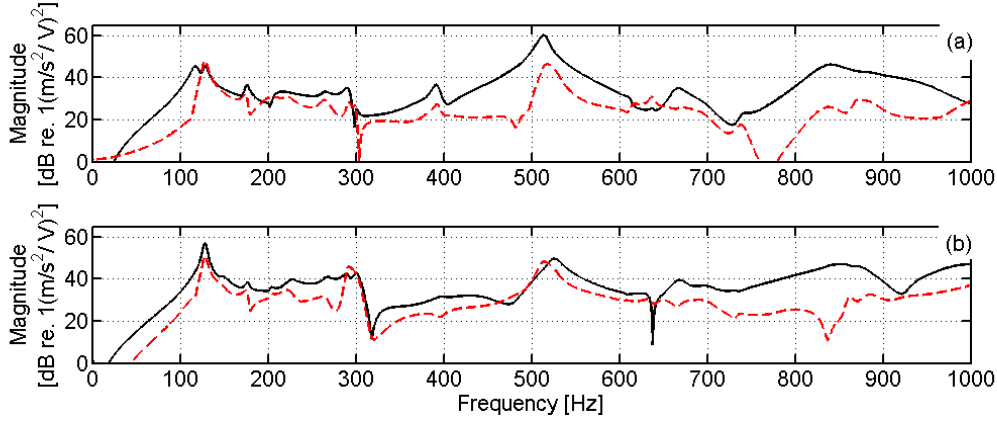


Figure 4.6: Magnitude of the open-loop frequency response for (a) G_{11} (solid black line) and G_{12} (dashed red line); (b) G_{22} (solid black line) and G_{21} (dashed red line).

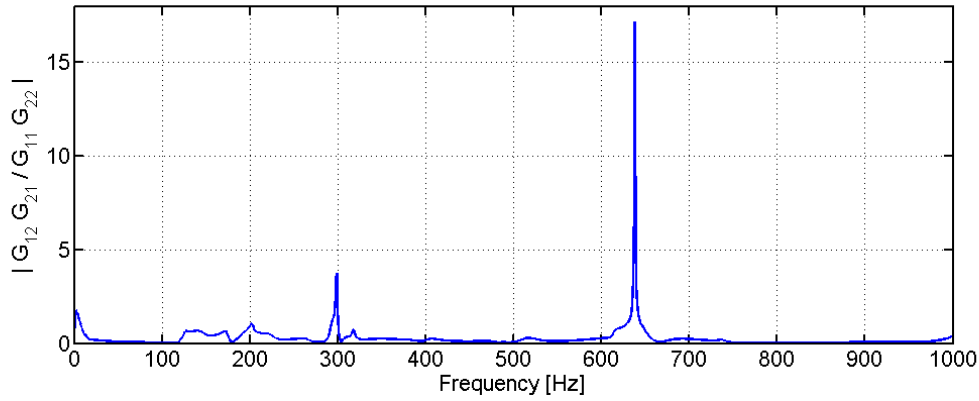


Figure 4.7: Interaction metric for the two-bay laboratory system.

bay. However, before designing each controller, state-space models of the diagonal plant terms must first be identified. This is accomplished using the observer/Kalman filter identification (OKID) algorithm described by Juang (1994). For this work, 75th order plant models are found to accurately represent the dynamics of each SISO system over the bandwidth of interest. Again we assume that random Gaussian noise enters the system through the control inputs, and so explicit disturbance modeling is unnecessary. Therefore the controllers are designed using the standard LQG design techniques discussed in Chapter 3. Both controllers use output weighting $\tilde{Q} = 1$, effort weighting $\tilde{R} = 10^4$, disturbance covariance $Q_n = 1$, and measurement noise covariance $R_n = 10$.

Figure 4.8 compares the open- and closed-loop power spectra measured on the upper bay. The nominal closed-loop response generated using only C_2 suppresses the dominant peaks with very little spillover. However the coupled system, which includes both C_1 and C_2 , generates excessive spillover at 640 Hz. While the interaction metric can be used to identify the frequency bands where spillover may occur, a simpler approach is to use the zeros of the control models (ie G_{11} and G_{22}) to estimate the regions where

spillover may occur. This could simplify the design process by eliminating the need to obtain a frequency response description of the entire coupled plant. Instead, C_2 could be designed such that the system is robust at the zeros of G_{22} , while C_1 could be used to address potential stability problems associated with the zeros of G_{11} . This concept is discussed in more detail in the following section.

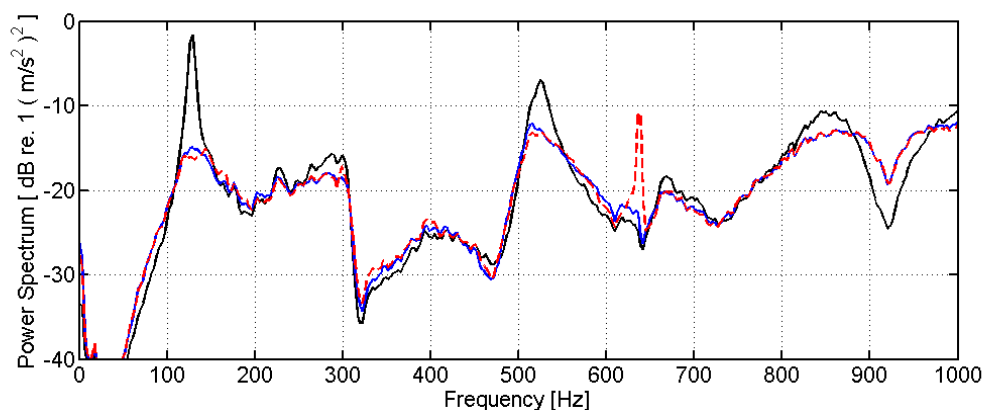


Figure 4.8: The figure shows the measured power spectra of the open-loop response on the upper bay (solid black line), the nominal closed-loop response (solid blue line), and the actual closed-loop response (dashed red line).

4.2 Frequency-shaped LQG

While it is difficult to predict exactly where spillover will occur *a priori*, we have shown that interaction is likely at the zeros of the control models (ie the diagonal terms in the plant model). Therefore, an obvious and often effective solution is to simply limit the control authority in the neighborhood of these zeros. This can be accomplished by modifying the state feedback design as described in Chapter 3. In particular, the effort weighting term can be shaped to penalize control and subsequently reduce performance in specific frequency bands.

For example, Figure 4.9 shows the amplitude of the frequency response function in the background, along with two different effort weighting terms. The first term, shown with the dashed red line, is the standard frequency independent effort weighting penalty, while the second term is shaped to reduce the control authority at the zeros of G_{22} . The shaping is implemented by augmenting the plant model with two Butterworth band-pass filters. The first is a 5th order filter with corner frequencies of 310 and 330 Hz, and the second is a 6th order filter with corner frequencies of 635 and 645 Hz. Recall that once the plant model is augmented with shaping filters, the design can be solved using the standard design procedures described in Chapter 3.

Figures 4.10 (a) and (b) compare the simulated and measured closed-loop responses generated using both the standard, and frequency-shaped effort-weighting terms. Since only the controller on the upper bay is changed, the power spectra are only shown for the sensor on the upper bay. Notice that the simulated and measured power spectra are very similar. Next, observe that while the standard design generates spillover at 640 Hz, frequency shaping the controller on the upper bay effectively reduces the spillover without sacrificing performance in neighboring frequency bands.

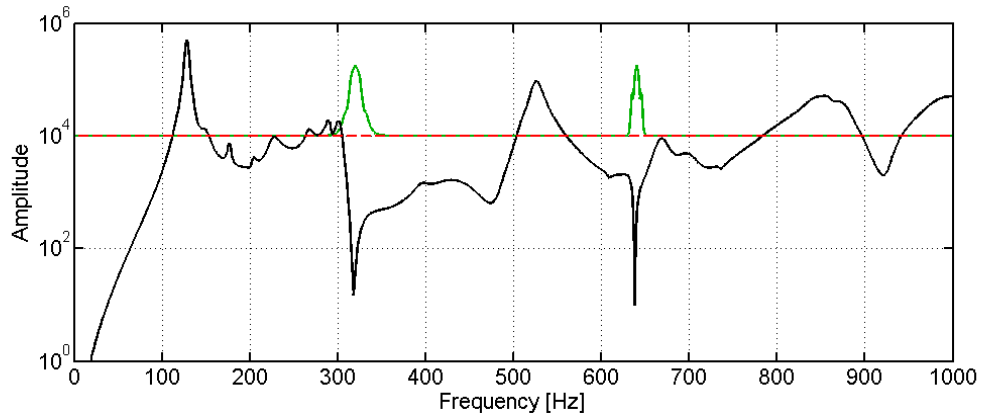


Figure 4.9: The figure shows the amplitude of the nominal plant model on the upper bay (solid black line), the standard frequency independent effort-weighting term (dashed red line), and the shaped effort-weighting term (solid green line).

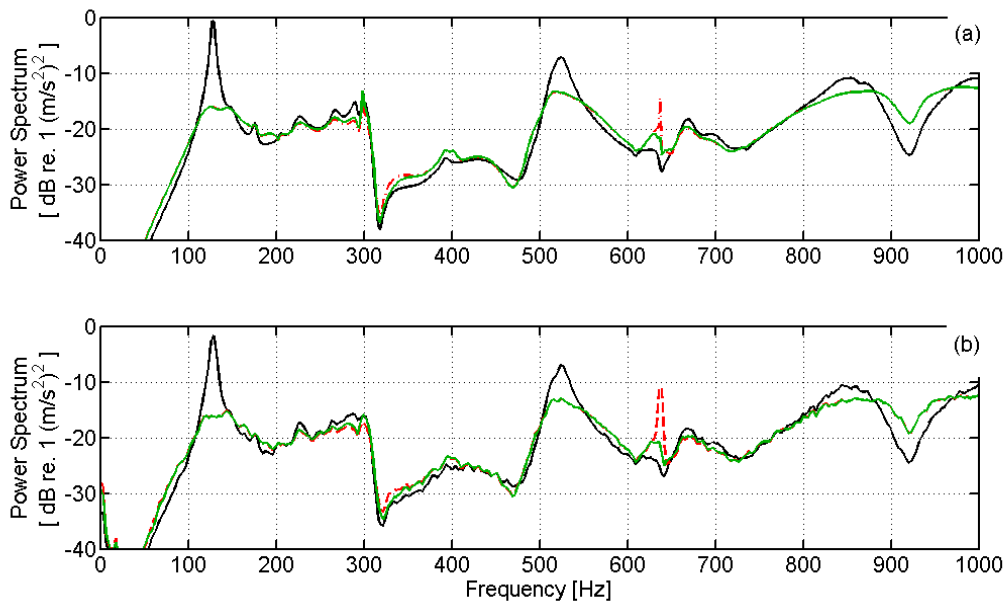


Figure 4.10: The open-loop response (solid black lines), standard LQG response (dashed red lines), and frequency-shaped LQG response (solid green lines). The figures show: (a) the simulated power spectra; and (b) the measured power spectra.

In addition to improving performance on the upper bay, limiting the control authority of C_2 also reduces the magnitude of the induced modeling error on the lower bay. Therefore, this approach is not only effective for the local subsystem, but also improves performance on neighboring subsystems. For instance, Figure 4.11 compares the power spectra measured on lower bay using the standard and frequency-shaped designs on the upper bay. Notice that the spillover at 640 Hz is significantly reduced.

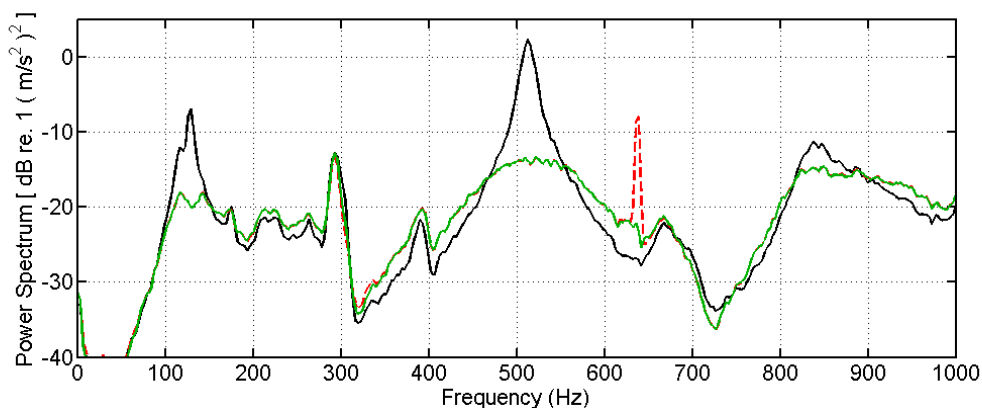


Figure 4.11: The figure shows the measured power spectra of the open-loop response (solid black line), the closed-loop response with the standard LQG controller on the lower bay (dashed red line), and the closed-loop response with the frequency-shaped LQG controller on the lower bay (solid green line).

While shaping the effort-weighting term is effective at the zeros of the open-loop control model, spillover may occur in other frequency bands as well. For instance, consider a more realistic example where the disturbance does not enter through the control path. Although the plant is identical to the last example, a shaped acoustic excitation is now used, as described in Chapter 3. In this case, the LQG controllers are designed using plant models augmented with 60th order disturbance models, which are estimated from open-loop measurements of y_1 and y_2 . Independent LQG controllers are then designed using the augmented plant models. The designs use output weighting $\tilde{Q} = 1$, effort weighting $\tilde{R} = 10^2$, disturbance covariance $Q_n = 1$, and measurement noise covariance $R_n = 10^{-2}$. As the previous example demonstrates, our simulations predict experimental performance reasonably well, and therefore this example is presented using numerical simulations.

Figure 4.12 shows the simulated power spectra on the lower bay with and without control. The solid blue curve shows the nominal performance simulated using only C_1 , while the dashed red curve shows the performance of the coupled system with controllers on both bays. From the figure, we can see that the interaction between the two controllers degrades performance in the 125 to 145 Hz frequency range. This low-frequency degradation is particularly troublesome in structural acoustic control applications since the low-frequency modes radiate sound efficiently. Therefore, excessive performance limitations at low frequencies are unacceptable. Unlike the spillover problem previously discussed, we can not simply penalize the control effort from 125 to 145 Hz and hope to improve closed-loop performance. Limiting control authority in this frequency range would severely limit achievable performance. Therefore the next section presents an alternate approach based on frequency-shaped loop recovery.

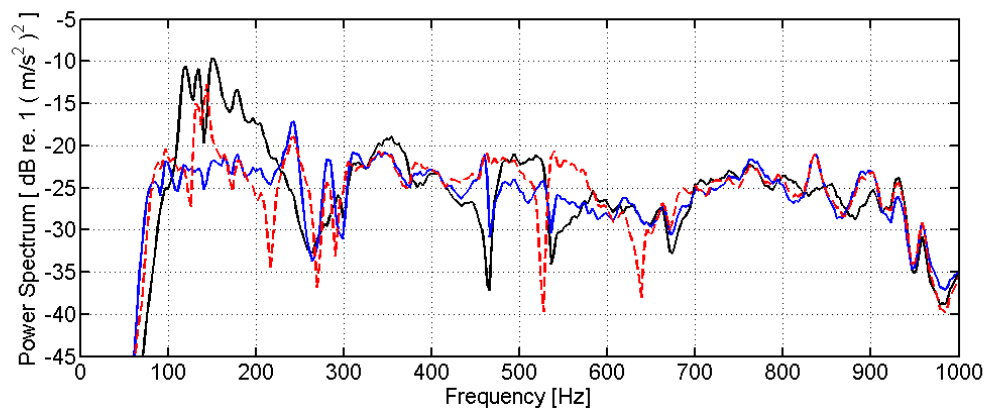


Figure 4.12: The figure shows the simulated power spectra of the open-loop response on the lower bay (solid black line), the nominal closed-loop response simulated using only the controller on the lower bay (solid blue line), and the actual closed-loop response simulated with both controllers (dashed red line).

4.3 Frequency-shaped loop recovery

As discussed in Chapter 3, loop recovery can often be used to improve robustness and subsequently performance. However, complete loop recovery is only possible if the plant is minimum phase, and even partial recovery is achieved at the expense of measurement noise sensitivity. Since real systems are rarely minimum phase, it is advantageous to exploit loop recovery only in frequency bands where the plant variations are known to limit achievable performance. This also allows the designer to avoid increasing measurement noise sensitivity unnecessarily in frequency bands where loop recovery is not required. Therefore, the following example focuses on frequency-shaped loop recovery and demonstrates that this technique can be used to improve low frequency robustness with very little impact on performance in neighboring frequency bands.

Again, consider the system discussed in the previous section, however, in this example the disturbance model is shaped to exploit loop recovery. In particular, the magnitude of the disturbance model is increased primarily in the 125 to 145 Hz range to address the interaction problem. The magnitude of the standard and frequency-shaped disturbance models are compared in Figure 4.13. In this example, the shaped model is generated by modifying the magnitude of the standard disturbance model by hand, and then fitting the response with a stable state-space model.

The simulated power spectra of the open- and closed-loop response on the lower bay are shown in Figure 4.14. The closed-loop spectra are simulated using controllers on both bays, which explains the poor low-frequency performance of the nominal design. However the 2nd design, which exploits loop transfer recovery, performs noticeably better from 125 to 145 Hz. In particular, the response is decreased by an average of 9 dB in this frequency range, with a relatively small 1 dB increase at neighboring frequencies.

Although frequency-shaped loop recovery can be effective, it is limited to recovering the characteristics of the LQR design. Therefore, the approach is only suitable if the underlying LQR design is robust. As a result, a two-step approach is advocated. First, the effort penalty is shaped to ensure the LQR design is sufficiently robust. This is accomplished by limiting the control authority at the zeros of the local control model. As

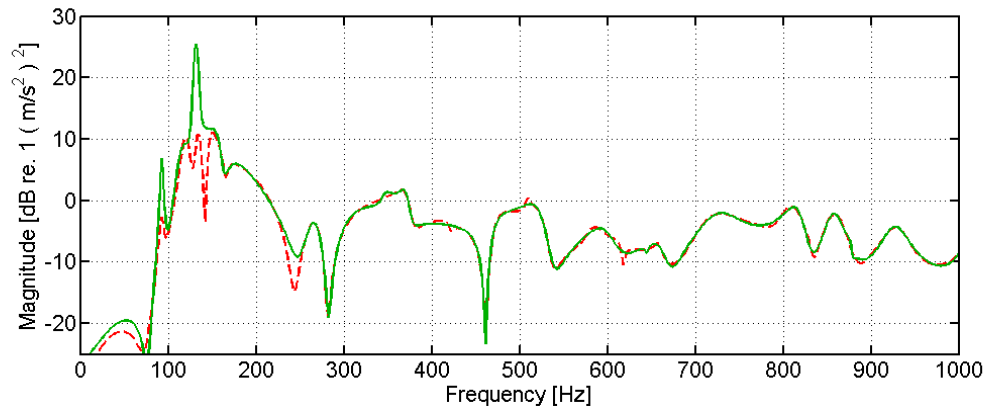


Figure 4.13: The figure shows the magnitude of the nominal disturbance model (dashed red line) and the modified disturbance model used to exploit loop recovery (solid green line).

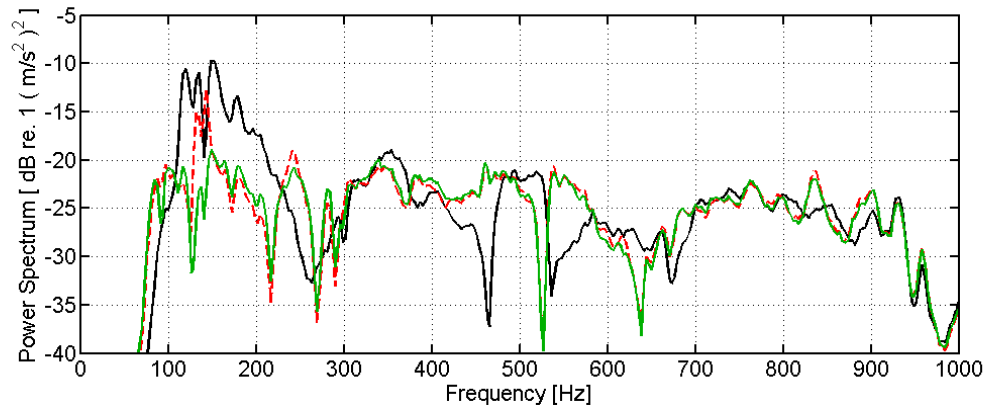


Figure 4.14: The figure shows the simulated power spectra of the open-loop response on the lower bay (solid black line), the closed-loop LQG response using the nominal disturbance model (dashed red line), and the closed-loop LQG response exploiting loop recovery (solid green line).

discussed earlier, this typically improves the robustness of the design without significantly reducing achievable performance. Next, frequency-shaped loop recovery is used in frequency bands where the interaction between controllers limits achievable performance. Unfortunately, as we have previously discussed, it is often difficult to accurately predict the frequency bands where loop recovery is required *a priori*. Therefore, the next chapter investigates low-authority control strategies, which can be used in combination with the frequency-shaped LQG design presented here. Chapter 6 then presents an adaptive frequency-shaped LQG/LTR strategy, which addresses the lack of *a priori* information.

Chapter 5

Low-authority control

The purpose of this chapter is to investigate low-authority control (LAC) strategies, which could be used to supplement or even replace the high-authority control (HAC) system discussed in the previous chapter. In the context of this work, low-authority control refers to low-order classical-control strategies including direct velocity feedback (DVF) and positive position feedback (PPF). Since LAC is simple and relatively robust to modeling error, the approach is particularly attractive for decentralized control applications. However, as the name implies, nominal performance is often limited due to the conservative nature of the approach.

Negative rate feedback using matched transducer pairs is a particularly simple and robust low-authority control strategy. This approach is also referred to as active damping since it augments the inherent damping in the structure. As a result, it is well suited for lightly damped metallic structures such as the aluminum sidewall of an aircraft (Clark et al. 1998; Preumont 2002). The popularity of this strategy is attributed to Balas (1979), who showed that if the transducer pairs are matched, then any passive control law, such as negative rate feedback, will guarantee the unconditional stability of the closed-loop system. The stability guarantee makes this approach particularly appealing for decentralized control applications, as discussed by Elliott et al. (2002). However, practical limitations inevitably limit the performance of the control system. For instance, real transducer pairs are never perfectly matched, which eliminates the passive property of the system at high frequencies. Therefore, the control gain must be limited to avoid spillover and stability problems. As a result, a considerable amount of research has focused on the development of "substantially collocated" actuator-sensor pairs.

One strategy suggested by Anderson et al. (1992) and Dosch et al. (1992) is to simultaneously use the same piezoelectric transducer as a sensor and actuator. When used in this way, the transducer is referred to as a sensor-actuator, or a self-sensing actuator. If the capacitance of the piezoelectric device is known, then the mechanical response of the structure can be found by subtracting the electrical response from the input signal to the sensor-actuator (Clark et al. 1998). However, as Anderson et al. (1992) noted, small changes in the capacitance can degrade control performance. Therefore Cole and Clark (1994) introduced an adaptive strategy to account for drift in the capacitance of the piezoelectric structure. Viperman and Clark (1996) proposed a practical way to implement the adaptive approach, which was later used for active structural acoustic control by Cox et al. (1999). However, since a small charge output must be extracted from a large input signal, signal-to-noise problems can limit achievable performance.

Another seemingly obvious way to generate a matched actuator-sensor pair is to mount strain based transducers on opposite sides of the structure. For instance, if a volume velocity sensor and uniform force actuator are bonded on opposite sides of a panel, then DVF can be used to target the first radiation mode (Johnson and Elliott 1995; Preumont 2002; Gardonio and Elliott 2004). However, in addition to coupling to the trans-

verse response, strain based transducer pairs also couple to the in-plane response. Unfortunately, when the transducers are mounted on opposite sides of the structure, the in-plane response is out of phase with the transverse response. Therefore, the control system is only conditionally stable, which limits achievable performance. In response to this problem, Yang and Huang (1998) proposed an alternate configuration using two sets of matched piezoelectric actuator-sensor pairs bonded on both sides of the structure. This approach was later investigated experimentally by Lee et al. (2003), who found that performance was limited since the inter-layer coupling between the sensor and actuator bonded on top of one another was much larger than the coupling to the motion of the structure. In addition, it is not always practical to access both sides of the structure. Therefore, another option is to use point sensors (accelerometers) along with inertial actuators mounted on one side of the structure. While this type of transducer pair can be effective at low frequencies, the transducer dynamics tend to erode achievable performance (Diaz et al. 2006; Baumann and Elliott 2007). In addition, the inertial actuators are not as light and compact as piezoelectric patch actuators.

Another way to generate substantially collocated transducer pairs is to use small strain based actuators along with point sensors. This combination of transducers is attractive because it only couples to the transverse modes. In addition, both types of transducers are typically compact and lightweight. Due to these advantages, the transducer pair has been used in numerous numerical (Bingham et al. 2001; Elliott et al. 2002; Gardonio et al. 2004a,b) and experimental (Petitjean and Legrain 1996; Petitjean et al. 2002; Bianchi et al. 2004) investigations. However, since the sensor-actuator response is only positive real at low frequencies where the bending wavelength is larger than the dimensions of the actuator, negative rate feedback is only conditionally stable (Gardonio et al. 2004a). Note that if the patch is small, then the frequency response function for the point sensor and strain based actuator can be positive real through relatively high-frequencies. Unfortunately, small patches do not couple efficiently to the low frequency modes. Therefore, a distributed array of relatively small transducer pairs is often used, as described by Elliott et al. (2002). For instance, Bianchi et al. (2004) showed that sixteen independent control units, each consisting of a single square piezoelectric patch actuator along with an accelerometer at its center, could be used to reduce the amplitude of the first five resonances of a panel by 12-18 dB. Recently, Gardonio and Elliott (2005) suggested that the performance of the control system could be improved using triangular actuators distributed around the perimeter of a simply supported panel. The triangular shape improves the stability bounds of the system, allowing higher feedback gains and therefore better performance.

One disadvantage of using small strain based actuators and point sensors is the need for a relatively large number of actuator-sensor pairs. Although the actuators and sensors are typically light and compact, the control electronics are not. Since a power amplifier is required for each independent control unit, the weight of the entire control system could make this type of approach impractical. Therefore, another alternative is to use a small number of relatively large strain based actuators in combination with a grid of accelerometers. For instance, Maillard and Fuller (1998) showed that the volume velocity of a panel can be estimated by summing (and integrating) the response from an array of accelerometers distributed over the structure. Lee et al. (2002) later implemented DVF using a uniform force actuator made from a quadratically shaped PVDF film in combination with a discrete volume velocity sensor consisting of an array of accelerometers. However, the frequency response function for this actuator-sensor pair was only positive real through 800 Hz due to shaping errors and aliasing effects caused by the discrete array of sensors.

Another LAC strategy, commonly used on large flexible space structures, is called positive position feedback

(PPF). This approach was first introduced by Goh and Caughey (1985) as an alternative to collocated direct velocity feedback. Essentially, structural displacement is fed back through a damped, resonant, low-pass filter tuned for a particular structural resonance. If the transducer pair is matched and the structure is lightly damped, then the phase of the actuator-sensor transfer function will be approximately -90° at the resonance frequencies. Since the 2nd order filter adds an additional -90° of phase, the output is fed back 180° out of phase with the input at the desired frequency. If the modes are also well separated, then several filters can be combined to simultaneously suppress multiple modes. For instance, Fanson and Caughey (1990) used PPF to simultaneously suppress the first six structural modes of a cantilevered beam. While effective, the modal density limits the achievable performance of the control system (Fanson and Caughey 1990). In particular, McEver (1999) showed that the amount of closed-loop damping a PPF filter can add is a function of the spacing between the poles and zeros.

Combined high-authority/low-authority control (HAC/LAC) strategies can also be effective. In particular, this type of two-level control architecture combines the robustness benefits of low-authority control with the performance benefits of modern control strategies (Aubrun 1980; Aubrun and Ratner 1984; Williams 1994; Hyland et al. 1993). The high-authority portion of the controller is typically designed to meet the performance objective, while the low-authority loops add damping and reduce the spillover problems associated with high-authority control of lightly damped systems. In addition to stabilizing high-frequency dynamics, LAC can also reduce the interaction between neighboring control loops by augmenting the in-bandwidth damping. Another purpose of LAC is to supplement performance by targeting resonances not suppressed by the HAC system.

The goal of this chapter is to identify a transducer pair that can be effective alone or in combination with the HAC strategy presented previously. In particular, DVF is investigated initially using point sensors and triangular actuators mounted along the perimeter of the structure. Simulations show that by augmenting the structural damping, this LAC system supplements the performance of the HAC system and reduces the interaction between neighboring HAC units. We also show that using triangularly shaped Macro-Fiber Composite (MFC) actuators can improve the stability bounds of the LAC system. Unfortunately, triangular actuators and point sensors are not effective if the boundaries of the structure are flexible. Therefore a second transducer configuration consisting of a large rectangular actuator with an array of point sensors is also investigated. These transducers are mounted along the stiffener in an effort to couple to the dominant low-frequency mode without interfering with the HAC transducers. While numerical simulations suggest that both DVF and PPF can be effective using a large rectangular MFC actuator, performance is limited in the laboratory. In particular, the experimental frequency response function is only passive through approximately 300 Hz and lacks sufficient pole-zero spacing for PPF control. As a result, DVF is only able to achieve a 1 dB integrated reduction in radiated sound power, while PPF reduces the response by only 1.5 dB. Therefore, this chapter demonstrates that while LAC and HAC/LAC strategies can be used for decentralized control, performance is ultimately dependent on the dynamics of the test structure.

5.1 Triangularly shaped strain actuators

Initially, negative rate feedback is investigated using point sensors and triangular actuators mounted along the clamped vertical edges of the structure, as shown in Figure 5.1. Note that this actuator-sensor pair is positioned along the flexible, horizontal boundary later in this chapter. The transducer configuration shown

in Figure 5.1 is investigated for a number of reasons. First, Gardonio and Elliott (2005) showed that the triangular shape improves the stability bounds of the system, which enables higher feedback gains and therefore better performance. In addition, by placing the transducers around the perimeter of the panel, the center of each bay is unobstructed. Therefore the control system can be used in combination with the HAC strategy without interfering with the center mounted transducers.

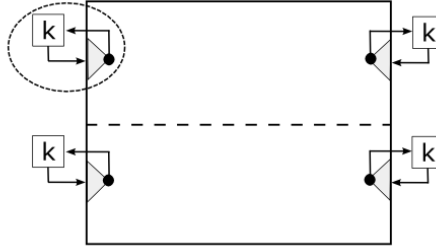


Figure 5.1: The figure shows closely located point velocity sensors positioned at the tip of triangular piezoelectric patch actuators.

Before continuing, it is beneficial to briefly consider the implications of using a shaped, distributed actuator. In particular, note that triangular actuators can be modeled using a point force at each vertex and a bending moment along each edge (Sullivan et al. 1996), as depicted in Figure 5.2. The moment excitation along the base edge is defined as (Gardonio and Elliott 2005)

$$m_b(t) = \frac{h_s}{2} e_{31} v_c(t) \quad (5.1.1)$$

where h_s is the combined thickness of the panel and the piezoelectric patch, e_{31} is a piezoelectric material constant relating the electric field applied in the 3-direction to stress in the 1-direction, and $v_c(t)$ is the applied voltage. Similarly, the moment excitation along the lateral edges is defined as

$$m_l(t) = \frac{h_s}{2} (m^2 e_{31} + e_{32}) v_c(t) \quad (5.1.2)$$

where $m = b/(2a)$ is the slope of the lateral edge, b is the base of the triangle and a gives its height. The point forces generated at the base vertices are

$$f_b(t) = 2m \frac{h_s}{2} e_{31} v_c(t) \quad (5.1.3)$$

while the point force at the tip of the triangular patch is defined as

$$f_t(t) = -4m \frac{h_s}{2} e_{31} v_c(t) \quad (5.1.4)$$

Note that the bending moments along the base and lateral edges produce flexural deformation opposite to the deformation produced by the point force at the tip of the actuator.

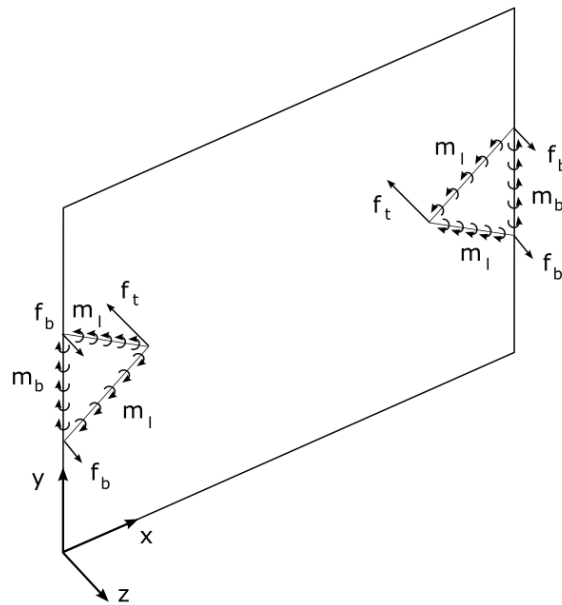


Figure 5.2: Triangular strain actuators represented in terms of point forces and line moments [adapted from Gardonio and Elliott (2005)].

Since the boundaries of the structure are assumed to be clamped, the point forces and moments along the base of the actuator do not couple to the structural response. Therefore, a single point sensor placed at the vertex opposite of the base edge can yield a substantially collocated frequency response. In fact, if the frequency response function for the transducer pair is simulated using the standard 60 mode numerical model described in Chapter 2, the phase response is bounded between $\pm 90^\circ$. This implies that direct velocity feedback is unconditionally stable and therefore the feedback gain could be made arbitrarily large. However, higher-frequency dynamics often limit achievable performance. Therefore, a higher-order model is necessary to provide a more accurate evaluation of the LAC system. Specifically, 250 modes are used to model the structural response through 5 kHz. Note that a continuous-time model is used for this analysis since a discrete implementation would necessarily add phase and degrade performance. While the analysis includes the additional mass and stiffness introduced by the piezoelectric patches, the dynamics of the accelerometers are neglected since they are expected to have little impact below 5 kHz. Note that if a more accurate model was required, the dynamics of the accelerometers could be approximated using a lumped parameter model as described by Gardonio et al. (2004b).

The solid black line in Figure 5.3 shows the frequency response function for the transducer pair circled in Figure 5.1. Note that for this investigation, the base and height dimensions of the triangular actuators are 0.07 m and 0.035 m, respectively. The figure shows that the amplitude is modulated and the phase is bounded between $\pm 90^\circ$ through 1.8 kHz. In general, as the frequency increases and the bending wavelength approaches the dimensions of the actuator, the moments along the lateral edges couple more efficiently to the structural response than the point force at the tip of the actuator. Therefore, the amplitude modulation

is attributed to the cancelation between the point force and line moments. The phase response rolls off when the moment excitation begins to dominate the forcing term. For comparison, the dashed red line in Figure 5.3 shows that decreasing the size of the actuator extends the minimum phase properties of the frequency response function. However, this is achieved at the expense of low-frequency control authority.

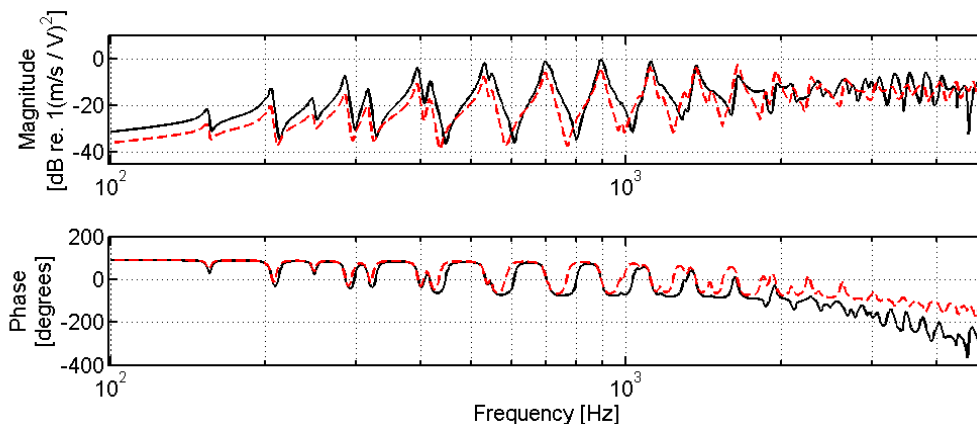


Figure 5.3: The frequency response function for the circled transducer pair shown in Figure 5.1 (solid black line), and the frequency response function using a 50% smaller actuator (dashed red line).

Figure 5.4 (a) shows the Nyquist diagram for the frequency response function between the large triangular actuator and point sensor using a gain of 1.1. Notice that the relatively large loops on the left-hand side of the plot limit the control gain and ultimately the performance of the control system. To improve performance, a first-order compensator can be used to roll-off high-frequency gain. This enables the use of higher feedback gains, which generate additional low-frequency damping (Preumont 2002). In this example, a first-order low-pass filter with a corner frequency at 2000 Hz is used to roll-off control effort. For comparison, Figure 5.4 (b) shows the Nyquist diagram for the compensated system. Including the low-pass filter allows us to increase the feedback gain from 1.1 to 2.4 while maintaining a 6 dB gain margin.

Figure 5.5 compares the open-loop and closed-loop response using the control system depicted in Figure 5.1. The figure demonstrates the advantages of incorporating the first-order compensator. In particular, DVF achieves a -0.6 dB reduction of radiated sound power from 50-800 Hz, while the first-order compensator achieves a -1.2 dB reduction over the same bandwidth. Although the integrated reduction is relatively small, the LAC system may be effective as part of a combined HAC/LAC control strategy. For example, this transducer configuration does not interfere with the HAC layout, and targets resonances not suppressed by the HAC system.

5.1.1 HAC/LAC

Before investigating the combined HAC/LAC strategy shown in Figure 5.6, it is beneficial to review the limitations of decentralized LQG control. In this example, each controller is designed independently using the standard design techniques discussed in Chapter 3. In particular, both controllers are designed without explicit disturbance models using output weighting $\tilde{Q} = 1$, effort weighting $\tilde{R} = 10^{-7}$, disturbance covariance $Q_n = 1$, and measurement noise covariance $R_n = 10^{-4.2}$. Figure 5.7 shows the radiated sound power

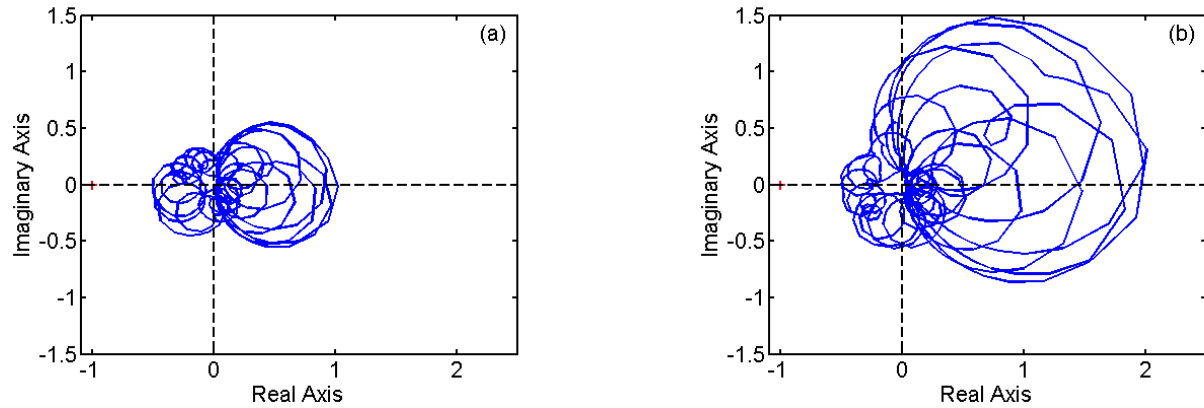


Figure 5.4: The figures show the Nyquist plots of the open-loop frequency response functions for the sensor-controller-actuator transfer functions from 0-5 kHz. A feedback controller with a gain of 1.1 is used in the figure on the left, while a first-order low-pass filter with a corner frequency at 2000 Hz and a gain of 2.4 is used in the figure on the right.

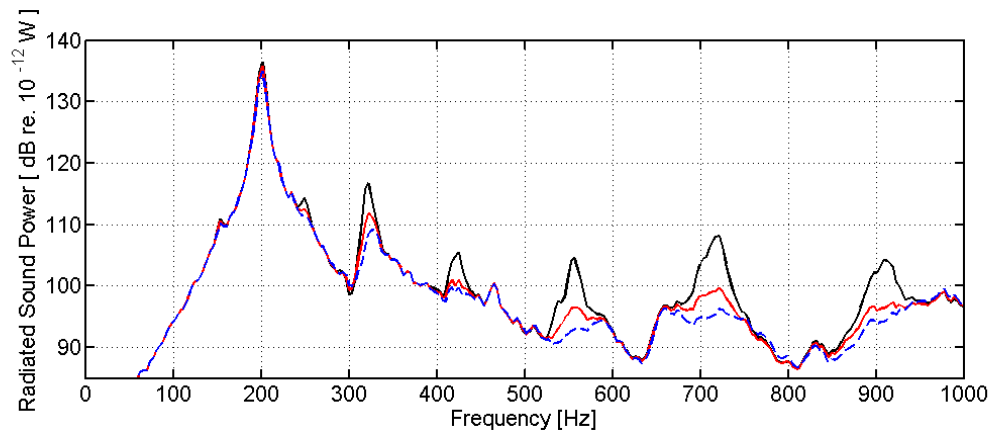


Figure 5.5: Radiated sound power from the structure with no control (solid black line), using DVF with a gain of 1.1 (solid red line), and using a first-order low-pass filter with a corner frequency at 2000 Hz and a gain of 2.4 (dashed blue line).

from the two-bay structure with and without control. Notice that the closed-loop system, which includes independent LQG controllers on each bay, generates excessive spillover at 185 Hz due to the interaction between the controllers. This interaction limits the maximum integrated reduction we can achieve using standard LQG controllers to -6.5 dB.

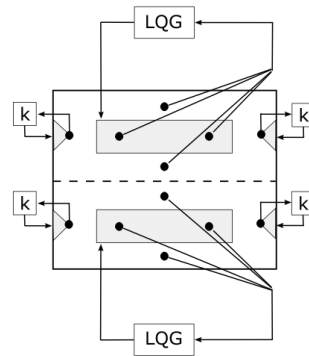


Figure 5.6: The diagram shows a combined HAC/LAC configuration using the triangular actuators along the boundaries.

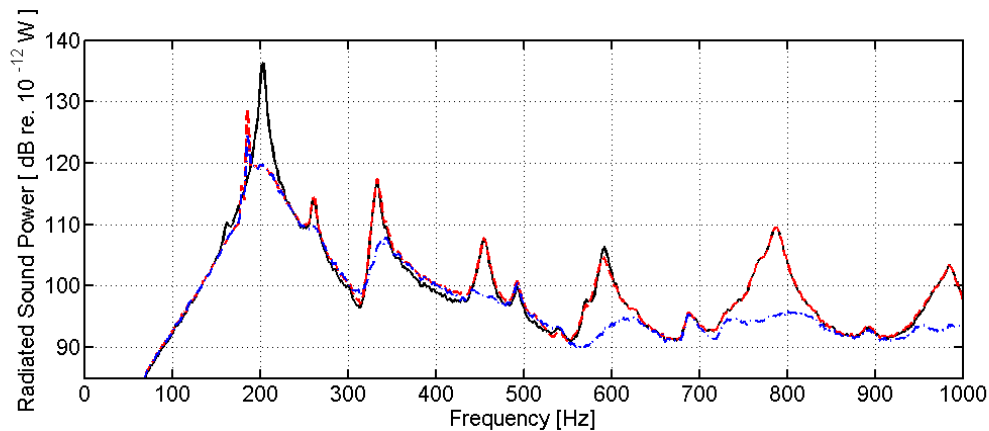


Figure 5.7: The radiated sound power from the structure before control (solid black line), using standard LQG controllers (dashed red line), and using both LQG and DVF (dash-dotted blue line).

Next consider the combined HAC/LAC strategy shown in Figure 5.6. The combined strategy is implemented by first incorporating the LAC system, and then identifying the system model and designing the LQG controllers. In this example, the HAC system is again designed using the same frequency-independent weighting terms presented in the previous paragraph. The only difference is that the system model now includes the dynamics of the LAC system. Note that for this simulation, each low-authority controller is implemented in continuous-time using a first-order low-pass filter with a gain of 2.4. Although the LAC system is continuous, the HAC system is digital with a sample rate of 3 kHz. The simulated performance of the combined control system is shown with the dash-dotted blue line in Figure 5.7. The combined system achieves a 8.1 dB integrated reduction, which is significantly better than either control system achieves on its own. In addition, the combined system is more robust than HAC alone, as demonstrated by the Nyquist plot shown Figure 5.8. In particular, including the LAC system improves the gain margin for the HAC

system from 2.5 dB to 5.6 dB and improves the phase margin from 126° to 134° .

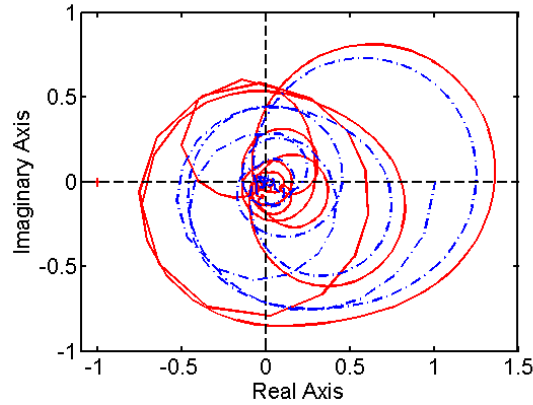


Figure 5.8: Nyquist plot of the sensor-controller-actuator transfer function using LQG control (solid red line), and using DVF and LQG control (dash-dotted blue line).

5.1.2 Macro-Fiber Composite (MFC) actuator

Recall that since the triangular actuator is mounted along a clamped boundary, the point forces and line moment along the base of the actuator do not couple to the structural response. Therefore the distributed actuator can be represented using a point force at the tip of the actuator and line moments along each lateral edge. Notice in Equation 5.1.2 that if we could make $e_{32} = -m^2 e_{31}$, then the line moments along the lateral edges of the triangle would equal zero. In that case, the distributed actuator could be represented by a single point force at the tip of the triangle, and therefore a point sensor located at the same location would be perfectly collocated with the actuator. While $e_{32} = e_{31}$ for traditional isotropic actuators, $e_{12} \neq e_{11}$ for anisotropic actuators such as the Macro-Fiber Composite (MFC) actuator. The MFC actuator has interdigitated electrodes and piezoceramic fibers embedded in an epoxy substrate (Wilkie et al. 2000). The interdigitated electrode pattern enables the application of the electric field in a particular in-plane direction. For instance, a typical MFC actuator from *Smart Material Corp.* generates a tensile stress in the x -direction that is 15 times larger than the compressive stress induced in the y -direction. In particular, $e_{11} = 11.9 \text{ Pa}/(\text{V}/\text{m})$ and $e_{12} = -0.77 \text{ Pa}/(\text{V}/\text{m})$.

One way to eliminate the line moments is to shape the actuator such that the slope of the edges is $m = \sqrt{-e_{12}/e_{11}}$. Recall that $m = b/(2a)$, where b is the base dimension and a is the height of the triangle. Therefore, if the height of the triangularly shaped MFC actuator is twice the length of the base, then $m = 0.25$ and the line moments along the lateral edges could be neglected. Another way to eliminate the line moments is to design the material such that $e_{12} = -m^2 e_{11}$. This might be accomplished by changing the elastic modulus in one direction by modifying the epoxy substrate or the fiber spacing.

To be consistent with previous examples, assume e_{12} is modified without changing the size and shape of the actuator. The solid black line in Figure 5.9 shows the frequency response function between the modified MFC actuator (tuned to cancel the lateral edge moments) and the point sensor. For comparison, the frequency response function for an ideal point force input and point velocity sensor is shown with the

dashed red line. Notice that the two curves lie on top of one another through 3 or 4 kHz. The difference at high frequencies is primarily due to shaping errors caused by the numerical integration routine used to simulate the response of the piezostucture. The additional mass and stiffness introduced by the piezoelectric patch also impacts the high frequency response. Note that while this type of transducer pair is very attractive theoretically, both shaping errors and high frequency transducer dynamics will cause high-frequency phase accumulation in practice. In addition, this transducer pair is only beneficial if the boundaries of the structure are clamped.

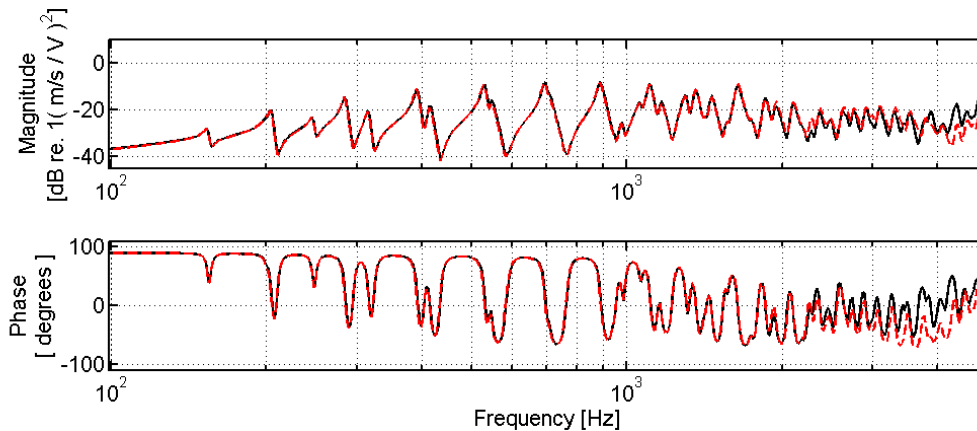


Figure 5.9: Frequency response functions for a modified MFC actuator and point sensor (solid black line), and an ideal point force actuator and velocity sensor located at the vertex of the triangular actuator (dashed red line).

5.1.3 Flexible boundary

The goal of this section is to investigate whether the triangle actuator and point sensor can be used to target the global mode at 200 Hz. Therefore, the transducer pair is mounted along the flexible boundary as shown in Figure 5.10.

The frequency response function for an isotropic piezoelectric actuator and point sensor is shown with the solid black line in Figure 5.11, while the frequency response for the tuned MFC actuator and point sensor is shown with the dashed red line. Notice that while both configurations couple to the low-frequency modes, the phase is not bounded between $\pm 90^\circ$. In fact, the transducer pairs couple to the 155 Hz resonance 180° out-of-phase with the resonance at 200 Hz. Therefore, gains that attenuate the response at 200 Hz generate spillover at 155 Hz. These findings indicate that triangular actuator and point sensor pairs are not suitable along flexible boundaries. This is due to the fact that the bending moment and transverse point loads at the base of the actuator couple to the structural response when the boundary is flexible. Therefore, a single point sensor at the tip is not sufficient to generate a substantially collocated response.

Since the stability bounds for the LAC system are sensitive to the boundary conditions, this type of transducer configuration may not be appropriate for the fuselage of an aircraft. Even though the ring frames are relatively stiff, they are not rigid, especially at low frequencies. Therefore, while triangular actuators and point sensors are attractive for certain applications, they are not investigated further here.

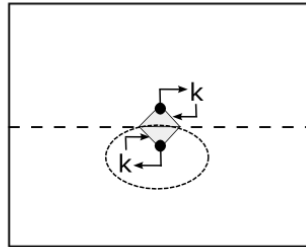


Figure 5.10: The diagram shows closely located point sensors and triangular actuators positioned on either side of the stiffener.

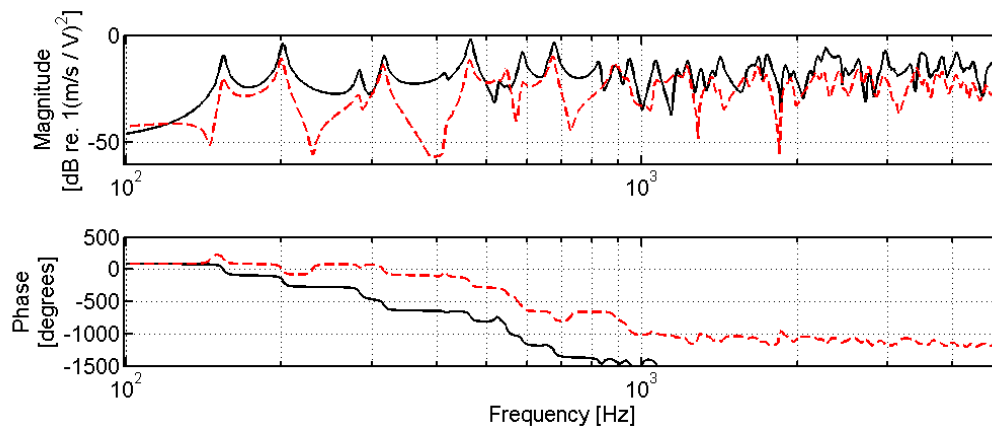


Figure 5.11: The frequency response functions for a standard triangularly shaped piezoelectric actuator and point sensor pair located along the flexible boundary (solid black line), and for the modified MFC actuator and point sensor pair (dashed red line).

5.2 Large rectangular actuator

Since the aircraft fuselage can contain hundreds of bays, it is advantageous to minimize the number of transducers used on each bay. However, it is also desirable to target the low-frequency modes that radiate sound most efficiently. Unfortunately, it is difficult to achieve both objectives using the small strain based actuators and point sensors. For example, individual control units often do not couple efficiently to the low-frequency modes if the spatial aperture of the actuator is much smaller than the structural wavelength. Therefore, arrays of control units are often used to couple to the low-frequency modes (Elliott et al. 2002). The purpose of this section is to investigate alternate transducer configurations designed to target the low-frequency modes without unnecessarily increasing the transducer count. In particular, large rectangular piezoelectric actuators mounted along the stiffener are used in combination with an array of point sensors.

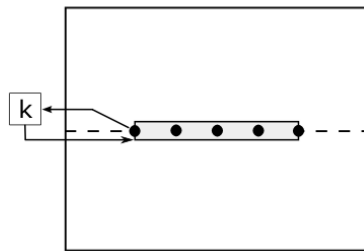


Figure 5.12: The diagram shows a large piezoelectric patch actuator with five point velocity sensors.

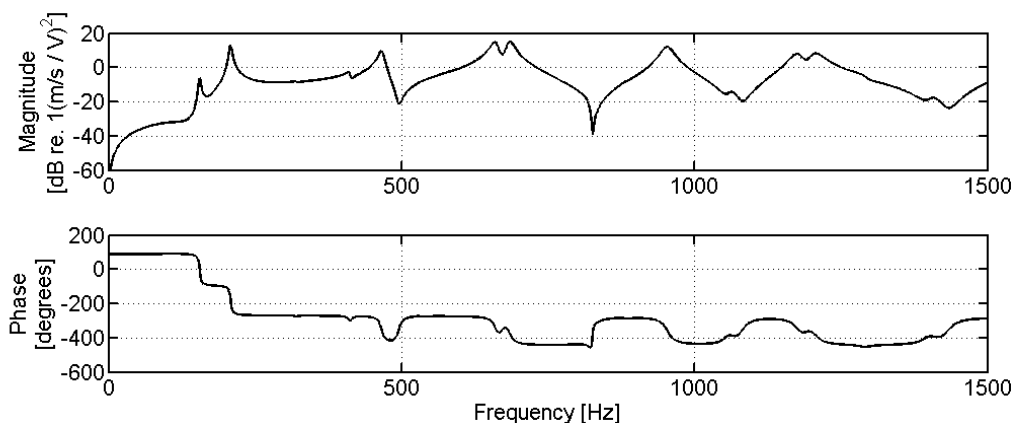


Figure 5.13: The frequency response function between the piezoelectric actuator and the sum of the point sensors shown in Figure 5.12.

The first transducer pair considered in this section is shown in Figure 5.12. Specifically, a 0.028 m by 0.255 m piezoelectric actuator is mounted along the stiffener. Since the actuator has a large spatial aperture, a single point sensor is not sufficient to achieve a substantially collocated response. Therefore, a discrete

1-D array of five accelerometers is investigated. In particular, the integrated and summed response from the five accelerometers is fed back to control the large piezoelectric actuator. The frequency response function between the actuator and sensor is shown in Figure 5.13. Notice that the transducer pair couples to the 200 Hz mode 180° out-of-phase with every other resonance in the bandwidth of interest. To explain the phase inversion at 200 Hz, consider Figure 5.14, which shows the 200 Hz mode shape along with a plot of the transverse displacement of the stiffener in the x- and y-directions. The red dots in Figure 5.14 (b) highlight the location of the actuator. Notice that the actuator is in compression in one direction while it is in tension in the other direction. Although the 1-D array of sensors estimates the response in the x-direction, the isotropic actuator couples to the structure in both directions. At 200 Hz, the curvature in the y-direction integrated over the spatial aperture of the transducer is almost 40 times larger than the integrated curvature in the x-direction. Therefore, the phase inversion is due to the 1-D characteristics of the sensor and the 2-D response of the actuator.

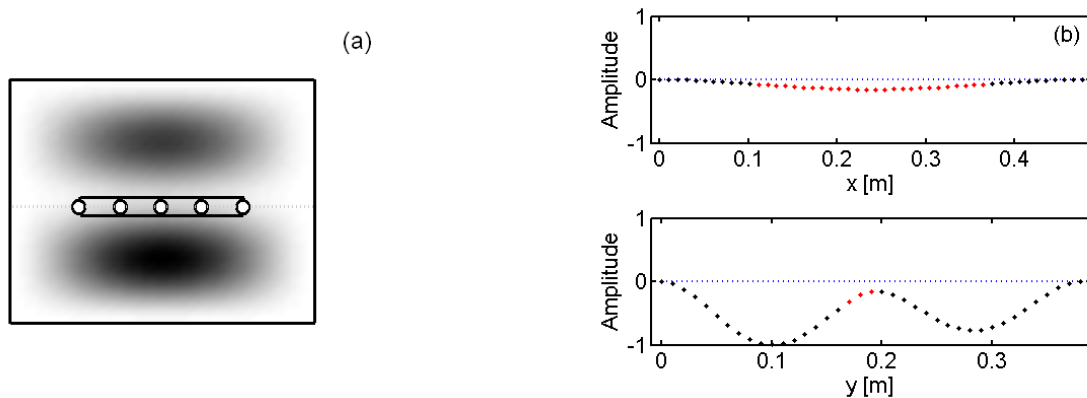


Figure 5.14: The diagrams show: (a) the 200 Hz mode shape and the transducer placement; and (b) the normalized transverse displacement of the stiffener in the top figure, and the normalized transverse displacement along a vertical line, centered on the plate, in the bottom figure.

To support this conclusion, assume a one-dimensional actuator is available such that the applied voltage induces a stress only in the x-direction. The frequency response function for this transducer pair is shown with the solid black line in Figure 5.15. Notice that the response is nearly passive through 1400 Hz. The deterioration in the phase is attributed to aliasing effects associated with the use of a discrete array of point sensors. For instance, if the number of sensors is increased from five to twenty, then the phase response also improves as shown by the dashed red line in Figure 5.15.

MFC

Unfortunately, an ideal 1-D actuator is not available. Therefore, an MFC actuator is considered since it has an interdigitated electrode pattern that enables the application of the electric field in a particular in-plane direction. Using the MFC actuator improves the phase characteristics of the actuator-sensor frequency response function, as shown in Figure 5.17. While the frequency response function for this transducer pair has better phase characteristics than the isotropic actuator-sensor pair, the response is only passive through approximately 500 Hz.

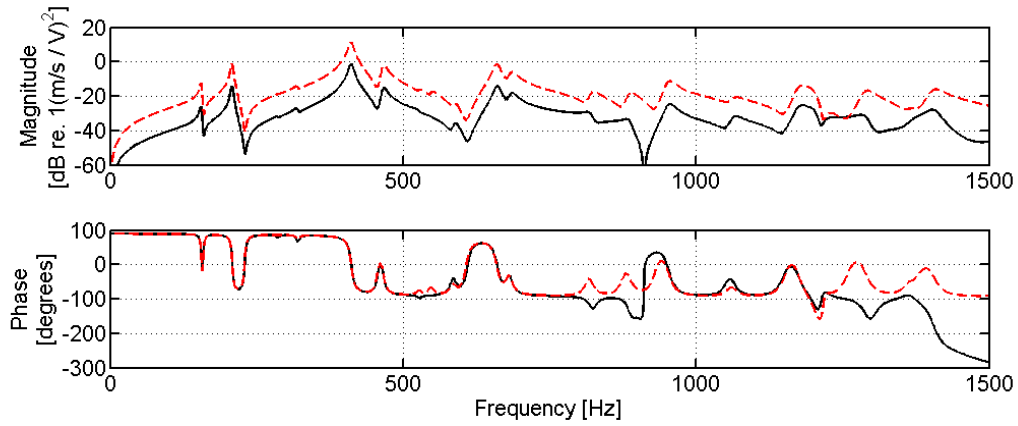


Figure 5.15: The frequency response functions using an ideal 1-D actuator and the sum of: five point sensors (solid black line); and twenty point sensors (dashed red line).

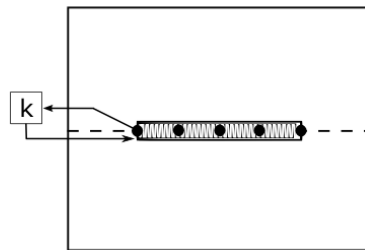


Figure 5.16: The diagram shows a large MFC actuator positioned along the stiffener along with five point velocity sensors.

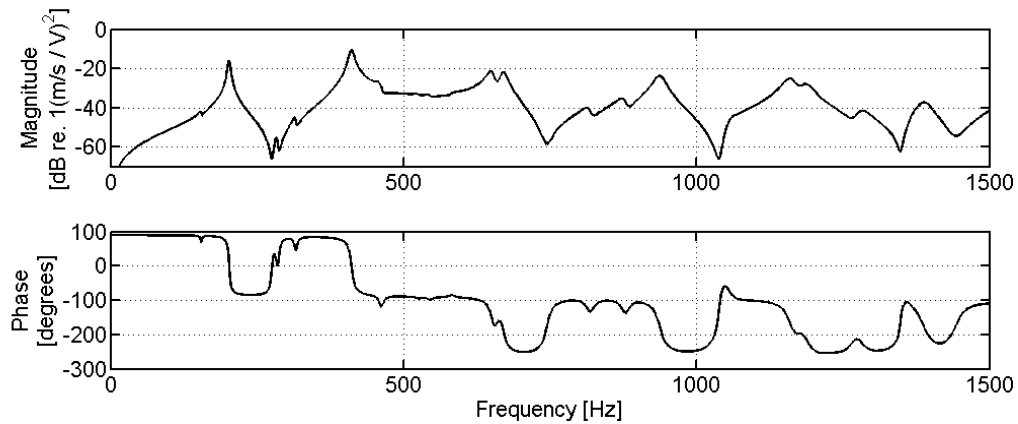


Figure 5.17: The frequency response function between the MFC actuator and the sum of the point sensors shown in Figure 5.16.

Since the response is not minimum phase, the feedback gain is limited. Therefore, it is beneficial to reposition the accelerometers as shown in Figure 5.18, to maximize low-frequency performance. The frequency response function for the new transducer pair is shown in Figure 5.19. Notice that while the response is still passive through approximately 500 Hz, the new sensor couples to the 200 Hz mode better than the previous configuration.

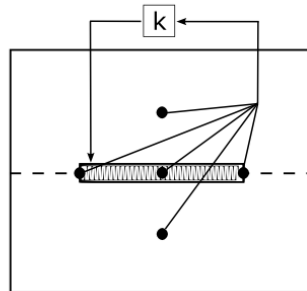


Figure 5.18: The diagram shows a large MFC actuator positioned along the stiffener along with five point sensors distributed over both bays.

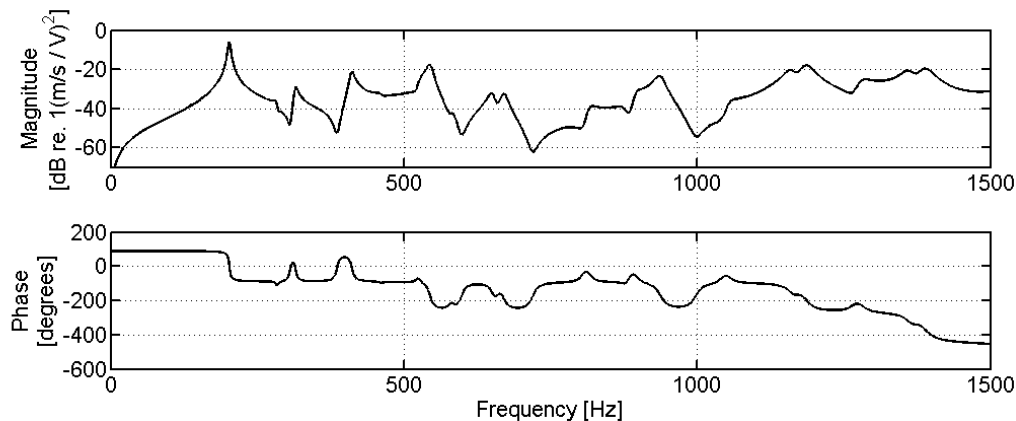


Figure 5.19: The frequency response function for the actuator-sensor pair shown in Figure 5.18.

Figure 5.20 shows the radiated sound power from the two-bay structure with and without the low-authority control system depicted in Figure 5.18. In this example, direct output feedback is considered using a gain of 5.3. Despite the spillover at 545 Hz, the system still achieves an integrated reduction of 5.1 dB over the frequency range from 50 to 800 Hz.

HAC/LAC

Next, consider the combined HAC/LAC configuration shown in Figure 5.21 (a). Once again, the combined approach is implemented by first incorporating the LAC system, and then designing the high-authority con-

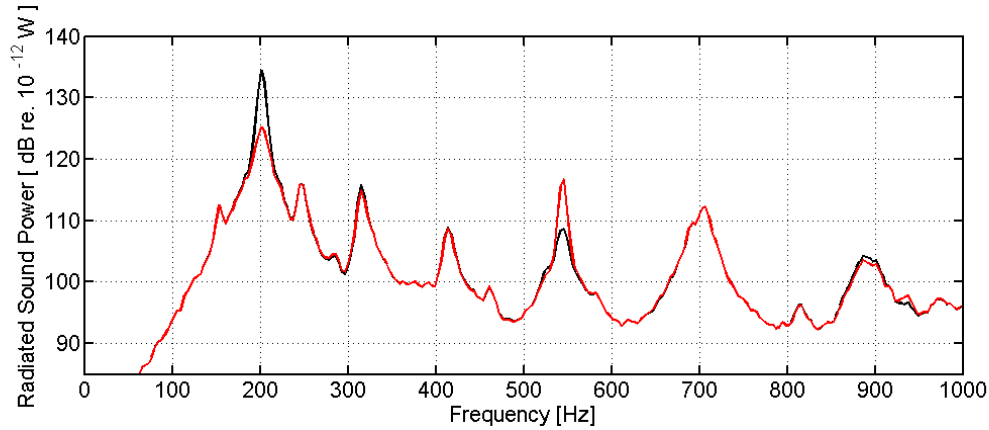


Figure 5.20: Radiated sound power with no control (solid black line) and using DVF (solid red line) with the transducer configuration shown in Figure 5.18.

trollers based on the damped system model. The performance of each control system is shown in Figure 5.22. While the LAC system achieves a 4.4 dB integrated reduction of radiated sound power, the LQG controllers achieve a 6.1 dB reduction. In comparison, the combined approach reduces the response by only 6.7 dB. The relatively small additional reduction achieved by combining the two approaches is due to the fact that both feedback strategies target the resonance at 200 Hz. While the performance benefits are marginal, the control strategies do stabilize one another. In particular, the HAC approach reduces the spillover generated by the low-authority controller at 580 Hz, while the low-frequency damping provided by the LAC strategy reduces the spillover caused by the decentralized LQG controllers. For example, Figure 5.21 (b) shows the Nyquist plots of the sensor-controller-actuator transfer functions. The solid line shows the response using only LQG control while the dash-dotted line shows the Nyquist diagram for the combined system. In this case, the gain margin for the LQG control system is improved from 2.7 dB to 9.4 dB by including the LAC system.

Positive position feedback

Instead of using DVF, which is limited by in-bandwidth spillover, another alternative is to use positive position feedback (PPF). Once again, the LAC transducer configuration shown in Figure 5.18 is investigated. However, since the sensors measure velocity and not position, an integrator must be added to the standard PPF controller such that

$$C(s) = 1/s \left(\frac{k\omega_n^2}{s^2 + 2\xi\omega_n s + \omega_n^2} \right) \quad (5.2.1)$$

where $C(s)$ is the compensator, k is the control gain, ω_n is the natural frequency of the filter, and ξ is the damping ratio. In this example, an iterative approach is used to select a control gain of 200, a damping ratio of 0.1, and a natural frequency of 208 Hz. Figure 5.23 shows the open- and closed-loop response using PPF. The control system achieves a 17 dB peak reduction at 200 Hz, and a 7.7 dB integrated reduction of radiated sound power. In addition, the controller is robust as shown in Figure 5.24, with a gain margin of

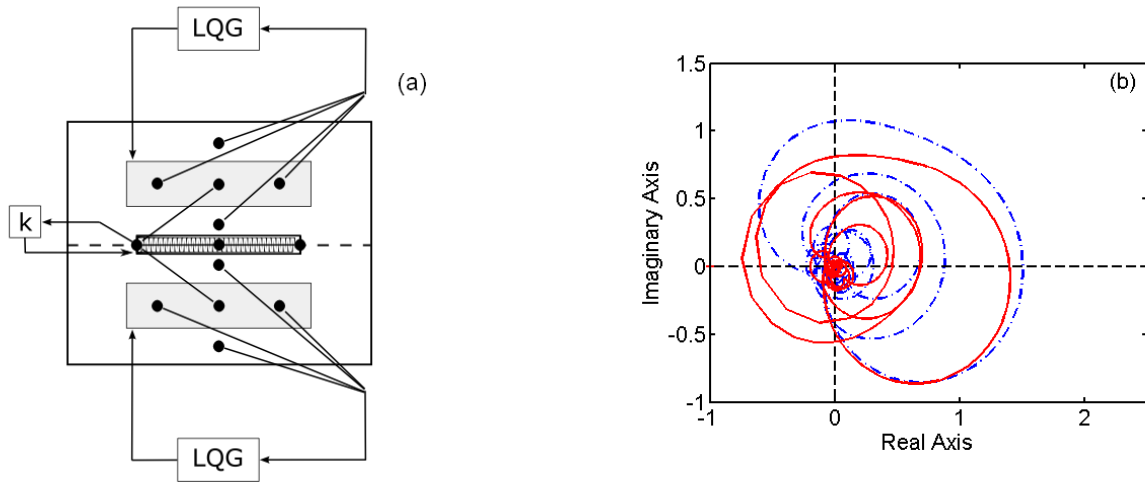


Figure 5.21: The diagrams show: (a) a combined HAC/LAC configuration with an MFC actuator along the stiffener; and (b) the Nyquist plot of the sensor-controller-actuator transfer function using LQG control (solid red line), and using DVF and LQG control (dash-dotted blue line).

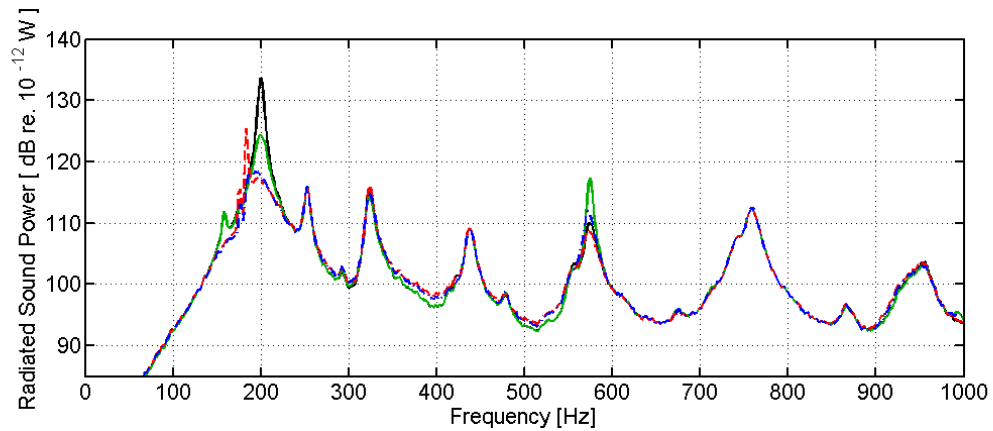


Figure 5.22: The radiated sound power from the structure before control (solid black line), using only DVF (solid green line), using LQG controllers (dashed red line), and using both LQG and DVF (dash-dotted blue line).

24.4 dB and a phase margin of 48° . Notice that this control system outperforms the HAC strategy as well as the other LAC approaches. In addition, the control system is robust and only requires a single transducer pair along each stiffener. Due to these advantages, this approach is evaluated experimentally on the stiffened aluminum test structure.

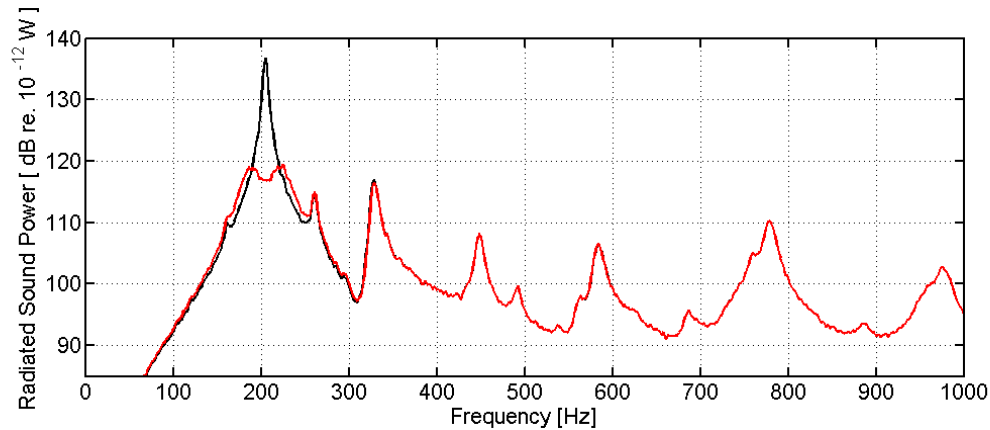


Figure 5.23: Radiated sound power before control (solid black line), and using PPF (solid red line).

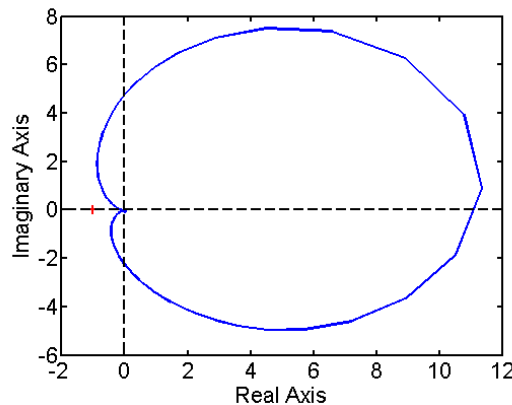


Figure 5.24: Nyquist plot of the sensor-controller-actuator transfer function shown in Figure 5.18. Positive position feedback is used for control.

5.3 Experimental results

The purpose of the experimental work is to study the limitations of both DVF and PPF using the transducer configuration shown in Figure 5.18. Both control systems are evaluated on the stiffened aluminum panel described in Chapter 2. Since the dynamics of the test structure differ drastically from the simple numerical model, this work provides a more realistic evaluation of each control strategy.

For convenience, the LAC system is implemented digitally with a sampling frequency of 10 kHz. While the digital implementation introduces additional phase lag, the frequency response function for this transducer pair is only expected to be passive at low frequencies anyway. Therefore, the additional phase introduced

by the digital controller is not expected to drastically reduce achievable performance. Note that since the system is sampled at 10 kHz, anti-aliasing and reconstruction filters are used on all inputs and outputs as described in Chapter 2. Since both direct velocity feedback and positive position feedback are evaluated, the summed response from the accelerometers is integrated once to yield velocity and twice for position. This is accomplished by filtering acceleration using the low-pass filter, $0.01/(z - 0.99)$. However, since this filter does not approximate an integrator at low frequencies, DC phase is still $+180^\circ$. Unfortunately, this can destabilize the DVF control system. Therefore the high-pass filter, $0.9922(z - 1)/(z - 0.9844)$, is included to roll off low-frequency gain.

Initially, the MFC actuator is driven with white noise while the summed, integrated, and filtered response from the five accelerometers is recorded. The input/output data is then used to calculate the frequency response function shown in Figure 5.25. Notice that the frequency response is only passive through approximately 300 Hz. Therefore direct output feedback is only conditionally stable, as shown by the Nyquist plot in Figure 5.26. In this example, a feedback gain of 0.7 yields a stable control system with a gain margin of 1 dB and a phase margin of 8° . The red line in Figure 5.27 shows the radiated sound power from the structure using direct output feedback with a gain of 0.7. Due to the poor stability bounds shown in Figure 5.26, this LAC system is only able to achieve a 1 dB integrated reduction in acoustic radiation from 50 to 800 Hz.

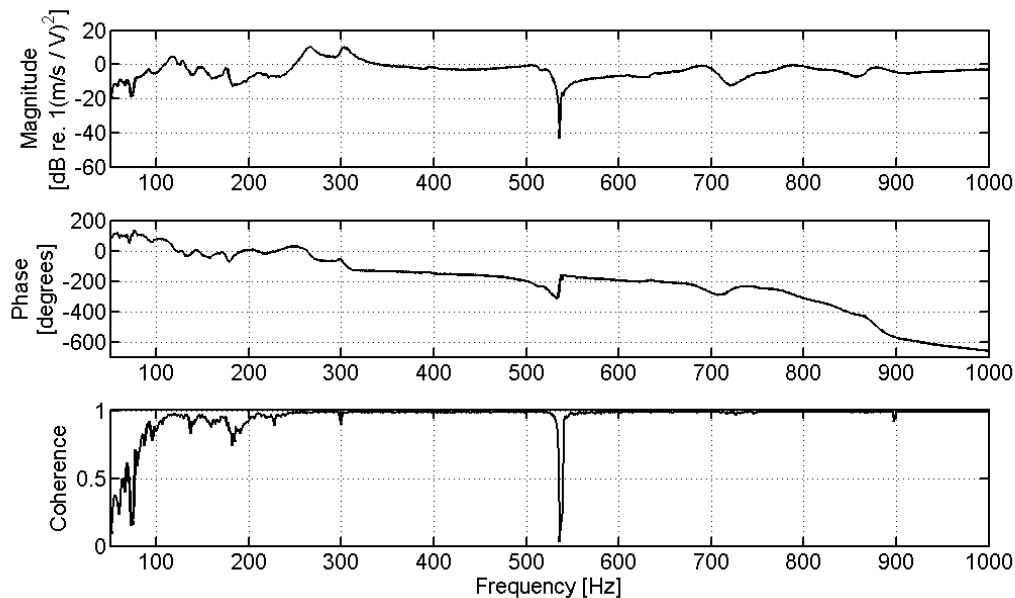


Figure 5.25: The experimental frequency response function estimated from the MFC drive signal to the summed and integrated accelerometers.

Next consider PPF control, which is used to target the dominant low-frequency resonance near 150 Hz. This controller is designed iteratively to maximize the performance of the closed-loop system, as shown by the dashed blue line in Figure 5.27. In particular, the filter frequency is 180 Hz while the damping ratio and control gain are 0.2 and 4.5, respectively. Although the dominant three peaks at 118 Hz, 134 Hz, and 150 Hz are each reduced by more than 4 dB, the integrated reduction is only 1.5 dB. To understand why additional performance was not possible, recall that PPF requires sufficient spacing between the poles and

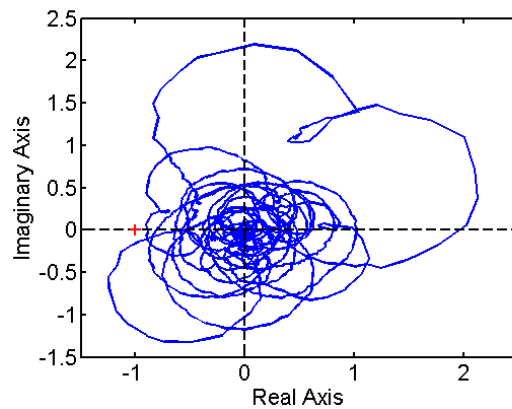


Figure 5.26: The Nyquist plot of the measured sensor-actuator frequency response function with a feedback gain of 0.7 .

zeros (McEver 1999; Preumont 2002). Unfortunately, the pole-zero separation for this system is relatively small due to high modal density.

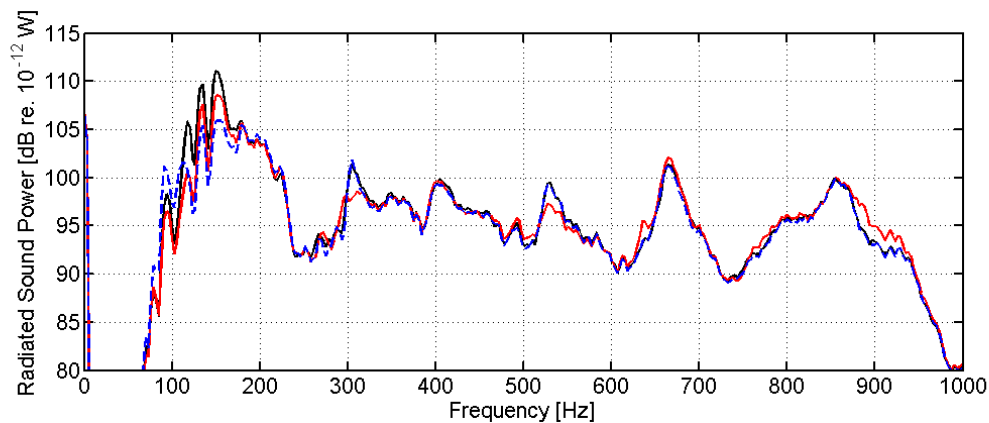


Figure 5.27: Radiated sound power without control (solid black line), using DVF (solid red line), and using PPF control (dashed blue line).

5.4 Summary

Negative rate feedback using triangular actuators and point sensors was investigated first. Numerical simulations showed that the frequency response function for this transducer pair was only minimum phase below 1.8 kHz since the line moments along the lateral edges of the actuator dominated the forcing term at higher frequencies. Since the response was not minimum phase, a first order compensator was shown to perform better than direct velocity feedback.

Next, the combined HAC/LAC strategy was investigated. Simulations showed that by augmenting in-bandwidth damping, the LAC system was able to supplement the performance of the HAC strategy and

also reduce the interaction between neighboring HAC loops.

Next, we showed that an MFC actuator could be used to extend the minimum-phase property of the frequency response function if the actuator was shaped, or if the material constants were tuned appropriately. Unfortunately, subsequent simulations demonstrated that triangular actuators and point sensors are not effective if the boundaries of the structure are flexible. Therefore, an alternate transducer configuration was investigated.

In particular, a transducer pair mounted along the flexible stiffener was found to couple to the dominant low-frequency mode without interfering with the HAC transducers. This transducer pair consisted of a large piezoelectric actuator along with an array of point sensors. While an isotropic piezoelectric actuator was not substantially collocated with the array of point sensors, an MFC actuator coupled more efficiently to the dominant low-frequency mode and had better stability margins due to the directional characteristics of the transducer. Simulations showed that while direct output feedback can be used to suppress the dominant global mode, performance was limited since the transducer pair was not truly matched. However, numerical simulations indicated that a combined HAC/LAC strategy did have advantages. In particular, the HAC system reduced the in-bandwidth spillover generated by the LAC system, while the LAC system augmented the structural damping and stabilized the decentralized LQG controllers.

Positive position feedback was then investigated as an alternative to direct velocity feedback. Numerical simulations showed that PPF was robust, and effectively suppressed the dominant low-frequency resonance. Due to the promising numerical results, both DVF and PPF were evaluated in the laboratory. Unfortunately, DVF was limited since the frequency response function between the MFC actuator and summed sensors was not minimum phase. Similarly, the frequency response function lacked sufficient pole-zero spacing for the PPF control system. Without an effective LAC system, the benefits of a combined HAC/LAC approach could not be validated experimentally.

In conclusion, this chapter demonstrated that while LAC and HAC/LAC strategies can be used for decentralized control, performance is dependent on the dynamics of the test structure. The following chapter revisits the decentralized LQG control problem using an adaptive approach, which periodically updates each controller in response to changes in the closed-loop measurements.

Chapter 6

Indirect adaptive control

Previous chapters have shown that decentralized control generates unavoidable errors in both the control and disturbance models. While this may not affect low-authority strategies such as collocated rate feedback, it can severely limit the performance of high-authority control strategies such as LQG control. Although robust control theory can be used to maintain the stability and performance of high-authority strategies in the presence of modeling error, uncertainty bounds are often difficult to estimate *a priori* (Cox et al. 1999).

Therefore, this chapter focuses on a time-varying control strategy designed to compensate for poor uncertainty models. In general, time-varying strategies can be divided into two categories, direct and indirect adaptive approaches. Direct adaptive strategies typically utilize simple filter structures and update the controller coefficients at every sample to minimize a given cost function. On the other hand, indirect strategies design the controller 'off-line' and update the control coefficients much less frequently (Elliott 2001).

Direct adaptive strategies typically use some form of internal model control (IMC) architecture to transform the feedback problem into an equivalent feedforward control structure (Elliott 2001). While some direct adaptive strategies include a system identification step, others assume the plant is stationary and are updated to account for time-varying or unknown disturbances (Bitmead et al. 1990; Baumann 1997; McEver et al. 2003). For instance, a technique originally proposed by Tay and Moore (1991) termed Q-parameterization combines a fixed controller with an adaptive filter. As the adaptive filter sweeps over all stable transfer functions, the combination of the fixed and adaptive controllers sweeps over all possible stabilizing controllers for the nominal plant. Baumann (1997) demonstrated that this technique can be used effectively for structural vibration suppression when disturbance information is not known *a priori*. Another direct adaptive technique called adaptive generalized predictive control (GPC) has been used by Kegerise et al. (2007) to reduce flow-induced cavity tones. A disadvantage of direct adaptive strategies in general, is that modeling inaccuracies can introduce residual feedback around the adaptive loop. This can affect the convergence of the adaptive algorithm and the stability of the feedback loop. As a result, Elliott (2001) demonstrates that directly adapted feedback control systems can be more sensitive to model inaccuracies than time-invariant controllers.

Indirect adaptive strategies update the controller infrequently and can therefore avoid residual feedback problems (Elliott 2001; Rafaely et al. 1999). Additionally, since the controller is not updated at each time step, control design can be performed as a background task on the primary processor, or even on a separate system altogether. Therefore, indirect adaptive strategies are not limited to simple filter structures. For instance, Gibbs and Cabell (2002) used an iterative sequential loop-closure technique with high-order optimal controllers to successfully reduce the sound radiation from multiple aircraft-style panels. Unfortunately, sequential strategies are not scalable since global coordination is required during the design process.

Another way to account for plant variations caused by neighboring control loops is to implement an adaptive system-identification strategy. While this could also be used to account for large plant variations caused by cabin pressurization or temperature changes, it would necessarily increase the complexity of the control system. In addition, a dither signal would be required, which may degrade the nominal performance of the system. The strategy also has to address issues associated with the affect of closed-loop control on parameter estimation, and determine how the accuracy of the plant estimate impacts control performance (Bitmead et al. 1990). Due to the increased theoretical and computational complexity associated with this approach, it is not investigated further in this paper.

The indirect adaptive strategy investigated in this chapter uses a fixed control model. In particular, an adaptive LQG/LTR based approach is used to account for parameter variations introduced by neighboring control loops. This approach requires no communication between control units, and is relatively simple. Figure 6.1 shows a diagram of the proposed control approach, which is implemented independently on each subsystem. The control strategy can be divided into two processes: a real-time process that occurs on a sample-by-sample basis, and an update procedure that occurs much less frequently. The physical system is shown as $G_i(z)$ and the disturbance is $d_i(n)$. The subscript i denotes that the control strategy is implemented on the i^{th} subsystem. Notice that the controller is designed using an internal plant model $\hat{G}_i(z)$, which is used to generate an estimate of the disturbance $\hat{d}_i(n)$ at each time step. Although this resembles an IMC structure, the input to the online controller $C_i(z)$ is the observed error signal $y_i(n)$ instead of the disturbance estimate.

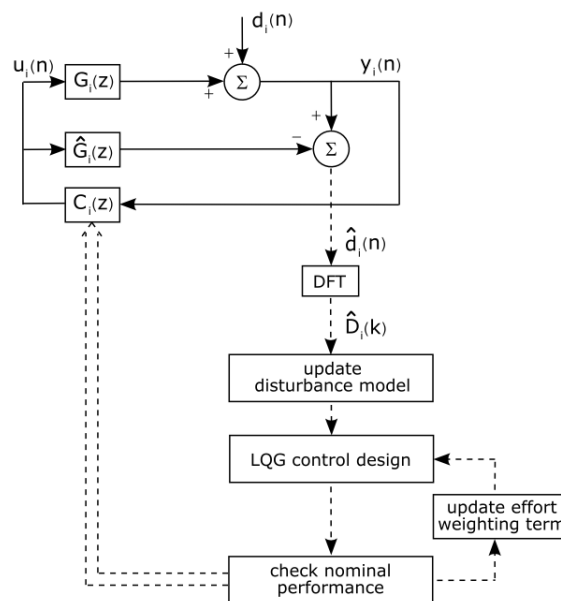


Figure 6.1: The indirect adaptive control strategy is divided into two separate processes: a real-time process occurring at every sample (solid lines), and a slower process that updates the controller infrequently (dashed lines).

Figure 6.1 also shows the steps involved in the update procedure connected with dashed lines. In essence, each LQG controller is updated periodically using a new effort weighting term and disturbance model. As shown in the figure, the disturbance model is calculated from the discrete Fourier transform of the

disturbance estimate, $\hat{D}_i(k)$. The purpose of updating the disturbance model is to track changes in the disturbance and maintain robust stability. Robustness is addressed using loop recovery, which means the amplitude of the disturbance model is artificially increased to recover LQR performance. After updating the disturbance model, the LQG controller is redesigned. If the new design satisfies basic constraints, then the online controller $C_i(z)$ is updated and the effort weighting term is reduced.

Note that while other procedures can be used to guarantee closed-loop stability, they are usually either overly conservative or computationally intensive. Recall that the purpose of this work is to investigate practical approaches to the decentralized control problem. Although there are no stability guarantees, this indirect adaptive strategy is simple, scalable, and effective. Therefore, while the presentation included in this chapter is not rigorous from a controls perspective, it does emphasize the practical significance and limitations of the strategy.

The design procedure is discussed in more detail in the following two sections. The first section explains how each controller is initialized, including a brief discussion on system identification, frequency-shaped LQR control, and disturbance estimation. The next section describes the update procedure, which is used to account for unmodeled dynamics introduced by neighboring control loops. After describing the control strategy, experimental results are used to validate the approach. A discussion pertaining to system scalability is then included.

6.1 Controller initialization

This section describes the initial design procedure, which begins by identifying a model of the subsystem. Next, the state regulator is designed and the disturbance is modeled. The LQG controller is then designed and evaluated to ensure minimum stability requirements are met. If the system does not meet minimum requirements, then the controller is redesigned.

The first step in the design process is to identify an accurate subsystem model. For this work, the plant model is computed using the observer/Kalman filter identification (OKID) algorithm (Juang 1994). The OKID algorithm uses experimental time-domain input/output data to compute observer Markov parameters, which are used to estimate the pulse-response sequence for the system. The eigensystem realization algorithm (ERA) is then used to extract a state-space model from the pulse-response sequence. The OKID algorithm is implemented using the `okid.m` function in the SOCIT toolbox for MATLAB.

After identifying an accurate system model, state feedback is considered. Although the LQG design must also incorporate some form of state estimator, it is beneficial to initially consider the state regulator for a few reasons. For one, recall that loop recovery is limited to recovering LQR performance. Therefore, if the LQR has poor stability margins in a particular bandwidth, then loop recovery may not be effective. In addition, if an acceptable design is not possible using full-state feedback, then it does not make sense to investigate other output feedback strategies employing anything less than full-state information. In that case, the actuators are inadequate and must be modified (Anderson and Moore 1990). Recall from Chapter 4, that one way to improve the robust characteristics of the design with little impact on nominal performance is to penalize control effort at the zeros of the open-loop transfer function (OLTF). Therefore the robust characteristics of the LQR are addressed by increasing the effort weighting term at the zeros of the OLTF. The simulated performance of the LQR is then evaluated to ensure that the actuators are adequate before continuing with

the LQG design.

Next, the Kalman estimator is designed to generate optimal state estimates in the presence of measurement and process noise. In general, the measurement noise can be estimated from baseline measurements of the noise floor, while the disturbance model is estimated directly from open-loop system measurements. Recall that for simple LQG control systems, the phase of the disturbance model is arbitrary and can be found through spectral factorization. Therefore in this work, a stable and minimum phase model that matches the spectral shape of the open-loop measurements is used to model the disturbance.

The initial LQG controller is then created by combining the state estimator and robust state regulator. To ensure an initial level of robustness, the design is required to meet minimum nominal gain and phase margins. If the design does not meet these requirements, then the state regulator is redesigned using a larger effort weighting term (ie more conservative design). However, if the design is acceptable then the control law is implemented.

In summary, the initial controller is designed by first identifying an accurate subsystem model. Next, the effort weighting term is shaped to limit excessive compensator gain at the zeros of the open-loop transfer function. This improves the robustness of the LQR design, which is necessary in order to effectively use loop recovery. A state estimator is then generated using an initial disturbance model created directly from open-loop measurements. An LQG controller is then formed by combining the estimator and robust state regulator. Finally, the stability margins of the design are verified before implementing the control system.

6.2 Update procedure

Since the initial controllers are designed independently, the interaction between control units can degrade the performance of the coupled system. Additionally, the conservative nature of the initial controller is likely to further limit achievable performance. Therefore, this section describes an iterative procedure used to update each controller in order to improve overall system performance. The iterative design process is performed in three steps: disturbance estimation and loop recovery; LQG design; and design evaluation. Disturbance estimation and loop recovery are used to improve the robust performance of the control system by modifying the disturbance model. Each LQG controller is then redesigned using the new disturbance model and an updated effort weighting term. If the design satisfies control effort and performance considerations, then the online controller is updated. The entire process is repeated until the control effort approaches predefined limits, or until no additional performance is achieved. Once the system has converged, the update procedure can be stopped until a change in the disturbance estimate is detected.

6.2.1 Disturbance model

The disturbance model is updated to make the system more robust to plant variations while tracking slow changes in the disturbance. These objectives are accomplished using frequency-shaped loop recovery and disturbance estimation. Both strategies are performed simultaneously by updating the disturbance model based on closed-loop system measurements.

Recall from Figure 6.1, that the control system uses an internal model to generate the disturbance estimate,

$\hat{d}_i(n)$. If the plant model is perfect, then the estimate will accurately track changes in the true disturbance. However, in frequency bands where $\hat{G}_i(z) \neq G_i(z)$, the amplitude of the disturbance estimate could be larger or smaller than the actual disturbance. Although increasing the amplitude of the disturbance model improves robustness by exploiting loop recovery, decreasing the amplitude of the model can make the design more sensitive to modeling error. Therefore, the disturbance model is updated by taking the maximum of the current disturbance estimate and the previous disturbance model on a frequency-by-frequency basis. In other words, the model is only changed if the magnitude of the disturbance estimate exceeds the magnitude of the previous disturbance model.

In order to implement this procedure, the spectral density of the disturbance is estimated as

$$S_{dd}(k) = \hat{D}_i(k)\hat{D}_i^*(k) \quad (6.2.1)$$

where $\hat{D}_i(k)$ is the discrete Fourier transform of one record of the disturbance estimate, $\hat{D}_i^*(k)$ is the complex conjugate of $\hat{D}_i(k)$, and k is the discrete frequency index. The spectral density of the new disturbance model $S_{pp_{\text{new}}}$ is then computed as

$$S_{pp_{\text{new}}}(k) = (1 - \alpha) \max[S_{dd}(k), S_{pp_{\text{old}}}(k)] + \alpha S_{dd}(k) \quad \text{for all } k \quad (6.2.2)$$

where $S_{pp_{\text{old}}}(k)$ is the spectral density of the old disturbance model, and α is a leakage parameter. Note that if the leakage parameter is set to zero, then the disturbance model can only increase. However, a leakage parameter of 0.1 is used in this work to address slow changes in the actual disturbance. This enables the model to be reduced slowly if the disturbance estimate is consistently low.

Note that $S_{pp_{\text{new}}}$ is the spectral density of the desired disturbance model, not the model itself. However recall that for simple LQG control systems, the phase of the disturbance model is arbitrary and can be found through spectral factorization. Therefore, a minimum phase spectral factor of $S_{pp_{\text{new}}}(k)$ is calculated using the complex-cepstrum algorithm (implemented in the MATLAB function `genphase.m`)

$$P(k) = \exp(\text{FFT}[c(n)\text{IFFT}[\ln(S_{pp_{\text{new}}}(k))]]) \quad (6.2.3)$$

where $c(n) = 0$ for $n < 0$, $c(n) = 1$ for $n > 0$, and $c(0) = 1/2$ (Elliott 2001). Note that the magnitude of the discrete-frequency response $P(k)$ equals the square root of $S_{pp_{\text{new}}}(k)$ and the phase corresponds to a stable and minimum-phase plant. Finally, a state-space model of the disturbance is fit to $P(k)$ using an equation error method, which is implemented using the MATLAB function `invfreqz.m`.

Figure 6.2 shows an example of how the disturbance model is updated. The magnitude of the initial disturbance model is shown with the solid black line, while the magnitude of the current disturbance estimate is shown in blue. In this example, the initial model is determined from open-loop measurements, while the current estimate is acquired during closed-loop operation. Differences between the two curves indicate that either the disturbance or the plant has changed. The magnitude of the new disturbance model is calculated by essentially taking the maximum amplitude of the past model and current estimate at each frequency, as shown by the dashed red line in Figure 6.2.

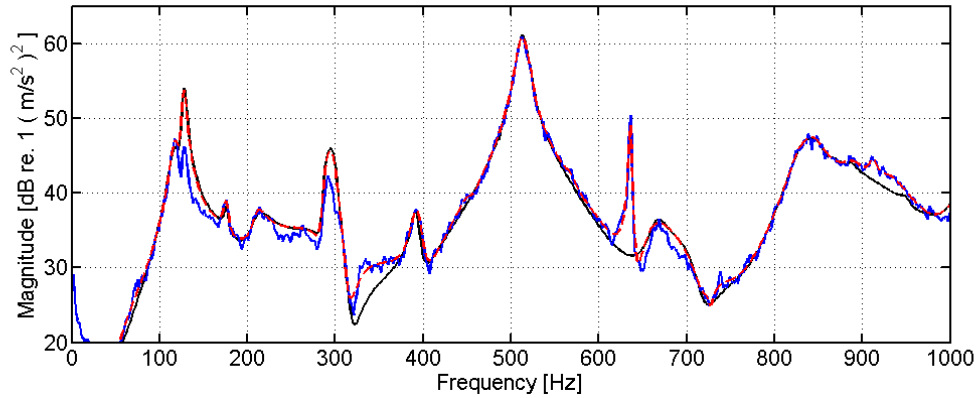


Figure 6.2: The amplitude of the old disturbance model (solid black line), the magnitude of the Fourier transform of the current disturbance estimate (solid blue line), and the amplitude of the new disturbance model (dashed red line).

6.2.2 Effort weighting term

The goal of the update procedure is to transition the conservative initial design to a more aggressive controller, which is still robust to the modeling error generated by neighboring control loops. To accomplish this, the magnitude of the effort weighting model is reduced incrementally while updating the disturbance model to address potential stability problems. The effort weighting model is updated according to

$$\lambda_{\text{new}}(z) = \lambda_{\text{old}}(z) - \tau \quad (6.2.4)$$

where $\lambda_{\text{new}}(z)$ is the new effort weighting model, $\lambda_{\text{old}}(z)$ is the old weighting model, and τ is an update term. Recall that since the control effort penalty is shaped to penalize effort at the zeros of the control model, it is necessary to update the effort weighting model instead of the frequency-independent effort weighting term \tilde{R} . The value of τ is updated after each iteration based on the control effort and performance criteria discussed in the next section.

6.2.3 Design evaluation

The purpose of the evaluation step is to ensure that the new controller is acceptable before updating the control system. A flow chart of the evaluation process is shown in Figure 6.3. Recall that the initial design must have minimum nominal gain and phase margins. Although this may limit performance, it ensures a certain level of robust stability. If the initial design is acceptable then the online controller is updated and the magnitude of the effort weighting model is decreased. However, if the design does not meet the requirements, then the magnitude of the effort weighting model is increased and the controller is redesigned.

Subsequent designs are evaluated based on control effort and performance criteria. The control effort restriction is designed to avoid overloading either the actuator or amplifier. As the measured control effort approaches predefined voltage limits of ± 12 V for this application, the constant τ is reduced to zero. However, if the out-of-bandwidth control effort limits performance, then either the effort weighting term or the

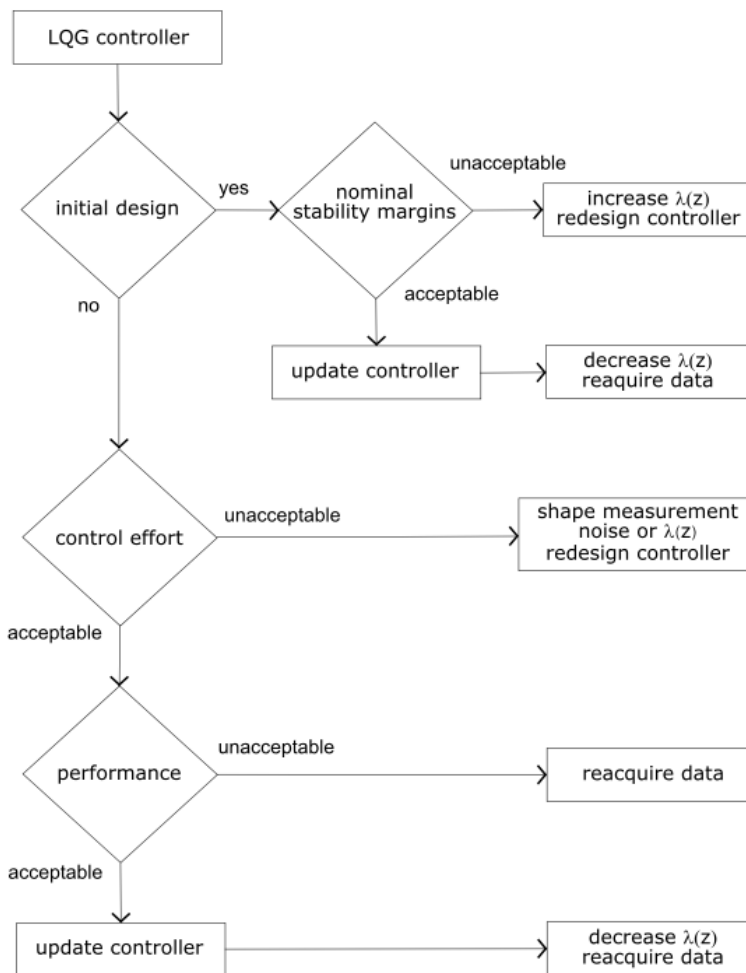


Figure 6.3: Flow chart of the evaluation process.

measurement noise model is shaped.

Each controller is also evaluated by comparing the measured response acquired using the current design with the predicted response using the new design. In particular, the magnitude of the discrete Fourier transform of the measured response is compared with the predicted response $\tilde{Y}(k)$. The predicted response is calculated using

$$\tilde{Y}(k) = \frac{DM(k)}{1 - \hat{G}(k)C(k)} \quad (6.2.5)$$

where $DM(k)$ is the new disturbance model, $\hat{G}(k)$ is the plant model, and $C(k)$ is the controller being evaluated. If the controller is expected to improve integrated performance, then the online controller is updated, and $\lambda(z)$ is reduced. However, if the new controller is not expected to improve integrated performance, then the control law is not updated. Instead, a new data set is acquired, and the controller is redesigned.

In summary, the first step in the proposed design process is to identify an accurate subsystem model. The effort weighting term is then shaped to penalize control effort at the zeros of the open-loop system. Shaping the effort term limits excessive compensator gain and improves the stability margins of the LQR design. After calculating full-state feedback gains, the measured response is used to generate an initial model of the disturbance. The disturbance model is then used to calculate the optimal state estimator. If the initial LQG controller meets minimum stability requirements, then the controller is implemented and the closed-loop performance is recorded. The process is then repeated by updating the disturbance model to account for changes introduced by neighboring control loops. The LQG controller is redesigned using the new disturbance model and a more aggressive effort weighting model. This design is evaluated based on control effort and performance criteria. If the new design is acceptable, then the online controller is updated. The process is repeated until the control effort approaches predefined limits, or until subsequent designs fail to improve control performance.

At this point, it is beneficial to review some of the limitations of this approach. First, the initial controller has to be sufficiently conservative such that the local control loop is robust to plant variations generated by neighboring controllers. This condition is not particularly restrictive since the initial controller can be made as conservative as necessary. Next, partial loop recovery is assumed to be sufficient to achieve acceptable decentralized control performance. Finally, since the strategy relies on the ability to estimate the disturbance model using only output measurements, the phase of the disturbance model must be arbitrary. Therefore the performance output has to be measurable. In addition, the error signal should be much larger than the measurement noise.

6.3 Validation

Ultimately, the closed-loop performance of any control system determines the success or failure of the design (Bitmead et al. 1990). For this system, closed-loop performance is evaluated experimentally using the stiffened aluminum test structure described in Chapter 2. The investigation is divided into three cases. First a relatively simple scenario is considered, in which the disturbance enters through the actuators, and the design is evaluated in terms of the sensed variable. Next, an acoustic disturbance is used and the design is evaluated in terms of radiated sound power. The final case demonstrates the advantage of feeding back radiation mode estimates in real-time.

6.3.1 Case 1: Structural excitation

The baseline transducer configuration described in Chapter 2 is used here. Recall that the PZT actuators are center mounted on each bay, and the "sensor" records the summed response from four accelerometers arranged in a diamond pattern around each actuator. In this case, the disturbance is generated by driving each actuator with a broadband random signal.

The first step in the design process is to identify a subsystem model using the OKID algorithm. The input/output data is obtained by driving the PZT actuator with a broadband random excitation while recording the sensor response. Each SISO subsystem is modeled using 75 states, which are sufficient to capture the relevant dynamics in the bandwidth of interest. Next, the effort weighting term is shaped to penalize control effort at the zeros of the open-loop transfer function. The amplitude of the initial effort penalty is then se-

lected in order to generate a conservative initial design. Next, the disturbance model is estimated from the Fourier transform of the open-loop disturbance response. Independent LQG controllers are then designed, evaluated, and implemented on each subsystem. The disturbance model is updated iteratively based on the closed-loop response, while the effort penalty is slowly reduced. A comparison of the amplitude of the initial and final disturbance models is shown in Figure 6.4 (a). Similarly, the amplitude of the initial and final effort penalties are shown in Figure 6.4 (b). The power spectra of the responses measured on the upper bay are shown in Figure 6.5. Note that the final design reduces the 130 Hz peak by more than 18 dB, and achieves a 4 dB integrated reduction from 50 to 800 Hz. The power spectrum of the response on the lower bay shows similar trends and is therefore not included.

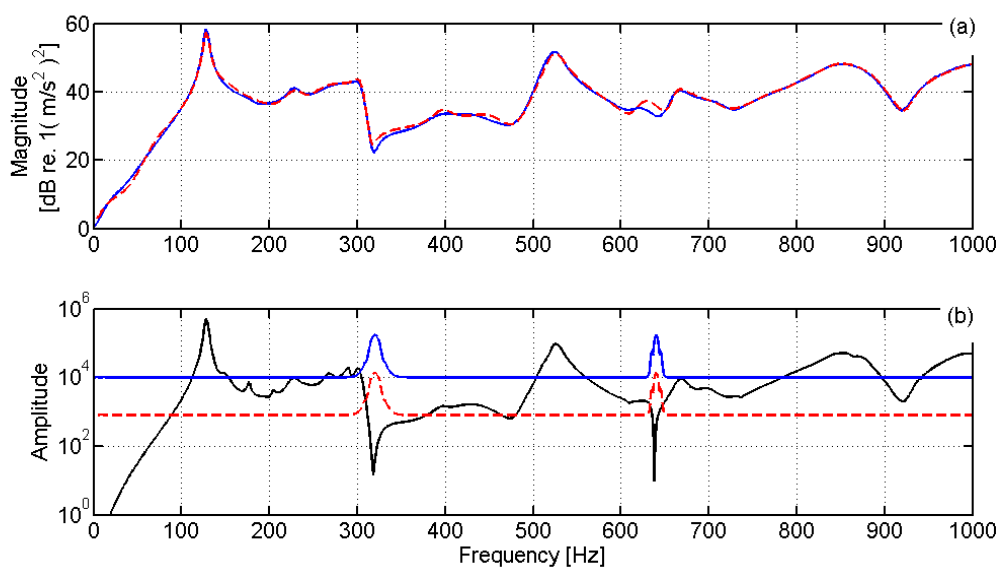


Figure 6.4: The amplitude of the initial LQG design (solid blue lines), and the amplitude of the final design (dashed red lines). The graphs show: (a) the amplitude of the disturbance model; and (b) the amplitude of the frequency-shaped effort weighting term.

For comparison, briefly consider Figure 6.6, which compares a standard LQG controller designed using a frequency-independent effort weighting term (solid green line), with a controller designed using the adaptive strategy presented above (dashed red line). Note that the standard LQG controller is designed using the same initial disturbance model as the adaptive design, and with a flat effort weighting term. Figure 6.6 shows that the traditional LQG design produces excessive spillover at 635 Hz, while the adaptive strategy does not. In this particular case, the difference between the two designs is primarily due to the frequency-shaped effort weighting term. However, subsequent examples will demonstrate the benefit of using an adaptive disturbance model.

6.3.2 Case 2: Acoustic disturbance

Once again, center mounted piezoelectric patches and summed accelerometers are used for control. However, the disturbance is now generated using an external acoustic source, as described in Chapter 2. Addi-

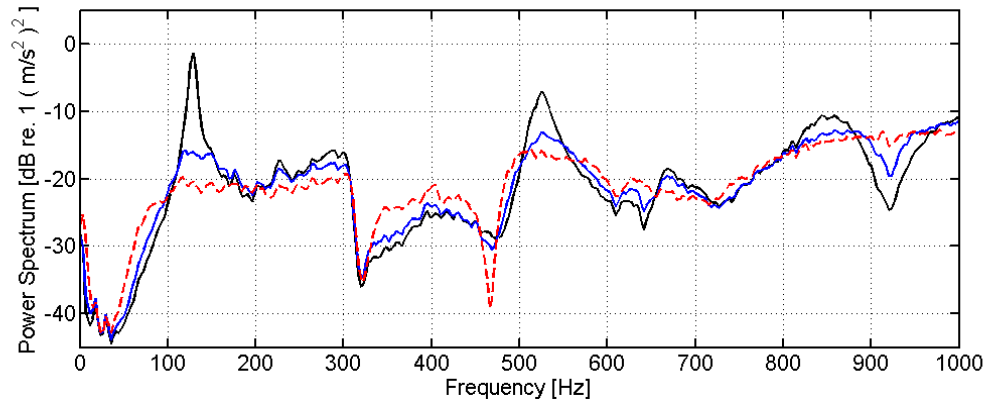


Figure 6.5: The power spectra of the sensor response on the upper bay, before control (solid black line), with the initial LQG controller (solid blue line), and with the final design (dashed red line).

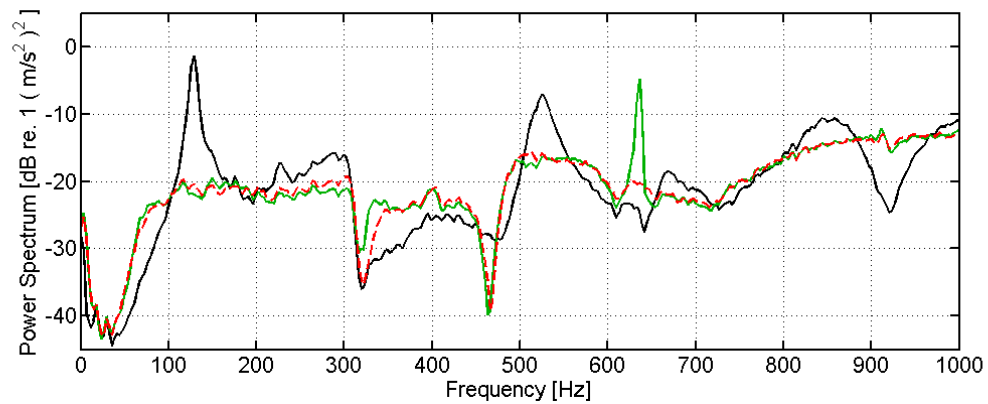


Figure 6.6: The power spectra of the sensor response on the upper bay, before control (solid black line), with a standard decentralized LQG design (solid green line), and with the adaptive control strategy (dashed red line).

tionally, performance is evaluated in terms of both the sensed variable and an estimate of radiated sound power.

As before, the first step is to model the subsystem using the OKID algorithm. A conservative initial effort weighting term is selected and shaped based on the zeros of the actuator/sensor transfer function. The initial disturbance model is then estimated and fit using the discrete Fourier transform of the disturbance estimate. The initial controller is designed, evaluated, and implemented. Once implemented, excessive low-frequency control effort is observed. Therefore, the measurement noise model is shaped as shown in Figure 6.7, to reduce low frequency effort and also to improve out-of-bandwidth stability margins. Note that shaping the effort weighting term is also an effective alternative to shaping the measurement noise model. The redesigned controller is then evaluated, and implemented. Again, the disturbance is updated iteratively as the effort weighting term is reduced. The initial and final disturbance models as well as the amplitude of the measurement noise model are shown in Figure 6.7. The corresponding power spectra of the summed acceleration measured on the upper bay are shown in Figure 6.8. The poor initial performance near 140 Hz increases the amplitude of the disturbance model at that frequency, which improves the performance of subsequent designs. Note that the interaction near 140 Hz could not be addressed effectively by simply shaping the effort weighting term since this would severely limit achievable performance. However, shaping the disturbance model is an effective solution to the problem. The final design achieves an integrated reduction of 3.3 dB from 50 to 800 Hz.

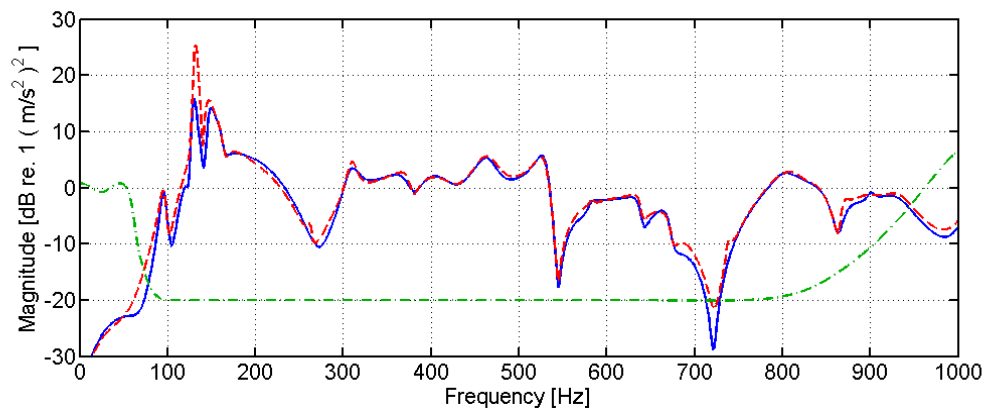


Figure 6.7: The amplitude of the initial disturbance model (solid blue line), the amplitude of the final disturbance model (dashed red line), and the amplitude of the measurement noise model (dash-dotted green line).

Next, performance is evaluated in terms of radiated sound power. An estimate of radiated sound power is calculated using 30 accelerometers evenly distributed over the two bays, as shown in Figure 2.14 (b). Recall from Chapter 2 that one way to calculate the total radiated sound power from the structure is to post process point-velocity or acceleration measurements using the radiation resistance matrix. However, a preferred approach is to develop a state-space representation of the frequency-dependent \mathbf{R} matrix using a curve fitting technique called radiation modal expansion (RME) (Gibbs et al. 2000). The sound power estimate used for this work is calculated using RME along with six radiation modes. In this application, six radiation modes account for more than 98 % of the total sound power radiated from the structure.

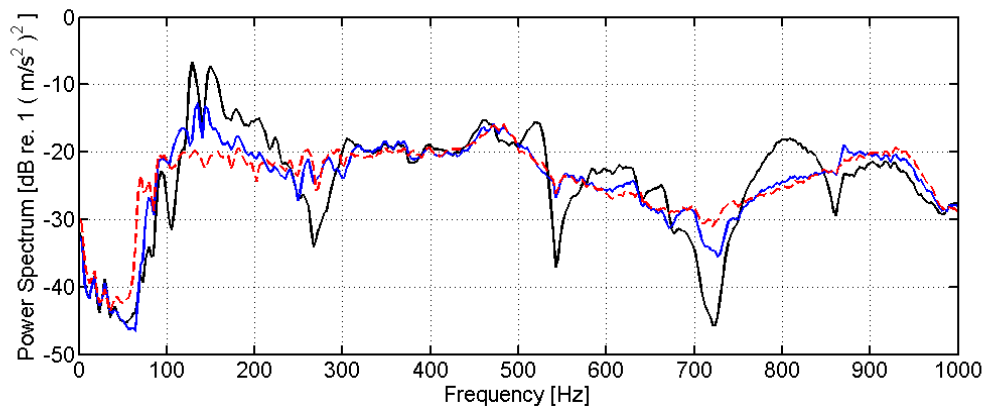


Figure 6.8: The power spectra of the measured response on the upper bay driven by an acoustic disturbance, before control (solid black line), using the initial controller (solid blue line), and using the final design (dashed red line).

Figure 6.9 shows the performance of the adaptive strategy in terms of the total radiated sound power from the two-bay structure. Notice that the closed-loop performance of the final design is relatively good through 600 Hz, with a 2.7 dB integrated reduction from 50 to 600 Hz. However at higher frequencies, the sensor does not provide a reasonable estimate of radiated sound power. The next section demonstrates that closed-loop performance can be improved by using more complicated sensors, which provide a better estimate of radiated sound power.

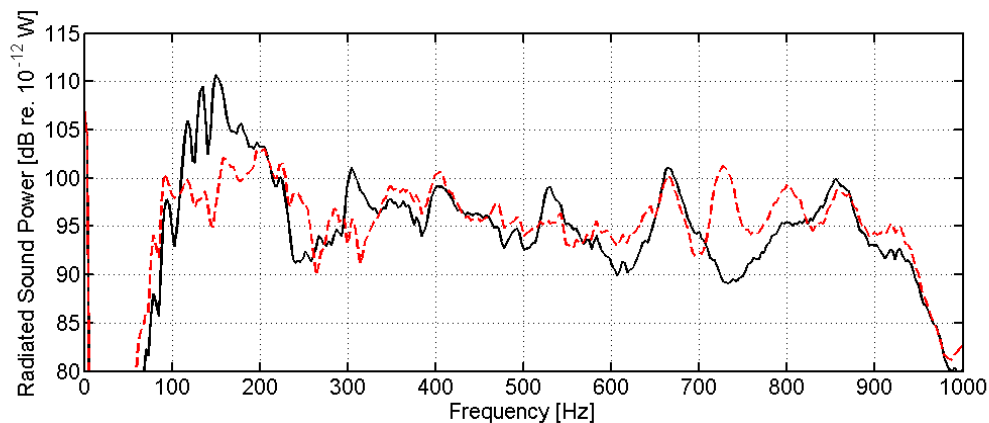


Figure 6.9: The total radiated sound power from the two-bay structure before control (solid black line), and using the final controller (dashed red line).

6.3.3 Case 3: Radiation mode estimates

Next, single-bay radiation mode estimates are fed-back in real-time instead of using summed acceleration. Although this increases the overall complexity of the control system, it demonstrates that performance can be improved if better sensors are available. Additionally, it shows that the adaptive strategy can be applied

to different types of systems, including ones with multiple inputs.

In these experiments, the first radiation mode accounts for 82 % of the total radiated sound power from the structure. One reason why summed accelerometers are effective for structural acoustic control is because they provide a low-frequency estimate of the first radiation mode. However, if a more accurate estimate is available from a distributed volume-velocity sensor for instance (Johnson et al. 1997), then the overall performance of the control system could be improved. To support this claim, an estimate of the first radiation mode on each bay, obtained using RME, is fed back to each decentralized control system in real-time. The controllers are then designed iteratively as previously described.

For comparison, a second control system using six radiation mode estimates is also evaluated. In this case, the design process is slightly different since six signals are fed back instead of one. However, modifying the design to account for multiple inputs is trivial. Instead of updating a single disturbance model based on the Fourier transform of one disturbance estimate, six disturbance models are now updated independently based on six separate disturbance estimates. Again, the disturbance models are updated iteratively as the effort weighting term is slowly reduced. Figure 6.10 compares the converged performance of the two controllers. Both controllers reduce the integrated response from 50 to 600 Hz by over 3.6 dB. As expected, the system designed using six radiation mode estimates performs slightly better from 600 to 800 Hz due to a better high frequency estimate of radiated sound power. However, in this particular experiment, the performance advantages are hardly worth the added complexity associated with feeding back all six radiation mode estimates.

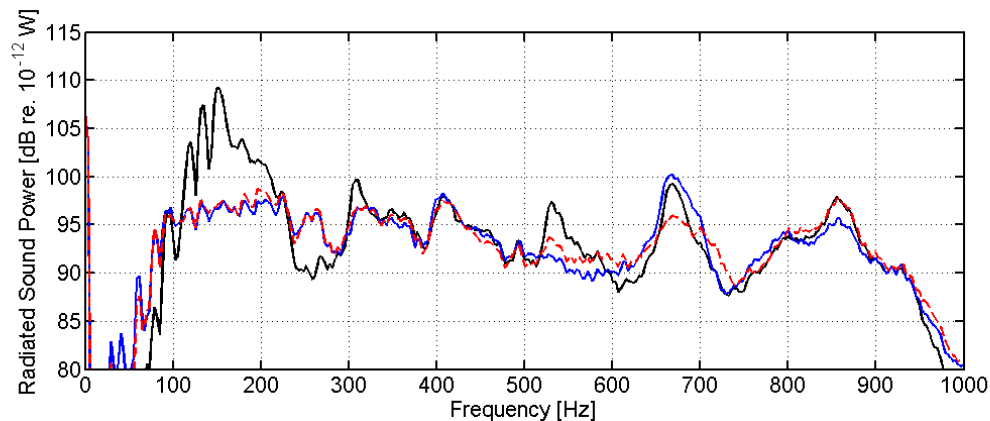


Figure 6.10: The total radiated sound power from the two-bay structure before control (solid black line), using a single radiation mode estimate (solid blue line), and using six radiation mode estimates (dashed red line).

6.4 Scalability

The previous section demonstrates that the adaptive decentralized LQG strategy can reduce the radiated sound power from two-bays simultaneously. However, the fuselage of an aircraft may contain several hundred bays, and therefore scalability is important. Since a decentralized control strategy is used, the complexity of each individual controller is not expected to change as the size of the system increases. For instance

consider Figure 6.4 (a), which depicts three decentralized controllers on an aircraft fuselage. Figure 6.4 (b) shows the associated block diagram assuming only adjacent systems are connected. Notice that the unmodeled dynamics can always be simplified into a single additive uncertainty term regardless of the number of interacting subsystems. Therefore, while multiple control units may generate more additive uncertainty than a single interacting control unit, the overall problem is essentially the same. Each system is still designed independently to account for unknown plant and disturbance variations. Therefore, the complexity of each control system will not be affected by the total number of independent control loops.

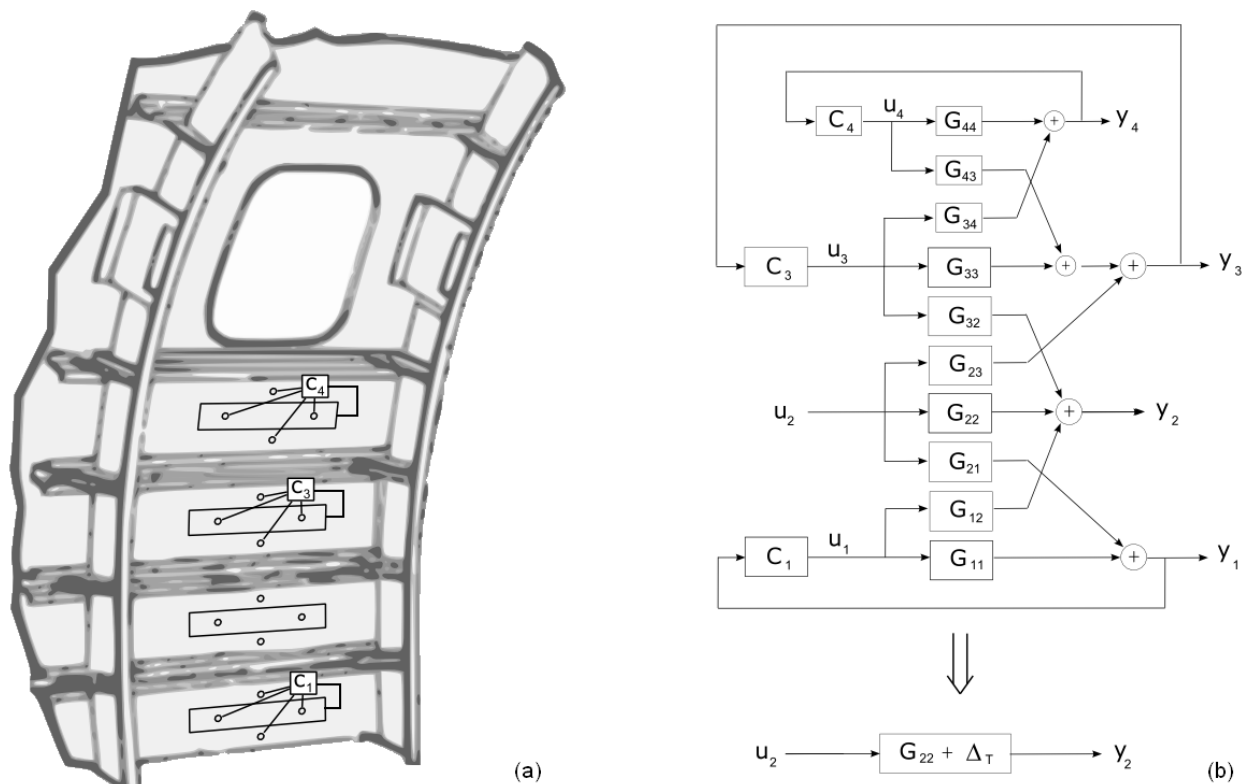


Figure 6.11: The figures show: (a) a sketch of the decentralized control problem; and (b) a block diagram of the system reduced to a simple model with an additive uncertainty term.

The overall weight of the system is expected to scale linearly with the number of independent control units. Therefore the weight of each control unit, which includes all transducers, power supplies, and control electronics, must be taken into account and minimized if possible. One of the advantages of piezoelectric patches and accelerometers is their small size and weight. For instance, the 0.292 in by 0.072 in piezoelectric patch along with the four accelerometers used in this work have a combined weight of only 0.045 kg. However, the power and control electronics are both bulky and heavy. Therefore, the size and weight of the electronics may limit the scalability of the current control system. While smaller and lighter electronics are commercially available, optimizing the electronics for this particular application was beyond the scope of the current investigation.

Decentralized control offers a number of advantages with respect to scalability, however minimizing a local

performance metric does not guarantee global performance. For instance, if the vibration of adjacent bays is correlated, then reducing the sound power radiated from a single bay may actually enhance the radiated sound power from the overall structure. For example, assume the panel response at a given frequency is primarily due to the contribution of two structural modes. If the sound radiated by each mode interferes destructively (ie the mutual radiation resistance between the pair of modes is negative), then suppressing a single mode could result in a small enhancement in the total radiated sound power. However, if the disturbance is largely uncorrelated, as is the case with turbulent boundary layer noise, then the vibration of adjacent bays may also be uncorrelated. In this case, the total radiated sound power could be estimated by summing the sound power radiated from each individual bay (Graham 1996). Therefore, reducing the sound power from one bay would be sufficient to guarantee a global reduction of sound power.

Although not investigated here, a distributed control strategy could potentially improve global performance in exchange for increased controller complexity. In the context of this work, distributed control implies that there is some level of coordination between local control units. For instance, Frampton describes a distributed control architecture based on groups, which are a collection of control units that share information (Frampton 2004). If each node is equipped with a wireless communication link, then the reach of the controller describes the radius over which information is transmitted and received. For instance, if the control system has a reach of two, then the center node receives sensor signals from all units within 2 "hops" (Frampton 2004). Since the group size is fixed, the complexity of each controller is not expected to change as the overall number of control units increases. Therefore, this type of control architecture could be scalable. In this application, the reach could be specified based on the extent over which the vibration of the structure is correlated. If the vibration is correlated over multiple bays, then the reach of the system could be selected accordingly to minimize a global performance metric.

In summary, this chapter describes an iterative decentralized control approach to address broadband disturbance rejection when the uncertainty bounds are poorly characterized or when the uncertainty and disturbance are time-varying. The interaction between subsystems is addressed using a robust state regulator with an estimator designed using adaptive disturbance estimation and loop recovery techniques. The proposed design strategy achieves a compromise between simplicity of design and performance. This approach has been validated experimentally with demonstrated radiated sound power reductions of up to 3.6 dB integrated from 50 to 600 Hz. In addition, more than 10 dB peak reductions of sound power have been measured.

Chapter 7

Summary and conclusions

This chapter begins with a summary of the project followed by the main conclusions of this work. Recall that our goal is to develop a scalable control system to reduce broadband sound transmission through the aft fuselage. Therefore, this work provides a thorough investigation of decentralized control on periodically stiffened structures, which are representative of the sidewall of a commercial aircraft. In an effort to make the study as realistic as possible, the forcing function used in this work is determined from exterior pressure measurements obtained during a 2001 flight test. These measurements are used to estimate the spectral and spatial characteristics of the aft-cabin noise source, as described in Appendix C.

The nature of the excitation suggests that feedforward control may be suitable for this application. As a result, Appendix D presents a study of feedforward control of aft-cabin noise. The analysis shows that it would be difficult to obtain a coherent reference signal that is sufficiently time-advanced. Therefore, the control system would be limited to augmenting the structural damping. Since feedback strategies can achieve the same result without a reference sensor, this project focuses primarily on feedback control strategies.

Numerical simulations demonstrate that the interaction between local control units can destabilize decentralized feedback control systems. Therefore robust, low-authority control (LAC) strategies are studied. In particular, direct velocity feedback (DVF) and positive position feedback (PPF) are both considered. If the transducer pair is matched, then DVF will yield an unconditionally stable system. Therefore, two different transducer configurations are investigated in an effort to obtain a substantially collocated transducer pair. Initially a triangular piezoelectric patch actuator and point sensor pair is investigated. Our analysis suggests that the transducer pair can be improved by using a directional Macro-Fiber Composite (MFC) actuator. However, simulations also indicate that the transducer pair will not be effective for DVF if the boundaries of the structure are flexible.

In contrast, the second transducer configuration that we considered is designed to be used along a flexible boundary. In particular, a large piezoelectric actuator and an array of point sensors is found to target the dominant low-frequency global mode when the transducers are mounted along the stiffener. While DVF is not effective with an isotropic patch actuator, an MFC actuator couples efficiently to the dominant low-frequency mode and has improved stability margins due to the directional characteristics of this transducer. However, performance is limited using DVF since the transducer pair is not truly matched.

Positive position feedback is investigated as an alternative to direct output feedback. While stability is not guaranteed, PPF is simple and relatively robust. Unfortunately, performance is dependent on adequate pole-zero separation, which is not necessarily available in practice. While PPF achieves substantial reductions in the numerical simulations, experiments show that local reductions of only 4 dB are available. This yields an integrated reduction of only 1.5 dB from 50 to 800 Hz.

Due to the limitations associated with low-authority control strategies, an in-depth analysis of decentralized model-based control is performed. Decentralized control of coupled systems is shown to introduce errors in both the plant and disturbance models. Specifically, this work demonstrates that the induced modeling error is the product of the complementary sensitivity function multiplied by a second term which quantifies the diagonal dominance of the plant. To ensure the coupled system is stable, each local controller has to be robust in the frequency bands where the plant is not diagonally dominant and at frequencies where the amplitude of the complementary sensitivity function is large.

Unfortunately, it is difficult to determine whether or not the plant is diagonally dominant without a frequency response description of the entire coupled system. Since this may not be available, it is beneficial to use the local control models to estimate the frequency bands where modeling error is likely to destabilize the control system. This work demonstrates that decentralized LQG control is particularly susceptible to spillover at the zeros of the local control models. Therefore, an obvious and often effective solution is to limit the control authority in the neighborhood of the open-loop zeros. This can be accomplished by shaping the effort weighting term to penalize control effort and subsequently reduce performance in the desired frequency bands. In addition to making the local controller more robust, limiting the control authority also reduces the magnitude of the induced modeling error on neighboring subsystems. However, this approach is not always effective since spillover can also occur near resonances of the control model. In that case, penalizing the control effort will improve robustness at the expense of local performance.

Frequency-shaped loop recovery is also investigated since it can be used to improve robustness without making the controller overly conservative. Essentially, loop recovery is used to modify the state estimator in an attempt to improve robustness and subsequently performance by "recovering" the properties of the state regulator. However, complete loop recovery is only possible if the plant is minimum phase, and even partial recovery is achieved at the expense of measurement noise sensitivity. Since real systems are rarely minimum phase, it is advantageous to exploit loop recovery only in frequency bands where the plant variations are known to limit achievable performance. While frequency-shaped loop recovery can be effective, it is limited to recovering the characteristics of the LQR design. Therefore, the approach is only suitable if the underlying LQR design is robust. As a result, a two-step approach is advocated. First, the effort penalty is shaped to ensure the LQR design is sufficiently robust. This is accomplished by limiting the control authority at the zeros of the local control model. As discussed earlier, this typically improves the robustness of the design without significantly reducing achievable performance. Next, frequency-shaped loop recovery is used in frequency bands where the interaction between controllers limits achievable performance. Unfortunately, it is often difficult to accurately predict the frequency bands where loop recovery is required *a priori*. Therefore, an adaptive frequency-shaped LQG/LTR strategy is proposed. This approach accounts for parameter variations introduced by neighboring control loops, requires no communication between control systems, and is relatively simple. The strategy is implemented by performing the following steps independently on each subsystem:

1. drive the system with white noise and identify the control model
2. design a robust state regulator by penalizing the effort at the zeros of the control model
3. estimate the disturbance model using open-loop measurements (ie spectral fit of the measured response)

4. evaluate the initial design by checking nominal stability margins
5. implement the controller
6. update the effort weighting term based on the closed-loop control effort
7. update the disturbance model based on closed-loop system measurements
8. redesign the LQG controller using the new disturbance model and an updated effort weighting term
9. evaluate the design based on control effort and performance criteria
10. repeat steps 5 - 10 until the system converges

Note that each LQG controller is updated periodically to account for parameter variations introduced by neighboring control loops. In particular, the controller is updated using a new effort weighting term and disturbance model. The disturbance model is calculated based on the disturbance estimate, which is generated using an internal plant model. If the plant model is perfect, then the estimate will track changes in the true disturbance. However, in frequency bands where the plant model is not accurate, the disturbance model is updated to make the design more robust to modeling error. At the same time, the effort weighting term is updated to make the design more or less aggressive based on the control effort and performance criteria.

The iterative LQG/LTR approach is validated using real-time control experiments performed on two bays of a large stiffened aluminum test structure. Experiments demonstrate that the adaptive control system can achieve an 18 dB peak reduction and a 4 dB integrated reduction from 50 to 800 Hz when the disturbance enters through the control inputs and the performance metric corresponds to the sensed variable (summed acceleration). Likewise, a 13 dB reduction of the dominant low frequency peaks and a 3.3 dB integrated reduction of summed acceleration is achieved when the acoustic disturbance is used.

While a reduction of summed acceleration can be beneficial, the real performance metric is radiated sound power. The adaptive control system achieves an 8.7 dB peak reduction and a 2.7 dB integrated reduction in radiated sound power from 50 to 600 Hz using error signals based on summed acceleration. However, if a more accurate estimate of the first radiation mode is available, then overall system performance can be improved. For example, when an estimate of the first radiation mode is calculated using all 15 accelerometers on each bay, the integrated sound power from 50 to 600 Hz is reduced by over 3.6 dB.

Conclusions

The purpose of this work is to lay the foundation for a scalable active structural acoustic control (ASAC) system. While existing control strategies have been used effectively on relatively small systems, significant implementation issues have to be addressed before these control strategies can be extended to large systems such as the fuselage of an aircraft. For instance, most centralized approaches require a high level of connectivity and are computationally intensive, while many decentralized strategies face stability problems caused by the unmodeled interaction between neighboring control units.

Since a scalable solution was desired, this work focused exclusively on decentralized control strategies. Decentralized control can be divided into two categories: high-authority model-based control such as LQG

control; and low-authority approaches such as direct velocity feedback (DVF) and positive position feedback (PPF). The first portion of this work focused on understanding the limitations of each approach. This was accomplished using numerical simulations of a multiple-bay structural-acoustic system.

Since decentralized control implies that each control loop is designed and implemented independently, the cross terms between neighboring control loops are neglected during the design process. Our work shows that neglecting the cross coupling introduces modeling error in both the control and disturbance models. In particular, the modeling error can be expressed as the product of the complementary sensitivity function for the neighboring control loops multiplied by a second term that quantifies the diagonal dominance of the plant. To ensure the coupled system is stable, each local controller has to be robust in the frequency bands where the plant is not diagonally dominant and at frequencies where the amplitude of the complementary sensitivity function is large. This work demonstrated that decentralized LQG control is particularly susceptible to spillover at the zeros of the local control models. Therefore an obvious and often effective solution is to penalize control authority near the zeros of the local control models. However, this approach is not always effective since the destabilizing interaction between neighboring control units can occur in other frequency bands as well. Therefore, frequency-shaped loop transfer recovery is also used. Loop recovery is exploited by artificially increasing the magnitude of the disturbance model. This modifies the estimator design in order to recover the characteristics of the LQR controller. The approach typically improves the robust performance and stability of the control system in exchange for a small reduction in nominal performance. Due to the reduction in nominal performance, it is beneficial to implement the approach only in the frequency bands where modeling error is known to limit closed-loop performance. Therefore, an iterative approach is proposed in which the controller is periodically redesigned based on closed-loop measurements. This approach was validated using real-time control experiments performed on a rib stiffened test structure. The iterative control strategy achieved a 12 dB peak reduction and a 3.6 dB integrated reduction in radiated sound power from the panel.

In summary, we found that:

- The modeling error introduced by neighboring subsystems can be expressed as the product of the complementary sensitivity function multiplied by a second term that quantifies the diagonal dominance of the plant.
- Frequency shaped error weighting and loop transfer recovery can be effective for decentralized LQG control if uncertainty bounds are known *a priori*.
- An iterative frequency-shaped LQG/LTR strategy can be a simple, effective, and scalable solution when uncertainty bounds are not known *a priori*.

Since the interaction between local control units can destabilize model-based control systems, robust low-authority control (LAC) strategies were also studied. In particular, direct velocity feedback (DVF) was considered since it can yield an unconditionally stable system if the transducer pair is matched. Unfortunately, real transducer pairs are never truly matched, and therefore it is necessary to approximate matched transducer pairs. Therefore a triangular piezoelectric patch actuator and point sensor pair was considered initially. Numerical simulations suggested that the phase characteristics of this popular transducer pair can be improved by using anisotropic actuators instead of traditional isotropic actuators. However, simulations

also suggested that the transducer pair is not substantially collocated unless the boundaries of the structure are rigid. Therefore an alternate transducer configuration was investigated. In particular, a large rectangular piezoelectric patch actuator was used in combination with an array point velocity sensors. While this transducer pair is not substantially collocated, it does target the global mode. However, real-time control experiments performed on a built-up aluminum test article demonstrated that low-authority controllers implemented with this transducer pair were unable to achieve significant reductions in radiated sound power. Performance was limited using direct velocity feedback since the transducer pair was not truly matched. Similarly, the lack of sufficient pole-zero separation limited the effectiveness of PPF.

While it was not verified experimentally, numerical simulations suggested that a combined high-authority control/low-authority control (HAC/LAC) architecture can be beneficial for decentralized control. In particular, the low-authority control system can be used to supplement the performance of the HAC strategy and also reduce the interaction between neighboring HAC loops. Therefore the performance of the combined system can be better than the sum of each individual strategy.

As a result of the investigation on low-authority control strategies, we found that:

- The anisotropic characteristics of an MFC actuator can improve the phase response between a triangularly shaped piezoelectric patch actuator and point sensor if the transducer pair is mounted along a rigid boundary.
- A triangular piezoelectric patch actuator mounted along a flexible boundary is not substantially collocated with a point sensor. This implies that the transducer pair may not be appropriate for DVF on the sidewall of an aircraft since the boundaries of each bay are not truly rigid.
- A large rectangular MFC actuator can be used along with an array of point sensors to target low-frequency global modes.
- The lack of sufficient pole-zero separation limits the effectiveness of PPF in practice.
- A combined HAC/LAC architecture can be beneficial for decentralized control. By augmenting the in-bandwidth damping, the LAC system can be used to supplement the performance of the HAC strategy and also reduce the interaction between neighboring HAC loops.

While the work presented here accomplishes our original goal of establishing the foundation for a scalable ASAC system, much more work is necessary to realize a practical ASAC system for commercial jets. For instance, a truly practical and scalable control system can not be developed without addressing important concerns about the size and weight of the power and control electronics. While, it was beyond the scope of the current project to investigate these issues, they are critical to the success of future control systems.

Future work

Since an aircraft fuselage can contain hundreds of bays, the control strategy should require little user interaction on the subsystem level. Automating the design process would therefore improve the scalability of the system. One way to accomplish this is by using a direct adaptive approach. However, as we have

previously discussed, modeling error can introduce residual feedback around the adaptive loop and limit the performance of direct adaptive strategies. Therefore, future work should focus on automating the iterative approach.

Changing flight conditions are likely to cause thermal variations as well as changes in cabin pressure. These changes can have a significant impact on the dynamics of the structure. Therefore, it may be advantageous to incorporate an intermittent system identification strategy to account for large plant variations, while the iterative strategy could be used to account for small plant variations.

Note that while decentralized control offers a number of advantages with respect to scalability, minimizing a local performance metric does not guarantee global performance. For instance, if the vibration of adjacent bays is correlated, then reducing the sound power radiated from a single bay may actually enhance the radiated sound power from the overall structure. For example, assume the panel response at a given frequency is primarily due to the contribution of two structural modes. If the sound radiated by each mode interferes destructively (ie the mutual radiation resistance between the pair of modes is negative), then suppressing a single mode could increase the total radiated sound power. Since aft-cabin noise is correlated over the span of multiple bays, it could be advantageous to implement a hierarchical control strategy with a reach that extends over multiple bays. In particular, the reach of the control system could be determined based on the extent to which the vibration of the structure is correlated. This would likely depend on both the spatial characteristics of the disturbance as well as the structural coupling between bays. Note that in addition to minimizing global metrics, a hierarchical control system may also improve low-frequency control authority.

Appendix A

Piezoelectric coupling

This section presents the equations of motion for a mechanical structure with embedded piezoelectric transducers. Since the formulation presented here is largely consistent with the work of Hagood et al. (1990) and Clark et al. (1998), many of the intermediate steps are excluded for the sake of brevity. The interested reader is referred to the references for a more thorough discussion of this topic. Since conventional piezoceramic actuators as well as actuators with interdigitated electrodes are used in this project, as shown in Figure A.1, the derivation includes the details required to model each type of transducer.

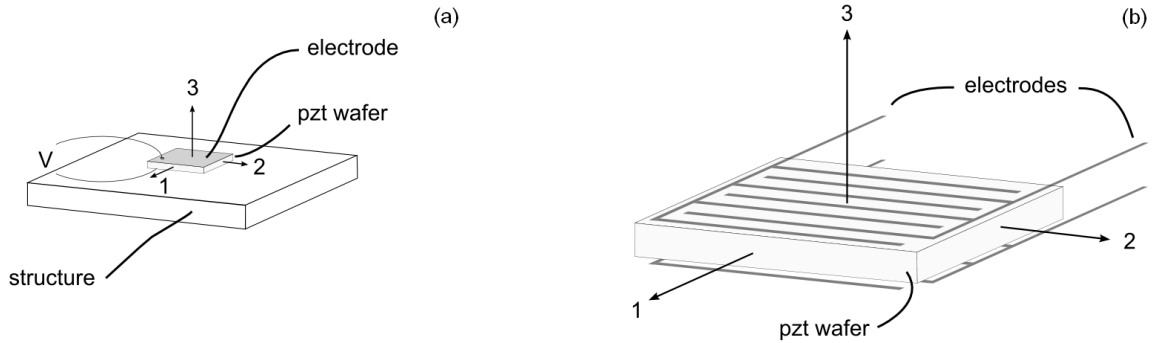


Figure A.1: The diagrams show: (a) a conventional piezoceramic wafer; and (b) an interdigitated electrode pattern.

As presented in Hagood et al. (1990), a generalized form of Hamilton's principle can be used to derive the coupled electromechanical equations of motion:

$$[M_s + M_p] \ddot{\eta} + C_s \dot{\eta} + [K_s + K_p] \eta = B_f f + \Theta v \quad (\text{A.0.1})$$

where η is a vector of generalized displacements, M_s is the structural mass matrix, M_p is the piezoceramic mass matrix, C_s is the structural damping matrix, K_s is the structural stiffness matrix, K_p is the piezoceramic stiffness matrix, B_f is the forcing matrix, Θ is the electromechanical coupling matrix, f is a vector of structural forces, and v is a vector of applied voltages (Clark et al. 1998; Viperman and Clark 1999).

While the structural mass and stiffness matrices are determined directly from the FE model described in Chapter 2, the structural damping matrix is defined separately using a modal damping ratio of 0.01. Meanwhile, the piezoelectric mass, stiffness, and electromechanical coupling matrices as well as the forcing matrix are calculated numerically using the eigenfunctions, Φ_r , obtained from the normal modes analysis.

In particular, the piezoelectric mass matrix is defined as,

$$M_p = \int_{\chi} \Phi_r^T S_p(\chi) \rho_p \Phi_r d\chi \quad (\text{A.0.2})$$

where χ is the domain of the structure, Φ_r are the eigenfunctions of the structure with no added mass or stiffness, S_p is the spatial aperture of the transducer, and ρ_p is the density of the piezoelectric material.

Similarly, the piezoelectric stiffness matrix is defined as

$$K_p = \int_{\chi} (L_u \Phi_r)^T S_p(\chi) c^E (L_u \Phi_r) d\chi \quad (\text{A.0.3})$$

where $L_u^T = [-z \frac{\partial^2}{\partial x^2} \quad -z \frac{\partial^2}{\partial y^2} \quad -2z \frac{\partial^2}{\partial x \partial y}]$ is the elastic differential operator, and c^E is the short circuit stiffness matrix. The short circuit stiffness matrix relates the stress and strain in the material

$$\begin{bmatrix} \sigma_1 \\ \sigma_2 \\ \sigma_3 \\ \tau_{12} \\ \tau_{23} \\ \tau_{31} \end{bmatrix} = c^E \begin{bmatrix} \epsilon_1 \\ \epsilon_2 \\ \epsilon_3 \\ \gamma_{12} \\ \gamma_{23} \\ \gamma_{31} \end{bmatrix} \quad (\text{A.0.4})$$

where the standard direction notation is defined as shown in Figure A.2 (a). For the case of a surface mounted patch, the transverse stresses, σ_3 , τ_{23} , and τ_{31} , are assumed to be small relative to the in-plane stresses. Therefore Equation A.0.4 can be expressed as (Leissa 1969)

$$\begin{bmatrix} \sigma_1 \\ \sigma_2 \\ \tau_{12} \end{bmatrix} = c^E \begin{bmatrix} \epsilon_1 \\ \epsilon_2 \\ \gamma_{12} \end{bmatrix} \quad (\text{A.0.5})$$

where

$$c^E = \begin{bmatrix} \frac{Y_1}{1 - \nu_{12}\nu_{21}} & \frac{\nu_{12}Y_2}{1 - \nu_{12}\nu_{21}} & 0 \\ \frac{\nu_{21}Y_1}{1 - \nu_{12}\nu_{21}} & \frac{Y_2}{1 - \nu_{12}\nu_{21}} & 0 \\ 0 & 0 & G_{12} \end{bmatrix}. \quad (\text{A.0.6})$$

For a monolithic actuator $Y = Y_1 = Y_2$, $\nu = \nu_{12} = \nu_{21}$, and $G = \frac{Y}{2(1+\nu)}$. Therefore c^E simplifies to,

$$c^E = \begin{bmatrix} \frac{Y}{1-\nu^2} & \frac{Y\nu}{1-\nu^2} & 0 \\ \frac{Y\nu}{1-\nu^2} & \frac{Y}{1-\nu^2} & 0 \\ 0 & 0 & \frac{Y}{2(1+\nu)} \end{bmatrix}. \quad (\text{A.0.7})$$

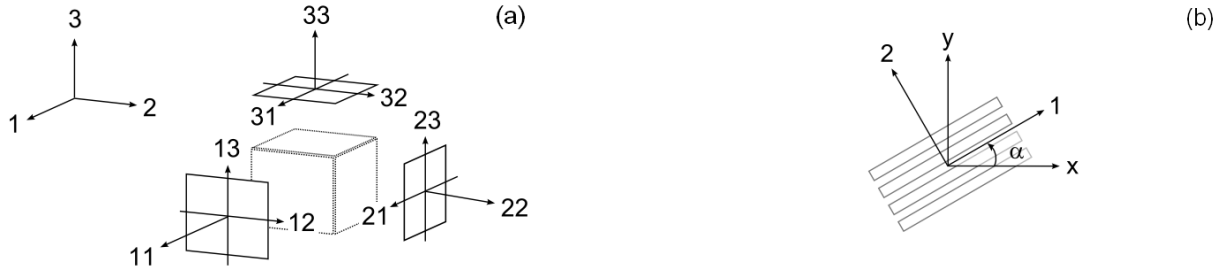


Figure A.2: The diagrams show: (a) the direction convention; and (b) the material and global coordinate systems.

For off-axis configurations where the material axes do not align with the global axes, as shown in Figure A.2 (b), transformation equations can be used to find the on-axis material properties (Tsai and Hahn 1980). For instance, the stress in the material coordinate system is defined as

$$\begin{bmatrix} \sigma_1 \\ \sigma_2 \\ \tau_{12} \end{bmatrix} = [T] \begin{bmatrix} \sigma_x \\ \sigma_y \\ \tau_{xy} \end{bmatrix} \quad (\text{A.0.8})$$

where the stress transformation matrix, T is

$$[T] = \begin{bmatrix} \cos^2 \alpha & \sin^2 \alpha & 2 \cos \alpha \sin \alpha \\ \sin^2 \alpha & \cos^2 \alpha & -2 \cos \alpha \sin \alpha \\ -\cos \alpha \sin \alpha & \cos \alpha \sin \alpha & \cos^2 \alpha - \sin^2 \alpha \end{bmatrix}. \quad (\text{A.0.9})$$

Similarly, the strain in the material coordinate system is defined as

$$\begin{bmatrix} \varepsilon_1 \\ \varepsilon_2 \\ \gamma_{12} \end{bmatrix} = (T^{-1})^T \begin{bmatrix} \varepsilon_x \\ \varepsilon_y \\ \gamma_{xy} \end{bmatrix} \quad (\text{A.0.10})$$

where $(T^{-1})^T$ is the strain transformation matrix. It follows that

$$\begin{bmatrix} \sigma_x \\ \sigma_y \\ \tau_{xy} \end{bmatrix} = T^{-1} c^E (T^{-1})^T \begin{bmatrix} \epsilon_x \\ \epsilon_y \\ \gamma_{xy} \end{bmatrix} \quad (\text{A.0.11})$$

where $T^{-1} c^E (T^{-1})^T$ is the transformed stiffness matrix.

Next, the electromechanical coupling matrix is defined as

$$\Theta = \int_{\chi} (L_u \Phi_r)^T S_p(\chi) e^T (L_\phi \Phi_v) d\chi \quad (\text{A.0.12})$$

where $e = dc^E$ is the matrix of piezoelectric material constants, d is the matrix of strain constants, $L_\phi^T = \left[-\frac{\partial}{\partial x} \quad -\frac{\partial}{\partial y} \quad -\frac{\partial}{\partial z} \right]$ is the electrical differential operator, and Φ_v is the assumed potential distribution. Recall that the strain constant, d , relates the applied electric field to the free strain in the material. For a traditional monolithic actuator,

$$d = \begin{bmatrix} 0 & 0 & 0 \\ 0 & 0 & 0 \\ d_{31} & d_{32} & 0 \end{bmatrix} \quad (\text{A.0.13})$$

and for an anisotropic actuator such as the one shown in Figure A.1 (b),

$$d = \begin{bmatrix} d_{11} & d_{12} & 0 \\ 0 & 0 & 0 \\ 0 & 0 & 0 \end{bmatrix}. \quad (\text{A.0.14})$$

If the material axes do not align with the global axes, then the strain transformation matrix can be used to express the strain constants in global coordinates (Bevan 2000)

$$[d]_{1,2,3} = (T^{-1})^T [d]_{x,y,z} \quad (\text{A.0.15})$$

and therefore

$$[d]_{x,y,z} = T^T [d]_{1,2,3}. \quad (\text{A.0.16})$$

At this point it is beneficial to discuss the significance of e . This matrix of piezoelectric material constants relates the voltage applied in the i^{th} direction to the stress applied in the j^{th} direction. Using values for the MFC actuator, given in Table 2.2,

$$e = dc^E = \begin{bmatrix} 11.9 & -0.77 & 0 \\ 0 & 0 & 0 \\ 0 & 0 & 0 \end{bmatrix}. \quad (\text{A.0.17})$$

Therefore, a positive voltage applied in the 1-direction induces a tensile stress in the 1-direction that is 15 times larger than the compressive stress induced in the 2-direction. In comparison, a positive voltage applied to a traditional piezoceramic actuator in the 3-direction induces equal compressive stresses in both the 1- and 2-directions. Therefore, the preferred actuation direction is an extra design parameter that can be used when designing systems with anisotropic actuators. The advantages offered by directional actuation are discussed in Chapter 5 with regards to improving the collocation characteristics of transducer pairs.

The assumed potential distribution depends on the electrode configuration, as shown in Figure A.3 (a) and (b). For an isotropic actuator, a linear varying voltage profile through the thickness is typically assumed:

$$\Phi_v = \frac{z - h_s/2}{h_p} \quad \text{for} \quad \frac{h_s}{2} < z < \frac{h_s}{2} + h_p \quad (\text{A.0.18})$$

where h_s is the thickness of the structure, and h_p is the thickness of the actuator. The voltage profile in an anisotropic actuator is more complicated, as shown in Figure A.3 (b), with alternating positive and negative gradients along the length of the fiber (1-direction). However, since these actuators are poled in situ, the poling direction also alternates in conjunction with the electric field. Therefore, an equivalent representation of the electric field in an MFC is shown in Figure A.4. Thus, a linear voltage profile along the length of the actuator is assumed for the MFC,

$$\Phi_v = \frac{Nx}{L_1} \quad \text{for} \quad 0 < x < L_1 \quad (\text{A.0.19})$$

where N is the number of interdigitated electrodes, and L_1 is the length of the actuator in the 1-direction.



Figure A.3: The figures show the electric fields in: (a) a conventional piezoceramic wafer; (b) an MFC actuator [adapted from Bevan (2000)].

Finally, the forcing matrix, B_f , is defined as

$$B_f = [\Phi_r^T(\mathbf{x}_{f_1}) \quad \dots \quad \Phi_r^T(\mathbf{x}_{f_n})] \quad (\text{A.0.20})$$

where \mathbf{x}_f are the coordinates of each point force input.

To make the model more amenable to control design, the system can be rewritten in state-variable form as,

$$\begin{aligned} \dot{\mathbf{x}} &= A\mathbf{x} + B\mathbf{u} \\ \mathbf{y} &= C\mathbf{x} + D\mathbf{u} \end{aligned} \quad (\text{A.0.21})$$

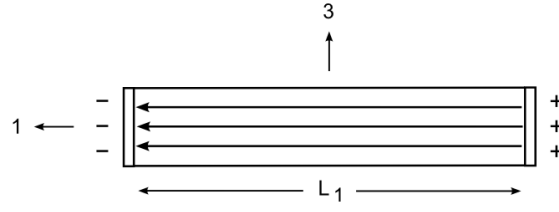


Figure A.4: Equivalent MFC configuration.

where

$$x(t) = \begin{bmatrix} \eta(t) \\ \dot{\eta}(t) \end{bmatrix}, \quad u(t) = \begin{bmatrix} f \\ v \end{bmatrix}, \quad (\text{A.0.22})$$

$$A = \begin{bmatrix} 0 & I \\ -M^{-1}K & -M^{-1}C_s \end{bmatrix}, \quad B = \begin{bmatrix} 0 & 0 \\ M^{-1}B_f & M^{-1}\Theta \end{bmatrix}, \quad (\text{A.0.23})$$

$$C = [0 \quad \Phi_r], \quad D = [0 \quad 0], \quad (\text{A.0.24})$$

and

$$M = M_s + M_p, \quad K = K_s + K_p. \quad (\text{A.0.25})$$

Note that the C matrix is defined such that the output of this system is velocity.

Appendix B

Disturbance rejection

Active vibration and acoustic control is often discussed in terms of the simple disturbance rejection system shown in Figure B.1. As the name implies, the controller is designed to reject the disturbance $d(t)$ at the physical output $y(t)$. In this example, the sensor noise is shown as $v(t)$ and $u(t)$ denotes the control input. The plant transfer function is labeled as $G(s)$ and the feedback controller is $C(s)$. For simplicity, we assume the system only has a single input and output.

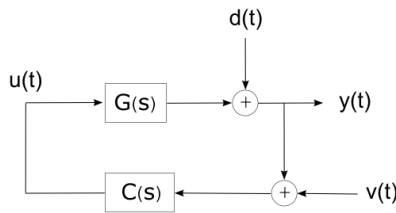


Figure B.1: Disturbance rejection.

The closed-loop transfer function (CLTF) from the disturbance to the plant output is

$$\frac{Y(s)}{D(s)} = S(s) = \frac{1}{1 - G(s)C(s)} \quad (\text{B.0.1})$$

which is referred to as the sensitivity function. Similarly, the CLTF from the sensor noise to the measured output is

$$\frac{Y(s)}{V(s)} = -T(s) = \frac{G(s)C(s)}{1 - G(s)C(s)} \quad (\text{B.0.2})$$

where $T(s)$ is the complementary sensitivity function since $S(s) + T(s) = 1$. To achieve disturbance rejection, it is desirable to design $C(s)$ such that $S(s)$ is small. However, since $T(s)$ affects the robust characteristics of the design and $S(s) + T(s) = 1$, feedback control involves a trade-off between performance and robustness.

B.1 Stability

The stability of the feedback system can be determined by the location of the poles of the CLTF. Notice that the poles of both transfer functions $S(s)$ and $T(s)$ are given by the roots of the characteristic equation

$$1 - G(s)C(s) = 0 \quad (\text{B.1.1})$$

where $1 - G(s)C(s)$ is commonly referred to as the return difference. The closed-loop system is stable if both $G(s)$ and $C(s)$ are stable, and the poles of the CLTF are in the open left half s-plane (Franklin et al. 1998).

Instead of explicitly calculating a pole/zero model of the plant, a frequency-response approach is often used to determine closed-loop stability. In particular, stability can be inferred from the Nyquist stability criterion, which is based on the polar plot of the open loop frequency response, $G(s)C(s)$. If the plant and controller are both stable, then the Nyquist stability definition states that the closed loop system will be stable if and only if the polar plot of the open-loop frequency response does not encircle the $(-1, 0)$ point as ω varies from $-\infty$ to ∞ (Elliott 2001). In addition to determining absolute stability, the Nyquist plot can also be used to determine the relative degree of stability, which is typically expressed in terms of the gain and phase margins. The gain margin defines the amount of additional gain that the system can tolerate before the system becomes unstable. Similarly, the phase margin defines the phase shift, which can be tolerated without making the closed-loop system unstable. These concepts are demonstrated in Figure B.2 (a). In this case, the gain margin is defined as $GM = 20 \log(1/g_c)$ and the phase margin is labeled as PM .



Figure B.2: The figures show: (a) a simple Nyquist diagram illustrating the concepts of gain and phase margins; and (b) an example demonstrating the relationship between multiplicative uncertainty and the required stability margins.

B.2 Unstructured uncertainty

The linear time-invariant models used throughout this work can only approximate the dynamics of the actual plant. Sources of modeling error include plant nonlinearities, poor system identification, model truncation, and time-varying systems (Morari and Zafriou 1998). To ensure robust stability and performance, an estimate of the modeling error, or uncertainty, is often necessary. When the structure of the error is unknown, unstructured additive or multiplicative uncertainty models are often used. For example, Figure B.3 shows

the actual plant G , along with examples of additive and multiplicative uncertainty. If the error is additive, then the actual plant G and nominal plant model \hat{G} are related by

$$G = \hat{G} + \Delta_A \quad (\text{B.2.1})$$

where Δ_A is the additive uncertainty term. However, a more common approach is to simply lump all plant uncertainty into a single multiplicative uncertainty term Δ_M . In this case,

$$G = \hat{G} (I + \Delta_M). \quad (\text{B.2.2})$$

Notice that the additive and multiplicative uncertainty terms are related to each other by

$$\Delta_M = \hat{G}^{-1} \Delta_A. \quad (\text{B.2.3})$$

In order to relate the concepts of multiplicative uncertainty with the stability margins, consider a simple example in which Δ_M is assumed to be bounded by B . From the geometric constraints illustrated in Figure B.2 (b), one can show that the gain margin must satisfy the inequality,

$$GM > 20 \log(1 + B) \quad (\text{B.2.4})$$

to ensure robust stability. Similarly, the phase margin must satisfy

$$PM > \tan^{-1} \left(\frac{B\sqrt{4 - B^2}}{B^2 - 2} \right). \quad (\text{B.2.5})$$

Therefore, if Δ_M is bounded by 0.5, then the gain margin must be at least 3.5 dB and the phase margin should be greater than 29° (Elliott 2001, pg. 283).

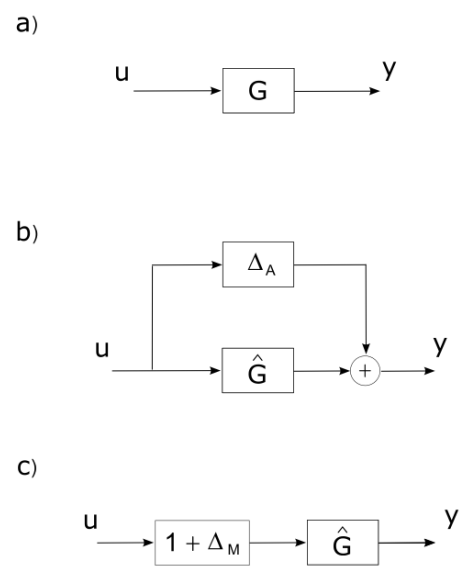


Figure B.3: The figure shows: a) the actual plant; b) the plant model with additive uncertainty; and c) the plant model with multiplicative uncertainty [adapted from Bitmead et al. (1990)].

Appendix C

Disturbance model

The spatial and spectral characteristics of the excitation necessarily affect the vibro-acoustic response of the structure. For instance, Maury et al. (2002) showed that diffuse excitations couple to a structure differently than TBL noise. As a result, noise control techniques that work effectively in a diffuse field, may not provide the same level of attenuation in more realistic noise environments. Therefore, it is important to evaluate control strategies using appropriate disturbance models. Since the control strategies investigated in this project are designed for the aft-cabin, this section describes the exterior aft-cabin noise source. Note that aft-cabin noise is dominated by TBL and shock-cell noise. While many empirical models have been developed to describe the random pressure field beneath a fully developed TBL (Graham 1997), relatively few descriptions of the pressure field generated by shock-cell noise are available. Therefore, the purpose of this section is to describe the characteristics of shock-cell noise using exterior pressure measurements acquired on the aft section of a Boeing 777-200. Note that the purpose of this section is not to provide new models for either type of disturbance, nor provide an in-depth analysis of the flight test data. Instead, the data is simply used to estimate the spectral characteristics of the disturbance and extract empirical constants used to describe shock-cell noise.

Note that shock-cell noise occurs when the supersonic exhaust flow from the jet engine generates shocks that form in a regular pattern in the exhaust plume. The interaction between these shocks and the convecting turbulence structures in the mixing layer generates broadband shock-associated noise (Tam 1991), as depicted in Figure C.1. One of the first investigations of shock-associated noise was performed in 1974 by Harper-Bourne and Fisher. Most subsequent investigations have either focused on developing a better physical understanding of the disturbance (Tam 1995; Lele 2005), or have focused on disrupting the noise source by modifying the exhaust nozzle (Kinzie et al. 2004; Mabe et al. 2005; Turner et al. 2006).

Since both TBL and shock-cell noise contribute to the aft cabin pressure field at cruise, it is beneficial to focus on the flight idle and maximum climb operating conditions. While the airspeed is approximately equal at both flight conditions, the core and fan exhaust flows are subsonic at flight idle and supersonic at maximum climb. Therefore, the pressure field at flight idle is assumed to be dominated by boundary layer noise, while the pressure field at maximum climb is due to both boundary layer and shock-cell noise. Before discussing each flight condition in more detail, note that the locations of the thirty pressure transducers used in this analysis are shown in Figure C.2.

C.1 Flight idle: Turbulent boundary layer noise

This section considers the flight idle operating condition, and focuses exclusively on boundary layer noise. One of the most popular boundary layer noise models was proposed by Corcos (1963). The Corcos model is

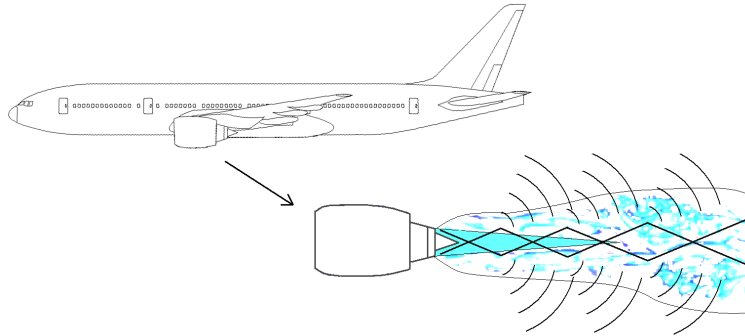


Figure C.1: Shock-cell noise is generated when shocks in the exhaust plume interact with turbulence structures in the mixing layer.

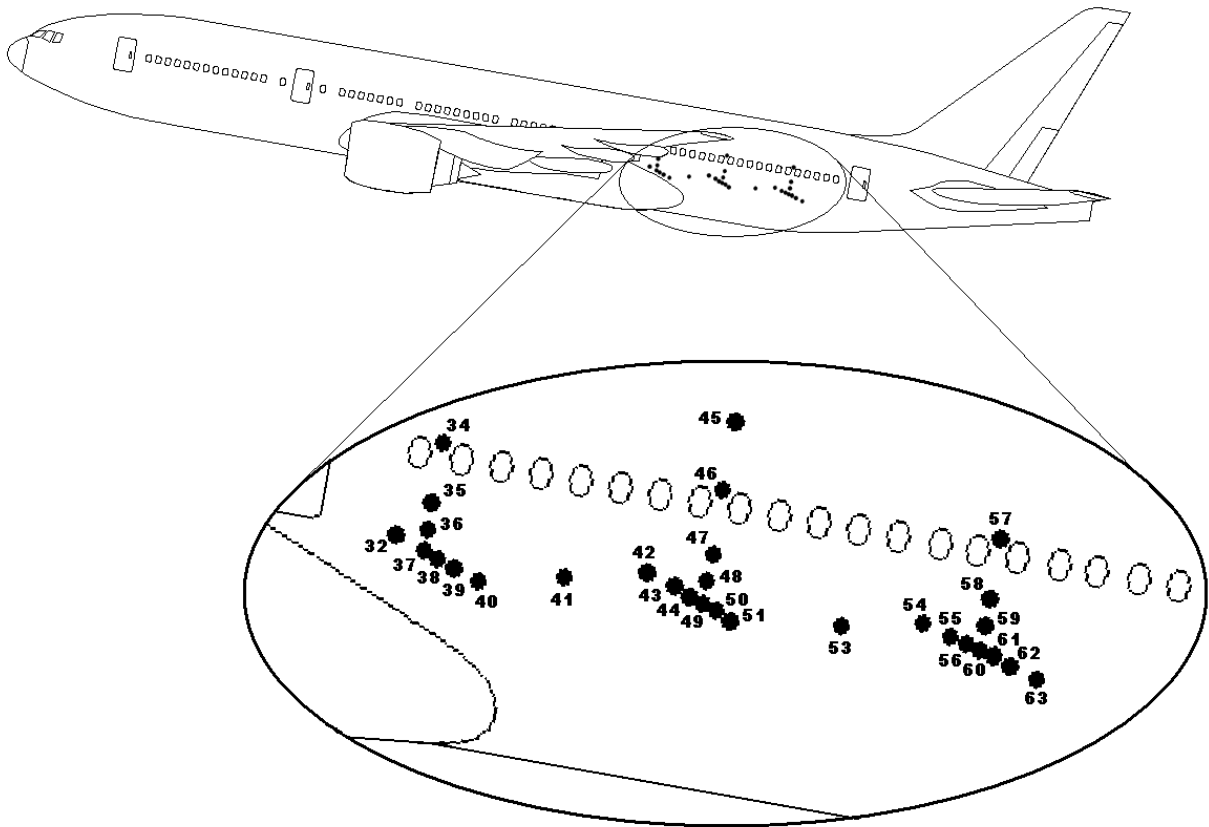


Figure C.2: Boeing QTD1 flight test.

a statistical representation based on experiments and is often used due to its simplicity. This model describes the cross-spectral density of a TBL excitation as

$$S_{AB}(r_x, r_y, \omega) = S_{pp}(\omega) e^{-\frac{|r_x|}{L_x}} e^{-\frac{|r_y|}{L_y}} e^{-\frac{j\omega r_x}{U_c}} \quad (\text{C.1.1})$$

where $S_{pp}(\omega)$ is the point power spectral density, r_x and r_y are the separation distances in the streamwise and spanwise directions respectively, ω is the angular frequency, and U_c is the convection velocity. The correlation lengths are defined as

$$\begin{aligned} L_x &= \frac{\alpha_x U_c}{\omega} \\ L_y &= \frac{\alpha_y U_c}{\omega} \end{aligned} \quad (\text{C.1.2})$$

where α_x and α_y are empirical constants. The correlation lengths are different in the spanwise and streamwise directions, and are also inversely proportional to frequency. Notice that the cross-spectral density of the pressure field is described in terms of the point power-spectral density, the spatial coherence in the x and y directions, and an $e^{-\frac{j\omega r_x}{U_c}}$ term that accounts for the time lag between points in the streamwise direction. The power-spectral density is not a function of position since TBL noise is typically assumed to be homogeneous in space. While boundary layer noise is spatially correlated, the correlation lengths are relatively small. As a result, the disturbance is essentially uncorrelated over the span of a typical aircraft panel (Graham 1996).

An analysis of the measured data at flight idle supports the assumption that the pressure field is dominated by boundary layer noise. In particular, the power-spectral densities at each measurement location are relatively uniform, indicating a homogenous pressure field. Additionally, the spatial coherence indicates that the pressure field is essentially uncorrelated between pressure transducers. Note that the empirical constants for TBL noise could not be determined from the flight test data, and are therefore assumed to equal: $\alpha_x = 8$ and $\alpha_y = 1.2$, which are consistent with the investigation performed by Elliott et al. (2005).

C.2 Maximum climb: Shock-cell and TBL noise

At maximum climb conditions the engine exhaust is supersonic, and therefore both shock-cell and TBL noise are expected to contribute to the measured pressure field. For this analysis, the cross-spectral density of shock-cell noise is assumed to be of the form (Montgomery 2004)

$$S_{AB}(r_x, r_y, \omega) = S_{pp}(\omega) e^{-\sqrt{\left(\frac{|r_x|}{L_x}\right)^2 + \left(\frac{|r_y|}{L_y}\right)^2}} e^{-j\omega \sqrt{\left(\frac{r_x}{U_x}\right)^2 + \left(\frac{r_y}{U_y}\right)^2}} \quad (\text{C.2.1})$$

where $L_x = \beta_x/\omega$, $L_y = \beta_y/\omega$, U_x is the phase velocity in the streamwise direction, U_y is the phase velocity in the spanwise direction, and β_x and β_y are empirical constants. While this formulation is similar to the traditional Corcos model, the more general non-separable form for the spatial coherence term is used, and the phase relationship has been modified to incorporate time delay in both the spanwise and streamwise directions.

At this point, consider Figure C.3, which shows the streamwise variation of the power spectral density during maximum climb. While the low frequency noise is relatively uniform in space, the spectral peak around 500 Hz is much more pronounced in the vicinity of pressure transducer 53. Figure C.4 shows the

power spectral density at position 53 for both the flight idle and maximum climb conditions. Since the airspeed at both flight conditions is approximately equal, the contribution due to TBL noise should also be approximately the same. Therefore, the power spectrum for shock-cell noise is estimated by subtracting the flight idle spectrum, dominated by TBL noise, from the combined excitation measured at maximum climb conditions. The three spectra are compared in Figure C.4.

Next, consider the coherence between pressure transducers 49 and 53, as shown in Figure C.5. Despite the fact that these two pressure transducers are separated by more than 2 m, the coherence around 500 Hz is still relatively high. Since TBL noise is essentially uncorrelated at 2 m, this finding supports the assumption that the broad spectral peak at 500 Hz is due to shock-cell noise.

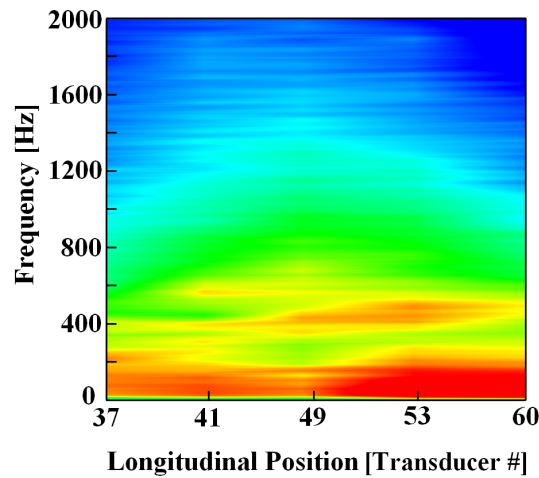


Figure C.3: Streamwise variation of the power spectral density during maximum climb.

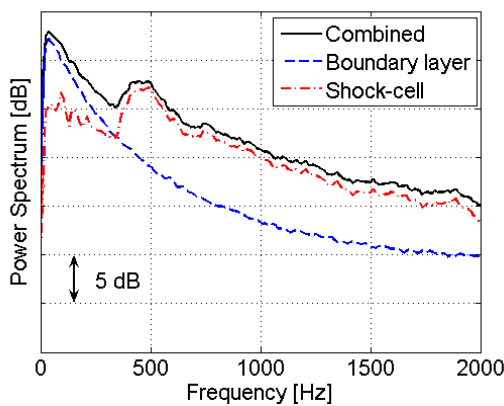


Figure C.4: Estimate of the power spectrum for shock-cell noise (at transducer 53).

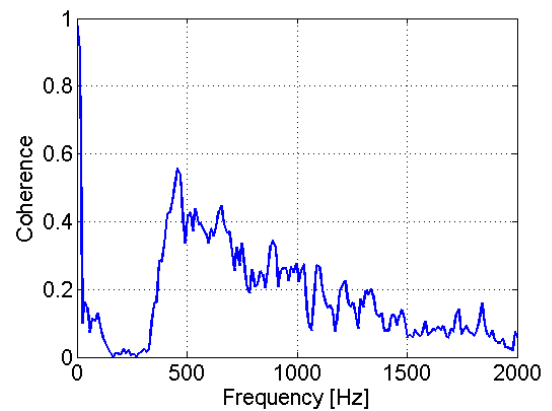


Figure C.5: Magnitude squared coherence between pressure transducers 49 and 53 during maximum climb.

Next, the phase velocities are approximated in the spanwise U_y and streamwise U_x directions. This is performed using the cross-correlation function. The cross-correlation is a measure of how much two signals

resemble each other as a function of lag time. A peak in the cross-correlation signal indicates that a common feature is measured by both pressure transducers at that lag time. For example, Figure C.6 shows the cross-correlation function for three pairs of pressure transducers. Notice that all three signals peak around 0.7 ms, while the cross-correlation function for transducers 42 and 48 also peaks around 3.7 ms. Pressure transducers 42 and 48 are separated by 0.76 m and are aligned in the streamwise direction. The peak at 3.7 ms corresponds to a phase speed of 205 m/s and is probably caused by vortices convected along the fuselage in the flow direction. Since the free-stream velocity at both flight conditions is approximately 250 m/s, a convection velocity of 205 m/s is reasonable. In contrast, the dominant peak at 0.7 ms is found in all of the pressure transducer pairs, not just the ones aligned in the flow direction. This peak in the correlation function is attributed to a relatively localized acoustic source aft of the jet engine, presumably the shock-cell noise source. The time delay associated with this peak is determined for a number of transducer pairs, and is summarized in Table C.1. An estimate of the phase velocity in the spanwise U_y and streamwise U_x directions is then calculated based on the separation distance between the transducers and the corresponding time delay. In particular, phase velocities of $U_x = 1000$ m/s and $U_y = 2000$ m/s are found to match the data reasonably well.

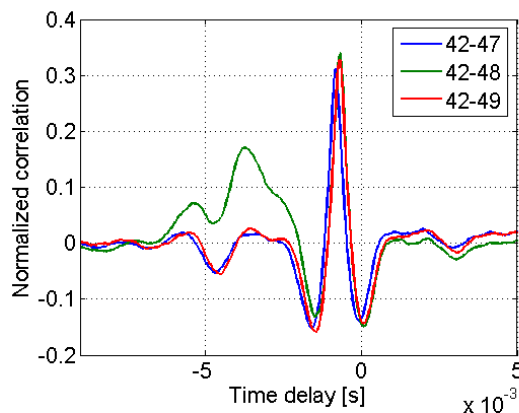


Figure C.6: Spatial correlation during maximum climb.

Table C.1: Time delay relative to pressure transducer 41

Transducer #	41	42	43	44	45	46	47	48	49	50	51
Time delay [ms]	0.0	0.8	1.1	1.3	4.6	2.6	1.7	1.5	1.5	1.8	2.0
Transducer #	53	54	55	56	57	58	59	60	61	62	63
Time delay [ms]	3.6	4.9	5.4	5.6	5.8	6.0	5.9	5.9	6.2	6.4	7.0

Finally, the empirical constants, β_x and β_y , are determined by performing a nonlinear least squares regression using the MATLAB function `nlinfit.m`. Fitting the data from all aft-cabin pressure transducers over the frequency range from 400-1000 Hz yields $\beta_x = 13200$ and $\beta_y = 12250$. Figure C.7 compares the measured and fit spatial coherence at 609 Hz. The measured coherence is shown with discrete filled circles, while the modeled coherence is the continuous background. Notice that unlike TBL noise, shock-cell noise is correlated over a large portion of the aft fuselage.

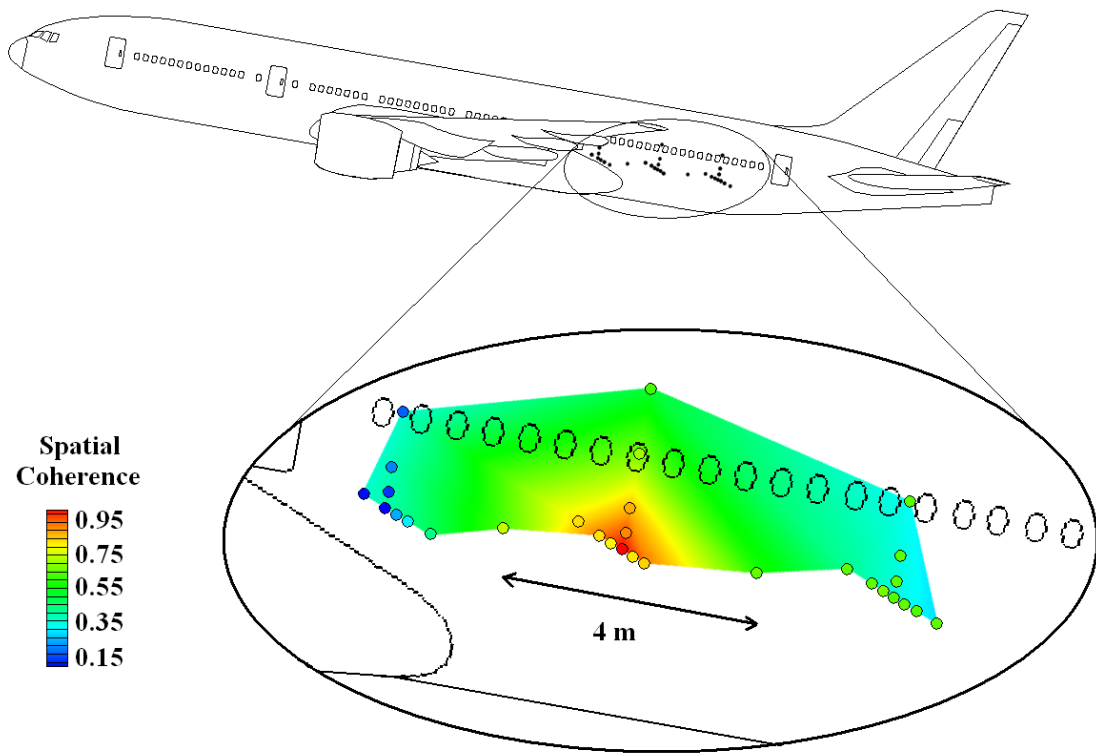


Figure C.7: Measured and fit spatial coherence at 609 Hz during maximum climb (relative to transducer 49).

Note that this work indicates that it may be possible to obtain a coherent and time-advanced reference signal using exterior pressure transducers. For example, the time delay between pressure transducers 49 and 53 is 2.1 ms. If the propagation time through the control path is less than 2.1 ms, then pressure transducer 49 could be used as a time-advanced reference for a control system located near transducer 53. The coherence between these transducers, shown in Figure C.5, is dependent on their spatial separation. Therefore, selecting a suitable reference sensor will involve a tradeoff between coherence and time delay.

Appendix D

Feedforward control

Feedforward control can be used to control sound and vibration when a coherent reference signal is available. Typically the reference is also assumed to be uncontrollable, which means that it is unaffected by the control inputs. For example, a signal obtained from an engine tachometer can be used to control interior noise at the blade passage frequency since the tachometer signal is coherent with interior noise and the signal is not affected by control inputs such as interior loudspeakers. While harmonic disturbances, such as propeller-induced noise, are relatively easy to control due to the deterministic nature of the signal, broadband control requires a time advanced reference signal for best performance (Burdisso et al. 1993).

The purpose of this section is to investigate the feasibility of using feedforward control to suppress aft-cabin noise. While boundary layer noise is largely uncorrelated over the dimensions of a typical panel, shock-cell noise is spatially correlated, as described in Appendix C. In addition, since the noise is generated from a relatively localized source aft of the jet engine, the disturbance propagates along the fuselage. Therefore, it may be feasible to use an exterior pressure transducer to provide a coherent and time-advanced reference signal. While feedback control strategies for broadband noise are limited to damping the structure, feedforward control can, in theory, completely cancel random signals if the filter is sufficiently long and enough time-advanced information is available.

This chapter begins with background information on feedforward control, including a description of the optimal FIR filter and the LMS algorithm. Next, the filtered-reference LMS (FX-LMS) algorithm is discussed. Simulations are then used to estimate the performance of a decentralized feedforward control system using the two-bay numerical model described in Chapter 2. Finally, experimental results are presented.

D.1 Background

Note that all of the background information presented in this section is available in other texts, including an excellent reference by Elliott (2001), and therefore many details are not repeated here. Begin by considering Figure D.1, which shows the schematic of a simple FIR filtering problem known as the electrical noise cancelation problem. In the figure, $x(n)$ denotes the reference signal, z^{-1} is the unit delay operator, w_i are the filter coefficients, N is the filter order, $y(n)$ is the output of the filter, $d(n)$ is the desired signal, and $e(n)$ is the error signal. For an FIR filter, the output, $y(n)$, is related to the input by

$$y(n) = w_0x(n) + w_1x(n-1) + \dots + w_{N-1}x(n-N+1) \quad (\text{D.1.1})$$

$$= \mathbf{w}^T \mathbf{x}(n) \quad (\text{D.1.2})$$

$$= \mathbf{x}^T(n) \mathbf{w} \quad (\text{D.1.3})$$

where

$$\mathbf{w} = [w_0 \ w_1 \ \cdots \ w_{N-1}]^T \quad (\text{D.1.4})$$

$$\mathbf{x}(n) = [x(n) \ x(n-1) \ \cdots \ x(n-N+1)]^T \quad (\text{D.1.5})$$

The error signal, $e(n)$, is defined as

$$e(n) = d(n) - y(n) \quad (\text{D.1.6})$$

$$= d(n) - \mathbf{w}^T \mathbf{x}(n) \quad (\text{D.1.7})$$

$$= d(n) - \mathbf{x}^T(n) \mathbf{w} \quad (\text{D.1.8})$$

where $d(n)$ is the desired response, and $y(n)$ is the output of the filter.

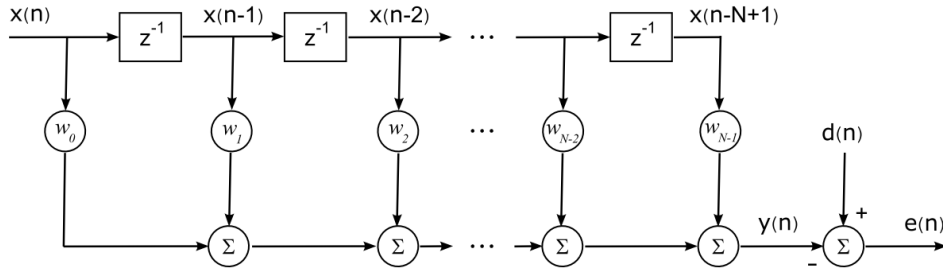


Figure D.1: General FIR filtering problem.

For this discussion, the sampled-data time series are assumed to be real-valued, which is consistent with most vibration control applications (Clark et al. 1998). In addition, the reference and desired signals are assumed to be zero-mean stochastic processes that are wide-sense stationary. Generally, the goal of the noise cancellation problem is to determine the filter coefficients, \mathbf{w} , which minimize the mean-square error

$$J = E[e^2(n)] \quad (\text{D.1.9})$$

$$= E[\mathbf{w}^T \mathbf{x}(n) \mathbf{x}^T(n) \mathbf{w} - 2\mathbf{w}^T \mathbf{x}(n) d(n) + d^2(n)] \quad (\text{D.1.10})$$

$$= \mathbf{w}^T E[\mathbf{x}(n) \mathbf{x}^T(n)] \mathbf{w} - 2\mathbf{w}^T E[\mathbf{x}(n) d(n)] + E[d^2(n)] \quad (\text{D.1.11})$$

$$= \mathbf{w}^T \mathbf{R} \mathbf{w} - 2\mathbf{w}^T \mathbf{p} + E[d^2(n)] \quad (\text{D.1.12})$$

where J is the cost function, $E[\]$ denotes the statistical expectation, $\mathbf{R} = E[\mathbf{x}(n) \mathbf{x}^T(n)]$ is the input autocorrelation matrix, and $\mathbf{p} = E[\mathbf{x}(n) d(n)]$ is the cross-correlation vector between the reference and desired signals. If \mathbf{R} is not singular, then the quadratic cost function will have a global minimum. The minimum is found by taking the derivative of the cost function with respect to each filter coefficient

$$\frac{\partial J}{\partial \mathbf{w}} = 2E[\mathbf{x}(n) \mathbf{x}^T(n) \mathbf{w} - \mathbf{x}(n) d(n)] \quad (\text{D.1.13})$$

$$= 2[\mathbf{R} \mathbf{w} - \mathbf{p}] \quad (\text{D.1.14})$$

The optimal filter coefficients can then be found by setting Equation D.1.14 equal to zero

$$\mathbf{R}\mathbf{w}_{opt} = \mathbf{p} \quad (\text{D.1.15})$$

where \mathbf{w}_{opt} are the optimal filter coefficients. If the reference signal is persistently exciting, then \mathbf{R} will be positive definite and therefore invertible. Persistently exciting means that there are at least half as many spectral components in the reference signal as filter coefficients (Elliott 2001). If \mathbf{R} is invertible, then \mathbf{w}_{opt} can be calculated as

$$\mathbf{w}_{opt} = \mathbf{R}^{-1}\mathbf{p} \quad (\text{D.1.16})$$

The optimal filter is commonly known as the Wiener filter.

Often complete knowledge of the relevant statistics is unavailable and therefore it may not be possible to design the optimum filter *a priori*. Therefore, adaptive digital filters have been developed that use recursive techniques to update the filter coefficients in real time. If the reference and disturbance are stationary, then the adaptive filter will converge towards the optimal solution. In addition, the adaptive filter can track changes if the statistics of the signals vary slowly compared to the convergence time of the adaptive algorithm.

The steepest descent algorithm is a common adaptation algorithm, which adjusts the filter coefficients towards the global minimum using the negative of the gradient of the cost function. Recall that the gradient of the cost function can be expressed as

$$\frac{\partial J}{\partial \mathbf{w}} = 2E [\mathbf{x}(n)\mathbf{x}^T(n)\mathbf{w} - \mathbf{x}(n)d(n)] \quad (\text{D.1.17})$$

$$= 2E [-\mathbf{x}(n)e(n)] \quad (\text{D.1.18})$$

where the final equation is found by substituting Equation D.1.8 into Equation D.1.17. The update equation for the filter coefficients can then be expressed as

$$\mathbf{w}(n+1) = \mathbf{w}(n) - \alpha \frac{\partial J}{\partial \mathbf{w}} \quad (\text{D.1.19})$$

$$= \mathbf{w}(n) + 2\alpha E [\mathbf{x}(n)e(n)] \quad (\text{D.1.20})$$

where α is a convergence parameter. Unfortunately, determining $E [\mathbf{x}(n)e(n)]$ can require long time histories, and is not feasible if the process is time varying. An alternative is to use an instantaneous estimate of the derivative of the cost function in the update equation

$$\mathbf{w}(n+1) = \mathbf{w}(n) + \mu \mathbf{x}(n)e(n) \quad (\text{D.1.21})$$

where $\mu = 2\alpha$. The convergence coefficient μ determines the speed and stability of the adaptation. While precise stability bounds on the convergence coefficient can be difficult to establish due to the instantaneous

estimate of the gradient, a common bound is given as (Elliott 2001)

$$0 < \mu < \frac{2}{\text{tr}(\mathbf{R})} \quad (\text{D.1.22})$$

where $\text{tr}(\mathbf{R})$ is the trace of the input autocorrelation matrix.

To this point, we have only considered the electrical noise cancellation problem. Generally, the term feedforward controller is used instead of digital filter if the system has plant dynamics between the output of the filter and the error sensor, as shown in Figure D.2 (a).

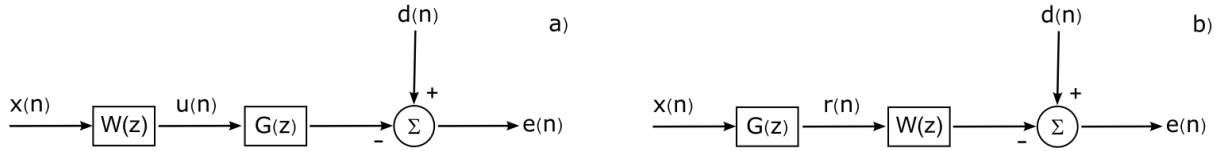


Figure D.2: The figures show: (a) a simple feedforward control system; and (b) a rearranged diagram valid for linear time-invariant systems.

The filtered-reference LMS algorithm is an extension of the electrical noise cancellation problem that takes into account plant dynamics between the filter output and error sensor. This algorithm is very popular for feedforward control and has been well documented in the literature (Widrow and Stearns 1985; Elliott 2001). If we assume that both the plant and controller are linear and time invariant, then the block diagram for the system can be redrawn as shown in Figure D.2 (b). Although an adaptive filter is not time-invariant, this approximation is valid as long as the filter coefficients are changing slowly relative to the timescales of the plant dynamics.

As discussed earlier, the LMS algorithm updates the filter coefficients in the opposite direction of the instantaneous gradient of the cost function. In this case, the gradient of the cost function is identical to Equation D.1.21 except \mathbf{x} has been replaced by \mathbf{r} , which is a filtered version of the reference signal. Therefore, the update equation can be written as

$$\mathbf{w}(n+1) = \mathbf{w}(n) + \mu \mathbf{r}(n)e(n) \quad (\text{D.1.23})$$

However, in practice \mathbf{r} must be calculated using an estimate of the plant model. Figure D.3 shows the block diagram of a practical implementation of the algorithm. The corresponding update equation is written as

$$\mathbf{w}(n+1) = \mathbf{w}(n) + \mu \hat{\mathbf{r}}(n)e(n) \quad (\text{D.1.24})$$

where $\hat{\mathbf{r}}$ is calculated using the estimated plant model, $\hat{G}(z)$.

For the moment, assume that the plant model is perfect, i.e. $\hat{\mathbf{r}} = \mathbf{r}$. In this case, the performance of the converged feedforward control system is determined by several factors including control authority, coherence between the reference signal and disturbance, and the controller's ability to recreate the frequency response required for perfect control. Note that the coherence provides a measure of the linear dependence between

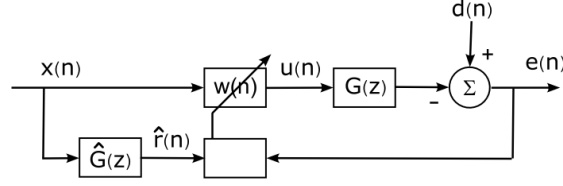


Figure D.3: Block diagram of the filtered reference LMS algorithm.

two signals and places a fundamental limit on the achievable performance of the control system, as presented by Elliott (2001)

$$\Delta = 1 - \gamma_{xd}^2 \quad (\text{D.1.25})$$

where Δ is the attenuation, and γ_{xd}^2 is the magnitude squared coherence function between the reference and disturbance. This equation is valid if the error signal is stationary, and the controller is time invariant and realizable. For example, if $\gamma_{xd}^2 = 0.9$, then the maximum achievable attenuation is limited to 10 dB. However, if the controller is not physically realizable because the required frequency response is too complicated to be recreated using the chosen filter (due to the filter structure or finite filter length), or the system is not causal (because a sufficiently time-advanced reference signal is unavailable), then the performance will be worse. In this context, causal means that the output of the system lags the input, or in other words, the filter responds to an input *after* the input is received.

Note that modeling error is inevitable in real control systems. Therefore, the leaky filtered-reference LMS algorithm is often used to improve robust stability in exchange for a small reduction in nominal performance. This algorithm minimizes a cost function based on the sum of the mean square error and the weighted sum of the squared filter coefficients

$$J = E[e^2(n)] + \beta \mathbf{w}^T \mathbf{w} \quad (\text{D.1.26})$$

where β is a positive leakage parameter. The derivative of the cost function with respect to each filter coefficient can be expressed as

$$\frac{\partial J}{\partial \mathbf{w}} = 2E[-\mathbf{r}(n)e(n)] + 2\beta \mathbf{w} \quad (\text{D.1.27})$$

Once again, the instantaneous version of the derivative is used to update the filter coefficients, such that

$$\mathbf{w}(n+1) = \mathbf{w}(n) - \alpha \frac{\partial J}{\partial \mathbf{w}} \quad (\text{D.1.28})$$

$$= (1 - \mu\beta)\mathbf{w}(n) + \mu\hat{\mathbf{r}}(n)e(n) \quad (\text{D.1.29})$$

where $\mu = 2\alpha$ is the convergence coefficient. Using a small leakage term β has been shown to improve robustness with only a small reduction in nominal performance (Elliott 2001). Therefore, the leaky FX-LMS algorithm is used exclusively in this study.

D.2 Numerical simulations

This section examines the possibility of obtaining useful reductions in shock-cell induced interior noise using feedforward control. The first part of this study is performed using the two-bay numerical model described in Chapter 2. The control strategy is depicted in Figure D.4. As shown in the figure, the reference signal, $x(n)$, is used to drive two center mounted piezoelectric patches in an effort to minimize the summed output from both sets of velocity sensors, $y_1(n)$ and $y_2(n)$.

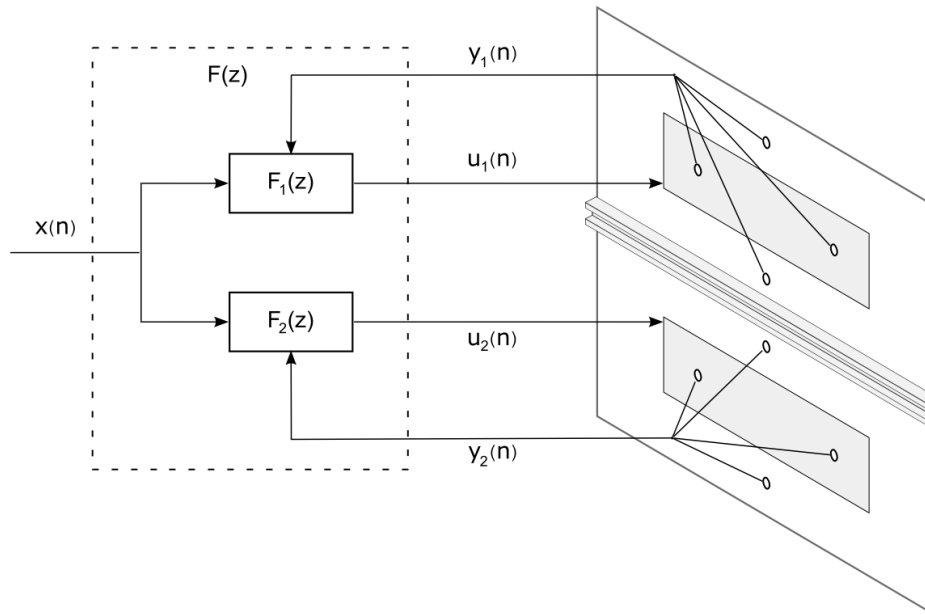


Figure D.4: Feedforward diagram showing the location of the transducers used for control.

Figure D.5 shows a block diagram of the control system. In this investigation, a single reference signal $x(n)$ is filtered by the decentralized control system $F(z)$ in order to generate control inputs $u(n)$ that couple to the measured outputs $y(n)$ via the plant $G(z)$. Although it is not shown in the figure, the filter coefficients are updated using the leaky filtered-reference LMS algorithm. Note that while the control system is adaptive, only the converged performance is discussed in this section for the sake of brevity.

Initial simulations are performed using two different disturbances with spectral characteristics matching the combined aft-cabin excitation shown with the solid black line in Figure D.7. While the spectral shape of both disturbances is identical, the spatial characteristics are significantly different. For instance, the first disturbance represents shock-cell noise, while the second matches the spatial characteristics of turbulent boundary layer noise. As described in Chapter 2, a discrete array of 50 correlated point loads is used to represent each distributed disturbance in the numerical model. The vibro-acoustic response of the structure with and without control is then simulated using $f_s = 3$ kHz, $\mu = 5 \times 10^{-5}$, and $\beta = 10^{-4}$. Figure D.6 (a) and (b) compare the converged performance of the feedforward control system using a reference sensor located directly between the two bays. Note that since similar trends were observed on both bays, only the response on the upper bay is presented here. The simulations show that when a spatially correlated disturbance such as shock-cell noise is used, the control system achieves a 12.9 dB integrated reduction

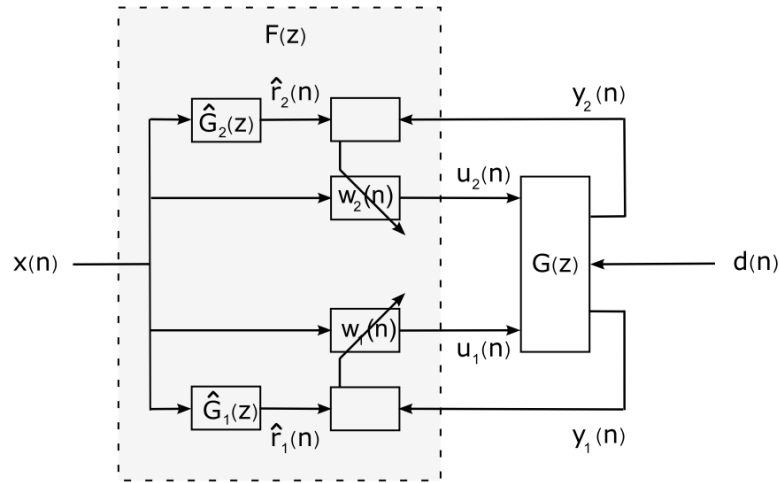


Figure D.5: Block diagram of the single-reference, two-channel decentralized feedforward control system.

in summed velocity from 50-800 Hz. However, if the disturbance matches the spatial characteristics of boundary layer noise, then the control system only reduces the response by 1.9 dB integrated over the same bandwidth. Note that although the reference signal is identical to the disturbance at the measurement location, the response of the structure is due to the spatially distributed excitation. If the excitation is not spatially correlated, then the reference will not be coherent with the sensed variable. Therefore, the performance of the control system is reduced as the spatial coherence of the excitation decreases.

Note that aft-cabin noise simulated by combining boundary layer and shock-cell noise with the power spectra shown in Figure D.7. Recall that since the test structure is not tensioned, the frequency shifted spectra are used to generate the disturbance, as described in Chapter 2. The closed-loop response of the converged system excited by the actual aft-cabin disturbance is shown in Figure D.8. In this case, the control system reduces the summed velocity by 8.8 dB integrated from 50-800 Hz.

To this point, the simulations have been performed using a reference sensor located directly between the two-bays of interest. Therefore, while the signal is correlated with the disturbance, it does not provide time-advanced information. To achieve a time-advanced signal, the reference sensor is typically positioned close to the disturbance, while the actuator is located near the error sensors (Sutton et al. 1990). However in this application, the coherence between the reference and disturbance rolls off as the separation distance increases. Therefore, there is a tradeoff between obtaining a time-advanced reference and maximizing coherence.

Note that the delay through the control path has been neglected to this point. However in practice, delay is caused by digital sampling, anti-aliasing filters, computation time, and even the physical system itself. Therefore, subsequent simulations are performed assuming a one sample delay through the control path. Therefore, if the system is sampled at 3 kHz, then the reference must lead the disturbance by more than 0.33 ms to provide a time-advanced reference. Since the phase velocity for shock-cell noise is approximately 1000 m/s in the streamwise direction, a time-advanced reference could be obtained by placing the reference sensor 0.476 m upstream of the panel. However, separating the reference sensor from the panel

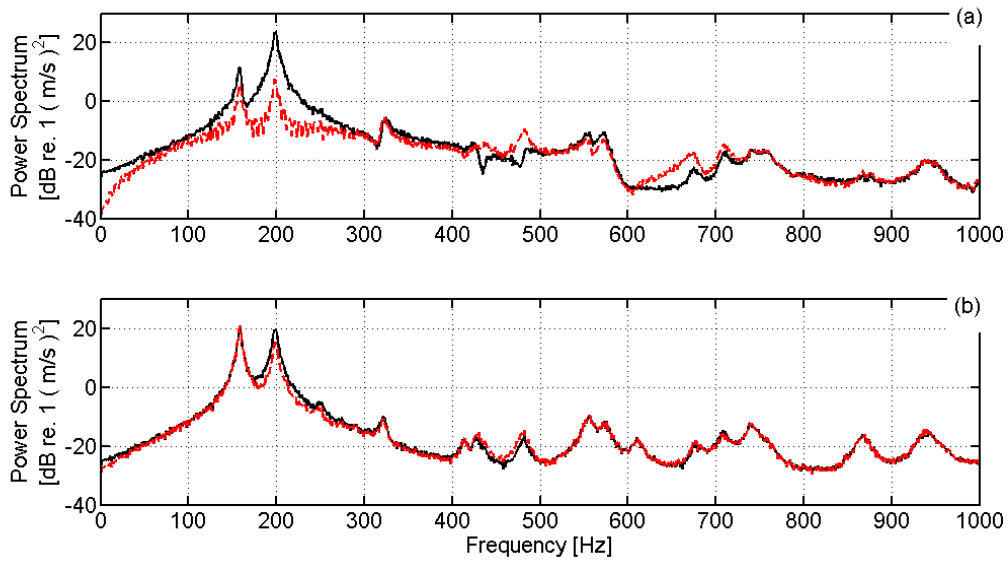


Figure D.6: Simulated power spectra of the open-loop responses (solid black lines) are compared with the closed-loop responses (dashed red lines). The simulation is performed using: (a) a spatially correlated disturbance representative of shock-cell noise; and (b) an uncorrelated disturbance similar to TBL noise.

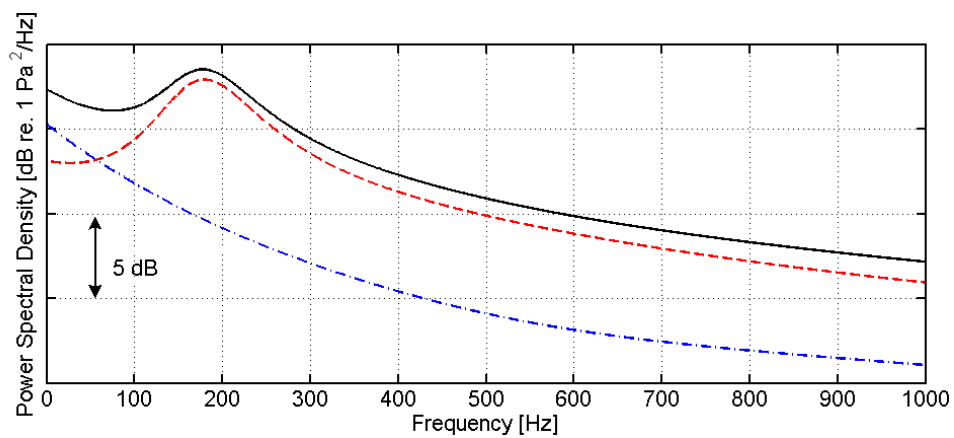


Figure D.7: The figure shows the frequency shifted spectra for TBL noise (dash-dotted blue line), shock-cell noise (dashed red line), and the combined excitation (solid black line).

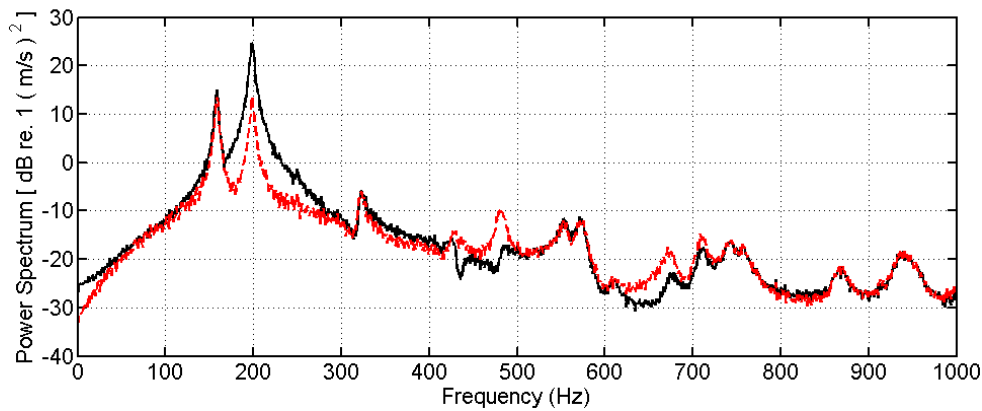


Figure D.8: The power spectra of the open-loop response (solid black line) and closed-loop response (dashed red line) simulated using the combined excitation.

reduces coherence in exchange for time-advanced information. For example, Figure D.9 shows the coherence between the reference and sensed signals for three different reference sensor locations. The dashed blue line shows the open-loop coherence between the reference and sensed signals when the reference sensor is located directly between the two bays of interest. In comparison, the solid red and dash-dotted green lines show the coherence when the reference sensor is located 0.476 m and 1.43 m upstream of the panel. While coherence is reduced, the upstream reference sensors provide time-advanced information about the disturbance.

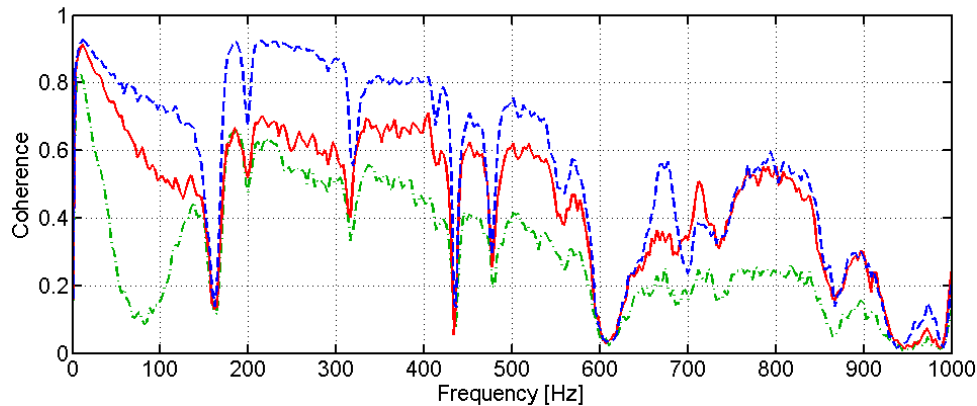


Figure D.9: Coherence between the reference signal and the error signal on the upper bay. The simulations are performed using a reference signal centered above the panel (dashed blue line), using a time-advanced reference signal 0.476 m upstream of the panel (solid red line), and using a time-advanced reference signal 1.43 m upstream of the panel (dash-dotted green line).

Figure D.10 shows the closed-loop performance simulated using the reference sensor centered between the two bays of interest and using the sensor located 0.476 m upstream of the panel. The control system achieves an 8.4 dB integrated reduction in summed velocity using the reference sensor centered above the panel, while the integrated response is only reduced by 4.6 dB using the upstream reference sensor. Also

note that while the response is not shown in this figure, the control system only achieves a 4.0 dB integrated reduction when the reference sensor is located 1.43 m upstream of the panel. These simulations suggest that for this application it is better to use a delayed reference signal directly above the panel of interest instead of a noisy reference signal providing time-advanced information. Note that since the structure is lightly damped and the disturbance is shaped, the response is "predictable" to some extent (Burdisso et al. 1993). Therefore, attenuation is possible even though the reference signal is not time advanced.

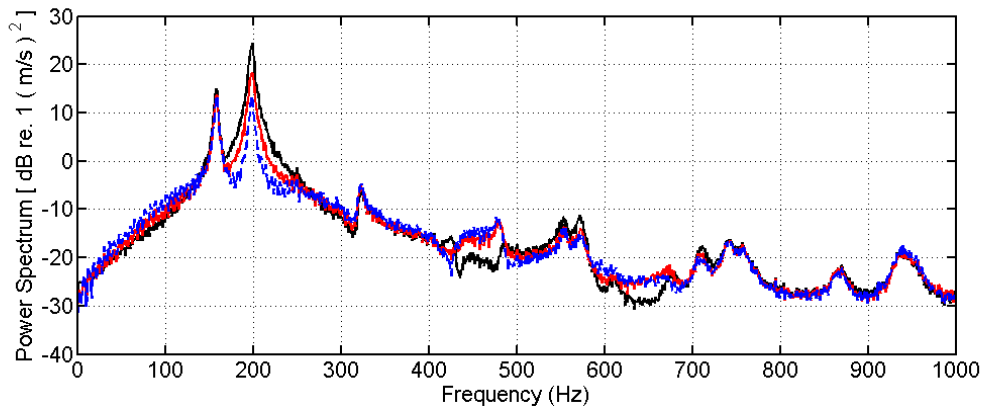


Figure D.10: Simulated power spectra of the open-loop response (solid black lines) is compared with the closed-loop response simulated using a delayed reference signal centered above the panel (dashed blue line) and using a time-advanced reference signal 0.476 m upstream of the panel (solid red line).

While the previous simulation suggests that an 8.4 dB reduction of summed velocity is possible using feedforward control, the real performance metric is radiated sound power. Therefore, Figure D.11 shows the radiated sound power from the structure with and without control. In this case, the control system reduces the dominant peak by 12 dB and reduces the integrated response by 9 dB over the 50-800 Hz bandwidth. Therefore, the numerical simulations suggest that feedforward control of aft-cabin noise may be feasible if the fuselage is lightly damped and the disturbance is spatially correlated.

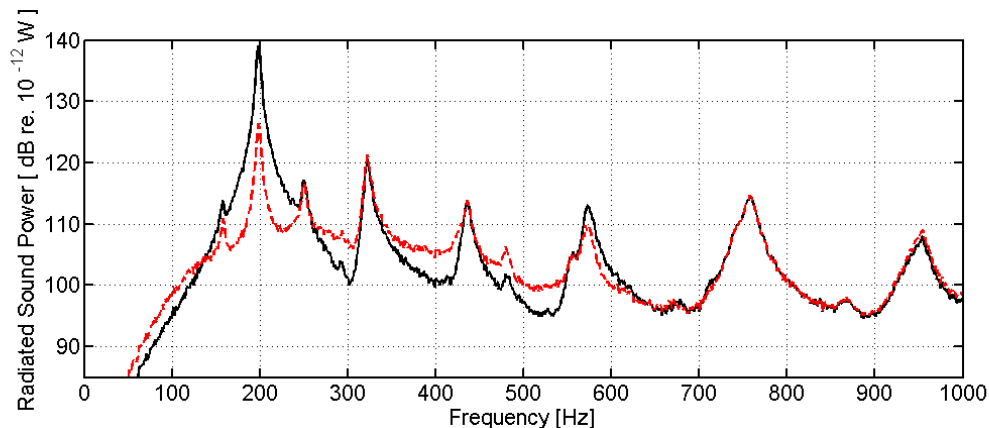


Figure D.11: Radiated sound power without control (solid black line), and using the delayed reference sensor directly above the panel (dashed red line).

D.3 Experimental results

The experimental investigation is performed on the stiffened aluminum test structure described in Chapter 2. While the control strategy and transducer layout shown in Figure D.4 are also used for the experimental study, the error sensors are now accelerometers instead of point velocity sensors. Note that for the experiments presented here, the reference signal is acquired using a microphone located directly in front of the structure. Once again, the acoustic excitation described in Chapter 2 is used to simulate the aft-cabin disturbance. The coherence between the microphone and error signals (summed acceleration) are shown in Figure D.12. While the low frequency coherence rolls off naturally due to the dynamics of the structure, the coherence is artificially high at other frequencies. Recall that coherence should roll off with frequency as shown by the dashed blue line in Figure D.9. This implies that the spatial characteristics of aft-cabin noise are not reproduced accurately in the lab. Since the laboratory disturbance is more correlated than the actual disturbance, this experiment is likely to overestimate the performance of the control system.

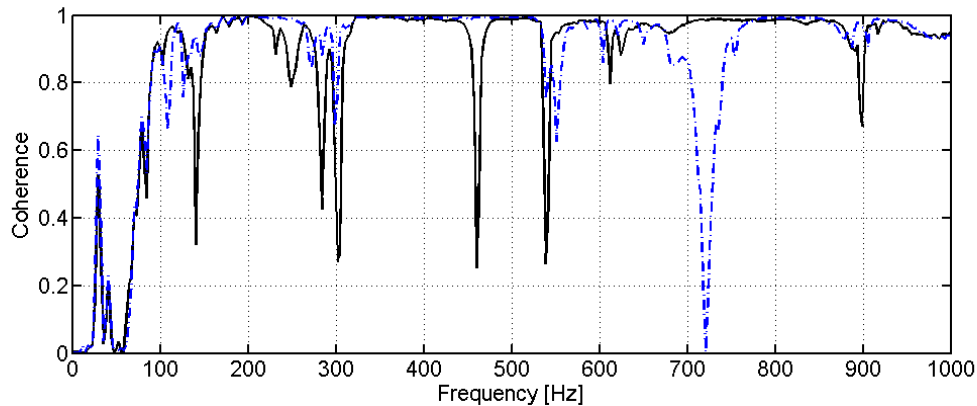


Figure D.12: Coherence between the reference signal and the error signal from the lower bay (solid black line), and the coherence between the reference signal and the error signal from the upper bay (dash-dotted blue line).

The first step in the design process is to identify system models by driving each actuator with white noise while recording the summed response from each set of accelerometers. Control models are then identified from the input/output data using the OKID algorithm (Juang 1994). The leaky FX-LMS algorithm is then used to update the filter coefficients in each controller. Note that the control system operates at 3 kHz, using $\beta = 10^{-6}$, $\mu = 10^{-5}$, and $N = 64$ (ie 64 filter coefficients per controller). While the transient response of the system is not the focus of this study, a sample time history of a subset of filter coefficients is shown in Figure D.13. Although the response is subject to random variations since only one set of data is plotted, in general the coefficients converge smoothly towards the optimal solution.

Once the controllers have converged, the closed-loop response is recorded. The power spectra of the summed acceleration measured on each bay are shown in Figure D.14 (a) and (b). The feedforward control system reduces the peaks by 4-6 dB and achieves an integrated reduction of 1-2 dB over the 50-800 Hz bandwidth. Although performance is limited, relatively little spillover is observed, except at 528 Hz in Figure D.14 (a).

Representing the control system as shown in Figure D.2 (a) implies that the reference signal is uncontrollable

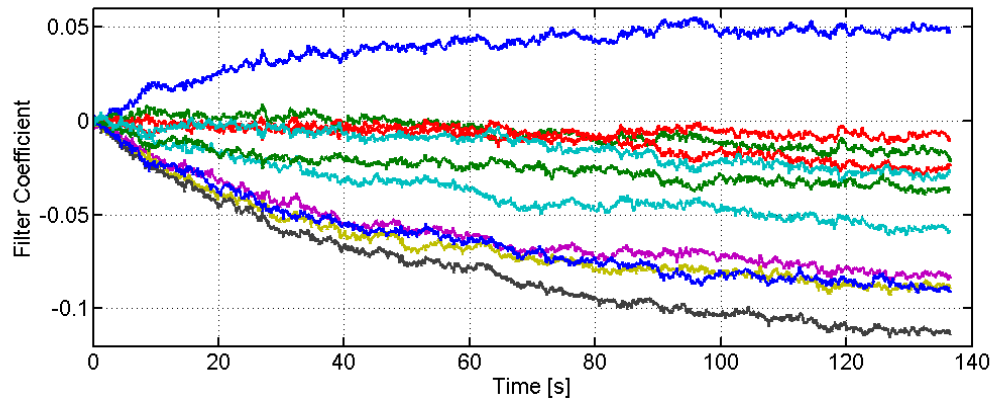


Figure D.13: The figure shows the time record for a subset of filter coefficients.

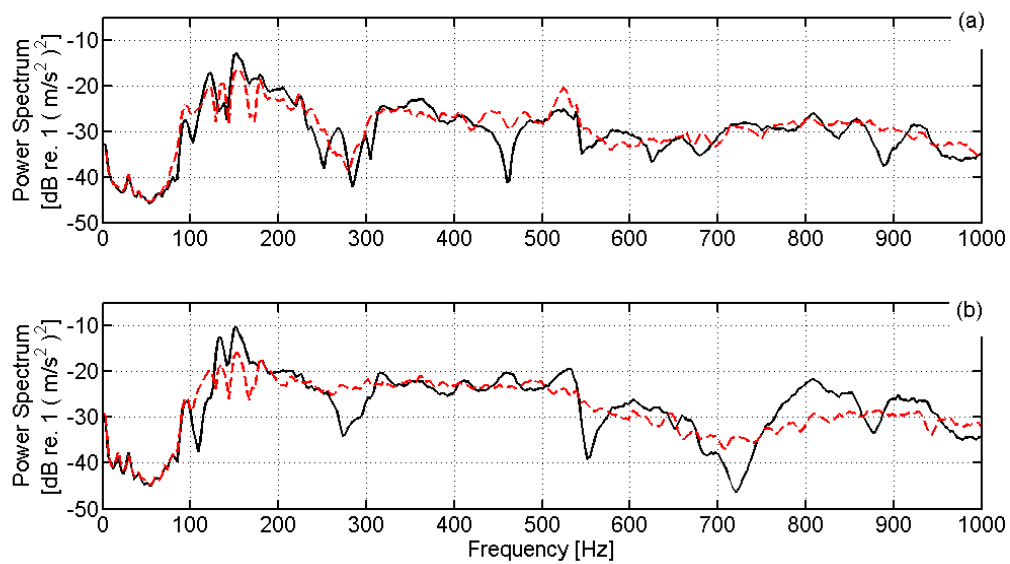


Figure D.14: The power spectra of the measured responses before control (solid black lines) and using the converged feedforward controller (dashed red lines). The figures show: (a) the measured response on the lower bay; and (b) the measured response on the upper bay.

via the control input. However in this application, there is a feedback path from the control input to the reference signal, as shown in Figure D.15. The magnitude of the feedback path from the actuator on the lower bay to the microphone is shown in Figure D.16. The feedback path changes the dynamics of the controller, resulting in the spillover observed at 528 Hz. Although a feedback cancellation architecture can be used if the feedback path is known *a priori* (Elliott 2001), the approach was not incorporated in this work.

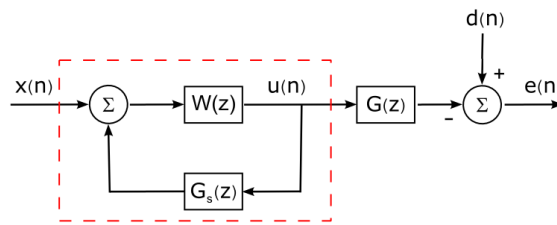


Figure D.15: A general block diagram for a feedforward control system.

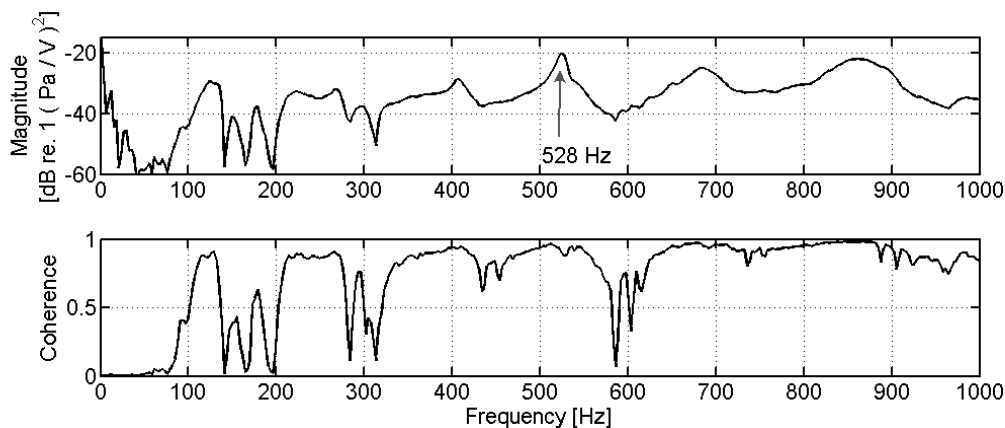


Figure D.16: The magnitude of the feedback path from the piezoelectric actuator on the lower bay to the microphone.

The radiated sound power from the structure with and without control is shown in Figure D.17. While the decentralized feedforward control system reduces the peak response by 5 dB, it only achieves a 0.6 dB integrated reduction from 50-600 Hz. The marginal performance is due to the dynamics of this particular structure. Since a time-advanced reference signal is not available, significant attenuation is only possible if the structure is lightly damped and/or the disturbance is shaped. At this point, recall that the experiment was expected to overestimate the performance of the control system due to the characteristics of the acoustic excitation. Therefore based on the experimental results, feedforward control of aft-cabin noise does not appear to be feasible. Although feedforward control might be used in specific applications, the performance of the system will ultimately depend on the dynamics of the structure and the characteristics of the disturbance.

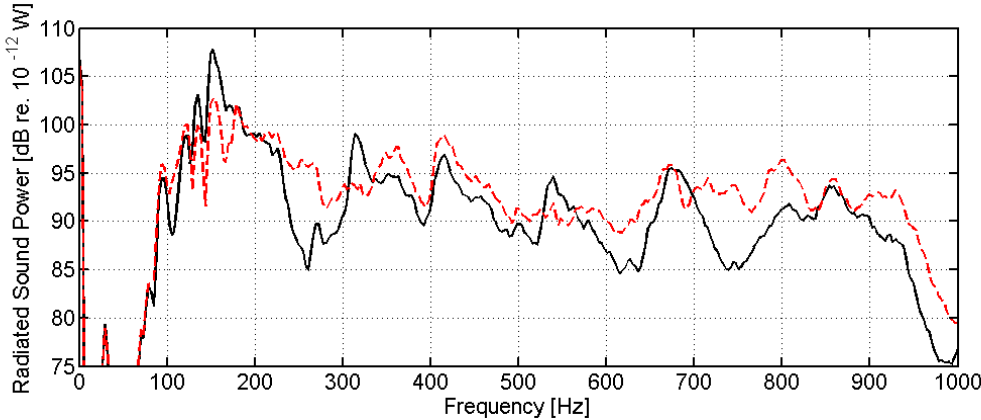


Figure D.17: The radiated sound power from the structure before control (solid black line) and using the converged feedforward control system (dashed red line).

Appendix E

Simulink diagrams

This section contains Simulink diagrams that were used to implement the control systems experimentally.

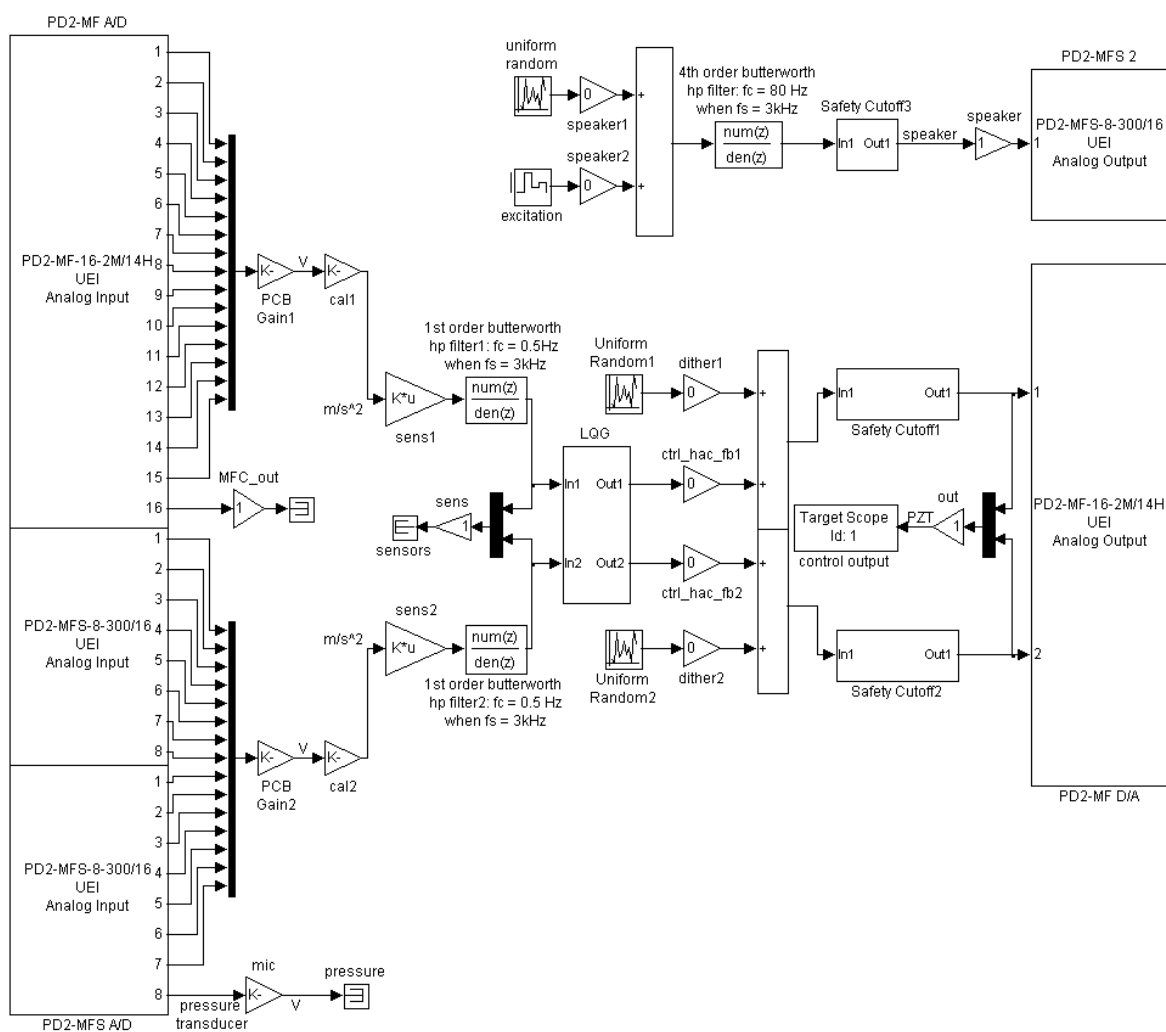
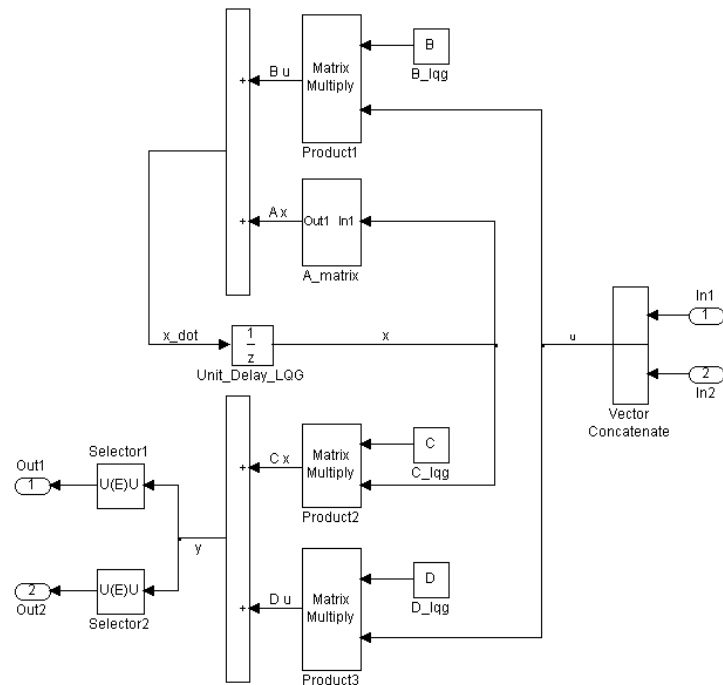


Figure E.1: Diagram of the high-authority feedback control system.



the decomposed canonical controller does not require the full matrix multiplication and can be updated without reloading the entire A matrix

Figure E.2: Diagram of the LQG subsystem.

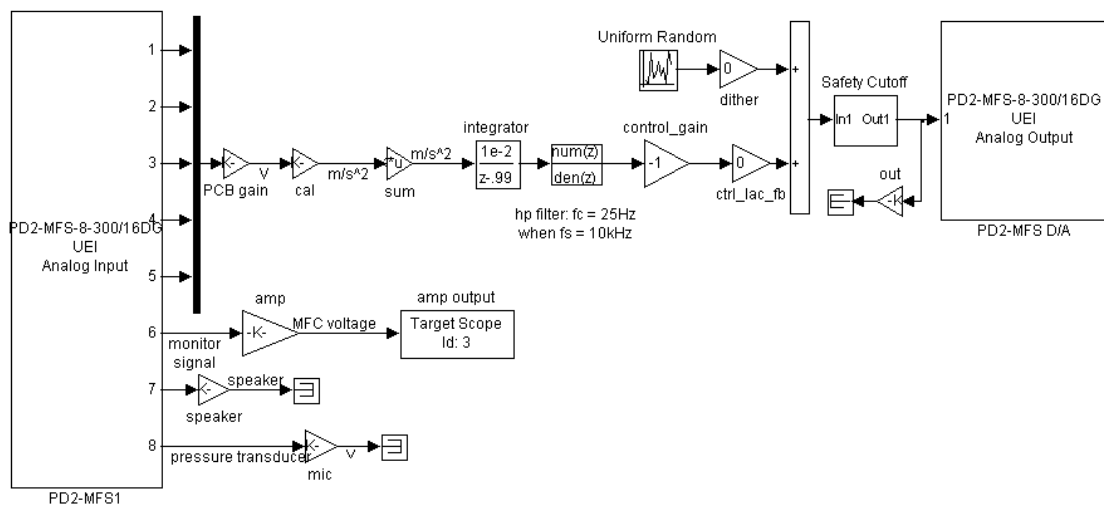


Figure E.3: Diagram of the low-authority feedback control system.

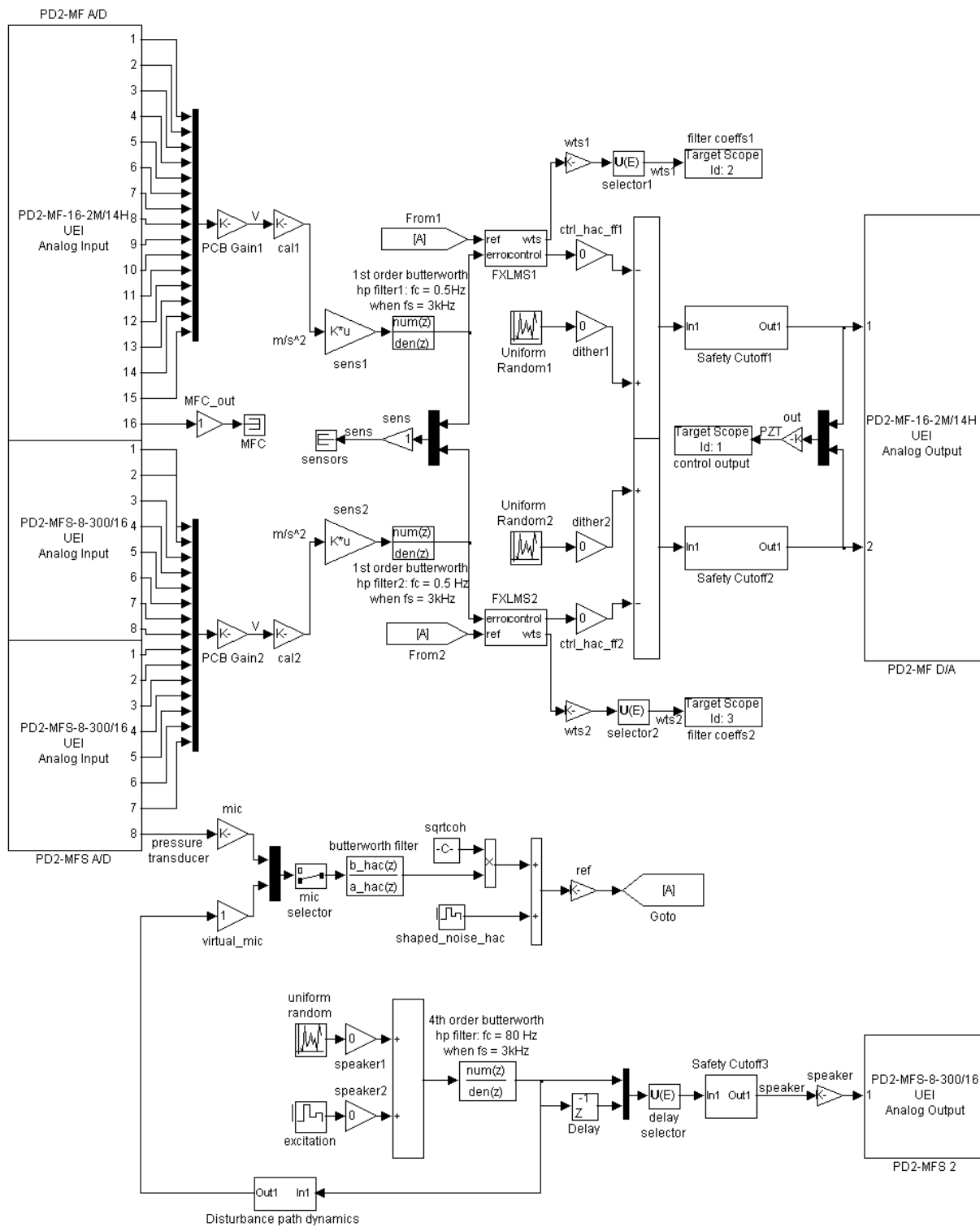


Figure E.4: Diagram of the feedforward control system.

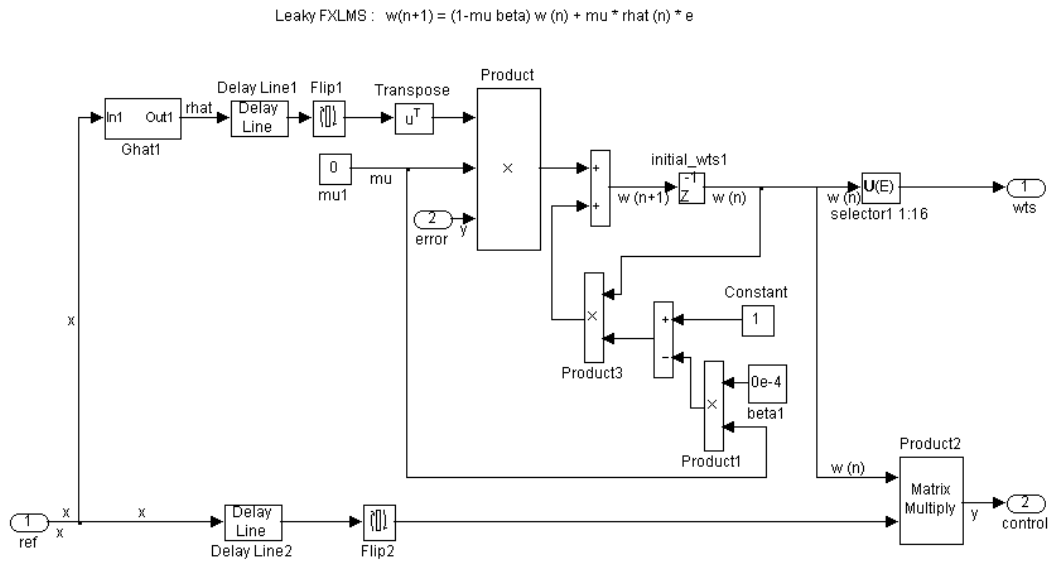


Figure E.5: Diagram of the FXLMS subsystem.

Bibliography

- Anderson, B.D.O. and Mingori, D.L. (1985). Use of frequency dependence in linear quadratic control problems to frequency-shape robustness. *Journal of Guidance, Control, and Dynamics*, **8**(3), 397–401.
- Anderson, B.D. and Moore, J.B. (1990). *Optimal Control: Linear Quadratic Methods*. Prentice Hall, Englewood Cliffs, New Jersey.
- Anderson, E.H., Hagood, N.W., and Goodliffe, J.M. (1992). Self-sensing piezoelectric actuation: analysis and application to controlled structures. *AIAA/ASME/ASCE/AHS/ASC Structures, Structural Dynamics and Materials Conference, Dallas, TX*. AIAA-92-2465-CP.
- Aubrun, J.N. (1980). Theory of the control of structures by low-authority controllers. *Journal of Guidance and Control*, **3**(5), 444–451.
- Aubrun, J.N. and Ratner, M.J. (1984). Structural control for a circular plate. *Journal of Guidance, Control, and Dynamics*, **7**(5), 535–545.
- Balas, M.J. (1979). Direct velocity feedback control of large space structures. *Journal of Guidance and Control*, **2**(3), 252–253.
- Baumann, O.N. and Elliott, S.J. (2007). The stability of decentralized multichannel velocity feedback controllers using inertial actuators. *Journal of the Acoustical Society of America*, **121**(1), 188–196.
- Baumann, W.T. (1997). An adaptive feedback approach to structural vibration suppression. *Journal of Sound and Vibration*, **205**(1), 121–133.
- Baumann, W.T., Saunders, W.R., and Robertshaw, H.H. (1991). Active suppression of acoustic radiation from impulsively excited structures. *Journal of the Acoustical Society of America*, **90**(6), 3202–3208.
- Bevan, J.S. (2000). *Piezoceramic actuator placement for acoustic control of panels*. Ph.D. thesis, Old Dominion University, Norfolk, Virginia.
- Bianchi, E., Gardonio, P., and Elliott, S.J. (2004). Smart panel with multiple decentralized units for the control of sound transmission. Part III: control system implementation. *Journal of Sound and Vibration*, **274**, 215–232.
- Bingham, B., Atalla, M.J., and Hagood, N.W. (2001). Comparison of structural-acoustic control designs on an active composite panel. *Journal of Sound and Vibration*, **244**(5), 761–778.
- Bitmead, R.R., Gevers, M., and Wertz, V. (1990). *Adaptive Optimal Control: The Thinking Man's GPC*. Prentice Hall, Englewood Cliffs, New Jersey.
- Boden-Albala, B. and Sacco, R.L. (2000). Lifestyle factors and stroke risk: Exercise, alcohol, diet, obesity, smoking, drug use, and stress. *Current Atherosclerosis Reports*, **2**(2), 160–166.

- Boeing (2007). 2007 Current Market Outlook. http://www.boeing.com/commercial/cmo/pdf/CMO_2007.pdf.
- Burdisso, R.A., Vipperman, J.S., and Fuller, C.R. (1993). Causality analysis of feedforward-controlled systems with broadband inputs. *Journal of the Acoustical Society of America*, **94**(1), 234–242.
- Cabell, R.H., Cox, D.E., and Gibbs, G.P. (2003). Interaction metrics for feedback control of sound radiation from stiffened panels. *Proceedings of the 44th AIAA/ASME/ASCE/AHS Structures, Structural Dynamics, and Materials Conference, Norfolk, Virginia, April 7-10*. AIAA-2003-1812.
- Cabell, R.H., Kegerise, M.A., Cox, D.E., and Gibbs, G.P. (2006). Experimental feedback control of flow-induced cavity tones. *American Institute of Aeronautics and Astronautics Journal*, **44**(8), 1807–1815.
- Carneal, J.P. and Fuller, C.R. (1995). A biologically inspired controller. *Journal of the Acoustical Society of America*, **98**(1), 386–396.
- Carneal, J.P. and Fuller, C.R. (2004). An analytical and experimental investigation of active structural acoustic control of noise transmission through double panel systems. *Journal of Sound and Vibration*, **272**, 749–771.
- Chang, M.T. and Vaicaitis, R. (1982). Noise transmission into semicylindrical enclosures through discretely stiffened curved panels. *Journal of Sound and Vibration*, **85**(1), 71–83.
- Charette, F., Berry, A., and Guigou, C. (1998). Active control of sound radiation from a plate using a polyvinylidene fluoride volume displacement sensor. *Journal of the Acoustical Society of America*, **103**(3), 1493–1503.
- Clark, R.L. and Cox, D.E. (1999). Experimental demonstration of a band-limited actuator/sensor selection strategy for structural control. *Journal of the Acoustical Society of America*, **106**(6), 3407–3414.
- Clark, R.L. and Fuller, C.R. (1992). Modal sensing of efficient acoustic radiators with polyvinylidene fluoride distributed sensors in active structural acoustic control approaches. *Journal of the Acoustical Society of America*, **91**(6), 3321–3329.
- Clark, R.L. and Gibbs, G.P. (1999). Analysis, testing, and control of a reverberant sound field within the fuselage of a business jet. *Journal of the Acoustical Society of America*, **105**(4), 2277–2286.
- Clark, R.L., Saunders, W.R., and Gibbs, G.P. (1998). *Adaptive Structures, Dynamics and Control*. John Wiley and Sons, NY.
- Cole, D.G. and Clark, R.L. (1994). Adaptive compensation of piezoelectric sensor/actuators. **5**, 665–672.
- Collins, S.A., Miller, D.W., and von Flotow, A.H. (1994). Distributed sensors as spatial filters in active structural control. *Journal of Sound and Vibration*, **173**(4), 303–308.
- Corcus, G.M. (1963). The resolution of pressures in turbulence. *Journal of the Acoustical Society of America*, **35**, 192–199.
- Cox, D.E., Gibbs, G.P., Clark, R.L., and Vipperman, J.S. (1999). Experimental robust control of structural acoustic radiation. *American Society of Mechanical Engineers Journal of Vibration and Acoustics*, **121**(4), 433–439.
- Cunefare, K.A. (1991). The minimum multimodal radiation efficiency of baffled finite beams. *Journal of the Acoustical Society of America*, **90**(5), 2521–2529.

- Czech, M. and Anderson, A. (2003). Fluidic wallpaper: An active control concept for low frequency broadband noise. *Proceedings of the 9th AIAA/CEAS Aeroacoustics Conference, Hilton Head, South Carolina, May 12-14*. AIAA-2003-3189.
- D'Andrea, R. and Dullerud, G.E. (2003). Distributed control design for spatially interconnected systems. *Institute of Electrical and Electronics Engineers Transactions on Automatic Control*, **48**(9), 1478–1495.
- D'Angelo, J.P. (2004). *Attenuation of turbulent boundary layer induced interior noise using integrated smart foam elements*. Ph.D. thesis, Virginia Polytechnic Institute and State University, Blacksburg, Virginia.
- Deffayet, C. and Nelson, P.A. (1988). Active control of low-frequency harmonic sound radiated by a finite panel. *Journal of the Acoustical Society of America*, **84**(6), 2192–2199.
- Deodatis, G. (1996). Simulation of ergodic multivariate stochastic processes. *Journal of Engineering Mechanics*, **122**(8), 778–787.
- Diaz, C.G., Gardonio, P., and Paulitsch, C. (2006). Smart panel with decentralised inertial actuator active damping units. *Proceedings of Active 2006, Adelaide, Australia, September 19-20*.
- Dosch, J.J., Inman, D.J., and Garcia, E. (1992). A self-sensing piezoelectric actuator for collocated control. **3**, 166–185.
- Doyle, J.C. (1978). Guaranteed margins for LQG regulators. *Institute of Electrical and Electronics Engineers Transactions on Automatic Control*, **AC-23**(4), 756–757.
- Doyle, J.C. and Stein, G. (1979). Robustness with observers. *Institute of Electrical and Electronics Engineers Transactions on Automatic Control*, **AC-24**(4), 607–611.
- Elliott, S.J. (2001). *Signal processing for active control*. Academic Press, London.
- Elliott, S.J., Gardonio, P., Sors, T.C., and Brennan, M.J. (2002). Active vibroacoustic control with multiple local feedback loops. *Journal of the Acoustical Society of America*, **111**(2), 908–915.
- Elliott, S.J. and Johnson, M.E. (1993). Radiation modes and the active control of sound power. *Journal of the Acoustical Society of America*, **94**(4), 2194–2204.
- Elliott, S.J., Maury, C., and Gardonio, P. (2005). The synthesis of spatially correlated random pressure fields. *Journal of the Acoustical Society of America*, **117**(3), 1186–1201.
- Elliott, S.J., Nelson, P.A., Stothers, I.M., and Boucher, C.C. (1990). In-flight experiments on the active control of propeller-induced cabin noise. *Journal of Sound and Vibration*, **140**(2), 219–238.
- Elliott, S.J. and Sutton, T.J. (1996). Performance of feedforward and feedback systems for active control. *Institute of Electrical and Electronics Engineers Transactions on Speech and Audio Processing*, **4**(3), 214–223.
- Emborg, U., Samuelsson, F., Holmgren, J., and Leth, S. (1998). Active and passive noise control in practice on the saab 2000 high speed turboprop. *Proceedings of the 4th AIAA/CEAS Aeroacoustics Conference, Toulouse, France, June 2-4*. AIAA-1998-2231.
- European Union (2003). Physical agents (noise) directive. <http://www.isvr.co.uk/reprints/padn.pdf>.
- Fanson, J.L. and Caughey, T.K. (1990). Positive position feedback control for large space structures. *American Institute of Aeronautics and Astronautics Journal*, **28**(4), 717–724.

- Frampton, K.D. (2001). Decentralized control of structural acoustic radiation. *Proceedings of the Symposium on noise control and acoustics IMECE 2001, NY, New York, November 11-16.*
- Frampton, K.D. (2004). Vibroacoustic control with a distributed sensor network. *Proceedings of Acitve-04, Williamsburg, Virginia, September 20-22.*
- Franklin, G.F., Powell, J.D., and Workman, M. (1998). *Digital Control of Dynamic Systems.* Addison Wesley Longman, Inc., Menlo Park, California.
- Fuller, C.R. (1987). Apparatus and method for global noise reduction. U.S. Patent No. 4715599.
- Fuller, C.R. and Carneal, J.P. (1993). A biologically inspired control approach for distributed elastic systems. *Journal of the Acoustical Society of America*, **93**(6), 3511–3513.
- Fuller, C.R., Elliott, S.J., and Nelson, P.A. (1996). *Active control of vibration.* Academic Press, London.
- Fuller, C.R., Hansen, C.H., and Snyder, S.D. (1991). Active control of sound radiation from a vibrating rectangular panel by sound sources and vibration inputs: an experimental comparison. *Journal of Sound and Vibration*, **145**(2), 195–215.
- Fuller, C.R., Johnson, M.E., and Griffin, J.R. (2000). Active-passive control of aircraft interior boundary layer noise using smart foam. *Proceedings of the 6th AIAA/CEAS Aeroacoustics Conference, Lahaina, HI, June 12-14.* AIAA-2000-2041.
- Fuller, C.R. and Jones, J.D. (1987). Experiments on reduction of propeller induced interior noise by active control of cylinder vibration. *Journal of Sound and Vibration*, **112**(2), 389–395.
- Gardonio, P., Bianchi, E., and Elliott, S.J. (2004a). Smart panel with multiple decentralized units for the control of sound transmission. Part I: theoretical predictions. *Journal of Sound and Vibration*, **274**, 163–192.
- Gardonio, P., Bianchi, E., and Elliott, S.J. (2004b). Smart panel with multiple decentralized units for the control of sound transmission. Part II: design of the decentralized control units. *Journal of Sound and Vibration*, **274**, 193–213.
- Gardonio, P. and Elliott, S.J. (1999). Active control of structure-borne and airborne sound transmission through double panel. *Journal of Aircraft*, **36**(6), 1023–1032.
- Gardonio, P. and Elliott, S.J. (2004). Smart panels for active structural acoustic control. *Smart Materials and Structures*, **13**, 1314–1336.
- Gardonio, P. and Elliott, S.J. (2005). Smart panels with velocity feedback control systems using triangularly shaped strain actuators. *Journal of the Acoustical Society of America*, **117**(4), 2046–2064.
- Gibbs, G.P. and Cabell, R.H. (2002). Simultaneous active control of turbulent boundary layer induced sound radiation from multiple aircraft panels. *Proceedings of the 8th AIAA/CEAS Aeroacoustics Conference, Breckenridge, CO, June 17-19.* AIAA-2002-2496.
- Gibbs, G.P., Cabell, R.H., and Juang, J. (2004). Controller complexity for active control of turbulent boundary layer noise from panels. *American Institute of Aeronautics and Astronautics Journal*, **42**(7), 1314–1320.
- Gibbs, G.P., Clark, R.L., Cox, D.E., and Vipperman, J.S. (2000). Radiation modal expansion: Application to active structural acoustic control. *Journal of the Acoustical Society of America*, **107**(1), 332–339.

- Gibbs, G.P., Eure, K.W., and Lloyd, J.W. (1999). Active control of turbulent boundary layer induced sound radiation from aircraft style panels. *Proceedings of Active-99, Ft. Lauderdale, Florida, Dec. 02-04.*
- Goh, C.J. and Caughey, T.K. (1985). On the stability problem caused by finite actuator dynamics in the control of large space structures. *International Journal of Control*, **41**(3), 787–802.
- Graham, W.R. (1996). Boundary layer induced noise in aircraft, Part I: The flat plate model. *Journal of Sound and Vibration*, **192**(1), 101–120.
- Graham, W.R. (1997). A comparison of models for the wavenumber-frequency spectrum of turbulent boundary layer pressures. *Journal of Sound and Vibration*, **206**(4), 541–565.
- Grosveld, F.W. (1999). Calibration of the structural acoustics loads and transmission facility at nasa langley research center. *Proceedings of Internoise 99, Fort Lauderdale, Florida, December 06-08.*
- Guigou, C. and Fuller, C.R. (1999). Control of aircraft interior broadband noise with foam-PVDF smart skin. *Journal of Sound and Vibration*, **220**(3), 541–557.
- Hagood, N.W., Chung, W.H., and Von Flotow, A. (1990). Modeling of piezoelectric actuator dynamics for active structural control. *Proceedings of the 31st AIAA/ASMO/ASCA/AHS Structures, Structural Dynamics, and Materials Conference, April 2-4. AIAA-90-1087-CP.*
- Harper-Bourne, M. and Fisher, M.J. (1974). The noise from shock waves in supersonic jets. *Proceedings of the AGARD Conference on Noise Mechanisms, Brussels, Belgium. AGARD CP-131.*
- Heatwole, C.M., Franchek, M.A., and Bernhard, R.J. (1997). Robust feedback control of flow-induced structural radiation of sound. *Journal of the Acoustical Society of America*, **102**(2), 989–997.
- Henry, J.K. and Clark, R.L. (1999). Smart aircraft panels: The effects of internal pressure loading on panel dynamics. *Proceedings of the SPIE Conference on Smart Structures and Integrated Systems, Newport Beach, CA.*
- Hyland, D.C., Junkins, J.L., and Longman, R.W. (1993). Active control technology for large space structures. *Journal of Guidance, Control, and Dynamics*, **16**(5), 801–821.
- Johnson, M.E. and Elliott, S.J. (1995). Active control of sound radiation using volume velocity cancellation. *Journal of the Acoustical Society of America*, **98**(4), 2174–2186.
- Johnson, M.E., Sors, T., Elliott, S.J., and Rafaely, B. (1997). Feedback control of broadband sound radiation using a volume velocity sensor. *Proceedings of Active 97, Budapest, HU, August 21-23.*
- Juang, J. (1994). *Applied System Identification*. PTR Prentice Hall, Engelwood Cliffs, New Jersey.
- Kegerise, M.A., Cabell, R.H., and Cattafesta III, L.N. (2007). Real-time feedback control of flow-induced cavity tones – Part 1: Fixed-gain control and Part 2: Adaptive control. *Journal of Sound and Vibration*, **307**(3–5), 906–923 and 924–940.
- Kidner, M. and Fuller, C.R. (2000). Control of large distributed structures with numerous actuators and a biologically inspired control architecture. *Proceedings of the 8th Conference on Nonlinear Vibrations, Stability and Dynamics of Structures, July 23-27.*
- Kinzie, K., Henderson, B., Whitmire, J., and Abeysinghe, A. (2004). Fluidic chevrons for jet noise reduction. *Proceedings of Active-04, Williamsburg, VA, September 20-22.*

- Lee, Y.S., Elliott, S.J., and Gardonio, P. (2003). Matched piezoelectric double sensor/actuator pairs for beam motion control. *Smart Materials and Structures*, **12**, 541–548.
- Lee, Y.S., Gardonio, P., and Elliott, S.J. (2002). Volume velocity vibration control of a smart panel using a uniform force actuator and an accelerometer array. *Smart Materials and Structures*, **11**, 863–873.
- Leissa, A.W. (1969). *Vibration of Plates*. National Aeronautics and Space Administration.
- Lele, S.K. (2005). Phased array models of shock-cell noise sources. *Proceedings of the 11th AIAA/CEAS Aeroacoustics Conference, Monterey, CA, May 23-25*. AIAA-2005-2841.
- Lin, Y.K. (1969). A brief survey of transfer matrix techniques with special reference to the analysis of aircraft panels. *Journal of Sound and Vibration*.
- Lueg, P. (1936). Process of silencing sound oscillations. U.S. Patent No. 2043416.
- Mabe, J.H., Cabell, R.H., and Butler, G. (2005). Design and control of a morphing chevron for takeoff and cruise noise reduction. *Proceedings of the 11th AIAA/CEAS Aeroacoustics Conference, Monterey, CA, May 23-25*. AIAA-2005-2889.
- Maciejowski, J.M. (1985). Asymptotic recovery for discrete time systems. *Institute of Electrical and Electronics Engineers Transactions on Automatic Control*, **AC-30**(6), 602–605.
- Maillard, J.P. and Fuller, C.R. (1998). Comparison of two structural sensing approaches for active structural acoustic control. *Journal of the Acoustical Society of America*, **103**(1), 396–400.
- Maury, C., Elliott, S.J., and Gardonio, P. (2004). Turbulent boundary-layer simulation with an array of loudspeakers. *American Institute of Aeronautics and Astronautics Journal*, **42**(2), 706–713.
- Maury, C., Gardonio, P., and Elliott, S.J. (2001). Active control of the flow-induced noise transmitted through a panel. *American Institute of Aeronautics and Astronautics Journal*, **39**(10), 1860–1867.
- Maury, C., Gardonio, P., and Elliott, S.J. (2002). A wave number approach to modelling the response of a randomly excited panel, Part I: General theory and Part II: Application to aircraft panels excited by a turbulent boundary layer. *Journal of Sound and Vibration*, **252**(1), 83–113 and 115–139.
- McEver, M.A. (1999). *Optimal vibration suppression using on-line pole/zero identification*. Master's thesis, Virginia Polytechnic Institute and State University, Blacksburg, Virginia.
- McEver, M.A., Moon, S., Cole, D.G., and Clark, R.L. (2003). Adaptive control for interior noise control in rocket fairings. *Proceedings of the 44th AIAA/ASME/ASCE/AHS Structures, Structural Dynamics, and Materials Conference, Norfolk, Virginia, April 7-10*. AIAA-2003-1811.
- Mixson, J.S. and Wilby, J.F. (1991). Interior noise. H.H. Hubbard, editor, *Aeroacoustics of Flight Vehicles, Theory and Practice*. NASA Langley Research Center, Hampton VA, pp. 271–355.
- Montgomery, J.M. (2004). Modeling of aircraft structural-acoustic response to complex sources using coupled FEM-BEM analyses. *Proceedings of 10th AIAA/CEAS Aeroacoustics Conference, Manchester, United Kingdom, May 10-12*. AIAA-2004-2822.
- Moore, J.B., Gangsaas, D., and Blight, J.D. (1981). Performance and robustness trades in lqg regulator design. *Proceedings of the 20th IEEE Conference on Decision and Control, San Diego, California*.
- Moore, J.B. and Xia, L. (1987). Loop recovery and robust state estimate feedback designs. *Institute of Electrical and Electronics Engineers Transactions on Automatic Control*, **AC-32**(6), 512–517.

- Morari, M. and Zafiriou, E. (1998). *Robust process control*. Prentice Hall, Upper Saddle River, New Jersey.
- Nelson, P.A., Curtis, A.R.D., Elliott, S.J., and Bullmore, A.J. (1987). The minimum power output of free field point sources and the active control of sound. *Journal of Sound and Vibration*, **116**.
- Nelson, P.A. and Elliott, S.J. (1992). *Active control of sound*. Academic press, London.
- Olson, H.F. and May, E.G. (1953). Electronic sound absorber. *Journal of the Acoustical Society of America*, **25**(6), 1130–1136.
- Petitjean, B. and Legrain, I. (1996). Feedback controllers for active vibration suppression. *Journal of Structural Control*, **3**, 111–127.
- Petitjean, B., Legrain, I., Simon, F., and Pautin, S. (2002). Active control experiments for acoustic radiation reduction of a sandwich panel: feedback and feedforward investigations. *Journal of Sound and Vibration*, **252**(1), 19–36.
- Preumont, A. (2002). *Vibration control of active structures: An introduction*. Kluwer Academic Publishers.
- Rafaely, B., Elliott, S.J., and Garcia-Bonito, J. (1999). Broadband performance of an active headrest. *Journal of the Acoustical Society of America*, **106**(2), 787–793.
- Scholte, E. and D'Andrea, R. (2003). Active vibro-acoustic control of a flexible beam using distributed control. *Proceedings of the American Control Conference, Denver, CO, June 4-6*. pp. 2640–2645.
- Shinozuka, M. and Deodatis, G. (1991). Simulation of stochastic processes by spectral representation. *Applied Mechanics Review*, **44**(4), 191–204.
- Shinozuka, M. and Jan, C.M. (1972). Digital simulation of random processes and its applications. *Journal of Sound and Vibration*, **25**(1), 111–128.
- Skogestad, S. and Postelthwaite, I. (1996). *Multivariable feedback control: analysis and design*. John Wiley and Sons, West Sussex, England.
- Stein, G. and Athans, M. (1987). The lqg/ltr procedure for multivariable feedback control design. *Institute of Electrical and Electronics Engineers Transactions on Automatic Control*, **AC-32**(2), 105–114.
- Strawderman, W.A. (1990). Wavevector-frequency analysis with applications to acoustics. Technical report.
- Sullivan, J.M., Hubbard, J.E., and Burke, S.E. (1996). Modeling approach for two-dimensional distributed transducers of arbitrary spatial distribution. *Journal of the Acoustical Society of America*, **99**(5), 2965–2974.
- Sutton, T.J., Elliott, S.J., Nelson, P.A., and Moore, I. (1990). Active control of multiple-source random sound in enclosures. volume 12. pp. 689–693.
- Tam, C.K.W. (1991). Jet noise generated by large-scale coherent motion. H.H. Hubbard, editor, *Aeroacoustics of Flight Vehicles, Theory and Practice*. NASA Langley Research Center, Hampton VA, pp. 311–390.
- Tam, C.K.W. (1995). Supersonic jet noise. *Annual Review of Fluid Mechanics*, **27**, 17–43.
- Tang, Y.Y., Silcox, R.J., and Robinson, J.H. (1996). Sound transmission through cylindrical shell structures excited by boundary layer pressure fluctuations. *Proceedings of the 2nd AIAA and CEAS Aeroacoustics Conference, State College, PA, May 6-8*. AIAA-96-1760.

- Tay, T.T. and Moore, J.B. (1991). Enhancement of fixed controllers via adaptive-q disturbance estimate feedback. *Automatica*, **27**(1), 39–53.
- Thomas, D.R. and Nelson, P.A. (1995). Feedback control of sound radiation from a plate excited by a turbulent boundary layer. *Journal of the Acoustical Society of America*, **98**(5), 2651–2662.
- Tsai, S.W. and Hahn, H.T. (1980). *Introduction to composite materials*. Technomic Publishing Company, Inc.
- Turner, T.L., Cabell, R.H., Cano, R.J., and Fleming, G.A. (2006). Design, fabrication, and testing of a SMA hybrid composite jet engine chevron. *Proceedings of SPIE – Volume 6173: Smart Structures and Materials*.
- Vaicaitis, R., Grosveld, F.W., and Mixson, J.S. (1985). Noise transmission through aircraft panels. *Journal of Aircraft*, **22**(4), 303–310.
- Vaicaitis, R., Slazak, M., and Chang, M.T. (1980). Noise transmission and attenuation by stiffened panels. *Proceedings of the 6th AIAA Aeroacoustics Conference, Hartford, Connecticut, June 4-6*. AIAA-80-1034.
- Vipperman, J.S. and Clark, R.L. (1996). Implementation of an adaptive piezoelectric sensor/actuator. *American Institute of Aeronautics and Astronautics Journal*, **34**(10), 2102–2109.
- Vipperman, J.S. and Clark, R.L. (1999). Implications of using colocated strain-based transducers for output active structural acoustic control. *Journal of the Acoustical Society of America*, **106**(3), 1392–1399.
- Widrow, B.J. and Stearns, S.D. (1985). *Adaptive Signal Processing*. Prentice-Hall, Englewood Cliffs, New Jersey.
- Wilkie, W.K., Bryant, R.G., High, J.W., Fox, R.L., Hellbaum, R.F., Jalink, A., Little, B.D., and Mirick, P.H. (2000). Low-cost piezocomposite actuator for structural control applications. *Proceedings of the SPIE 7th Annual International Symposium on Smart Structures and Materials, Newport Beach, CA*.
- Williams, T. (1994). Transmission zeros and high-authority/low-authority control of flexible space structures. *Journal of Guidance, Control, and Dynamics*, **17**(1), 170–174.
- Willich, S.N., Wegscheider, K., Stallmann, M., and Keil, T. (2006). Noise burden and the risk of myocardial infarction. *European Heart Journal*, **27**(3), 276–282.
- Yang, S.Y. and Huang, W.H. (1998). Is a colocated piezoelectric sensor/actuator pair feasible for an intelligent beam? *Journal of Sound and Vibration*, **216**(3), 529–538.
- Zhang, Z. and Freudenberg, J.S. (1990). Loop transfer recovery for nonminimum phase plants. *Institute of Electrical and Electronics Engineers Transactions on Automatic Control*, **35**(5), 547–553.

Vita

Noah was born on December 17, 1979 in Dyke, Virginia. In 1997, he followed his older brother to Virginia Tech and began studying Mechanical Engineering. After graduating with a Bachelor's Degree in 2002, he began his Master's degree under the direction of Dr. Will Saunders. The title of his Master's thesis was "Design and Validation of a Proportional Throttle Valve System for Liquid-Fuel Active Combustion Control." In 2003, Noah received a fellowship from the National Institute of Aerospace, which enabled him to continue graduate study at Virginia Tech while residing with the Structural Acoustics Branch at NASA Langley Research Center in Hampton, Virginia. His research was performed under the guidance of Dr. Ran Cabell and Dr. Chris Fuller.